Hydrogeochemical changes impacting radium activity in the Midwestern Cambrian-Ordovician aquifer system

By

Amy K. Wiersma

A dissertation submitted in partial fulfillment of the requirements for the degree of

Doctor of Philosophy

(Environmental Chemistry and Technology)

at the

UNIVERSITY OF WISCONSIN-MADISON

2023

Date of final oral examination: 02/03/2023

The dissertation is approved by the following members of the Final Oral Committee:

Matthew Ginder-Vogel, Associate Professor, Environmental Chemistry and Technology, Civil and Environmental Engineering
Madeline Gotkowitz, Hydrogeologist, Wisconsin Department of Natural Resources
Christopher Zahasky, Assistant Professor, Geoscience
James Hurley, Professor, Environmental Chemistry and Technology, Civil and Environmental Engineering
Gregory Harrington, Professor, Environmental Chemistry and Technology, Civil and Environmental Engineering

Abstract

Hydrogeochemical changes impacting radium activity in the Midwestern Cambrian-Ordovician aquifer system

by

Amy K. Wiersma

Doctor of Philosophy – Environmental Chemistry and Technology Program

University of Wisconsin-Madison

Associate Professor Matthew Ginder-Vogel

The Midwestern Cambrian-Ordovician aquifer system (MCOAS) is a valuable source of drinking water in the North Central United States, but can contain elevated levels of naturally occurring radium (Ra). Long-term consumption of Ra in drinking water is linked to an increased risk of bone cancer, and is therefore federally regulated in the U.S. at 185 millibecquerels per liter (mBq/L) or 5 picocuries per liter (pCi/L) for the total of ^{226}Ra and ^{228}Ra. While the hydrogeochemical conditions associated with elevated activity Ra in the MCOAS are well documented, less is known about how Ra occurrence is affected due to hydrogeochemical changes initiated by natural and anthropogenic aspects. This dissertation uses field and modeling studies to explore Ra occurrence when hydrogeochemical change is instigated by factors including natural hydrogeologic conditions, release of organic contaminants to the subsurface, and well field management. Radium activity increases as groundwater evolves along a regional flow path and approaches the boundary of the Maquoketa shale, a regional confining unit; here, the aquifer becomes locally confined and groundwater is older with geochemical conditions conducive to Ra

mobility, including low dissolved oxygen and elevated total dissolved solids (TDS). A complex organic chemical mixture released to the subsurface alters aquifer pH, redox, and TDS conditions, resulting in elevated Ra activity within the dissolved phase plume that highlights the importance of characterizing Ra at hydrocarbon-contaminated sites. As demonstrated by groundwater flow modeling, well construction and pumping rates can alter hydraulic gradients that enhance groundwater exchange between units of different geochemistry and modify the contribution of groundwater from stratigraphic units with different Ra activity to wells. Overall, this dissertation provides insight into how environmental and anthropogenic factors influence hydrogeochemical conditions and Ra occurrence in groundwater, and can help guide long-term groundwater management strategies for mitigating Ra activity in groundwater pumped from the MCOAS.

Table of Contents

List of Figures

List of Tables

Acknowledgements

Thank you to my wonderful colleagues, friends, and family for supporting me throughout my time as a graduate student and for helping me develop into the scientist I am today. I truly appreciated all of the encouragement as I was working on this dissertation, whether it was in the form of conversation, constructive feedback, or adventures.

Thank you to my advisor, Matt Ginder-Vogel, for all of your support and feedback. I am thankful that you gave me the opportunity to explore my research interests while in graduate school. You helped me build confidence in myself and my science, and for that I will be forever grateful. Also, thank you for encouraging me to maintain a healthy work-life balance. I truly appreciated all of our discussions about science and beyond.

Thank you to Madeline Gotkowitz, for your mentorship and for helping me find my footing when I started graduate school. Thank you for encouraging me to take action by telling me to just "get out there and sample" when I was hung up on the details. I have enjoyed our many discussions, where I have learned a great deal from you about data analysis and how to think critically as a hydrogeologist. Your passion and excitement for science are contagious.

I would also like to thank the other members of my dissertation committee, including Jim Hurley, Greg Harrington, and Chris Zahasky, for taking the time to provide valuable feedback on this dissertation. I appreciate your support and discussions in thinking more critically about the implications of this work, as well as future directions.

I appreciated the opportunity to join a team of researchers working on radium when I started graduate school, including Madeline Gotkowitz, Florence Udenby, Marie Dematatis, and Madeleine Mathews. Florence, thank you for your help with accessing well construction reports

and your insights on radium regulation in drinking water. Marie, thank you for teaching me ArcGIS skills and for being a great office mate. I have fond memories of going through well construction reports and presenting at conferences with you. To Maddie, thank you for being a positive role model, mentor, and friend. Thank you for your willingness to share the radium domain with me. I appreciated your patience and willingness to teach me so many skills in grad school, whether it was how to collect and preserve groundwater samples, use the glovebox, or plan an experiment. Thank you for being a sounding board and providing constructive feedback. I enjoyed our many discussions about radium, isotopes, and beyond. Your excitement about radium and science truly made me feel like I was part of something special.

Thank you to Sean Scott, a wonderful collaborator, mentor, and friend. You helped me develop valuable lab and analytical skills that will be helpful beyond graduate school, from sample purification to running the multi-collector. I am grateful for your willingness to share your knowledge and enthusiasm about the world of isotopes. Your positive outlook and anecdotes made me excited to come into the lab every day.

I am thankful for the opportunity to collaborate with the University Consortium and the Morwick G360 Groundwater Research Institute, particularly Beth Parker, Jessica Meyer, and Glen Hook. Thank you for your eagerness to pursue an interesting research direction with us, and for sharing the multi-level systems, rock core, and wealth of data associated with the site. A big thanks also to Jessica Bulova and Olenka Forde for sampling assistance.

I appreciate the many other groups and individuals that made this dissertation work possible. I would like to thank the Fond du lac Water Utility, Ripon Water Utility, and Fond du Lac County Health Department, as well as the participating residents, businesses, and public water systems in Fond du Lac County for help with executing the field sampling campaign associated

with Chapter 2 of this dissertation. Thank you also to Madeleine Mathews and Gabrielle Campagnola for sampling assistance. I am grateful to many folks at the Wisconsin Geological and Natural History Survey, including Pete Schoephoester, Pete Chase, and Kathy Roushar for sharing field equipment, geologic logs, and shapefiles. Thank you also to Carsyn Ames for curating rock core and performing pXRF analysis, and Esther Stewart for the many conversations early in graduate school about Precambrian geology. I appreciate the speedy replies from Jim Rumbaugh to my many emails with questions about Groundwater Vistas and MODFLOW. Many thanks to the Wisconsin State Laboratory of Hygiene Trace Metals Laboratory for sharing lab space with me, and the UW-Madison Biotechnology Isotope Ratio Laboratory for performing stable water isotope analysis on groundwater samples. To James Lazarcik, for keeping WSEL running and making it such a great place to work. Thank you for your patience in answering all of my random questions, and teaching me how to run and care for instruments. I also want to thank my WSEL colleagues and members of the Ginder-Vogel Group for maintaining such a positive work culture and providing support and feedback on papers, presentations, and more.

To my family and friends, thank you for your love and encouragement while I was in school all of this time. I would also like to thank my family-in-law for welcoming me with open arms and supporting me while I pursued my Ph.D. Special thanks to my husband, Justin, whom I met just before beginning graduate school. You have been my rock every step of the way, supporting and encouraging me to keep going.

Chapter 1

Introduction

1.1 Motivation

This dissertation examines the impact of natural and anthropogenic-induced hydrogeochemical changes on the mobility of radium (Ra) in the Midwestern Cambrian-Ordovician aquifer system (MCOAS), an important drinking water source in the North Central United States. Groundwater is 100 times more abundant than lakes and streams,[1] and provides nearly half of the global drinking water supply.[2] However, groundwater recharge is unevenly distributed on Earth due to spatial variation in factors such as precipitation, temperature, and geology; recharge is expected to shift as a result of climate change.[3, 4] Population increases and scientific and technological advancements have increased the use of groundwater in the last half-century.[5] This has resulted in groundwater depletion, especially in semi-arid and arid regions with little modern recharge and large 'fossil' or non-renewable groundwater resources.[3, 6]

The prevalence of anthropogenic and naturally occurring contaminants can also limit the quantity of groundwater available for drinking. Radium is an example of a naturally-occurring, or geogenic, groundwater contaminant that can degrade groundwater quality. Elevated Ra activity is most prevalent in the MCOAS among all other U.S. aquifer systems,[7] and can pose a challenge for public drinking water systems using the MCOAS for drinking water. Public drinking water systems out of compliance with Ra drinking water regulations may need to install expensive treatment systems or invest in an alternative water supply. While geochemical conditions impacting Ra mobility in the MCOAS at broad and local scales are well-documented, relatively few studies have documented Ra mobility under hydrogeochemical changes arising from natural

and anthropogenic factors. This work combines field and modeling studies to examine the impact of changing hydrogeochemical conditions on Ra mobility in the MCOAS, arising from factors including 1) natural groundwater evolution at the transition between unconfined and confined aquifer conditions, 2) anthropogenic hydrocarbon spills, and 3) human-controlled well construction and groundwater withdrawal.

1.2 Contaminants in groundwater

The release of anthropogenic and geogenic contaminants into groundwater can limit drinking water availability. Naturally-occurring contaminants such as arsenic, uranium, and Ra are more prevalent than anthropogenic contaminants in U.S. aquifer systems,[8] highlighting the need to understand factors affecting geogenic contaminant occurrence in groundwater. Geochemical factors that can impact geogenic contaminant partitioning from solid phases to groundwater include 1) pH, 2) oxidation-reduction (redox) conditions, 3) presence of ions that form soluble complexes with metals, 4) sorption processes and effects of ion competition, 5) evaporative concentration, and 6) mixing and dilution.[9, 10] Contaminant occurrence in groundwater is also impacted by transport processes including advection, dispersion, and diffusion.[9] New wells in the U.S. are being drilled deeper, accessing more fossil (> 12,000 years) groundwater; this trend is not always associated with declining water levels, and in some cases may be related to reducing exposure to surface-borne contaminants typically found in shallow groundwater.[11] For example, some public water systems in Wisconsin have drilled wells deeper to avoid anthropogenic nitrate elevated in the shallow aquifer system, but as a result access older water with geochemical conditions conducive to Ra mobility (e.g., high total dissolved solids, low dissolved oxygen).

1.3 Radium as a groundwater contaminant

1.3.1 Chemical behavior of radium

Radium is a radioactive, alkaline earth metal with four naturally-occurring isotopes: ^{223}Ra, ^{224}Ra, ^{226}Ra, and ^{228}Ra. All of these isotopes are derived from the alpha decay of thorium parent nuclides within the thorium (Th)-232, uranium (U)-235, and U-238 decay chains, and ultimately decay to stable lead isotopes (Figure 1.1). The prevalence of each isotope is dictated by differences in half-lives and the quantity of parent nuclides in the environment. For example, ^{223}Ra has both a short half-life (11.4 d) and a parent nuclide of low abundance (^{235}U) that exists as < 1% of natural U. Therefore, ^{223}Ra is difficult to analyze and generally not a concern for water quality. On an activity (decay rate) basis, ^{224}Ra, ^{226}Ra, and ^{228}Ra are approximately equally abundant due to the equal abundance of ^{232}Th and ^{238}U in the crust. However, the shorter half-life of ^{224}Ra (3.6 d) results in a lower environmental prevalence compared to ^{226}Ra (1600 yr) and ^{228}Ra (5.8 yr). The relatively short half-life of ^{228}Ra compared to ^{226}Ra may limit its potential for 'unsupported' transport, transport without the presence of an equivalent amount of the parent in solution.[7] Radium exhibits similar chemical behavior as other alkaline earth metals (e.g., barium, strontium), has one oxidation state of Ra(II), and exists primarily as Ra^{2+}(aq) under environmental conditions.[12]

1.3.2 Radium health effects and drinking water standards

Radium is a human health concern due to its radioactivity. Upon ingestion, Ra accumulates in the bone similar to calcium, increasing the risk of bone cancer and other detrimental health effects.[13-15] The World Health Organization recommends drinking water guidance levels of 100 mBq/L for ^{228}Ra and 1,000 mBq/L for ^{224}Ra and ^{226}Ra, based on an annual individual dose criterion of 0.1 mSv.[16] In 2000, the U.S. Environmental Protection Agency (EPA) implemented the Radionuclide Rule to set limits for radioactivity levels in drinking water.[17] The U.S. EPA Maximum Contaminant Level (MCL) for Ra in drinking water is 185 millibecquerels per liter

(mBq/L) or 5 picocuries per liter (pCi/L) for the combined activity of ^{226}Ra and ^{228}Ra. Public water systems out of compliance with the Ra MCL often employ several strategies for reducing Ra levels in pumped groundwater, including well reconstruction or blending with groundwater from a different well. If these strategies are unsuccessful, public water systems must install expensive treatment systems or switch to an alternative water supply. Treatment options for Ra in drinking water include lime softening, cation exchange, reverse osmosis, and hydrous manganese oxide and manganese greensand filtration; these methods leave waste concentrated in Ra that creates environmental and disposal concerns.[18, 19]

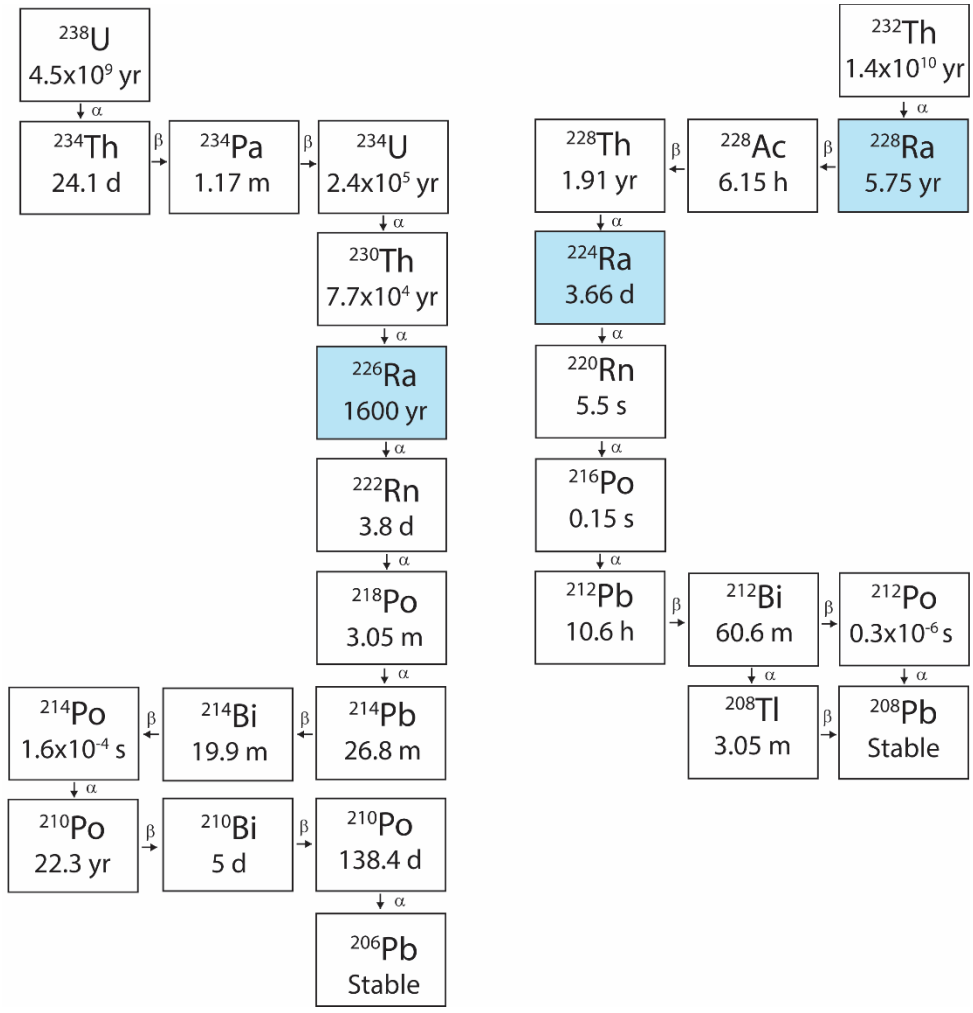

Figure 1.1 ^{238}U and ^{232}Th decay chains denoting nuclide half-lives and type of radiation (alpha, α, or beta, β). Radium nuclides ^{224}Ra, ^{226}Ra, and ^{228}Ra are highlighted in blue.

1.3.3 Radium prevalence in aquifer systems

Radium occurs at elevated levels in aquifers worldwide. For example, elevated Ra activity has been observed in sandstone aquifers lacking sufficient sorption sites such as the Saq aquifer in Saudi Arabia, the Disi aquifer in Jordan, and the Nubian aquifer in Egypt.[20-22] In the U.S., elevated Ra activity above the MCL in public drinking water supplies derived from aquifer systems affects approximately 5 million or more people.[8] Elevated Ra activity above U.S. drinking water standards has been measured in aquifer systems including the MCOAS, the North Atlantic Coastal Plain, the Floridan carbonate aquifer, the felsic crystalline rocks and glacial sands and gravels in New England, the Gulf Coastal Plain, and the Mesozoic basins of the Appalachian Piedmont.[7]

Among all principal U.S. aquifer systems, the greatest number of exceedances of the MCL for combined Ra occur in the MCOAS, a productive aquifer composed primarily of sandstone and dolostone (Figure 1.2).[7] Many studies have examined geochemical influences on Ra mobilization to the MCOAS at the broad scale, and demonstrate that Ra sorption efficiency in the MCOAS is impacted by geochemical conditions including low pH, as well as high total dissolved solids (TDS) and low dissolved oxygen typically associated with older groundwater.[7, 23-26] Examination of Ra activity within discrete stratigraphic intervals of the MCOAS demonstrates that the association of elevated Ra with these geochemical conditions can vary at the local scale.[27, 28] Elevated Ra activity is more commonly found where the Maquoketa shale, a regional confining unit, overlies the MCOAS and limits modern groundwater recharge.[23, 29] This dissertation investigates Ra mobility within three different regional hydrogeologic settings, where the MCOAS is: 1) unconfined by the Maquoketa shale (Chapter 3), confined by the Maquoketa shale (Chapter 4), and 3) at the boundary of the Maquoketa shale (Chapter 2) (Figure 1.2).

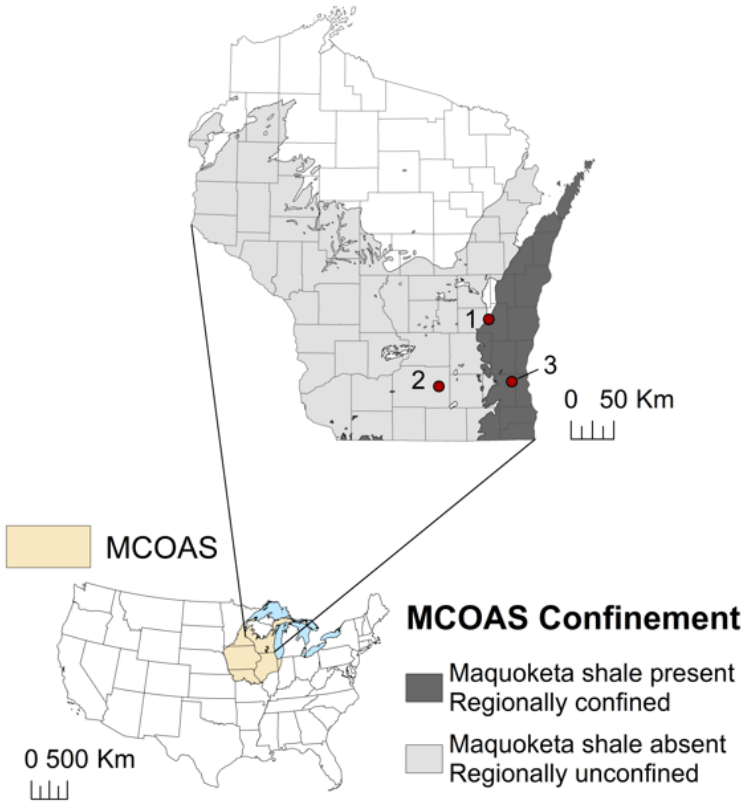

Figure 1.2 Map showing the extent of the Midwestern Cambrian-Ordovician aquifer system (MCOAS) and the location of study sites in Wisconsin where the MCOAS is 1) at the boundary of the Maquoketa shale (Chapter 2), 2) unconfined by the Maquoketa shale (Chapter 3), and 3) confined by the Maquoketa shale (Chapter 4).

1.4 Radium sources to groundwater

1.4.1 Alpha recoil and the distribution of parent isotopes

Radium activities in groundwater reflect the net balance between Ra inputs from aquifer solids (e.g., recoil, desorption, dissolution) and Ra outputs (sorption, co-precipitation, decay) (Figure 1.3).[30] The primary source of radionuclides in aquifer systems is alpha recoil, a process in which the parent nuclide emits an alpha particle and daughter nuclide in opposite directions. Parent nuclides ^{230}Th and ^{232}Th undergo alpha recoil to produce the two major Ra isotopes: ^{226}Ra and ^{228}Ra, respectively. Alpha recoil is a powerful process and has the potential to eject Ra to groundwater from within the mineral lattice, depending on the proximity of the parent nuclide to

the edge of the mineral.[31] Secular equilibrium is achieved when the rate of daughter nuclide generation is the same as the rate of parent nuclide decay, and the activities of the parent and daughter nuclides become equal. Deviation from secular equilibrium can indicate physical or geochemical factors are removing Ra from the site of parent decay.[28, 32]

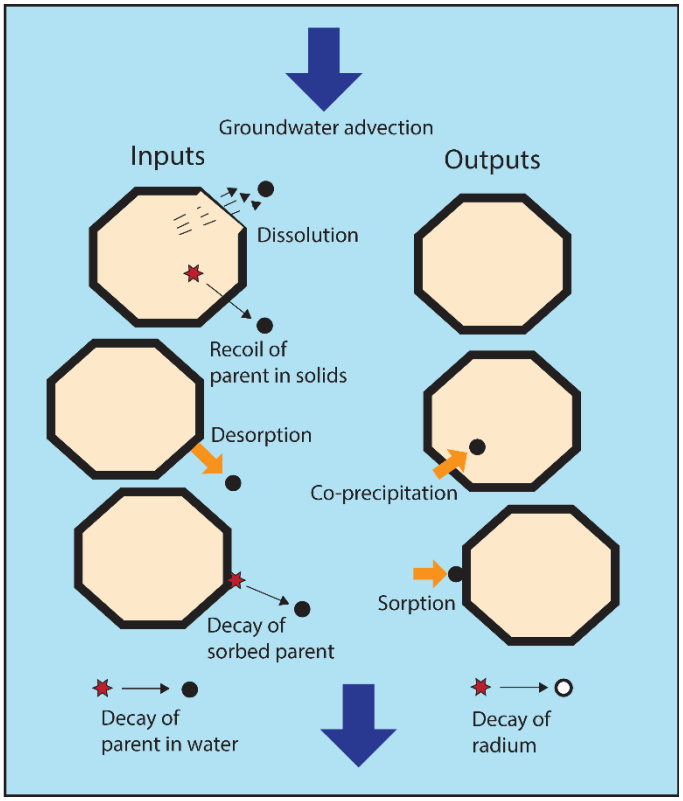

Figure 1.3 Schematic illustration of inputs and outputs controlling radium activities in a porous aquifer system. Adapted from Vengosh et al. (2021).[30]

The distribution of parent nuclides in aquifer solids controls the distribution of Ra in groundwater. The $^{228}Ra/^{226}Ra$ ratio in groundwater can provide information about the relative importance of U and Th sources within aquifer solids. For example, a $^{228}Ra/^{226}Ra > 1$ typical of sandstone aquifers suggests the prevalence of silicate minerals enriched in Th, while a $^{228}Ra/^{226}Ra < 1$ typical of carbonate aquifers suggests the prevalence of carbonate minerals enriched in U.[33] Whole-rock analysis of MCOAS stratigraphic units indicates shale and dolostone units are

enriched in ^{238}U and ^{226}Ra; the highest amount of extractable or 'geochemically mobile' ^{238}U is also associated with shale and dolostone units, while the highest amount of extractable ^{226}Ra is associated with shales and feldspathic, glauconitic sandstones.[28, 34] The main sources of Th in the MCOAS are mineral surface coatings as well as feldspar and accessory minerals present in shale and sandstone units.[23, 27]

The locations of ^{226}Ra and ^{228}Ra production are dictated by the location of parent isotopes U and Th, respectively. The mineral lattice damage associated with alpha decay of ^{238}U to ^{234}U can increase the potential for ^{234}U leaching to groundwater, resulting in typical aqueous $^{234}U/^{238}U$ ratios > 1.[35, 36] Uranium is mobile in groundwater under oxic conditions, where it is present in the U(VI) oxidation state and forms aqueous carbonate complexes.[37, 38] In contrast, Th is relatively immobile in groundwater and sorbs strongly to aquifer solids.[39] Similar to Ra, Th has one oxidation state (IV) under environmentally-relevant conditions and therefore does not undergo redox chemistry.

1.5 Geochemical mechanisms controlling radium activity in groundwater

1.5.1 Sorption

Radium sorbs rapidly to solid phases, occurring on the order of minutes within fresh groundwater systems.[40] Therefore, ^{226}Ra and ^{228}Ra will participate in sorption processes (e.g., adsorption and desorption) many times before their own decay. Radium has a strong sorption affinity for transition metal (hydr)oxide minerals, clay minerals, and organic materials; therefore, the presence or absence of these sorbents within hydrostratigraphic units is an important factor for determining Ra sorption capacity. While manganese (Mn) (hydr)oxides are a stronger adsorbent of trace elements, iron (Fe) (hydr)oxides are typically more abundant in groundwater systems.[12,

[41-43] Clay minerals such as illite and glauconite can also sorb considerable concentrations of Ra.[44-46] Radium sorption to organic materials can be important in organic-rich shales.[47] Additionally, low concentrations of Ra can sorb to carbonate, sulfate, and silicate minerals at circumneutral pH.[44, 48, 49] While Ra sorption is most efficient in oxic systems with neutral pH, low TDS, and high sorption capacity, changes in aquifer geochemical conditions can decrease Ra sorption efficiency.

1.5.1.1 Geochemical conditions impacting radium sorption efficiency

Radium sorption efficiency can be impacted by changes in geochemical conditions including salinity, pH, and dissolved oxygen concentrations (i.e., redox conditions). Increased Ra activities can occur when there are high levels of total dissolved solids (TDS), due to competition between Ra and divalent cations (e.g., calcium, magnesium) for sorption sites.[50-52] Additionally, elevated TDS can increase ion-ion interactions (i.e., ionic strength) and increase the stability of uncharged Ra complexes (e.g., $RaCl_2$ and $RaSO_4$) that do not readily sorb to mineral surfaces.[30] Radium sorption efficiency is low under acidic pH (< 5), due to the more positive surface charge of mineral surfaces as pH drops below the point of zero charge of the mineral surface.[12] Redox impacts on radium mobility are related to the stability of Fe and Mn (hydr)oxide minerals, important sorption surfaces for Ra. Under anoxic conditions Fe and Mn (hydr)oxides will be absent or undergo reductive dissolution, reducing the number of sorption sites available for Ra.[7, 24, 41, 48]

While geochemical conditions impacting Ra mobility can change naturally in aquifer systems, they can also arise as a result of human-induced factors. Heavily pumped aquifer systems can draw modern, shallow groundwater elevated in anthropogenic contaminants downward to deeper aquifers.[53, 54] For example, the release of agricultural waste elevated in nitrate paired with high groundwater pumping rates can result in increased Ra levels in groundwater due to decreased pH.[55] Salt used for de-icing roads can migrate to groundwater, increasing cation competition for

sorption sites and stability of Ra-chloride complexes.[56] Long open boreholes typical of many public water system wells can foster groundwater exchange between hydrostratigraphic units with different geochemistry, releasing geogenic contaminants such as Ra.[57] A better understanding of anthropogenic factors influencing the mobility of Ra and other geogenic contaminants is necessary to develop long-term groundwater management strategies.

1.5.2 Co-precipitation

While Ra activities in groundwater are too low to form pure Ra phases, Ra can co-precipitate with other cations in sulfate and carbonate minerals.[58, 59] Barite ($BaSO_4$) precipitation occurs in a solid solution, incorporating cations including Ba^{2+}, Sr^{2+}, and Ra^{2+}.[60] Competition with these other cations can limit Ra co-precipitation into barite.[61, 62] Additionally, sulfate-reducing aquifer conditions may cause reductive dissolution of barite, releasing associated Ra and preventing further precipitation of barite.[63-65] To co-precipitate Ra, the host mineral must be close to saturation. However, barite precipitation is considered slow at slight supersaturation and is therefore likely less efficient than adsorption in sequestering Ra.[66] While not as well understood, Ra can also be incorporated into carbonate solid solutions (e.g., aragonite, $CaCO_3$).[67]

1.6 Research objectives and approach

While the geochemical conditions enhancing Ra mobility in groundwater are well-studied, less is known about the impact of evolving hydrogeochemical conditions on Ra mobility. Identification of the natural and anthropogenic factors that alter geochemical conditions and increase Ra activity in groundwater will support long-term groundwater management strategies designed to minimize concentrations of Ra and other geogenic contaminants in public water supply wells. In this dissertation, field and model-based approaches are used to identify hydrogeochemical

changes affecting Ra activity in the MCOAS where or when 1) the aquifer transitions from unconfined to confined, 2) the aquifer is contaminated with a complex organic mixture, and 3) the aquifer is subjected to different well construction and pumping scenarios.

Chapter 2 investigates Ra mobility along a groundwater flow path in east-central Wisconsin, where the MCOAS transitions from regionally unconfined to confined. While previous work noted that Ra activities are typically higher where the Maquoketa shale confining unit overlies the MCOAS, the mechanisms responsible for elevated Ra at the boundary of the Maquoketa shale are not well understood. Samples from wells with various depths were collected along the flow path and analyzed for Ra and a suite of isotopic tracers. Radium activities increase as groundwater naturally evolves from a younger, (Mg, Ca)-HCO_3-type upgradient to an older, Ca-(SO_4, Cl)-type downgradient. Downgradient (west of the Maquoketa shale), the flow system is impacted by uneven Precambrian basement topography and confinement from Quaternary glacial lake clays, highlighting the importance of local conditions. Radium is moderately correlated with TDS, suggesting that cation competition for sorption sites contributes to elevated Ra in groundwater. The highest Ra activities occur in wells with a 'mixed' redox process, where young, oxic water mixes with old, anoxic water over long open boreholes. These wells likely receive more of the old, anoxic water with high dissolved Fe, Mn, and Ra concentrations associated with the absence or dissolution of Fe and Mn (hydr)oxides. Along with identifying Ra mobilization mechanisms in a complex hydrogeologic setting, these results highlight the impacts of well location and construction on Ra activity in pumped groundwater.

Chapter 3 examines a site within the MCOAS that is contaminated with a complex organic mixture of organic chemicals released from a chemical recycling facility. While other studies have documented the mobilization of other geogenic contaminants in hydrocarbon-contaminated

aquifers due to changes in geochemical conditions, none have examined Ra occurrence. The released mixture consists of chlorinated solvents, ketones, and aromatics that migrated as a dense non-aqueous phase liquid (DNAPL) to the subsurface. Multi-level monitoring systems are used to collect groundwater samples at discrete depths near the DNAPL source zone and the middle of the dissolved phase plume, in the direction of groundwater flow. Changes in geochemical conditions including pH, TDS, and redox result in ^{226}Ra activities near the source zone up to ten times higher than background activities. Correlations support Ra release from Fe and Mn (hydr)oxide dissolution and cation competition with high concentrations of divalent cations. ^{226}Ra activities return to near background levels near the middle of the dissolved phase plume, where geochemical modeling identifies sorption to secondary mineral phases (e.g., illite) as the primary Ra sink within the plume. Results demonstrate the importance of aquifer mineralogy and emphasize the importance of examining Ra and other geogenic contaminants at hydrocarbon-contaminated sites.

Chapter 4 evaluates the impact of different well construction and pumping rates on Ra activities in a region where the MCOAS is heavily pumped by public water systems. Recent increases in Ra activity in the Wisconsin MCOAS have raised questions about potential human-induced factors impacting Ra mobility in groundwater, but these factors have not yet been investigated. Here, a steady-state groundwater flow model is developed to simulate hydrogeologic conditions in southeast Wisconsin, and evaluate the contribution of several units enriched in Ra activity to public supply wells under different well construction and pumping rate scenarios. Public water systems experiencing elevated Ra activity in this region are often advised to extend casing past shale facies within the Eau Claire Formation, an assumed source of Ra. Model results reveal that while casing through the Eau Claire Formation eliminates direct contribution from the shale facies to the well, pumping from deeply-cased wells creates stronger a vertical gradient. This

increases the flux from the simulated shale-rich layer to the underlying sandstone; this flux increases with the pumping rate. The model also demonstrates that reconstruction (extending the depth of casing) doubles the contribution of deep groundwater from the base of the sandstone, presumably older water elevated in TDS and Ra activity. These results highlight how pumping can alter hydraulic gradients, potentially impacting Ra mobility by changing flow paths and fostering groundwater exchange between units with different geochemistry.

1.7 References

1. Shiklmanov, I.A., *World fresh water resources*, in *Water in Crisis*, P.H. Gleick, Editor. 1993, Oxford University Press: New York. p. 13-24.
2. Smith, M., Cross, K., Paden, M., and Laban, P., *Spring — Managing groundwater sustainability*. IUCN. 2016, Gland, Switzerland.
3. Döll, P., *Vulnerability to the impact of climate change on renewable groundwater resources: a global-scale assessment.* Environmental Research Letters, **2009**. *4*(3).
4. Gleeson, T., Befus, K.M., Jasechko, S., Luijendijk, E., and Cardenas, M.B., *The global volume and distribution of modern groundwater.* Nature Geoscience, **2016**. *9*(2): p. 161-167.
5. Llamas, M.R. and Martínez-Santos, P., *Intensive groundwater use: Silent revolution and potential source of social conflicts.* Journal of Water Resources Planning and Management, **2005**. *131*(5): p. 337-341.
6. Konikow, L.F. and Kendy, E., *Groundwater depletion: A global problem.* Hydrogeology Journal, **2005**. *13*(1): p. 317-320.
7. Szabo, Z., dePaul, V.T., Fischer, J.M., Kraemer, T.F., and Jacobsen, E., *Occurrence and geochemistry of radium in water from principal drinking-water aquifer systems of the United States.* Applied Geochemistry, **2012**. *27*(3): p. 729-752.
8. Belitz, K., Fram, M.S., Lindsey, B.D., Stackelberg, P.E., Bexfield, L.M., Johnson, T.D., Jurgens, B.C., Kingsbury, J.A., McMahon, P.B., and Dubrovsky, N.M., *Quality of groundwater used for public supply in the continental United States: A comprehensive assessment.* ACS ES&T Water, **2022**. *2*(12): p. 2645–2656.
9. Drever, J.I., *The Geochemistry of Natural Waters*. 1988, Englewood Cliffs, NJ: Prentice-Hall.
10. Hem, J.D., *Study and interpretation of the chemical characteristics of natural water*. 1992, U.S. Geological Survey,.
11. Gebreegziabher, M., Jasechko, S., and Perrone, D., *Widespread and increased drilling of wells into fossil aquifers in the USA.* Nature Communications, **2022**. *13*(1).
12. International Atomic Energy Agency, *The Environmental Behaviour of Radium: Revised Edition*, in *Technical Report No. 476 44–51*. 2014, IAEA: Vienna.
13. Mays, C.W., Rowland, R.E., and Stehney, A.F., *Cancer risk from the lifetime intake of Ra and U isotopes.* Health Physics, **1985**. *48*(5): p. 635-47.
14. Lyman, G.H., Lyman, C.G., and Johnson, W., *Association of leukemia with radium groundwater contamination.* Journal of the American Medical Association, **1985**. *254*(5): p. 621-626.
15. Finkelstein, M. and Kreiger, N., *Radium in drinking water and risk of bone cancer in Ontario youths: a second study and combined analysis.* Journal of Occupational and Environmental Medicine, **1996**. *53*: p. 305-311.
16. World Health Organization, *Guidelines for drinking-water quality: fourth edition incorporating the first and second addenda*. 2022: Geneva.
17. U.S. Environmental Protection Agency, *National primary drinking water regulations*, in *Federal Register*. 2000.
18. Qureshi, N. and Nelson, S., *Radium removal by HMO and manganese greensand.* Journal - American Water Works Association, **2003**. *95*(3): p. 101-108.

19. Szabo, Z., Jacobsen, E., Kraemer, T.F., and Parsa, B., *Concentrations and environmental fate of Ra in cation-exchange regeneration brine waste disposed to septic tanks and accumulation in sludge, New Jersey Coastal Plain, USA.* Journal of Environmental Radioactivity, **2008**. *99*(6): p. 947-64.
20. Vengosh, A., Hirschfeld, D., Vinson, D., Dwyer, G., Raanan, H., Rimawi, O., Al-Zoubi, A., Akkawi, E., Marie, A., Haquin, G., Zaarur, S., and Ganor, J., *High naturally occurring radioactivity in fossil groundwater from the Middle East.* Environmental Science & Technology, **2009**. *43*(6): p. 1769-1775.
21. Faraj, T., Ragab, A., and El Alfy, M., *Geochemical and hydrogeological factors influencing high levels of radium contamination in groundwater in arid regions.* Environmental Research, **2020**. *184*: p. 109303.
22. Sherif, M.I., Lin, J.J., Poghosyan, A., Abouelmagd, A., Sultan, M.I., and Sturchio, N.C., *Geological and hydrogeochemical controls on radium isotopes in groundwater of the Sinai Peninsula, Egypt.* Science of the Total Environment, **2018**. *613*: p. 877-885.
23. Stackelberg, P.E., Szabo, Z., and Jurgens, B.C., *Radium mobility and the age of groundwater in public-drinking-water supplies from the Cambrian-Ordovician aquifer system, north-central USA.* Applied Geochemistry, **2018**. *89*: p. 34-48.
24. Sturchio, N.C., Banner, J.L., Binz, C.M., Heraty, L.B., and Musgrove, M., *Radium geochemistry of ground waters in Paleozoic carbonate aquifers, midcontinent, USA.* Applied Geochemistry, **2001**. *16*(1): p. 109-122.
25. Gilkeson, R.H., Perry, E.C., Cowart, J.B., and Holtzman, R.B., *Isotopic studies of the natural sources of radium in groundwater in Illinois*, in *Research Report 187*. 1984, Final Report submitted to the Bureau of Reclamation, U.S. Department of the Interior.
26. Gilkeson, R.H.S., Susan A.; Cartwright, Keros; Griffin, Robert Alfred; Larson, Thurston Eric, *Geologic studies to identify the source for high levels of radium and barium in Illinois ground-water supplies: a preliminary report.* University of Illinois at Urbana-Champaign. Water Resources Center, **1978**.
27. Mathews, M., Gotkowitz, M., and Ginder-Vogel, M., *Effect of geochemical conditions on radium mobility in discrete intervals within the Midwestern Cambrian-Ordovician aquifer system.* Applied Geochemistry, **2018**. *97*: p. 238-246.
28. Mathews, M., Scott, S.R., Gotkowitz, M.B., Hunt, R.J., and Ginder-Vogel, M., *Isotopic analysis of radium geochemistry at discrete intervals in the Midwestern Cambrian-Ordovician aquifer system.* Applied Geochemistry, **2022**. *142*.
29. Luczaj, J. and Masarik, K., *Groundwater quantity and quality issues in a water-rich region: Examples from Wisconsin, USA.* Resources, **2015**. *4*(2): p. 323.
30. Vengosh, A., Coyte, R.M., Podgorski, J., and Johnson, T.M., *A critical review on the occurrence and distribution of the uranium- and thorium-decay nuclides and their effect on the quality of groundwater.* Science of the Total Environment, **2021**: p. 151914.
31. Sun, H. and Semkow, T.M., *Mobilization of thorium, radium and radon radionuclides in ground water by successive alpha-recoils.* Journal of Hydrology, **1998**. *205*(1-2): p. 126-136.
32. Tricca, A., Porcelli, D., and Wasserburg, G.J., *Factors controlling the groundwater transport of U, Th, Ra, and Rn.* Journal of Earth System Science, **2000**. *109*(1): p. 95-108.
33. Vinson, D.S., Lundy, J.R., Dwyer, G.S., and Vengosh, A., *Implications of carbonate-like geochemical signatures in a sandstone aquifer: Radium and strontium isotopes in the Cambrian Jordan aquifer (Minnesota, USA).* Chemical Geology, **2012**. *334*: p. 280-294.

34. Mathews, M., Scott, S., Gotkowitz, M., and Ginder-Vogel, M., *Association of radionuclide isotopes with aquifer solids in the Midwestern Cambrian-Ordovician aquifer system* ACS Earth and Space Chemistry, **2021**. *5*(2): p. 268-278.
35. Fleischer, R.L., *Isotopic disequilibrium of uranium: alpha-recoil damage and preferential solution effects.* Science, **1980**. *207*(4434): p. 979-81.
36. Faure, G. and Mensing, T., *Isotopes: Principles and Applications*. 3rd ed. 2005, Hoboken, New Jersey: John Wiley & Sons, Inc. 897.
37. Craft, E., Abu-Qare, A., Flaherty, M., Garofolo, M., Rincavage, H., and Abou-Donia, M., *Depleted and natural uranium: chemistry and toxicological effects.* Journal of Toxicology and Environmental Health, **2004**. *7*(4): p. 297-317.
38. Ginder-Vogel, M. and Fendorf, S., *Chapter 11 Biogeochemical uranium redox transformations: Potential oxidants of uraninite*. 2007, Elsevier. p. 293-319.
39. Langmuir, D. and Herman, J.S., *The mobility of thorium in natural waters at low temperatures.* Geochimica et Cosmochimica Acta, **1980**. *44*(11): p. 1753-1766.
40. Krishnaswami, S., Graystein, W.C., and Turekian, K.K., *Radium, thorium and radioactive lead isotopes in groundwaters: Application to the in situ determination of adsorption-desorption rate constants and retardation factors.* Water Resources Research, **1982**. *18*(6): p. 1633-1675.
41. Ames, L.L., McGarrah, J.E., Walker, B.A., and Salter, P.F., *Uranium and radium sorption on amorphous ferric oxyhydroxide.* Chemical Geology, **1983**. *40*(1): p. 135-148.
42. Borch, T., Kretzschmar, R., Kappler, A., Cappellen, P.V., Ginder-Vogel, M., Voegelin, A., and Campbell, K., *Biogeochemical redox processes and their impact on contaminant dynamics.* Environmental Science & Technology, **2010**. *44*(1): p. 15-23.
43. Koulouris, G., *Dynamic studies on sorption characteristics of 226Ra on manganese dioxide.* Journal of Radioanalytical and Nuclear Chemistry, **1995**. *193*(2): p. 269-279.
44. Ames, L.L., McGarrah, J.E., and Walker, B.A., *Sorption of trace constituents from aqueous solutions onto secondary minerals. II. Radium.* Clays & Clay Minerals, **1983**. *31*(5): p. 335-342.
45. Missana, T., Colàs, E., Grandia, F., Olmeda, J., Mingarro, M., García-Gutiérrez, M., Munier, I., Robinet, J.-C., and Grivé, M., *Sorption of radium onto early cretaceous clays (Gault and Plicatules Fm). Implications for a repository of low-level, long-lived radioactive waste.* Applied Geochemistry, **2017**. *86*: p. 36-48.
46. Alhajji, E., Al-Masri, M.S., Khalily, H., Naoum, B.E., Khalil, H.S., and Nashawati, A., *A study on sorption of (226)Ra on different clay matrices.* Bulletin of Environmental Contamination and Toxicology, **2016**. *97*(2): p. 255-60.
47. Landis, J.D., Sharma, M., Renock, D., and Niu, D., *Rapid desorption of radium isotopes from black shale during hydraulic fracturing. 1. Source phases that control the release of Ra from Marcellus Shale.* Chemical Geology, **2018**. *496*: p. 1-13.
48. Chen, M.A. and Kocar, B.D., *Radium sorption to iron (hydr)oxides, pyrite, and montmorillonite: implications for mobility.* Environmental Science & Technology, **2018**. *52*(7): p. 4023-4030.
49. Jones, M.J., Butchins, L.J., Charnock, J.M., Pattrick, R.A.D., Small, J.S., Vaughan, D.J., Wincott, P.L., and Livens, F.R., *Reactions of radium and barium with the surfaces of carbonate minerals.* Applied Geochemistry, **2011**. *26*(7): p. 1231-1238.
50. Nathwani, J.S. and Phillips, C.R., *Adsorption of 226Ra by soils in the presence of Ca2+ ions. Specific adsorption (II).* Chemosphere, **1979**. *8*(5): p. 293-299.

51. Tamamura, S., Takada, T., Tomita, J., Nagao, S., Fukushi, K., and Yamamoto, M., *Salinity dependence of 226Ra adsorption on montmorillonite and kaolinite.* Journal of Radioanalytical and Nuclear Chemistry, **2014**. *299*(1): p. 569-575.
52. Vinson, D.S., Tagma, T., Bouchaou, L., Dwyer, G.S., Warner, N.R., and Vengosh, A., *Occurrence and mobilization of radium in fresh to saline coastal groundwater inferred from geochemical and isotopic tracers (Sr, S, O, H, Ra, Rn).* Applied Geochemistry, **2013**. *38*: p. 161-175.
53. Jurgens, B.C., Fram, M.S., Belitz, K., Burow, K.R., and Landon, M.K., *Effects of groundwater development on uranium: Central Valley, California, USA.* Ground Water, **2010**. *48*(6): p. 913-28.
54. Thaw, M., Gebreegziabher, M., Villafañe-Pagán, J.Y., and Jasechko, S., *Modern groundwater reaches deeper depths in heavily pumped aquifer systems.* Nature Communications, **2022**. *13*(1).
55. Szabo, Z., dePaul, V.T., Kraemer, T.F., and Parsa, B., *Occurrence of radium-224, radium-226, and radium-228 in water of the unconfined Kirkwood-Cohansey aquifer system, southern New Jersey*, in *Scientific Investigations Report 2004-5224*. 2005, U.S. Geological Survey: Reston, VA.
56. Lindsey, B.D., Cravotta, C.A., Szabo, Z., Belitz, K., and Stackelberg, P., *Relation between road-salt application and increasing radium concentrations in a low-pH aquifer, Southern New Jersey.* ACS ES&T Water, **2021**. *1*(12): p. 2541-2547.
57. Ayotte, J.D., Szabo, Z., Focazio, M.J., and Eberts, S.M., *Effects of human-induced alteration of groundwater flow on concentrations of naturally-occurring trace elements at water-supply wells.* Applied Geochemistry, **2011**. *26*(5): p. 747-762.
58. Grundl, T. and Cape, M., *Geochemical factors controlling radium activity in a sandstone aquifer.* Groundwater, **2006**. *44*(4): p. 518-527.
59. Langmuir, D. and Melchior, D., *The geochemistry of Ca, Sr, Ba and Ra sulfates in some deep brines from the Palo Duro Basin, Texas.* Geochimica et Cosmochimica Acta, **1985**. *49*(11): p. 2423-2432.
60. Zhu, C., *Coprecipitation in the barite isostructural family: 1. binary mixing properties.* Geochimica et Cosmochimica Acta, **2004**. *68*(16): p. 3327-3337.
61. Ceccarello, S., Black, S., Read, D., and Hodson, M.E., *Industrial radioactive barite scale: suppression of radium uptake by introduction of competing ions.* Minerals Engineering, **2004**. *17*(2): p. 323-330.
62. Shao, H., Dmytrieva, S.V., Kolditz, O., Kulik, D.A., Pfingsten, W., and Kosakowski, G., *Modeling reactive transport in non-ideal aqueous–solid solution system.* Applied Geochemistry, **2009**. *24*(7): p. 1287-1300.
63. Landa, E.R., *Mobilization of radionuclides from uranium mill tailings and related waste materials in anaerobic environments.* Journal of Radioanalytical and Nuclear Chemistry, **2003**. *255*(3): p. 559-563.
64. Phillips, E.J.P., Landa, E.R., Kraemer, T., and Zielinski, R., *Sulfate-reducing bacteria release barium and radium from naturally occurring radioactive material in oil-field barite.* Geomicrobiology Journal, **2001**. *18*(2): p. 167-182.
65. Martin, A.J., Crusius, J., Jay McNee, J., and Yanful, E.K., *The mobility of radium-226 and trace metals in pre-oxidized subaqueous uranium mill tailings.* Applied Geochemistry, **2003**. *18*(7): p. 1095-1110.

66. Vinson, D.S., *Radium isotope geochemistry in groundwater systems: The role of environmental factors*, in *Divison of Earth and Ocean Sciences*. 2011, Duke University. p. 266.
67. McDevitt, B., McLaughlin, M., Cravotta, C.A., Ajemigbitse, M.A., Van Sice, K.J., Blotevogel, J., Borch, T., and Warner, N.R., *Emerging investigator series: radium accumulation in carbonate river sediments at oil and gas produced water discharges: implications for beneficial use as disposal management.* Environmental Science: Processes & Impacts, **2019**. *21*(2): p. 324-338.

Chapter 2

Strontium and radium occurrence at the boundary of a confined aquifer system

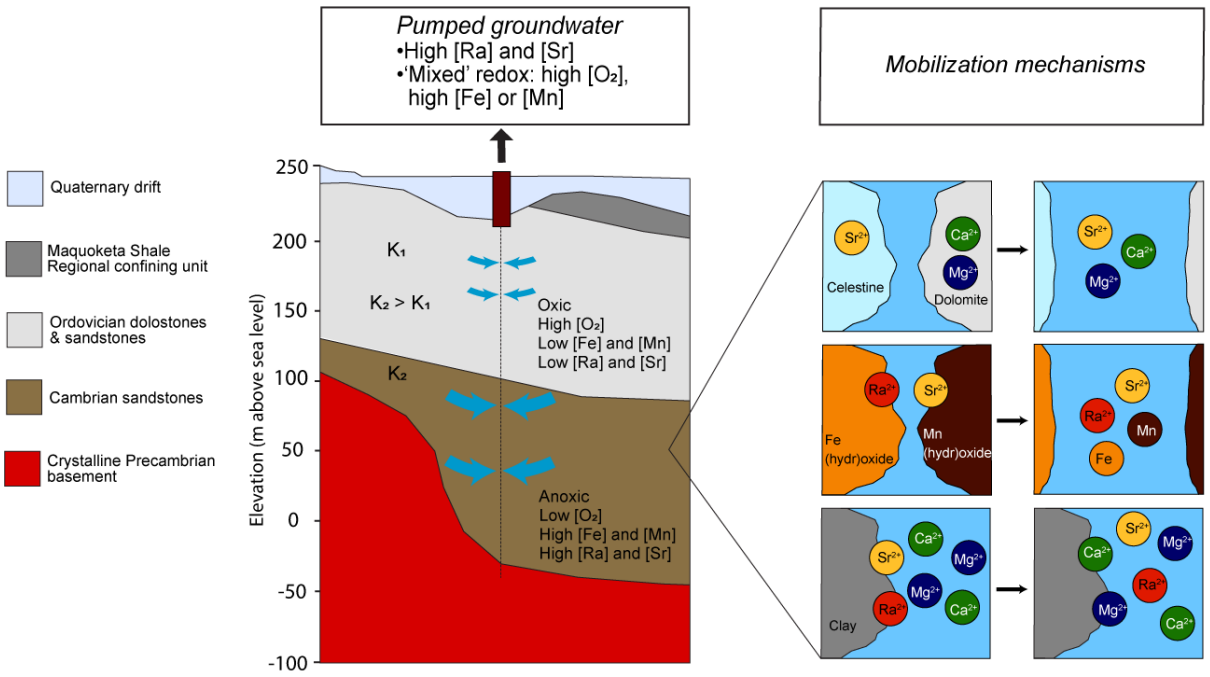

2.1 Abstract

Aquifers are susceptible to contamination by naturally occurring metals and radionuclides that limits the quantity of groundwater available for drinking. The Midwestern Cambrian-Ordovician aquifer system (MCOAS) is an important drinking water source in the North Central region of the U.S., but can contain elevated levels of geogenic radium (Ra) and strontium (Sr). Here, the occurrence of Ra and Sr is investigated with respect to natural groundwater evolution

Reproduced with permission from *Applied Geochemistry*. Plechacek, A., Scott, S.R., Gotkowitz, M.B., and Ginder-Vogel, M., **2022**. *142*: p. 105332. **Amy Plechacek**: Funding Acquisition, Conceptualization, Methodology, Investigation, Formal Analysis, Writing – Original Draft and Review & Editing, Visualization. **Sean R. Scott**: Methodology, Resources, Writing – Review & Editing. **Madeline B. Gotkowitz**: Conceptualization, Methodology, Writing – Review & Editing. **Matthew Ginder-Vogel**: Funding Acquisition, Conceptualization, Writing – Review & Editing, Supervision.

and water-rock interactions using a multi-isotope approach ($\delta^{18}O$, $\delta^{2}H$, $\delta^{34}S_{SO4}$, $^{87}Sr/^{86}Sr$, and [$^{234}U/^{238}U$]), in a portion of the MCOAS that straddles regionally unconfined and regionally confined conditions. Hierarchical cluster analysis reveals three distinct groups of groundwater geochemistry, evolving from a young (< 10,000 years) HCO_3^--dominant groundwater located upgradient to old (> 10,000 years) SO_4^{2-} and Cl^--dominant groundwater located downgradient. Strontium and Ra concentrations are highest downgradient, where extreme [$^{234}U/^{238}U$] disequilibrium indicates increased water-rock interactions due to local confinement or a stagnant groundwater zone. Geochemical conditions evolve as a consequence of water-rock interaction, resulting in Ra and Sr mobilization mechanisms including enhanced mineral dissolution and weathering, and decreased sorption efficiency due to competitive sorption and the absence or dissolution of iron and manganese (hydr)oxides with sorbed Ra and Sr. Relative to redox processes, 'mixed' redox samples have the highest median Sr and Ra concentrations, where young, oxic groundwater mixes with old, anoxic groundwater over long open boreholes. Isotopic results ($\delta^{18}O$ and $\delta^{2}H$, $^{87}Sr/^{86}Sr$) indicate these wells with long open boreholes are receiving more of the old, deep groundwater elevated in Ra and Sr, suggesting that well construction is an important consideration for Ra and Sr occurrence. The presented framework can be used to examine the occurrence of geogenic contaminants with respect to recharge history, water-rock interactions, and evolving geochemical conditions in other aquifer systems with a range of groundwater residence times and geochemistry.

2.2 Introduction

Groundwater provides nearly half of all drinking water worldwide.[1] Drinking water availability is limited by both quantity and quality; therefore, an understanding of the hydrological processes affecting water quality is critical to meeting increased water demand. In regional U.S.

aquifer systems, approximately 80 percent of contaminants found at concentrations exceeding a human-health benchmark are geogenic contaminants such as arsenic (As), uranium (U), radium (Ra), and strontium (Sr).[2] Long-term ingestion of water elevated in Ra is linked to development of bone cancer and other detrimental health effects[3, 4] and is therefore regulated in drinking water by the U.S. Environmental Protection Agency (EPA) at a Maximum Contaminant Level (MCL) of 185 mBq/L (5 pCi/L) for the combined activity of ^{226}Ra and ^{228}Ra.[5] Radium exceeds the MCL in U.S. aquifer systems such as the Cambrian-Ordovician aquifer system, the North Atlantic Coastal Plain, and the Floridan aquifer system.[6] In some locations, Ra activity in groundwater is increasing over time.[7, 8] Consumption of elevated Sr concentrations is associated with tooth enamel mottling and strontium rickets.[9, 10] Although the U.S. does not regulate Sr in drinking water, the U.S. EPA is evaluating Sr as a drinking water contaminant on the Contaminant Candidate List 3 with a recommended non-cancer Health Reference Level (HRL) of 1.5 mg/L.[11] In 2016 and 2020, the U.S. EPA delayed a final decision on the regulation of Sr to continue gathering additional data.[12, 13] In the U.S., public water supplies with Sr above the U.S. Geological Survey 4 mg/L health-based screening level (HBSL)[14] affect about 2.2 million people, the majority of which are supplied by carbonate aquifers such as the Floridan aquifer system, Edwards-Trinity aquifer system, and the Cambrian-Ordovician aquifer system.[15]

The Midwestern Cambrian Ordovician aquifer system (MCOAS) is a source of drinking water to millions of people in the North Central region of the U.S., but contains elevated levels of both Ra and Sr that can pose regulatory challenges for water utilities.[16] For example, Ra and Sr occur at elevated levels in the MCOAS in Wisconsin, with maximum concentrations on the order of 1665 mBq/L and 52 mg/L, respectively.[7, 17, 18] Water utilities with wells that exceed the Ra MCL must install treatment systems or switch to an alternative water source. For example, the municipal

water supply for Fond du Lac, Wisconsin, required a $32.1M investment in groundwater treatment to comply with the Ra MCL.[19] Elevated levels of Ra and Sr are distributed similarly in the MCOAS in Wisconsin, occurring along an arc-shaped band in the eastern part of the state.[20] It has been recognized that high Ra concentrations often occur in contact zones between unconfined and confined conditions, such as in the MCOAS or the Saq aquifer in Saudi Arabia.[20, 21] Previous studies examined Ra and Sr occurrence at this transitional setting in the Wisconsin MCOAS;[22-25] however, the mechanisms responsible for elevated levels at this boundary remain poorly understood. An enhanced understanding of Ra and Sr occurrence and geochemistry with regard to natural groundwater evolution may inform improvements in well design and well-field management to reduce their concentrations in pumped groundwater.

Although the oxidation states of the alkaline earth metals Ra and Sr (i.e., +2) do not change under typical groundwater conditions, their mobility in aquifers is indirectly affected by changes in geochemical conditions. For example, Ra and Sr concentrations in the MCOAS are typically correlated with factors associated with old (pre-1953) groundwater, such as high total dissolved solids (TDS) content and reducing conditions.[26] In carbonate aquifers, enhanced dissolution of minerals, including Sr-bearing minerals (e.g., gypsum, dolomite, celestine), occurs as water-rock interactions increase, releasing Sr to solution.[15] Once released to groundwater, Ra and Sr sorb to negatively charged clay minerals, and redox-sensitive iron (Fe) and manganese (Mn) (hydr)oxides.[27-32] However, elevated TDS due to enhanced mineral dissolution can result in competitive sorption, where elevated concentrations of cations compete with Ra and Sr for available sorption sites on aquifer solids, leaving more Ra and Sr in the aqueous phase.[33-35] Additionally, reducing aquifer conditions may either dissolve or limit the formation of Fe and Mn (hydr)oxides, resulting in fewer sorption sites available for Ra and Sr.[28, 36] Aquifer geochemical

conditions can change due to anthropogenic activities; for example, the injection of oxygenated water during managed aquifer recharge releases certain geogenic contaminants from solid phases to groundwater.[37] Geochemical conditions (e.g., redox and TDS) can also change naturally as groundwater evolves along regional flow paths and hydrogeologic conditions, such as the presence of confining units, vary.

The recharge history of the MCOAS provides insight into where changes in geochemical conditions enhancing natural contaminant partitioning to groundwater will occur. For example, groundwater further downgradient of primary recharge areas generally becomes more mineralized and reduced compared to groundwater located near primary recharge areas. These geochemical trends are often established due to confining conditions, where the aquifer is hydraulically separated from overlying aquifers and longer flow paths and residence times allow for mineral dissolution and reactions that consume dissolved oxygen to occur.[26, 38, 39] During the Pleistocene glaciation, the Laurentide Ice Sheet provided pulses of glacial meltwater recharge to aquifers in North America, including the MCOAS in Illinois, Minnesota, and Wisconsin.[40, 41] Furthermore, the weight of the overlying ice sheet reversed the flow of groundwater, previously toward the Michigan basin, and transported saline, sulfate-rich water away from the Michigan basin west into the MCOAS in eastern Wisconsin and northeastern Illinois.[42, 43] Confining units, such as the Maquoketa Shale in the MCOAS, preserve Pleistocene meltwater by limiting the influx of modern recharge. Due to the effects of temperature dependent isotope fractionation,[40, 44] groundwater recharged during the Pleistocene and modern precipitation have distinct isotopic signatures (e.g., $\delta^{18}O$, $\delta^{2}H$) that can be used to examine contaminant occurrence (e.g., Ra, Sr) in relation to groundwater residence time. Therefore, throughout this paper young groundwater is defined as <

10,000 years old (after the Pleistocene glaciation), while old groundwater is defined as > 10,000 years old (during the Pleistocene glaciation).

The goal of this study is to identify important controls on Sr and Ra concentrations where the MCOAS straddles regionally unconfined and confined conditions. We examine geogenic Ra and Sr occurrence in relation to groundwater evolution at this boundary in the MCOAS of east-central Wisconsin, where variability in hydrogeologic conditions (e. g., confinement) influences aquifer recharge and results in stratified aquifer geochemistry. A targeted geochemical approach enhances understanding of Ra and Sr occurrence with respect to recharge processes (e.g., $\delta^{18}O$, $\delta^{2}H$, $\delta^{34}S_{SO4}$), water-rock interactions (e.g., [$^{234}U/^{238}U$] and $^{87}Sr/^{86}Sr$), and corresponding changes in groundwater geochemistry (e.g., TDS, redox conditions). Hierarchical cluster analysis objectively groups groundwater samples with respect to their chemical characteristics. This approach identifies distinct regions of water quality, as well as important Ra and Sr mobilization and sequestration mechanisms, as groundwater evolves at the boundary of a confined portion of the MCOAS.

2.3 Hydrogeologic framework

2.3.1 Regional hydrogeology

The MCOAS is composed of Paleozoic sandstone, shale, and carbonate sequences deposited in near and offshore marine environments.[45] The sedimentary rocks of the MCOAS are overlain by the glacial aquifer system, except within the Driftless Area of southeast Minnesota, northeastern Iowa, southwestern Wisconsin, and northwestern Illinois. The MCOAS is bounded below by Precambrian basement, a crystalline metamorphic and igneous rock complex. The structural highs and lows of the Precambrian basement influence the structure of the MCOAS,

with the MCOAS units dipping away from structural highs and towards structural basins.[39] In Wisconsin, the MCOAS units dip and thicken from the Wisconsin Arch toward the south and east, into the structural basins in southwestern Iowa, central Illinois, and western Michigan. The Ordovician Maquoketa Formation, referred to as the Maquoketa Shale, is a 122–183 m thick calcareous, silty shale interstratified with thin beds of dolomite and limestone that forms a regional confining unit in eastern Wisconsin (Figure 2.1).[26, 39]

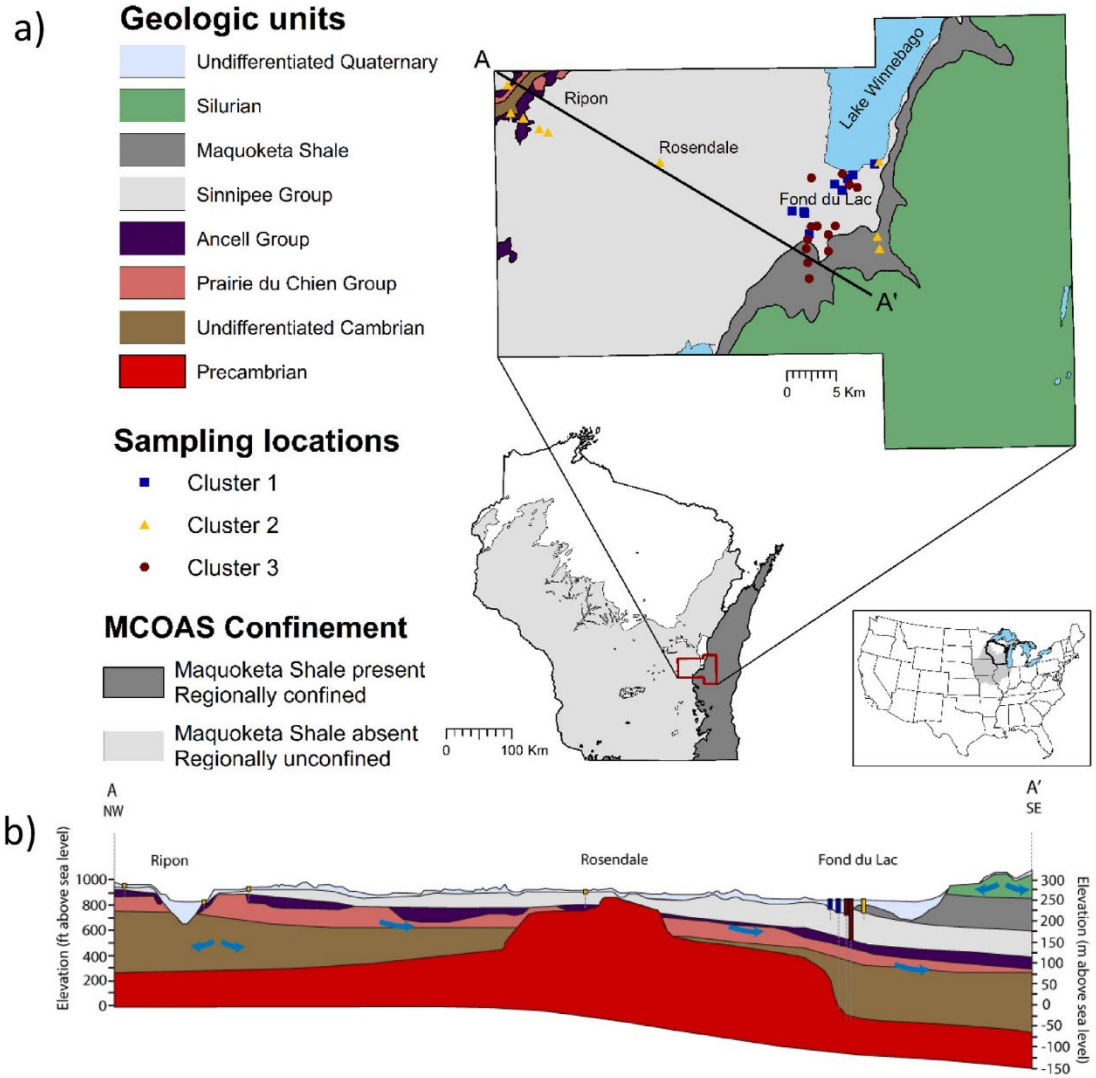

Figure 2.1 a) Geologic map of Fond du Lac County, Wisconsin, and the location of sampled wells completed in the Midwestern Cambrian-Ordovician aquifer system (MCOAS). Sample clusters 1 and 2 are HCO_3^--dominant groundwater, while Cluster 3 is comprised of SO_4^{2-} and Cl^--dominant groundwater. b) Conceptual geologic cross section from A-A′ showing the general construction of wells from each sample cluster and the relative groundwater flow direction. Geologic map is adapted from Batten (2018).[45]

2.3.2 Study site hydrogeology

Fond du Lac County, Wisconsin, encompasses the transition of the MCOAS from regionally unconfined to regionally confined conditions, determined by the absence or presence of the Maquoketa Shale (Figure 2.1). The well field in the city of Fond du Lac straddles the Maquoketa Shale subcrop, and locally confined areas or groundwater stagnation zones created by relief on the Precambrian basement surface may lead to geochemical conditions favorable for Ra and Sr mobility.

In Fond du Lac County, the bedrock dips gently to the east and southeast and is composed of undifferentiated Cambrian sandstones overlain by Ordovician and Silurian dolostones, shales, and sandstones.[46] The bedrock is buried by Quaternary glacial drift that ranges in thickness from < 1.5 m to > 91 m and consists of poorly sorted till, as well as glacial meltwater lake and stream sediment composed of gravel, sand, silt, clay, and peat.[45] The Precambrian basement is highly uneven in Fond du Lac County and is commonly referred to as the "Fond du Lac Range." [46-48] A prominent Precambrian-surface high in the west-central part of the county, with about 335 m of relief, results in the absence or near absence of the Cambrian sandstones at that location (Figure 2.1).[45, 46, 49] In the eastern half of the county, the uppermost bedrock unit is undifferentiated Silurian dolostone, a massive dolostone with abundant fractures and a thickness of ~24 m (Figure 2.1).[45, 46] Throughout most of the western part of the county, the uppermost bedrock unit is the Ordovician Sinnipee Group, a massive dolostone and the youngest unit of the MCOAS, ranging in thickness from ~60 to 72 m.[45] The Maquoketa Shale varies in thickness from approximately 61 to 82 m in eastern Fond du Lac County.[45] To the west, where the Maquoketa Shale is absent, the Sinnipee Group dolostone confines the underlying formations where there is a sufficient layer of overlying, fine-grained Quaternary drift, such as the glacial lake clays.[46, 50]

A groundwater divide trends southwestward across the western part of the county, with groundwater in the MCOAS west of the divide flowing toward the city of Ripon and groundwater in the MCOAS east of the divide flowing toward the larger city of Fond du Lac, where pumping for municipal and industrial use has resulted in a deep cone of depression (Figure 2.1).[46] From the city of Fond du Lac, groundwater in the MCOAS continues to flow east towards Lake Michigan. Another groundwater divide is present east of the Niagara (Silurian) Escarpment, with groundwater in the Silurian aquifer west of the divide flowing toward the city of Fond du Lac and groundwater in the Silurian aquifer east of the divide flowing toward Lake Michigan (Figure 2.1).

2.4 Materials and methods

2.4.1 Sampling sites

Groundwater samples were collected from 23 public water system wells, an irrigation well, and eight household wells open to the MCOAS (Figure 2.1). The wells were selected to achieve a diverse spatial sampling with depth (see Table A-1 for well depth and construction) along a northwest to southeast transect through Fond du Lac County, corresponding closely to the geologic cross section characterized in Batten (2018)[45] (A-A' in Figure 2.1). City of Fond du Lac municipal wells with historically elevated Ra and Sr[18] have long boreholes open to all or most of the MCOAS (Figure 2.1b, Table A-1). Geologic logs indicate that only three of the 17 municipal wells in the city of Fond du Lac pump water from the regionally confined portion of the MCOAS, while all other wells are considered unconfined. Two additional wells sampled in this study are considered unconfined based on lithologic descriptions from well construction reports, despite being located in an area where the regional geologic map[45] indicates the Maquoketa Shale is present. This discrepancy is attributed to the difference in scale between the geologic map and the site-scale observations of drill cuttings.

2.4.2 Groundwater characterization

Groundwater samples were collected in the summers of 2018 and 2019. Prior to sample collection, taps were run until a stable pH and conductivity were reached. Samples from municipal wells were collected near the wellhead prior to treatment or blending of water from other sources. Samples from other public supply wells and household wells were collected from outside taps when possible. If an outside tap was not available, samples were collected from the tap nearest to the well in the basement, prior to any treatment (e.g., softening). The irrigation well sample was collected from a pipe discharging to a pond on site.

Parameters including pH, specific conductance, dissolved oxygen (DO), and temperature were measured in the field. Samples for alkalinity, cation, and anion analyses were filtered with a 0.45 μm Nylon filter, and samples for cation analysis were acidified to pH < 2 with trace metal grade nitric acid (HNO_3). Unfiltered samples were collected for Ra analysis to comply with Standard Method 7500-Ra,[51] and preserved with concentrated HNO_3 to pH < 2. All samples were kept on ice in the field and stored at 4˚C until analysis.

Alkalinity, cation, and anion analyses were performed at the University of Wisconsin-Madison Core Facility for Advanced Water Analysis. Total alkalinity was determined by the Gran titration method, using a Mettler Toledo G-20 compact titrator within 24 h of sample collection. Trace metal and cation chemistry (Ca^{2+}, Mg^{2+}, Na^{+}, K^{+}, Sr^{2+}, Ba^{2+}, Si, total Fe, total Mn) was determined by inductively-coupled plasma optical emission spectrometry with an Agilent 5110 VDV system. Anions (chloride, sulfate, bromide) were measured by ion chromatography using a Thermo Scientific Dionex ICS-2100 system with a Dionex IonPac AS-11 separation column and IonPac AG-11 guard column. The concentration of bicarbonate (HCO_3^-) was determined via PHREEQC v. 3 from alkalinity and pH measurements, with < 5% ion balance error.[52]

Stable isotopes of water ($^{2}H/^{1}H$ and $^{18}O/^{16}O$) were analyzed at the University of Wisconsin-Madison Biotechnology Center Isotope Ratio Mass Spectrometry Laboratory with a Picarro L2140-i Cavity Ring-down Analyzer. The analyzer was calibrated with IAEA standards VSMOW-II and VSLAP-II. Additionally, two calibrated working standards (e.g., tap water and a spiked standard) were analyzed with every batch of unknown water samples. Standard delta (δ) notation was used to report stable isotopes in per mille (‰) relative to the Vienna Standard Mean Ocean Water (VSMOW), with a long-term precision of 0.1‰ for $\delta^{2}H$ and 0.03‰ for $\delta^{18}O$.

Samples for strontium isotopes ($^{87}Sr/^{86}Sr$), uranium isotope activity ratios ($[^{234}U/^{238}U]$), and sulfur isotopes of sulfate ($^{34}S/^{32}S$ of SO_4^{2-}, referred to after as $\delta^{34}S_{SO4}$) were purified by ion exchange chromatography and measured using a Neptune Plus multi-collector inductively coupled plasma mass spectrometer (MC-ICPMS) at the Wisconsin State Laboratory of Hygiene (WSLH). Sample purification methods for $^{87}Sr/^{86}Sr$ and $[^{234}U/^{238}U]$ analyses are described in detail in Mathews et al. (2022).[53] The primary, secondary, and additional standards used for $^{87}Sr/^{86}Sr$, $[^{234}U/^{238}U]$, and $\delta^{34}S_{SO4}$ analyses are summarized in Table A-2. Samples for $[^{234}U/^{238}U]$ analysis were analyzed on the MC-ICPMS by sample-standard bracketing using the NIST Natural Uranium isotopic standard, with $^{234}U/^{238}U$ = 18,919.[54, 55] ^{234}U was measured with the single secondary electron multiplier/retarding potential quadrupole (SEM/RPQ) detector on the MC-ICPMS, while ^{238}U and ^{235}U were measured using Faraday cups. Samples for $^{87}Sr/^{86}Sr$ analysis were bracketed between MC-ICPMS measurements of the NIST SRM 987 standard. The isotope ratios were internally corrected for mass bias using $^{86}Sr/^{88}Sr$ = 0.1194,[56] and the final $^{87}Sr/^{86}Sr$ values were normalized to the days average of SRM 987 with values reported relative to $^{87}Sr/^{86}Sr$ = 0.71024.[57] Samples for $\delta^{34}S_{SO4}$ were purified using the methodology of Craddock et al. (2008),[58] and analyzed and bracketed with a High Purity Standards Sulfur standard on the MC-ICPMS. The IAEA-S-1

standard was also analyzed and used to report final $\delta^{34}S_{SO4}$ values relative to the Vienna Canyon Diablo Troilite (VCDT), using the assigned value of -0.30.[59] The CASS-6 seawater standard was analyzed alongside samples, with measured $^{87}Sr/^{86}Sr$, [$^{234}U/^{238}U$], and $\delta^{34}S_{SO4}$ isotopic values consistent with values reported in the literature (Table A-3). The absolute standard errors (2σ) associated with samples analyzed for $^{87}Sr/^{86}Sr$, [$^{234}U/^{238}U$], and $\delta^{34}S_{SO4}$ values are presented in Table A-1 and displayed as error bars on figures.

Radium isotopes (^{226}Ra and ^{228}Ra) were measured at Eaton Eurofins Analytical, Inc., following Standard Method 7500-Ra.[51] One sample with Ra values (^{228}Ra and $^{226}Ra + ^{228}Ra$) below the detection level was designated as less than the Minimum Detectable Activity (< MDA), defined as the activity that can be counted with a precision of ±100% certainty at the 95% confidence level. Values < MDA were replaced with the MDA for statistical analyses and are displayed as the MDA on figures. Measurements were reported with standard error estimates.

2.4.3 Additional data sources

In addition to the wells sampled for this study, we used datasets of Ra activities (^{226}Ra, ^{228}Ra, $^{226}Ra + ^{228}Ra$) in groundwater samples from seven municipal wells, available from the Wisconsin Department of Natural Resources (2021).[18] Average Ra measurements were computed from results that spanned August 2008 to February 2019. These data were reported without a standard error; therefore, sample standard deviations were computed where possible.

2.4.4 Data analysis and statistics

Water samples were classified into groups based on 18 measured geochemical parameters using hierarchal cluster analysis (HCA), a multivariate statistical method with a robust and objective approach to sampling classification.[60-62] The data was prepared for HCA following the

procedure established by Cloutier et al. (2008).[60] The 18 parameters used in the analysis (DO, HCO_3^-, Cl^-, SO_4^{2-}, Br^-, Ca^{2+}, Mg^{2+}, Na^+, K^+, Si, Fe, Mn, Ba^{2+}, $\delta^{18}O$, δ^2H, $\delta^{34}S_{SO4}$, [$^{234}U/^{238}U$], and $^{87}Sr/^{86}Sr$) were the parameters remaining after excluding parameters that were additive (e. g., specific conductance), had many values below limits of detection (e. g., nitrate), or demonstrated small regional geographic variation (e.g., pH). Measurements of Sr and Ra were also excluded as parameters to be able to objectively evaluate their occurrence relative to the generated sample clusters. Additional details on data treatment and methods for HCA are provided in A-1.

Nonparametric Spearman rank correlation coefficients with a 0.95 confidence level were used to evaluate the associations between measured parameters. Correlations were performed in R using the cor() function and visualized in a matrix using the corrplot() function.[63] Measurements below the limit of detection were replaced with the limit of detection, and variables with more than 25% of values below limits of detection were excluded to prevent effects associated with a high percentage of data with the same value.[64] Wilcoxon rank-sum nonparametric tests were computed in R using the wilcox.test() function to evaluate the null hypothesis that mean-ranked values were statistically similar among sample groups.[65-67]

Redox states associated with samples were assigned as either oxic, suboxic, anoxic, mixed, or undetermined based on the concentration of indicator constituents of DO, dissolved Fe, and dissolved Mn (Table 2.1).[68] Similar to Stackelberg et al. (2018),[69] an anoxic threshold of Fe > 50 µg/L rather than Fe > 100 µg/L was used to identify Fe-reducing conditions important for evaluating Ra and Sr mobility. Saturation indices (SI) of relevant mineral phases were calculated with PHREEQC v. 3[52] using the WATEQ4F database.[70]

Table 2.1 Redox process designation.[68, 69]

Redox Process	DO (mg/L)	Fe (mg/L)	Mn (mg/L)
Anoxic[a]	< 0.5	≥ 0.05	≥ 0.05
Suboxic	< 0.5	< 0.05	< 0.05
Oxic	> 0.5	< 0.05	< 0.05
Mixed[a]	> 0.5	≥ 0.05	≥ 0.05
Undetermined	Missing indicator constituent measurement(s)		

[a]To be designated as anoxic or mixed, the sample can have Fe ≥ 0.05, Mn ≥ 0.05, or both Fe and Mn ≥ 0.05.

2.5 Results

2.5.1 Water types, redox conditions, and recharge processes

Hierarchical cluster analysis yields three clusters with distinct geochemistry (Figure 2.1; Figure A-1; Figure 2.2, Table A-1). Cluster 1 is composed of ten samples that are primarily Mg^{2+} and HCO_3^--dominant, while Cluster 2 consists of nine samples with HCO_3^- as the dominant anion and either Mg^{2+} or Ca^{2+} as the dominant cation. Cluster 3 is comprised of 13 samples with Ca^{2+} as the dominant cation and for the majority of samples, SO_4^{2-} or Cl^- as the dominant anion. Clusters 1 and 2 have similar specific conductance values, with medians of 681 ± 279 µS/cm and 671 ± 152 µS/cm. Specific conductance is higher in Cluster 3 samples, with a median of 973 ± 220 µS/cm. Cluster 1 consists of both shallow (< 100 m) and deep (> 225 m) wells, while Cluster 2 consists of shallow (< 150 m) wells only and Cluster 3 consists of deep (> 225 m) wells only (Figure A-2; Table A-1).

Redox classification yields twelve oxic samples, six suboxic samples, eight anoxic samples, seven mixed samples, and one ‘undetermined’ sample without a dissolved oxygen measurement (Table A-1). There is no relationship between sample clusters and redox processes. Cluster 1 includes five oxic samples, three suboxic samples, and two anoxic samples. Cluster 2 consists of three oxic samples, two suboxic samples, and four anoxic samples, while Cluster 3 has

four oxic samples, one suboxic sample, six mixed samples, one anoxic sample, and one undetermined sample.

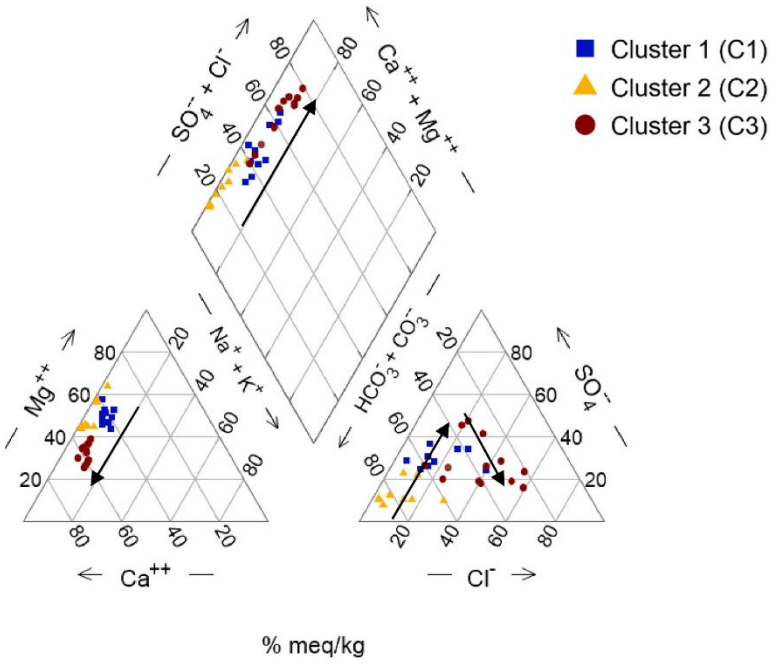

Figure 2.2 Piper diagram showing the major chemical composition of sample clusters. Black arrows indicate the general direction of groundwater evolution from younger, low-TDS water to older, high-TDS water.

Groundwater samples from the study area have $\delta^{18}O$ and $\delta^{2}H$ values that plot near the global meteoric water line (GMWL)[71] and the local meteoric water line (LMWL) for southeast Wisconsin (Figure 2.3).[72] The $\delta^{18}O$ and $\delta^{2}H$ values for samples range from -8.1 to -16.9‰ and -54.0 to -119.5‰, respectively (Figure 2.3, Table A-1). The $\delta^{18}O$ and $\delta^{2}H$ values for Clusters 1 and 2 plot closest to the range for modern precipitation in southeast Wisconsin,[72] while the values for Cluster 3 are within the range for Pleistocene meltwater.[40] The $\delta^{34}S_{SO4}$ value for groundwater samples ranges from -2.09 to +21.0‰ (Figure A-3). Cluster 1 has the most variable $\delta^{34}S_{SO4}$ values, ranging from -2.1 to +19.1‰. Cluster 2 $\delta^{34}S_{SO4}$ values range from -1.5 to +11.6‰, while Cluster 3 values range from +8.0 to +21.0‰.

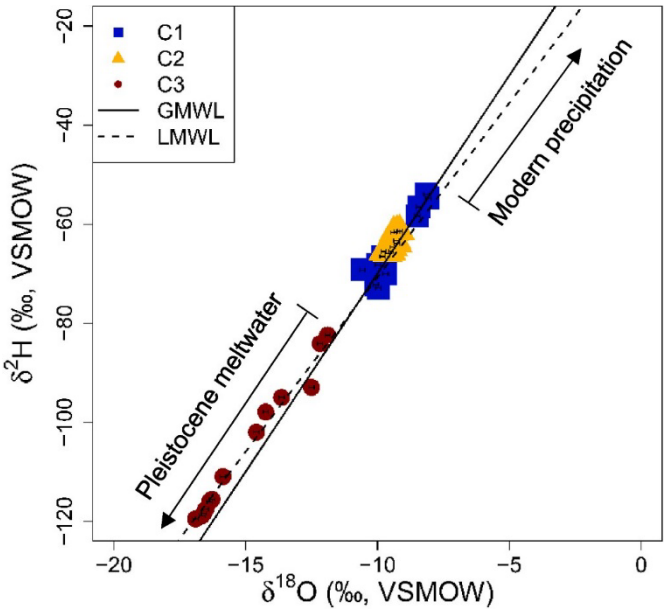

Figure 2.3 δ^2H vs. $\delta^{18}O$ values for groundwater sample clusters. The solid black line is the Global Meteoric Water Line (GMWL)[71] and the dashed black line is the Local Meteoric Water Line (LMWL) for southeast Wisconsin.[72] VSMOW = Vienna Standard Mean Ocean Water.

2.5.2 Strontium and uranium isotopes

The collected groundwater samples have $^{87}Sr/^{86}Sr$ ratios ranging from 0.709248 to 0.711155 (Figure A-4; Table A-1). Cluster 1 has $^{87}Sr/^{86}Sr$ ratios ranging from 0.710429 to 0.710952. Cluster 2 has the lowest $^{87}Sr/^{86}Sr$ ratios, ranging from 0.709248 to 0.710880, while Cluster 3 has the highest $^{87}Sr/^{86}Sr$ ratios, ranging from 0.710459 to 0.711155. The plot of 1/Sr vs. $^{87}Sr/^{86}Sr$ (Figure A-4) is approximately linear, indicating two-component mixing.[44] The first component is characterized by high $^{87}Sr/^{86}Sr$ and high Sr concentrations, and the second component is characterized by low $^{87}Sr/^{86}Sr$ and low Sr concentrations. The $[^{234}U/^{238}U]$ of groundwater samples from the study area range from 1.9 to 18.0, with the most extreme U isotope disequilibrium in Cluster 3 samples with a median of 11.2 ± 3.2 (Figure 2.4b, Figure 2.4e, Table A-1). Lower $[^{234}U/^{238}U]$ are associated with Cluster 1 and 2 samples with higher $\delta^{18}O$ and δ^2H values, while higher $[^{234}U/^{238}U]$ are associated with Cluster 3 samples with lower $\delta^{18}O$ and δ^2H values.

2.5.3 Occurrence and distribution of Sr and Ra

Strontium and Ra concentrations range from 0.07 to 34.3 mg/L and 26.6 to 377 mBq/L in groundwater samples, respectively (Figure 2.4, Table A-1). Concentrations of Sr and Ra are lowest in Cluster 2 samples, with median concentrations of 0.4 ± 1.0 mg/L (standard deviation) and 53 ± 33 mBq/L, respectively. Median Sr and Ra concentrations for Cluster 1 are 3.2 ± 2.7 mg/L and 137 ± 91 mBq/L, respectively. The highest concentrations of Sr and Ra are associated with the groundwater samples of Cluster 3, with median concentrations of 10.4 ± 7.5 mg/L and 211 ± 79 mBq/L, respectively. Evaluation of Sr and Ra concentrations relative to redox processes reveals the highest median Sr and Ra concentrations are associated with samples with a 'mixed' redox process (Figure 2.5).

Strontium and Ra concentrations increase with well depth (Sr: $\rho = 0.76$, $p < 0.001$; Ra: $\rho = 0.61$, $p < 0.001$), with the highest concentrations occurring in wells completed at depths > 225 m (Figure A-2). Strontium and Ra concentrations are also negatively correlated with $\delta^{18}O$ values (Sr: $\rho = -0.76$, $p < 0.001$; Ra: $\rho = -0.72$, $p < 0.001$) (Figure 2.4a and Figure 2.4d), and positively correlated with $\delta^{34}S_{SO4}$ (Sr: $\rho = 0.69$, $p < 0.001$; Ra: $\rho = 0.64$, $p < 0.001$), [$^{234}U/^{238}U$] (Sr: $\rho = 0.73$, $p < 0.001$; Ra: $\rho = 0.60$, $p < 0.001$) (Figure 2.4b and Figure 2.4e), and specific conductance (Sr: $\rho = 0.63$, $p < 0.001$; Ra: $\rho = 0.42$, $p < 0.03$) (Figure 2.4c and Figure 2.4f). Overall, Sr concentrations are moderately correlated with Mn ($\rho = 0.40$, $p < 0.03$) and weakly correlated with Fe ($\rho = 0.30$, $p = 0.1$), while Ra concentrations are weakly correlated with both Mn ($\rho = 0.13$, $p = 0.5$) and Fe ($\rho = 0.31$, $p = 0.1$) (Figure A-5, Figure A-6). Cluster 3 samples with elevated Sr and Ra have moderate correlations between Sr and Mn concentrations ($\rho = 0.49$, $p = 0.09$), and between Ra and Fe concentrations ($\rho = 0.46$, $p = 0.1$).

Saturation indices for gypsum ($CaSO_4 \cdot 2H_2O$), dolomite ($CaMg(CO_3)_2$)), calcite ($CaCO_3$), aragonite ($CaCO_3$), celestine ($SrSO_4$), strontianite ($SrCO_3$) and barite ($BaSO_4$) are also included to evaluate potential sources and sinks for Sr and Ra (Table A-4). All samples are undersaturated with respect to gypsum, with an overall median of -1.7 ± 0.3. Samples in Clusters 1 and 2 are dominantly saturated or oversaturated with respect to dolomite, with only one sample in Cluster 1 and one sample in Cluster 2 considered undersaturated. In Cluster 3, nine of 13 samples are considered undersaturated with respect to dolomite. With respect to calcite, samples are at saturation or oversaturated, with the exception of two samples in Cluster 3. Samples are also at saturation or oversaturated with respect to aragonite, with only five samples considered undersaturated. All three sample clusters are dominantly undersaturated with respect to celestine, with only one sample at saturation, and an overall median SI of -1.3 ± 0.86. Similarly, most samples are considered undersaturated with respect to strontianite, with only three of 32 samples total at saturation and an overall median SI of -0.58 ± 0.65. Samples are dominantly at saturation or oversaturated with respect to barite, with seven of ten samples in Cluster 1, five of nine samples in Cluster 2, and 11 out of 13 samples in Cluster 3 considered saturated or oversaturated.

2.6 Discussion

2.6.1 Occurrence of Ra and Sr

Radium and Sr concentrations increase as groundwater evolves along the cross section from the younger, (Mg^{2+}, Ca^{2+})-HCO_3^--dominant groundwater of Clusters 1 and 2 to the older, Ca^{2+}-(SO_4^{2-}, Cl^-)-dominant groundwater of Cluster 3 (Figure 2.2). This composition shift along flow paths in the MCOAS has been documented in other studies,[50, 69, 73] and is attributed to sulfide oxidation, SO_4^{2-}-rich brines transported from the Michigan Basin during the Pleistocene, and the increased dissolution of gypsum and Cl-bearing minerals as the aquifer becomes confined by the

Maquoketa Shale (see A-2 for a detailed discussion on sources of SO_4^{2-} and Cl^-). The sources of SO_4^{2-} are identified with $\delta^{34}S_{SO4}$ results, where low (~0 ‰) values indicate sulfide oxidation where the aquifer is unconfined and high values (~20 ‰) indicate Silurian gypsum as a source of SO_4^{2-} where the aquifer is confined.[43] Silurian evaporites do not occur locally within the MCOAS of eastern Wisconsin, but are present in the nearby Michigan Basin.[43, 74, 75] Therefore, this $\delta^{34}S_{SO4}$ signature reflects the recharge of saline, SO_4^{2-}-rich water to eastern Wisconsin from the Michigan Basin during a Pleistocene glaciation flow-reversal event.[43] In the region of our study, the composition shift occurs west of the Maquoketa Shale subcrop. This may be because the regional flow system is recharged on the western edge of the glacial lake clays, or a possible groundwater stagnation zone has developed at the base of the aquifer, on the flank of a substantial low in Precambrian basement (Figure 2.1b). Local confinement and a possible groundwater stagnation zone result in estimated groundwater residence times > 100,000 years[69] in the city of Fond du Lac. These conditions permit enhanced mineral dissolution and reactions that consume DO. In regions where the aquifer is unconfined, sulfide oxidation generates an additional source of SO_4^{2-}. The wide range of redox processes associated with samples is likely a reflection of the varying thickness and composition of overlying glacial drift, which influences the confining conditions in this region.

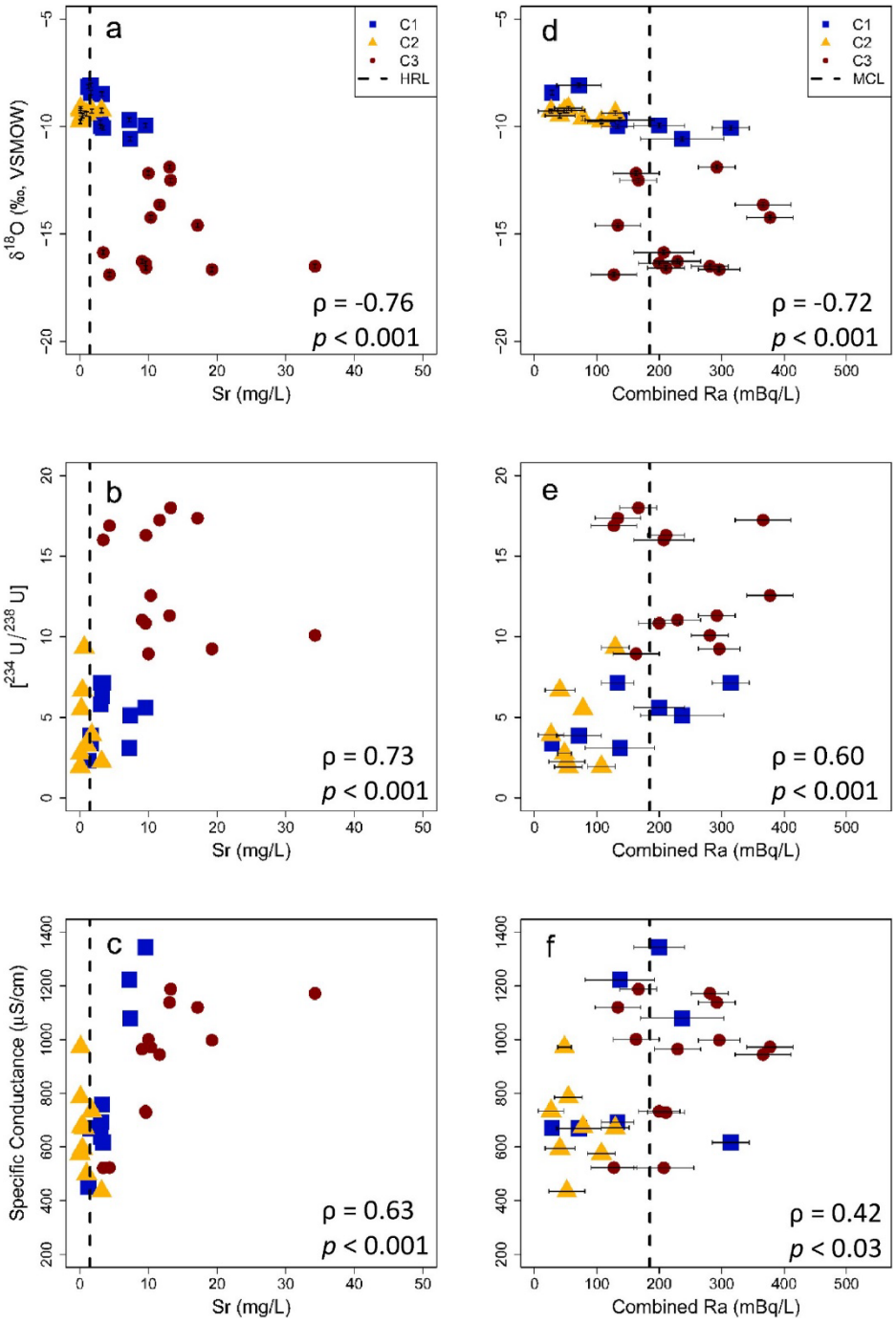

Figure 2.4 Strontium (Sr) concentration a) $\delta^{18}O$, b) [$^{234}U/^{238}U$], c) specific conductance, and combined Ra (^{226}Ra + ^{228}Ra) activity vs d) $\delta^{18}O$, e) [$^{234}U/^{238}U$], and f) specific conductance. Sample clusters are distinguished by shape and color. Here, HRL is the U.S. EPA non-cancer health reference level for Sr, MCL is the U.S. EPA maximum contaminant level for Ra, ρ is the Spearman rank correlation coefficient, and *p* is the significance level. The strong negative correlations with the $\delta^{18}O$ value indicate Sr and Ra levels are higher in Pleistocene meltwater located downgradient along a regional flow path. Here, groundwater residence time is longer and water-rock interactions increase, as indicated by the higher [$^{234}U/^{238}U$], resulting in geochemical conditions that enhance Sr and Ra mobility (e.g., elevated TDS).

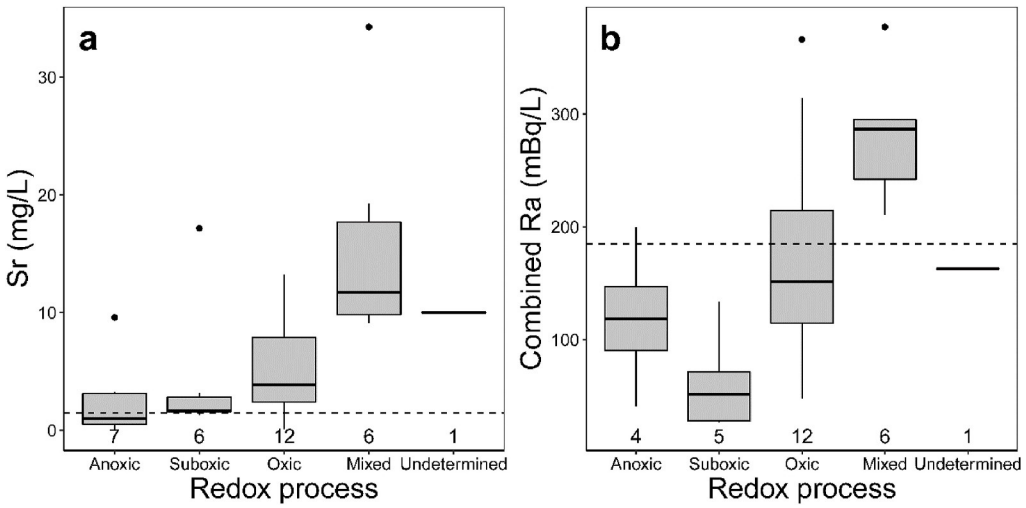

Figure 2.5 Boxplot of a) strontium (Sr) concentration and b) combined radium ($^{226}Ra + ^{228}Ra$) activity vs. redox process. The numbers below the boxes represent the number of samples associated with each redox process. The dashed line in (a) is the U.S. EPA health reference level of 1.5 mg/L for Sr and in (b) is the U.S. EPA maximum contaminant level of 185 mBq/L for Ra. Statistics displayed include (from bottom of plot): smallest value < 25th percentile, 25th percentile, 50th percentile (median), 75th percentile, and largest value > 25th percentile. Outliers are >1.5 times the interquartile range beyond either end of the box.

Sample clusters are derived based on similar geochemical characteristics. Cluster 2 samples have geochemical characteristics consistent with young (< 10,000 years) groundwater, and have the lowest Sr and Ra concentrations. These wells are shallow (< 150 m) wells with boreholes or screened intervals open to Ordovician stratigraphy, with the exception of one well (#15) open to Cambrian stratigraphy only. Cluster 2 wells include all wells sampled west of the city of Fond du Lac and three shallow (< 65 m) wells located in the city of Fond du Lac (Figure 2.1, Table A-1). The stable water isotope values for Cluster 2 samples plot close to the range for modern precipitation in southeast Wisconsin, suggesting this groundwater has received more recent recharge (Figure 2.3). Low $\delta^{34}S_{SO4}$ values suggest wells in Cluster 2 are unconfined, with the exception of the three Fond du Lac wells (#17-19) with $\delta^{34}S_{SO4}$ values around +10 ‰ indicating possible mixing of groundwater from the unconfined and confined systems (Figure A-3). While Cluster 2 samples have the lowest median Ra and Sr concentrations, two of the three wells in Cluster 2 located in the city of Fond du Lac (#17 and #19) exceed the Sr HRL of 1.5 mg/L. These

results indicate that young, HCO_3^-- dominated groundwater upgradient generally does not exceed the Sr HRL or Ra MCL, but can contain Sr concentrations above the HRL downgradient in the city of Fond du Lac (Figure 2.4a, Figure 2.4d).

Ra and Sr concentrations increase in Cluster 1 samples, which consists of a mix of five shallow (< 90 m) wells open to Ordovician stratigraphy and five deep (> 225 m) wells open to Cambrian and Ordovician stratigraphy, all located downgradient in the city of Fond du Lac (Figure 2.1). Stable water isotopes indicate that similar to Cluster 2 samples, Cluster 1 samples receive young (< 10,000 years) groundwater (Figure 2.4a, Figure 2.4d). Samples in Cluster 1 have low (~0 ‰) $\delta^{34}S_{SO4}$ values consistent with SO_4^{2-} sourced from sulfide oxidation where the aquifer is unconfined, with the exception of three samples (#1, #9, and #10) (Figure A-3). Sample #1 and #9 have $\delta^{34}S_{SO4}$ values consistent with mixing of both sources of SO_4^{2-}, while sample #10 is near +20 ‰, consistent with SO_4^{2-} sourced from marine gypsum where the aquifer is confined. Three of the seven wells with available Ra data in Cluster 1 exceed the MCL, while all but one sample exceeds the Sr HRL, revealing that young groundwater located downgradient can contain elevated Ra and Sr concentrations above EPA guidelines (Figure 2.4a, Figure 2.4d).

Cluster 3 samples have the highest median Ra and Sr concentrations, and have chemical characteristics consistent with old (> 10,000 years) groundwater. These samples are collected from deep (> 235 m) wells located downgradient in the city of Fond du Lac with boreholes open to Cambrian and Ordovician stratigraphy, with the exception of one well open to Cambrian stratigraphy only. Cluster 3 samples have stable water isotope values within the range for Pleistocene meltwater, indicating these samples are associated with the oldest groundwater at the study site (Figure 2.3). Additionally, the $\delta^{34}S_{SO4}$ values are near the +20 ‰ indicative of Silurian gypsum, suggesting that these samples were collected within a region where the aquifer system is

confined (Figure A-3). All six wells assigned with a 'mixed' redox process are in Cluster 3, presumably indicating the mixing of younger, oxic water from shallow MCOAS units and older, anoxic water from deeper MCOAS units over long open boreholes. The low stable water isotope values associated with Cluster 3 samples suggest that these wells are receiving more of the deep, older water from Cambrian sandstones, which are considered the most transmissive units of the MCOAS. This is further supported by the radiogenic $^{87}Sr/^{86}Sr$ values associated with Cluster 3 samples, since Cambrian stratigraphy is more radiogenic than Ordovician stratigraphy (Hunt et al., 1998) (Figure A-4). Nine out of 13 wells in Cluster 3 exceed the Ra MCL, while all wells in Cluster 3 exceed the Sr HRL, indicating that old, SO_4^{2-} and Cl^--dominated groundwater located downgradient often contains elevated Ra and Sr concentrations (Figure 2.4a, Figure 2.4d).

2.6.2 Ra and Sr sources and mobilization mechanisms

Radium and Sr are geogenic contaminants sourced from aquifer bedrock within the MCOAS. Radium is produced from the decay of parent nuclides (e.g., ^{238}U, ^{232}Th) present within mineral grains (e.g., feldspar), sorbed on mineral surfaces (e.g., Fe (hydr)oxides, clays), and in the aqueous phase. Observed Ra activity in groundwater reflects the net balance between Ra mobilization from aquifer solids (e.g., desorption, recoil) and retention (adsorption, mineral co-precipitation).[76] Radium typically remains close to the site of parent nuclide decay in the MCOAS; therefore, Ra mobilization to groundwater is strongly dependent on Ra association with reactive solid phases within each stratigraphic unit, and local geochemical conditions.[77] In the MCOAS, Sr is derived from Sr-bearing minerals in carbonates such as celestine ($SrSO_4$) and strontianite ($SrCO_3$) present in Mississippi Valley Type deposits formed from a Paleozoic hydrothermal event, which brought brines from the Michigan Basin to the eastern Wisconsin.[78, 79] Throughout the study region, mineral SI results demonstrate the aquifer is undersaturated with respect to both celestine

and strontianite. These Sr-bearing minerals could have also been emplaced by the dissolution, transport, and re-precipitation of sulfate-rich evaporites from the Michigan Basin during the Pleistocene glaciation.[26] This emplacement is supported by $\delta^{34}S_{SO4}$ results, where $\delta^{34}S_{SO4}$ values between +16.4 and +21.0‰ correspond with high Sr concentrations (>10 mg/L) indicating Sr association with marine sulfate from the Michigan Basin. Additionally, Sr is strongly correlated with Cl ($\rho = 0.74$, $p < 0.001$) and Br ($\rho = 0.93$, $p < 0.001$), also of marine origin. Strontium can also substitute for Ca^{2+} in dolomite, calcite, and gypsum, and for potassium (K^{+}) in authigenic K-feldspars, and sorbs to negatively-charged mineral surfaces (e.g., Fe (hydr)oxides, clays). In the MCOAS, Ra and Sr concentrations are positively correlated with concentrations of constituents indicative of mineralization and reducing conditions,[26] suggesting that water-rock interactions and local geochemical conditions are important for their occurrence in groundwater.

The [$^{234}U/^{238}U$] increase from Clusters 2 and 1 to Cluster 3 indicates enhanced water-rock interactions as groundwater evolves, and is associated with higher Ra and Sr concentrations (Figure 2.4b, Figure 2.4e). The [$^{234}U/^{238}U$] of water from natural systems is generally >1, with alpha (α) recoil of ^{238}U and preferential dissolution of ^{234}U being the dominant mechanism responsible for the disequilibrium between ^{234}U and ^{238}U in solution.[44, 80] Samples have extreme U isotope disequilibrium, with [$^{234}U/^{238}U$] as high as 18. Extreme U disequilibrium has been documented in other regions of the MCOAS,[81] and has been attributed to a slow and stable U roll-front system[82] (see A-3 for further discussion on extreme U isotope disequilibrium). As alpha recoil efficiency and the degree of water-rock interactions increase, geochemical conditions become favorable for Sr and Ra mobility.

Strontium and Ra can be mobilized from solid phases to groundwater as groundwater age increases and geochemical reactions progress, and are therefore often correlated with elevated TDS

from enhanced mineral dissolution, or reducing conditions. Here, Sr and Ra are moderately correlated with specific conductance (Sr: $\rho = 0.63$, $p < 0.001$; Ra: $\rho = 0.42$, $p < 0.03$) (Figure 2.4c and Figure 2.4f) and cations including Na^+ (Sr: $\rho = 0.63$, $p < 0.001$; Ra: $\rho = 0.46$, $p < 0.02$) and Ca^{2+} (Sr: $\rho = 0.49$, $p < 0.006$; Ra: $\rho = 0.42$, $p < 0.03$) suggesting that there is increased mineral dissolution (e.g., dolomite, gypsum, and other Sr-bearing minerals) and competition for sorption sites on aquifer solids as TDS levels rise in deep (> 225 m) wells located downgradient along the regional west to east flow path. Additionally, Ra and Sr are strongly correlated ($\rho = 0.74$, $p < 0.001$), but likely do not compete with each other for sorption sites due to their low concentrations in comparison to other cations such as Ca^{2+} and Mg^{2+}. Strontium and Ra concentrations are highest in samples associated with a mixed redox process, where young (< 10,000 years), oxic water mixes with old (> 10,000 years), anoxic water (Figure 2.5). These wells receive more of the old, anoxic water with high Ra and Sr concentrations, and high dissolved Fe and Mn concentrations consistent with the absence or dissolution of Fe and Mn (hydr)oxides. In Cluster 3 samples, Sr is more strongly correlated with Mn ($\rho = 0.49$, $p = 0.09$) than with Fe ($\rho = 0.19$, $p = 0.59$, while Ra is more strongly correlated with Fe ($\rho = 0.46$, $p = 0.1$) than with Mn ($\rho = 0.17$, $p = 0.59$) (Figure A-5, Figure A-6). This suggests Sr favors association with Mn (hydr)oxides, while Ra favors association with Fe (hydr)oxides in this system. Radium association with reducible phases such as Fe and Mn (hydr)oxides has been confirmed at other locations in the MCOAS,[77] but future work should further examine Sr association with metal (hydr)oxides in the MCOAS.

Additional potential sources of Sr in the aquifer include dedolomitization (i.e., dissolution of dolomite and precipitation of calcite) and weathering of authigenic K-feldspar cements. When dolomite is calcitized, it is no longer able to incorporate Sr at concentrations as high as pure dolomite can, leaving more Sr in the dissolved phase.[83] Cluster 3 samples demonstrate three trends

suggesting possible dedolomitization[22]: Samples are 1) undersaturated with respect to gypsum, with a median SI of -1.4 ± 0.3, 2) at saturation with respect to calcite, with a median SI of 0.01 ± 0.2, and 3) undersaturated with respect to dolomite, with a median SI of -0.28 ± 0.3. This indicates dedolomitization may contribute to Sr mobility in these samples. Strontium concentrations are strongly correlated with K^+ ($\rho = 0.92$, $p < 0.001$). K-feldspars are documented in dolomites in eastern Wisconsin;[78] thus, weathering of authigenic K-feldspars cannot be ruled out as a potential mobilization mechanism for Sr. Radium and Sr concentrations rise as geochemical conditions evolve from Cluster 2 and 1 to Cluster 3. Dissolution of Sr-bearing phases (e.g., gypsum, celestine, strontianite) is the dominant source of Sr for all three sample clusters, and progresses with enhanced water-rock interaction downgradient. Increased levels of TDS and the dissolution or absence of Fe and Mn (hydr)oxides result in decreased Sr and Ra sorption efficiency. Strontium and Ra correlations with Mn and Fe for Cluster 3 samples suggest the dissolution of Mn (hydr)oxides is important for Sr mobility, while the dissolution of Fe (hydr)oxides is important for Ra mobility. In addition to geochemical conditions, the distribution of contaminant sources in aquifer solids is an important consideration for their occurrence in groundwater.[53] Elevated Ra concentrations at the contact between unconfined and confined conditions in the Saq sandstone aquifer of Saudi Arabia were attributed to potential uneven distribution of parent isotopes (e.g., U and Th) in overlying paleoplacer deposits.[21] Concentrations of Ra and Sr in solid samples were not examined in this study due to a lack of existing deep cores in the study region; therefore, we acknowledge that a heterogeneous distribution of U, Th, Ra, and Sr in the aquifer solids of our study region could further contribute to differences in the observed Ra and Sr levels.

2.6.3 Ra and Sr sequestration mechanisms

Sequestration mechanisms such as sorption, cation exchange, and mineral co-precipitation can control concentrations of geogenic contaminants in groundwater. Radium and Sr readily sorb to clays and Fe and Mn (hydr)oxide minerals; however, changes in geochemical conditions such as increased TDS or reducing conditions decrease Ra and Sr sorption efficiency to these surfaces. Cation exchange can sequester divalent cations such as Ra and Sr when they are removed from solution to solid phase surfaces (e.g., clay mineral surfaces) in exchange for another divalent cation (e.g., Ca^{2+}) or two monovalent cations (e.g., Na^{+}), which are then released to the aqueous phase.[84, 85] As cation exchange progresses, the molar ratio of Na^{+} to divalent cations in solution increases; therefore, in regions where cation exchange is dominant the Na^{+}: Ca^{2+}+Mg^{2+} molar ratio is typically greater than 15.[86]

Molar ratios of Na^{+}: Ca^{2+}+Mg^{2+} and Na^{+}:Cl^{-} were used as indicators of cation exchange at the study site. Results for Na^{+}: Ca^{2+}+Mg^{2+} range from 0.02 to 0.30 with a median of 0.15 ± 0.08, with no samples having a Na^{+}: Ca^{2+}+Mg^{2+} ratio >15 (Table A-1). This ratio is lower than the median Na^{+}:Ca^{2+}+Mg^{2+} of 0.44 reported for the entire MCOAS.[69] Na^{+}:Cl^{-} at the study site ranges from 0.12 to 1.52 with a median of 0.20 ± 0.28, which is also lower than the Na^{+}:Cl^{-} reported by Stackelberg et al. (2018)[69] for oxic and mixed/anoxic samples in the MCOAS, with medians of 0.8 and 3.5, respectfully (Table A-1). These differences may reflect the absence of the Maquoketa Shale in most of our study region, whereas the Stackelberg et al. (2018)[69] study included samples from the regionally confined MCOAS where the clay-rich Maquoketa Shale provides more opportunity for cation exchange. Our results are in agreement with Stackelberg et al. (2018),[69] indicating that cation exchange with Na^{+} is not an effective sequestration mechanism for Ra and Sr due to the low clay content within the MCOAS.

Radium activities and Sr concentrations can also be controlled by co-precipitation with sulfate minerals such as barite,[23, 28, 87, 88] and carbonate minerals such as aragonite ($CaCO_3$).[28, 89, 90] Calculated SI for barite indicate that barite co-precipitation may play a role in controlling Ra activities and Sr concentrations, with 23 out of 32 samples either at saturation or oversaturated with respect to barite. Barite SI is variable for Cluster 2 samples, and becomes more consistently saturated in Cluster 1 and 3 samples, which are all located in the city of Fond du Lac, downgradient of the regional west to east flow path. The median molar ^{226}Ra:Ba ratio of samples is 4.14 (±2.8) × 10^{-8}, within the range reported in similar studies (Table A-1).[23, 69] ^{226}Ra:Ba and Sr:Ba ratios increase as groundwater evolves from Clusters 2 and 1 to Cluster 3, indicating that while barite co-precipitation may play a role in sequestering Ra and Sr, it is insufficient at curbing elevated levels of Ra and Sr. Radium and Sr may also be partially sequestered by dolomite and calcite/aragonite co-precipitation, particularly in Cluster 1 and 2 samples which are at saturation with respect to dolomite, aragonite, and calcite. However, the sequestration potential of Sr and Ra in dolomite decreases in Cluster 3 samples, which are primarily undersaturated with respect to dolomite. Furthermore, carbonate minerals dissolve more readily than barite,[91] indicating that carbonates are less likely to serve as an effective Sr and Ra sink.

2.7 Conclusions

The occurrence of Ra and Sr was examined with respect to natural groundwater evolution at the boundary of a confined portion of the MCOAS. Groundwater evolves from young (< 10,000 years) HCO_3^--dominant groundwater of Clusters 2 and 1 to old (> 10,000 years) SO_4^{2-} and Cl^--dominant groundwater of Cluster 3, likely as a result of local confinement and stagnation at the base of the aquifer due to uneven Precambrian topography. As groundwater residence time increases downgradient, [^{234}U/^{238}U] and water-rock interactions increase, resulting in multiple

geochemical mechanisms that influence Sr and Ra mobility. The enhanced dissolution of gypsum, dolomite, and other Sr- bearing minerals (e.g., celestine, strontianite) releases Sr to groundwater and increases the concentration of divalent cations (e.g., Ca^{2+}, Mg^{2+}) that compete with Ra and Sr for sorption sites on aquifer solids, resulting in elevated aqueous Ra and Sr concentrations above U.S. EPA guidelines. The highest median Sr and Ra levels occur in samples with a mixed redox classification, where young, oxic water and old, anoxic water mix over long open boreholes. Isotopic results suggest that these wells receive more of the old, anoxic water, where the dissolution of Sr-bearing phases and the dissolution or absence of Mn or Fe (hydr)oxides has released Sr and Ra to solution.

This study provides important insights on Ra and Sr occurrence with respect to groundwater evolution at the boundary of a confined aquifer system, and employs an objective approach to sample grouping to identify distinct regions of groundwater geochemistry in a complex flow system. In aquifer systems which are stratified with respect to groundwater geochemistry, public water systems must often consider the tradeoffs related to pumping shallow or deep groundwater. For example, shallow groundwater from the Silurian dolomite aquifer in eastern Wisconsin is easily accessible, but has elevated concentrations of anthropogenically-sourced nitrate in many locations. An alternative source in eastern Wisconsin is the underlying, very productive MCOAS; however, this requires that wells be drilled deeper, with groundwater frequently exceeding the Ra MCL. Some water utilities may choose to drill multi-aquifer wells that draw water from both shallow and deep groundwater, such as the municipal wells with long open boreholes in the city of Fond du Lac. However, this uncontrolled blending of shallow and deep groundwater across long open boreholes still results in elevated levels of Ra and Sr at the study site, likely because the wells are receiving more water from the deeper, more transmissive

Cambrian sandstones. This suggests that controlled blending of water from two different wells (e.g., one shallow and one deep well) or advanced treatment options (e.g., reverse osmosis, pre-formed hydrous manganese oxide filtration) may be more effective at reducing levels of Ra and Sr in pumped groundwater. These results provide data on the distribution of Ra and Sr in public and private drinking water supplies sourced from the MCOAS, and can be used by decision-makers as they evaluate regulation of Sr in drinking water. Furthermore, the multi-isotope approach and objective sample grouping method applied here can be used to examine the occurrence and geochemistry of Sr, Ra, and other geogenic contaminants with respect to natural groundwater evolution and recharge history in such aquifer systems with a wide range of geochemistry and residence times.

2.8 Acknowledgements

The authors thank the Fond du Lac Water Utility, Ripon Water Utility, non-community public water supply systems, businesses, and homeowners for their assistance with this work. We are grateful for sample analyses support from the Wisconsin State Laboratory of Hygiene, the UW-Madison Biotechnology Isotope Ratio Laboratory, and James Lazarcik. Additionally, we would like to acknowledge Peter Chase, Peter Schoephoester, and Kathy Roushar at the Wisconsin Geological and Natural History Survey for access to field equipment, and geologic logs and shapefiles. We thank Florence Udenby, formerly of the Wisconsin Department of Natural Resources, and Danielle Vollendorf from Fond du Lac County Health Department for helping us establish communication with public non-community water systems. Sampling assistance provided by Gabrielle Campagnola, Madeleine Mathews, Marie Dematatis, and Anna Frehner was greatly appreciated. Many thanks to Madeleine Mathews and Stephanie Napieralski for providing constructive feedback that greatly improved the quality of this manuscript.

This study was funded by the Wisconsin Groundwater Research and Monitoring Program and the University of Wisconsin System. A.P. is supported by the National Science Foundation Graduate Research Fellowship Program under Grant No. DGE-1747503. Any opinions, findings, and conclusions or recommendations expressed in this material are those of the author(s) and do not necessarily reflect the views of the National Science Foundation. Support was also provided by the Graduate School and the Office of the Vice Chancellor for Research and Graduate Education at the University of Wisconsin–Madison with funding from the Wisconsin Alumni Research Foundation.

2.9 References

1. Smith, M., Cross, K., Paden, M., and Laban, P., *Spring — Managing groundwater sustainability*. IUCN. 2016, Gland, Switzerland.
2. DeSimone, L.A., McMahon, P.B., and Rosen, M.R., *The quality of our Nation's waters: Water quality in principal aquifers of the United States, 1991-2010*, in *U.S. Geological Survey Circular 1360*. 2015: Reston, VA. p. 161.
3. Finkelstein, M. and Kreiger, N., *Radium in drinking water and risk of bone cancer in Ontario youths: a second study and combined analysis.* Journal of Occupational and Environmental Medicine, **1996**. *53*: p. 305-311.
4. Lyman, G.H., Lyman, C.G., and Johnson, W., *Association of leukemia with radium groundwater contamination.* Journal of the American Medical Association, **1985**. *254*(5): p. 621-626.
5. U.S. Environmental Protection Agency, *National primary drinking water regulations*, in *Federal Register*. 2000.
6. Szabo, Z., dePaul, V.T., Fischer, J.M., Kraemer, T.F., and Jacobsen, E., *Occurrence and geochemistry of radium in water from principal drinking-water aquifer systems of the United States.* Applied Geochemistry, **2012**. *27*(3): p. 729-752.
7. Dematatis, M., Plechacek, A., Mathews, M., Wright, D., Udenby, F., Gotkowitz, M., and Ginder-Vogel, M., *Spatial and temporal variability of radium in the Wisconsin Cambrian-Ordovician aquifer system* AWWA Water Science, **2020**.
8. Lindsey, B.D., Cravotta, C.A., Szabo, Z., Belitz, K., and Stackelberg, P., *Relation between road-salt application and increasing radium concentrations in a low-pH aquifer, Southern New Jersey.* ACS ES&T Water, **2021**. *1*(12): p. 2541-2547.
9. Curzon, M.E.J. and Spector, P.C., *Enamel mottling in a high strontium area of the USA.* Community Dent. Oral Epidemiol, **1977**. *5*: p. 243-247.
10. Özgür, S., Sümer, H., and Koçoğlu, G., *Rickets and soil strontium.* Arch. Dis. Child., **1996**. *75*: p. 524-526.
11. U.S. Environmental Protection Agency, *Announcement of the Preliminary Regulatory Determinations for Contaminants on the Third Drinking Water Contaminant Candidate List; Proposed Rule*, in *Federal Register Volume 79, Number 202*. 2014. p. 62715-62750.
12. U.S. Environmental Protection Agency, *Announcement of the Final Regulatory Determinations for Contaminants on the Third Drinking Water Contaminant Candidate List*, in *Federal Register 81 FR 13*. 2016.
13. U.S. Environmental Protection Agency, *Announcement of Preliminary Regulatory Determinations for Contaminants on the Fourth Drinking Water Contaminant Candidate List*, in *Federal Register 85 FR 14098*. 2020.
14. Norman, J.E., Toccalino, P.L., and Morman, S.A. *Health-based screening levels for evaluating water-quality data (2nd ed.)*. U.S. Geological Survey web page 2018; Available from: https://water.usgs.gov/water-resources/hbsl/.
15. Musgrove, M., *The occurrence and distribution of strontium in U.S. groundwater.* Applied Geochemistry, **2020**. *126*: p. 104867.
16. Stackelberg, P.E., *Groundwater quality in the Cambrian-Ordovician aquifer system, midwestern United States*, in *U.S. Geological Survey Fact Sheet 2017-3056*. 2017: Reston, VA. p. 4.

17. White, D.E., Hem, J.D., and Waring, G.S., *Data of Geochemistry, Chapter F: Chemical composition of subsurface waters*, in *U.S. Geological Survey Professional Paper 440-F*, M. Fleischer, Editor. 1963.
18. Wisconsin Department of Natural Resources. *Public Drinking Water System Data*. 2021; Available from: https://dnr.wi.gov/dwsviewer.
19. Bergquist, L., *Fond du Lac to pay settlement over radium in drinking water*, in *Milwaukee Journal Sentinel*. 2009.
20. Luczaj, J. and Masarik, K., *Groundwater quantity and quality issues in a water-rich region: Examples from Wisconsin, USA.* Resources, **2015**. *4*(2): p. 323.
21. Faraj, T., Ragab, A., and El Alfy, M., *Geochemical and hydrogeological factors influencing high levels of radium contamination in groundwater in arid regions.* Environmental Research, **2020**. *184*: p. 109303.
22. Grundl, T., Bradbury, K.R., Feinstein, D.T., Friers, S., and Hart, D., *A Combined Hydrologic/Geochemical Investigation of Groundwater Conditions in the Waukesha County Area, WI*, in *Final Report submitted to the Wisconsin Groundwater Research Program*. 2006.
23. Grundl, T. and Cape, M., *Geochemical factors controlling radium activity in a sandstone aquifer.* Groundwater, **2006**. *44*(4): p. 518-527.
24. Luczaj, J.A., Zorn, M., and Baeten, J., *An evaluation of the distribution and sources of dissolved strontium in the groundwater of eastern Wisconsin, with a focus on Brown and Outagamie Counties*, in *Groundwater Research Report WR12R004*. 2013, Final report submitted to the Wisconsin Water Resources Insitute.
25. Weaver, T.R. and Bahr, J.M., *Geochemical Evolution in the Cambrian-Ordovician Sandstone Aquifer, Eastern Wisconsin: 2. Correlation Between Flow Paths and Ground-Water Chemistry.* Groundwater, **1991**. *29*(4): p. 510-515.
26. Wilson, J.T., *Water Quality Assessment of the Cambrian-Ordovician Aquifer System in the Northern Midwest, United States: Scientific Investigations Report 2011-5229, 154 p.* 2012: U.S. Geological Survey.
27. Chen, M.A. and Kocar, B.D., *Radium sorption to iron (hydr)oxides, pyrite, and montmorillonite: implications for mobility.* Environmental Science & Technology, **2018**. *52*(7): p. 4023-4030.
28. International Atomic Energy Agency, *The Environmental Behaviour of Radium: Revised Edition*, in *Technical Report No. 476 44–51*. 2014, IAEA: Vienna.
29. Karaseva, O.N., Ivanova, L.I., and Lakshtanov, L.Z., *Strontium adsorption on manganese oxide (δ-MnO2) at elevated temperatures: Experiment and modeling.* Geochemistry International, **2019**. *57*(10): p. 1107-1119.
30. Koulouris, G., *Dynamic studies on sorption characteristics of 226Ra on manganese dioxide.* Journal of Radioanalytical and Nuclear Chemistry, **1995**. *193*(2): p. 269-279.
31. Sahai, N., Carroll, S.A., Roberts, S., and O'Day, P.A., *X-Ray absorption spectroscopy of strontium(II) coordination: II. Sorption and precipitation at kaolinite, amorphous silica, and goethite surfaces.* Journal of Colloid and Interface Science, **2000**. *222*(2): p. 198-212.
32. Watts, P.H., P., *Strontium and strontium compounds*, in *Concise International Chemical Assessment Document 77*. 2010, World Health Organization.
33. Bunde, R.L., Rosentreter, J.J., Liszewski, M.J., Hemming, C.H., and Welhan, J., *Effects of calcium and magnesium on strontium distribution coefficients.* Environmental Geology, **1997**. *32*(3): p. 219-229.

34. Tamamura, S., Takada, T., Tomita, J., Nagao, S., Fukushi, K., and Yamamoto, M., *Salinity dependence of 226Ra adsorption on montmorillonite and kaolinite.* Journal of Radioanalytical and Nuclear Chemistry, **2014**. *299*(1): p. 569-575.
35. Vinson, D.S., Tagma, T., Bouchaou, L., Dwyer, G.S., Warner, N.R., and Vengosh, A., *Occurrence and mobilization of radium in fresh to saline coastal groundwater inferred from geochemical and isotopic tracers (Sr, S, O, H, Ra, Rn).* Applied Geochemistry, **2013**. *38*: p. 161-175.
36. Langley, S., Gault, A.G., Ibrahim, A., Takahashi, Y., Renaud, R., Fortin, D., Clark, I.D., and Ferris, F.G., *Strontium desorption from bacteriogenic iron oxides (BIOS) subjected to microbial Fe(III) reduction.* Chemical Geology, **2009**. *262*(3): p. 217-228.
37. Fakhreddine, S., Prommer, H., Gorelick, S.M., Dadakis, J., and Fendorf, S., *Controlling arsenic mobilization during managed aquifer recharge: The role of sediment heterogeneity.* Environmental Science & Technology, **2020**. *54*(14): p. 8728-8738.
38. Eberts, S.M., Thomas, M.A., and Jagucki, M.L., *The quality of our Nation's waters—Factors affecting public-supply-well vulnerability to contamination—Understanding observed water quality and anticipating future water quality*, in *U.S. Geological Survey Circular 1385*. 2013: Reston, VA.
39. Young, H.L. and Siegel, D.I., *Summary of Ground-Water Hydrology of the Cambrian-Ordovician Aquifer System in the Northern Midwest, United States*, in *U.S. Geological Survey Professional Paper 1405-A*. 1992: Washington, D.C.
40. Person, M., McIntosh, J., Bense, V., and Remenda, V.H., *Pleistocene hydrology of North America: The role of ice sheets in reorganizing groundwater flow systems.* Reviews of Geophysics, **2007**. *45*(3).
41. Siegel, D.I. and Mandle, R.J., *Isotopic evidence for glacial meltwater recharge to the Cambrian-Ordovician aquifer, North-Central United States.* Quaternary Research, **1984**. *22*(3): p. 328-335.
42. Franz, K.E., *Geochemistry of the sandstone and Silurian aquifers in eastern Wisconsin*. 1985, MS Thesis, Syracuse University. p. 103.
43. Siegel, D.I., *Sulfur isotope evidence for regional recharge of saline water during continental glaciation, North-Central United States.* Geology, **1990**. *18*: p. 1054-1056.
44. Faure, G. and Mensing, T., *Isotopes: Principles and Applications*. 3rd ed. 2005, Hoboken, New Jersey: John Wiley & Sons, Inc. 897.
45. Batten, W., *Bedrock Geology of Fond du Lac County, Wisconsin. Plate 1: Bedrock Geology Map of Fond du Lac County, Wisconsin*. 2018: Wisconsin Geological and Natural History Survey.
46. Newport, T.G., *Geology and ground-water resources of Fond Du Lac County, Wisconsin*, in *Water Supply Paper 1604*. 1962, U.S. Geological Survey: Washington, D.C. p. 197.
47. Skalbeck, J.D., Koski, A.J., and Peterson, M.T., *Estimation of Precambrian basement topography in Central and Southeastern Wisconsin from 3D modeling of gravity and aeromagnetic data.* Journal of Applied Geophysics, **2014**. *106*: p. 187-195.
48. Thwaites, F.T., *Buried pre-Cambrian of Wisconsin. Wisconsin Geological and Natural History Survey*. 1957, Wisconsin Geological and Natural History Survey.
49. Ryling, R.W., *A preliminary study of the distribution of saline water in the bedrock aquifers of Eastern Wisconsin*, in *U.S. Geological Survey Information Circular Number 5*. 1961.

50. Grundl, T., Magnusson, N., Brennwald, M., and Kipfer, R., *Mechanisms of subglacial groundwater recharge as derived from noble gas, 14C, and stable isotopic data.* Earth and Planetary Science Letters, **2013**. *369-370*: p. 78-85.
51. Baird, R.B. and Eaton, A.D., *7500-Ra RADIUM*, in *Standard Methods For the Examination of Water and Wastewater*, E.W. Rice, Editor. 2017, American Water Works Association.
52. Parkhurst, D.L. and Appelo, C.A.J., *Description of input and examples for PHREEQC version 3: a computer program for speciation, batch-reaction, one-dimensional transport, and inverse geochemical calculations*, in *Techniques and Methods*. 2013: Reston, VA. p. 519.
53. Mathews, M., Scott, S.R., Gotkowitz, M.B., Hunt, R.J., and Ginder-Vogel, M., *Isotopic analysis of radium geochemistry at discrete intervals in the Midwestern Cambrian-Ordovician aquifer system.* Applied Geochemistry, **2022**. *142*.
54. Cheng, H., Lawrence Edwards, R., Shen, C.-C., Polyak, V.J., Asmerom, Y., Woodhead, J., Hellstrom, J., Wang, Y., Kong, X., Spötl, C., Wang, X., and Calvin Alexander, E., *Improvements in 230Th dating, 230Th and 234U half-life values, and U–Th isotopic measurements by multi-collector inductively coupled plasma mass spectrometry.* Earth and Planetary Science Letters, **2013**. *371-372*: p. 82-91.
55. Cheng, H., Edwards, R.L., Hoff, J., Gallup, C.D., and Asmerom, Y., *The half-lives of uranium-234 and thorium-230.* Chemical Geology, **2000**. *169*: p. 17-33.
56. Nier, A.O., *The isotopic constitution of strontium, barium, bismuth, thallium and mercury.* Physical Review, **1938**. *54*(4): p. 275-278.
57. Kagami, H., Okano, O., Sudo, H., Hiroji, H, *Isotopic analysis of Rb and Sr using a full automatic thermal ionization mass spectrometer.* Okayama Daigaku Onsen Kenkyusho Hokoku, **1982**. *52*: p. 51-70.
58. Craddock, P.R., Rouxel, O.J., Ball, L.A., and Bach, W., *Sulfur isotope measurement of sulfate and sulfide by high-resolution MC-ICP-MS.* Chemical Geology, **2008**. *253*(3-4): p. 102-113.
59. International Atomic Energy Agency, *Reference sheet for IAEA-S-1, IAEA-S-2, IAEA-S-3*. 2020: IAEA, Vienna. p. 6.
60. Cloutier, V., Lefebvre, R., Therrien, R., and Savard, M.M., *Multivariate statistical analysis of geochemical data as indicative of the hydrogeochemical evolution of groundwater in a sedimentary rock aquifer system.* Journal of Hydrology, **2008**. *353*(3): p. 294-313.
61. Liu, F., Wang, S., Yeh, T.C.J., Zhen, P., Wang, L., and Shi, L., *Using multivariate statistical techniques and geochemical modelling to identify factors controlling the evolution of groundwater chemistry in a typical transitional area between Taihang Mountains and North China Plain.* Hydrological Processes, **2020**. *34*(8): p. 1888-1905.
62. Monjerezi, M., Vogt, R.D., Aagaard, P., Gebru, A.G., and Saka, J.D.K., *Using 87Sr/86Sr, δ18O and δ2H isotopes along with major chemical composition to assess groundwater salinization in lower Shire valley, Malawi.* Applied Geochemistry, **2011**. *26*(12): p. 2201-2214.
63. Wei, T. and Simko, V., *R package "corrplot": Visualization of a Correlation Matrix (Version 0.84)*. 2017.
64. Bondu, R., Cloutier, V., Rosa, E., and Roy, M., *An exploratory data analysis approach for assessing the sources and distribution of naturally occurring contaminants (F, Ba, Mn, As)*

in groundwater from southern Quebec (Canada). Applied Geochemistry, **2020**. *114*: p. 104500.
65. Bauer, D.F., *Constructing confidence sets using rank statistics.* Journal of the American Statistical Association, **1972**. *67*: p. 687-690.
66. Helsel, D.R., Hirsch, R.M., Ryberg, K.R., Archfield, S.A., and Gilroy, E.J., *Statistical Methods in Water Resources*, in *U.S. Geological Survey Techniques and Methods, Book 4*. 2020, U.S. Geological Survey. p. 458.
67. Hollander, M. and Wolfe, D.A., *Nonparametric Statistical Methods*. 1973, New York: John Wiley & Sons.
68. McMahon, P.B. and Chapelle, F.H., *Redox Processes and Water Quality of Selected Principal Aquifer Systems.* Groundwater, **2008**. *46*(2): p. 259-271.
69. Stackelberg, P.E., Szabo, Z., and Jurgens, B.C., *Radium mobility and the age of groundwater in public-drinking-water supplies from the Cambrian-Ordovician aquifer system, north-central USA.* Applied Geochemistry, **2018**. *89*: p. 34-48.
70. Ball, J.W. and Nordstrom, D.K., *User's manual for WATEQ4F, with revised thermodynamic data base and text cases for calculating speciation of major, trace, and redox elements in natural waters*, in *Open-File Report 91-183*. 1991: U. S. Geological Survey. p. 193.
71. Craig, H., *Isotopic variations in meteoric waters.* Science, **1961**. *133*(3465): p. 1702-1703.
72. Simpkins, W.W., *Genesis and spatial distribution of variability in the lithostratigraphic, geotechnical, hydrogeological, and geochemical properties of the Oak Creek Formation in southeastern Wisconsin*. 1989, PhD Dissertation, University of Wisconsin - Madison p. 901.
73. Weaver, T.R. and Bahr, J., *Geochemical Evolution in the Cambrian-Ordovician Sandstone Aquifer, Eastern Wisconsin: 1. Major Ion and Radionuclide Distribution.* Groundwater, **1991**. *29*(3): p. 350-356.
74. Claypool, G.E., Holser, W.T., Kaplan, I.R., Sakai, H., and Zak, I., *The age curves of sulfur and oxygen isotopes in marine sulfate and their mutual interpretation.* Chemical Geology, **1980**. *28*: p. 199-260.
75. Perry, E.C., Grundl, T., and Gilkeson, R.H., *H, O, and S isotopic study of the groundwater in the Cambrian-Ordovician aquifer system of northern Illinois*, in *Isotope Studies of Hydrologic Processes*. 1982, NIU Press. p. 35-43.
76. Vengosh, A., Coyte, R.M., Podgorski, J., and Johnson, T.M., *A critical review on the occurrence and distribution of the uranium- and thorium-decay nuclides and their effect on the quality of groundwater.* Science of the Total Environment, **2021**: p. 151914.
77. Mathews, M., Scott, S., Gotkowitz, M., and Ginder-Vogel, M., *Association of radionuclide isotopes with aquifer solids in the Midwestern Cambrian-Ordovician aquifer system* ACS Earth and Space Chemistry, **2021**. *5*(2): p. 268-278.
78. Luczaj, J.A., *Evidence against the Dorag (mixing-zone) model for dolomitization along the Wisconsin arch: A case for hydrothermal diagenesis.* AAPG Bulletin, **2006**. *90*(11): p. 1719-1738.
79. Luczaj, J.A., McIntire, M.J., and Olson Hunt, M.J., *Geochemical characterization of trace MVT mineralization in Paleozoic sedimentary rocks of Northeastern, Wisconsin, USA.* Geosciences, **2016**. *6*(29).
80. Fleischer, R.L., *Isotopic disequilibrium of uranium: alpha-recoil damage and preferential solution effects.* Science, **1980**. *207*(4434): p. 979-81.

81. Gilkeson, R.H., Perry, E.C., Cowart, J.B., and Holtzman, R.B., *Isotopic studies of the natural sources of radium in groundwater in Illinois*, in *Research Report 187*. 1984, Final Report submitted to the Bureau of Reclamation, U.S. Department of the Interior.
82. Osmond, J.K., Cowart, J.B., and Ivanovich, M., *Uranium isotopic disequilibrium in ground water as an indicator of anomalies.* The International Journal of Applied Radiation and Isotopes, **1983**. *34*(1): p. 283-308.
83. Bathurst, R.G.C., *Carbonate Sediments and Their Diagenesis*. 1st ed. Vol. 12. 1972: Elsevier Science. 657.
84. Appelo, C.A.J., *Cation and proton exchange, pH variations, and carbonate reactions in a freshening aquifer.* Water Resources Research, **1994**. *30*(10): p. 2793-2805.
85. Carroll, D., *Ion exchange in clays and other minerals.* Geological Society of America Bulletin, **1959**. *70*(6): p. 749.
86. Oden, J.H. and Szabo, Z., *Arsenic and radionuclide occurrence and relation to geochemistry in groundwater of the Gulf Coast Aquifer System in Houston, Texas, 2007–11*, in *Scientific Investigations Report 2015-5071*. 2015, U.S. Geological Survey: Reston, VA.
87. Hunter, H.A., Ling, F.T., and Peters, C.A., *Metals Coprecipitation with Barite: Nano-XRF Observation of Enhanced Strontium Incorporation.* Environmental Engineering Science, **2020**. *37*(4): p. 235-245.
88. Zhu, C., *Coprecipitation in the barite isostructural family: 1. binary mixing properties.* Geochimica et Cosmochimica Acta, **2004**. *68*(16): p. 3327-3337.
89. McDevitt, B., McLaughlin, M., Cravotta, C.A., Ajemigbitse, M.A., Van Sice, K.J., Blotevogel, J., Borch, T., and Warner, N.R., *Emerging investigator series: radium accumulation in carbonate river sediments at oil and gas produced water discharges: implications for beneficial use as disposal management.* Environmental Science: Processes & Impacts, **2019**. *21*(2): p. 324-338.
90. Pingitore, N.E. and Eastman, M.P., *The coprecipitation of Sr2+ with calcite at 25°C and 1 atm.* Geochimica et Cosmochimica Acta, **1986**. *50*(10): p. 2195-2203.
91. Dove, P.M. and Platt, F.M., *Compatible real-time rates of mineral dissolution by Atomic Force Microscopy (AFM).* Chemical Geology, **1996**. *127*(4): p. 331-338.

Chapter 3

Elevated radium activity in a hydrocarbon-contaminated aquifer

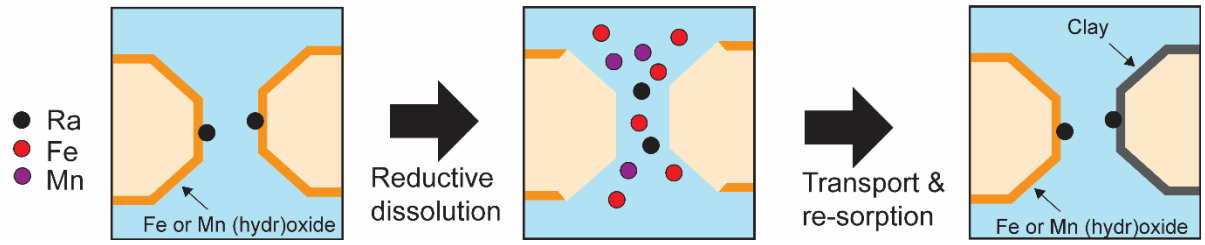

3.1 Abstract

In hydrocarbon-contaminated aquifers, the introduction of organic matter modifies geochemical conditions. Biogeochemical zones form proximal to the source zone that include iron (Fe(III)) and manganese (Mn(IV)) (hydr)oxide reduction, with the potential to release associated geogenic contaminants to groundwater. Here, multi-level monitoring systems are used to investigate radium (^{226}Ra, ^{228}Ra) activities in an aquifer contaminated with a mixture of chlorinated solvents, ketones, and aromatics occurring as a dense non-aqueous phase liquid in the source zone. ^{226}Ra activities are up to ten times higher than background 60 m downgradient of the source zone, where pH is lower, total dissolved solids concentrations are higher, and conditions are more anoxic (methanogenic) than background. Statistical correlations indicate Fe and Mn (hydr)oxide reduction and sorption site competition likely play a role in the elevated Ra activities within the

Amy K. Wiersma: Funding Acquisition, Conceptualization, Methodology, Investigation, Formal Analysis, Writing – Original Draft and Review & Editing, Visualization. **Glen Hook**: Investigation, Writing – Review & Editing, Visualization. **Madeleine Mathews**: Conceptualization, Formal Analysis, Writing – Review & Editing. **Sean R. Scott**: Conceptualization, Methodology, Resources, Validation, Formal Analysis, Writing – Review & Editing. **Jessica R. Meyer**: Conceptualization, Methodology, Visualization, Writing – Review & Editing. **Beth L. Parker**: Funding Acquisition, Conceptualization, Methodology, Resources, Writing – Review & Editing. **Matt Ginder-Vogel**: Funding Acquisition, Conceptualization, Writing – Review & Editing, Supervision.

plume. ^{226}Ra activities return to near background within the Fe(III)-reducing zone 600 m downgradient of the source and near the middle of the dissolved phase plume. Geochemical models indicate sorption to secondary phases (e.g., clays) is an important Ra attenuation mechanism within the plume. The elevated Ra activity due to geochemical conditions within the plume emphasizes the importance of investigating Ra and other trace elements at hydrocarbon-contaminated sites.

3.2 Introduction

Thousands of oil, gas, and chemical spills occur annually in the U.S. that pose threats to surface water and groundwater quality.[1] The release of reducing organic mixtures to the subsurface modifies the redox environment of a pristine aquifer, affecting both the organic and inorganic chemistry within the aquifer. Important processes include dissolution/precipitation of minerals, complexation, ion exchange, sorption, and organic matter biodegradation.[2] Strongly reducing conditions typically develop close to the source and the plume develops a redox gradient, or biogeochemical zones, along and transverse to the dominant groundwater flow direction.[3] The introduced organic matter has a great capacity to donate electrons and is oxidized with corresponding reduction reactions including that of oxygen to water, nitrite to elementary nitrogen N_2, manganese (III/IV) to manganese(II), iron(III) to iron(II), sulfate to sulfide, and CO_2 to methane.[3] Microbial communities play a key role in these redox reactions, including those related to organic contaminant biodegradation and inorganic elemental cycling within the developed biogeochemical zones.[4, 5] The resulting redox changes associated with organic contaminant spills can result in metal (hydr)oxide reduction and subsequent release of naturally occurring contaminants to groundwater, particularly those with a strong sorption affinity to Fe(III) and Mn(IV) (hydr)oxides. For example, elevated concentrations of arsenic (As), cobalt (Co), chromium (Cr), and nickel (Ni) have been observed in groundwater at crude-oil contaminated

sites,[6-12] and elevated concentrations of As and Ni can occur in groundwater at sites contaminated with chlorinated solvents.[13, 14] Radium (Ra) is another geogenic contaminant with a strong sorption affinity for Fe(III) and Mn(IV) (hydr)oxides,[15, 16] but its occurrence in relation to redox zonation and geochemical conditions in a hydrocarbon-contaminated aquifer has not yet been examined. Recent studies have emphasized the critical need for a holistic view of hydrocarbon-contaminated sites that considers both primary contamination and potential secondary water quality impacts, including the persistence of hydrocarbon partial transformation products (e.g., oxyhydrocarbons)[17-20] and the release of geogenic contaminants from aquifer sediments.[8] This holistic view can improve the assessment of the potential ecological and health effects associated with hydrocarbon-contaminated sites.[21] For example, the mobilization of Ra to aquatic systems and drinking water sources located downgradient creates potential exposure risks to biota and humans.[22]

Consumption of Ra over extended periods is linked to an elevated risk of bone cancer,[23, 24] and is therefore regulated in drinking water by the U.S. Environmental Protection Agency (EPA) at a maximum contaminant level (MCL) of 185 millibecquerel per liter (mBq/L), or 5 picocuries per liter (pCi/L), for the combined total of ^{226}Ra and ^{228}Ra. An alkaline earth metal, Ra primarily exists as a divalent cation (Ra^{2+}) under environmentally relevant conditions.[25] Radium is produced within the uranium-238 (^{238}U) and thorium-232 (^{232}Th) decay series, with ^{226}Ra produced along the ^{238}U decay chain and ^{228}Ra produced directly from the alpha decay of ^{232}Th. Therefore, the distribution of parent nuclides ^{238}U and ^{232}Th are important considerations for Ra occurrence in groundwater. Ultimately, Ra activity (concentration) in groundwater is controlled by sorption to Fe and Mn (hydr)oxide and clay minerals, and co-precipitation with sulfate and carbonate minerals.[26-29]

Geochemical conditions that limit sorption, including elevated total dissolved solids (TDS), low pH, and reducing conditions, can result in elevated Ra in groundwater.[30] While these settings occur naturally, anthropogenic activities can also alter aquifer geochemical conditions and subsequently influence Ra occurrence in groundwater. For example, increased TDS due to road salt application results in competition for sorption sites and the prevalence of mobile Ra-chloride complexes, increasing Ra activities in groundwater over decadal timescales.[31-33] Seawater intrusion can also increase aquifer TDS, subsequently mobilizing Ra.[34, 35] The infiltration of brines from oil production into groundwater can alter salinity, pH, and redox conditions, releasing Ra from bedrock to groundwater.[36, 37]

The spill of organic chemicals to the subsurface is another example of anthropogenic influence on aquifer geochemical conditions that could potentially impact Ra occurrence in groundwater. This study evaluates Ra (^{226}Ra + ^{228}Ra) and parent nuclide (e.g., ^{238}U) occurrence in a sandstone aquifer contaminated with a mixture of chlorinated solvents, ketones, and aromatics occurring as a dense non-aqueous phase liquid (DNAPL) in the source zone. The objectives of this study are to 1) compare Ra occurrence within the influence of contamination relative to a background reference location, 2) identify geochemical conditions associated with elevated Ra activity within the influence of contamination, and 2) evaluate potential Ra attenuation mechanisms. A network of high-resolution multi-level monitoring systems is used to compare Ra activities in groundwater at three locations: 1) directly downgradient, but not in the DNAPL source zone, 2) near the middle of the dissolved phase hydrocarbon plume, and 3) background conditions outside the influence of hydrocarbon contamination.[38] Measured aqueous parameters used to assess ^{226}Ra activities in relation to geochemical conditions induced by contaminant occurrence and biodegradation include redox parameters (e.g., nitrate, sulfate, methane, Fe, Mn), total

dissolved solids (TDS), and pH. Geochemical modeling is applied to evaluate Ra sequestration mechanisms (e.g., co-precipitation, sorption). Overall, this study assesses the potential for geogenic Ra release in hydrocarbon-contaminated aquifers and highlights the importance of characterizing trace elements at hydrocarbon-contaminated sites.

3.3 Materials and methods

Groundwater samples were collected near Cottage Grove, Wisconsin, USA, using Westbay MP® multi-level systems (MLS) installed in cored holes between 2008 and 2014 to characterize groundwater flow[39] and contaminant distribution[40, 41] within a 2.8 km long[42, 43] mixed organic contaminant plume migrating through the Tunnel City Group fractured sandstone. The source of the dissolved phase plume is a mixture of chlorinated solvents, ketones, and aromatics occurring as a DNAPL in the source zone (Figure 3.1). The contaminants were released from a chemical recycling facility between 1950 and 1970 and migrated into the subsurface as a DNAPL, accumulating primarily in the upper hydrologic units within the Tunnel City Group from 45-56 m below ground surface.[39] Groundwater samples collected from 4 of 46 ports in the MP-16 MLS by Mathews, et al.[38] were used to characterize background aquifer conditions and ^{226}Ra activities outside the area impacted by the dissolved phase plume. As part of this study, groundwater samples were collected from 4 of the 13 monitoring intervals in the MP-24S MLS and 3 of the 16 monitoring intervals in the MP-19S MLS, located 60 and 600 m downgradient of the DNAPL source zone, respectively, within the dissolved phase plume. Selected intervals have variable organic contaminant composition and concentrations; the lateral and vertical distribution of the dissolved phase plume at each location is conveyed using total volatile organic compound (TVOC) concentrations. All but one of the monitoring intervals were completed in the upper Tunnel City Group. Field parameters included total dissolved solids (TDS), pH, and oxidation-reduction

potential (ORP). Constituents measured in the laboratory included major ions, trace elements, total alkalinity, and isotopes (^{238}U, ^{232}Th, ^{226}Ra, ^{228}Ra, $^{87}Sr/^{86}Sr$, [$^{234}U/^{238}U$]). The predominant redox process was determined using dissolved sulfate, nitrate, Fe, and Mn concentrations and assuming negative ORP values correspond to $[O_2] < 0.5$ ppm and positive ORP values correspond to $[O_2] \geq 0.5$ ppm.[38, 44] Groundwater sampling and analytical methods are described in B-1.

The Tunnel City Group was targeted for sampling in this study because the high-concentration organic contaminant plume is co-located with a stratigraphic unit where the majority (> 94%) of extractable or "geochemically-mobile" ^{226}Ra is associated with reducible phases, such as Fe and Mn (hydr)oxides.[45] The upper Tunnel City Group is a very fine- to medium-grained glauconitic and feldspathic sandstone within the Midwestern Cambrian-Ordovician aquifer system (MCOAS), an important regional aquifer composed of sandstones, dolostones, siltstones, and shales draped by Quaternary glacial sediments (study site stratigraphy in Figure B-1). The study site is located where the Maquoketa Formation is absent (Figure 3.1). The Maquoketa Formation is an upper Ordovician shale unit with low hydraulic conductivity that, where present, overlies the MCOAS and generally results in anoxic, high-TDS water recharged thousands of years ago in the underlying units. One sample was also collected from a port within the Readstown Member of the St. Peter Formation at MP-24S, where previous sampling indicated high (> 200 ppm) concentrations of dissolved Fe.[46] The Readstown Member is composed of a sandstone and a conglomerate with fragments of shale, chert, sandstone, and dolostone, or any combination of these lithologies in a matrix of fine to coarse sand or clay.[47] Elemental analysis of samples from cores Hydrite Cottage Grove MP-16 (WID: 13001214) and Hydrite Cottage Grove MP-24S (WID: 13006132) was performed by Wisconsin Geological and Natural History Survey (WGNHS) personnel using a hand-held X-ray fluorescence (XRF) analyzer.[48]

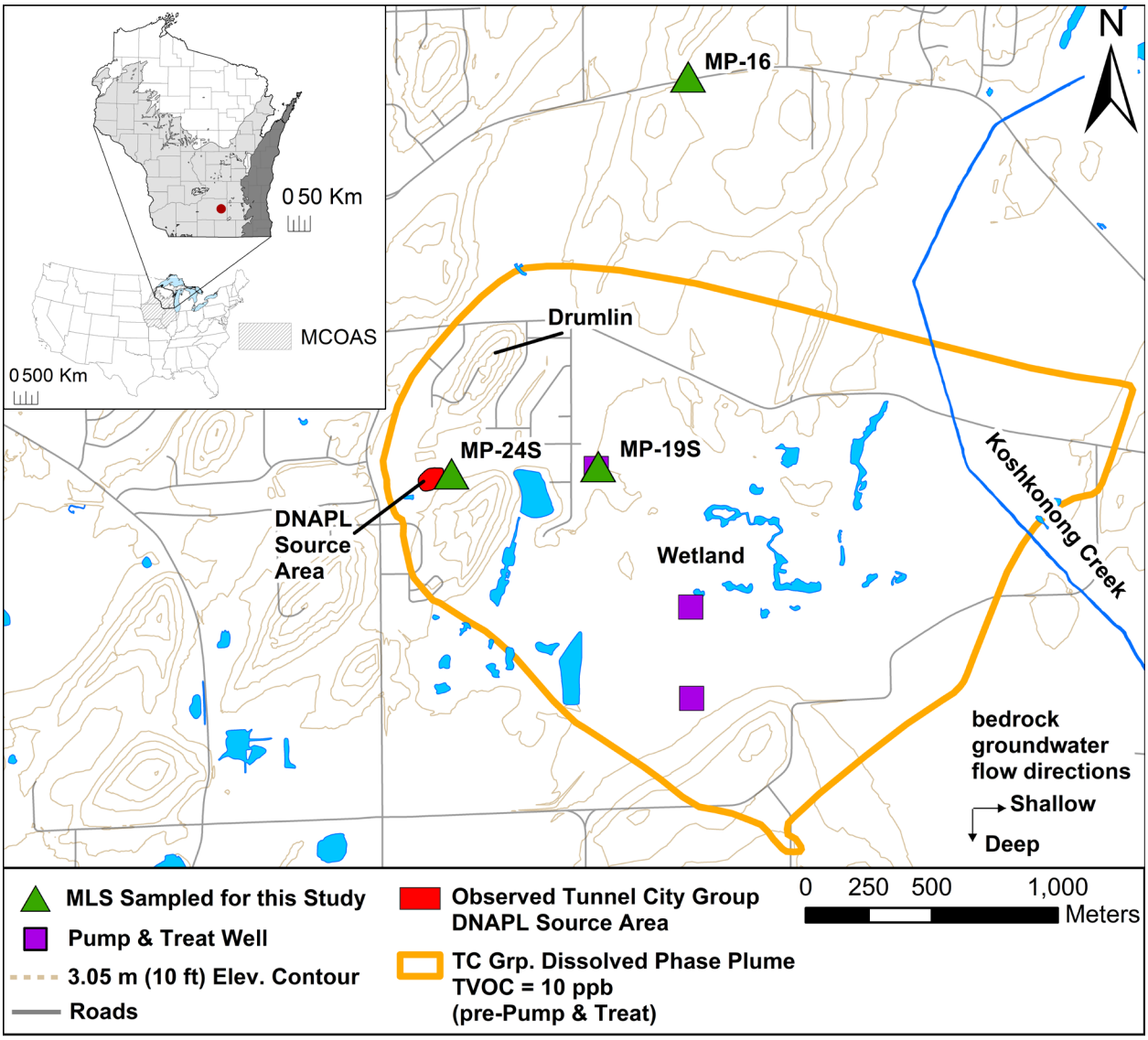

Figure 3.1 Site map showing the Tunnel City Group DNAPL source zone, dissolved phase plume extent, pump and treat wells, and the multi-level systems (MLS) sampled for groundwater in this study. The inset map in the top left shows the study site location within the Midwestern Cambrian-Ordovician aquifer system (MCOAS), with the dark gray area denoting regional confinement of the MCOAS by the Maquoketa Formation. MLS MP-16 is used to represent background aquifer conditions and was sampled by Mathews, et al.[38] TVOC = Total volatile organic compounds.

Wilcoxon-Mann-Whitney rank-sum tests were used to evaluate whether the median constituent concentration of samples collected at a well was significantly greater or less than the median constituent concentration of samples collected at the background well, while Spearman

rank correlation tests were used to evaluate correlations between two continuous variables.[49] Both statistical tests were performed using the R 'stats' package.[50]

Geochemical modeling was performed using PHREEQC 3.7.0 to determine mineral saturation indices and evaluate potential Ra sinks. The "phreeqc.dat" thermodynamic database was used and supplemented with additional phases from the "wateq4f.dat" database,[51] and Ra species and phases from the "sit.dat" database.[52] The two Ra solid phases relevant to this study, $RaSO_4$ and $RaCO_3$, use thermodynamic equilibrium constants from Langmuir and Riese.[25] The first model version considered Ra co-precipitation with the binary non-ideal solid solutions $(Ba,Ra)SO_4$ and $(Ca,Ra)CO_3$. Guggenheim parameters for non-ideal solid solutions were estimated based on Sr behavior in Glynn.[53] A separate model evaluated Ra sorption to hydrous Fe (hydr)oxide ($(Fe(OH)_3$, referred to as HFO), and hydrous Mn (hydr)oxide (MnO_2, referred to as HMO). Sorption of Ra on HFO considered the monoprotic, diffuse double layer (MDDL) model of Dzombak and Morel,[54] with surface binding coefficients for Ra reported by Sajih, et al.[26] The binding coefficient for Ra on HMO was obtained from Van Sice, et al.,[55] which estimated the coefficient using the first hydrolysis constant and linear free energy relation reported by Pourret and Davranche[56] and based on the data of Tonkin, et al.[57] A final model version assessed the potential of Ra sorption to illite, used as a proxy for clay minerals in the glauconite-rich, feldspathic Tunnel City Group. Sorption of Ra to Na-illite was evaluated using the two-site protolysis nonelectrostatic surface complexation and cation exchange model of Bradbury and Baeyens,[58] using Sr surface binding coefficients for Ra. Sorption to carbonate phases was not considered but may sequester Ra in systems actively precipitating carbonates.[59] Additional details and example PHREEQC codes used for simulations are included in Appendix B.

3.4 Results and discussion

3.4.1 Elevated radium activities

Radium activities are higher within the dissolved phase hydrocarbon plume, where geochemical conditions include lower pH, lower ORP, and higher TDS compared to background (Figures 3.2-3.4, Table B-1, with additional measured parameters and major ions presented in Table B-2). ^{226}Ra activities 60 m downgradient of the source zone at MP-24S range from 3.2 ± 0.2 to 42 ± 2 mBq/L, with geochemical conditions resulting in ^{226}Ra activities up to ten times higher than average background activities ranging from 0.7 ± 0.02 to 8.0 ± 0.2 mBq/L (Figure 3.5, Table B-3). ^{226}Ra activities decrease to near background levels 600 m downgradient of the source zone at MP-19S, ranging from 3.3 ± 0.3 to 6.5 ± 0.8 mBq/L. Barium (Ba) and strontium (Sr) are alkaline earth metals similar to Ra, and demonstrate similar trends with elevated concentrations near the source zone at MP-24S (Table B-3, Figures B-2 to B-4). ^{226}Ra activities at MP-24S and MP-19S are strongly correlated with total Fe and Mn concentrations (R_s = 0.86, p = 0.02 and R_s = 0.75, p = 0.07, respectively), suggesting ^{226}Ra release from the reductive dissolution of Fe and Mn (hydr)oxides (Figure 3.6a, Figure B-5). Redox conditions at MP-24S are predominantly methanogenic, except for Port 2, which is considered Fe(III) to SO_4^{2-}-reducing (Figure 3.3, Table B-1). Methanogenic conditions indicate that the majority of available Fe(III) and Mn(III/IV) was reduced in the past, when Fe and Mn were the dominant terminal electron acceptors in that region. In contrast, conditions are predominantly Fe(III)-reducing at MP-19S where Mn(III/IV) has been reduced in the past and Fe(III) is actively being reduced (Figure 3.4, Table B-1). Elevated ^{226}Ra activities also correspond with elevated DOC (R_s = 0.93, p < 0.01) and TDS (R_s = 0.82, p = 0.03) concentrations, likely resulting from organic contaminant concentrations (Figure 3.6b, Figure B-6). Elevated TDS concentrations can impact Ra sorption efficiency in aquifer systems; for

example, Ra activities increase linearly with TDS concentrations in the Atlantic Coastal Plain aquifer when TDS concentrations are > 3,000-10,000 ppm.[34] However, TDS concentrations are relatively low (500-2,300 ppm) within the plume (Figures 3.3-3.4, Table B-1). Additional water-rock interactions, such as the reduction of Fe and Mn (hydr)oxides, likely have a more pronounced impact on the observed Ra activities in groundwater than salinity alone.

Trends in Ra activities also vary with depth, generally decreasing with depth at MP-24S and increasing with depth at MP-19S likely as a result of shifting geochemical conditions within the dissolved phase plume (Figures 3.3-3.4). Overall, the highest Ra (total Ra, ^{226}Ra) activity is observed in the Readstown Member sample collected from MP-24S Port 4. This sample has different mineralogy than the Tunnel City Group (and presumably different solid phase Ra activity) but also has the highest dissolved Fe concentration and TDS concentration among all samples, which suggests dissolution of Fe (hydr)oxides and cation competition for sorption sites are important factors resulting in the elevated Ra activities at this port. Conditions become more oxic with depth at MP-24S ports within the Tunnel City Group, with decreases in dissolved Fe and Mn concentrations and an increase in ORP leading to lower Ra activities with depth. At MP-19S conditions become more anoxic (i.e., higher dissolved Fe and Mn concentrations and lower ORP) and demonstrate higher TDS concentrations with depth that correspond with an overall increase in Ra activity with depth. Overall, these trends suggest that both reductive dissolution of Fe and Mn (hydr)oxides and sorption site competition between Ra and elevated concentrations of other cations play a role in the observed trends in Ra activity with depth.

Aqueous strontium isotope ratios (^{87}Sr/^{86}Sr) demonstrate the influence of carbonate (e.g., aragonite, dolomite) mineral dissolution on aquifer chemistry (Figure B-7). Aqueous ^{87}Sr/^{86}Sr is dependent on Sr inputs from weatherable Sr-bearing solid phases present in aquifer systems, and

is not fractionated by chemical or mechanical processes.[60-62] ^{87}Sr is produced from the decay of ^{87}Rb ($t_{1/2}$ = 49 Ga); therefore, minerals with higher Rb/Sr ratios (e.g., silicates) will have more radiogenic (higher) $^{87}Sr/^{86}Sr$.[53] $^{87}Sr/^{86}Sr$ results are in agreement with background measurements at MP-16[38] and other locations within the MCOAS[63-65] (Table B-3) and are positively correlated with the Sr/Ca ratio (R_s =0.79, p = 0.05; Figure B-7a), indicating carbonate mineral influence on $^{87}Sr/^{86}Sr$.[66] Within the hydrocarbon plume, aqueous ^{226}Ra activities are negatively correlated with aqueous $^{87}Sr/^{86}Sr$ (R_s = -0.68, p = 0.1), indicating aqueous ^{226}Ra activity is higher where the prevalence of low Rb/Sr minerals (e.g., carbonates) dominates aqueous $^{87}Sr/^{86}Sr$ (Figure B-7b). While it is possible that some ^{226}Ra is released from carbonate mineral dissolution, $^{228}Ra/^{226}Ra$ ratios > 1 indicate silicates, rather than carbonates, are the main source of Ra in the aquifer system.[67] Furthermore, sequential extractions performed on Tunnel City Group core indicate extractable ^{226}Ra activities are over 15 times more abundant in the reducible fraction than in the acido-soluble fraction (e.g., sorbed metals, carbonate minerals).[45] Therefore, ^{226}Ra association with Fe and Mn (hydr)oxides is likely to be a more dominant control on aqueous ^{226}Ra activities than association with carbonate phases in the Tunnel City Group.

The aqueous concentration of ^{238}U, the parent isotope of ^{226}Ra, decreases to near or below limits of detection within the dissolved phase plume at MP-24S and MP-19S, likely due to the direct impact of redox conditions on U speciation (Figure B-8). At MP-16, elevated ^{238}U concentrations are associated with increased alkalinity, likely because U(VI) forms soluble and mobile uranyl carbonate complexes.[38, 68, 69] In contrast, the more reducing conditions within the contaminant plume make the less soluble U(IV) more thermodynamically favorable, resulting in lower aqueous ^{238}U concentrations. Median [$^{234}U/^{238}U$] values of 3.5 ± 0.2 and 2.1 ± 0.8 at MP-19S and MP-24S, respectively, are significantly lower compared to the background value of 6.7 ±

2.6 at MP-16 (p = 0.03 and 0.01, respectively) (Figure B-8). Disequilibrium of aqueous [$^{234}U/^{238}U$] is dependent on factors such as alpha recoil, the size of the U-bearing mineral grain, the distribution of parent ^{238}U near rock-water interfaces, as well as duration and intensity of water-rock interactions.[70, 71] A mass balance calculation using measured aqueous ^{238}U concentrations and [$^{234}U/^{238}U$] estimates the total U concentration that would have to be released from rock to water (assuming [$^{234}U/^{238}U$] in the rock is in secular equilibrium, i.e., equivalent parent/daughter activities) to account for the lower [$^{234}U/^{238}U$] values within the plume compared to background conditions at MP-16, and the corresponding ^{226}Ra activity supported by the released ^{238}U assuming [$^{226}Ra/^{238}U$] secular equilibrium (Equation 3.1):

$$\frac{[^{234}U](aq,initial)+[^{234}U](s)}{[^{238}U](aq,initial)+[^{238}U](s)} = \left[\frac{^{234}U}{^{238}U}\right]_{aq,final} \qquad (3.1)$$

Where initial ^{234}U and ^{238}U concentrations are at the background well (MP-16), [^{234}U](s) and [^{238}U](s) are the concentrations released from rock to water, and final indicates aqueous [$^{234}U/^{238}U$] observed in samples within the plume. Calculations indicate that about 5-7 times the initial ^{238}U concentration at MP-16 would have been released from the rock to account for the lower [$^{234}U/^{238}U$] at MP-24S Ports 2, 3, and 4. The ^{238}U concentrations released from rock to water within the plume are sufficient to account for the elevated aqueous ^{226}Ra activities at all sampled ports, except for the Readstown Member sample collected from MP-24S Port 4, suggesting that ^{226}Ra has not traveled far from the site of ^{238}U decay.

Secular equilibrium between ^{226}Ra and ^{238}U is expected in systems remaining undisturbed for periods much longer than the daughter isotope half-life ($t_{1/2}$ (^{226}Ra) = 1600 yr). Therefore, disequilibrium ([$^{226}Ra/^{238}U$] < 1) indicates the potential removal of the daughter isotope (^{226}Ra) from the site of parent decay (e.g., transported downgradient). Whole-rock [$^{226}Ra/^{238}U$]

measurements of MP-16 core indicate Tunnel City Group samples are within the equilibrium range, while Readstown Member samples demonstrate minor disequilibrium and potential ^{226}Ra and/or ^{238}U leaching.[38] Although whole-rock [$^{226}Ra/^{238}U$] measurements were not analyzed for MP-24S or MP-19S core samples, it is interesting to note that the Readstown Member, which demonstrates whole-rock [$^{226}Ra/^{238}U$] disequilibrium at the background well location, is the sample with the highest aqueous ^{226}Ra activity within the plume at MP-24S.

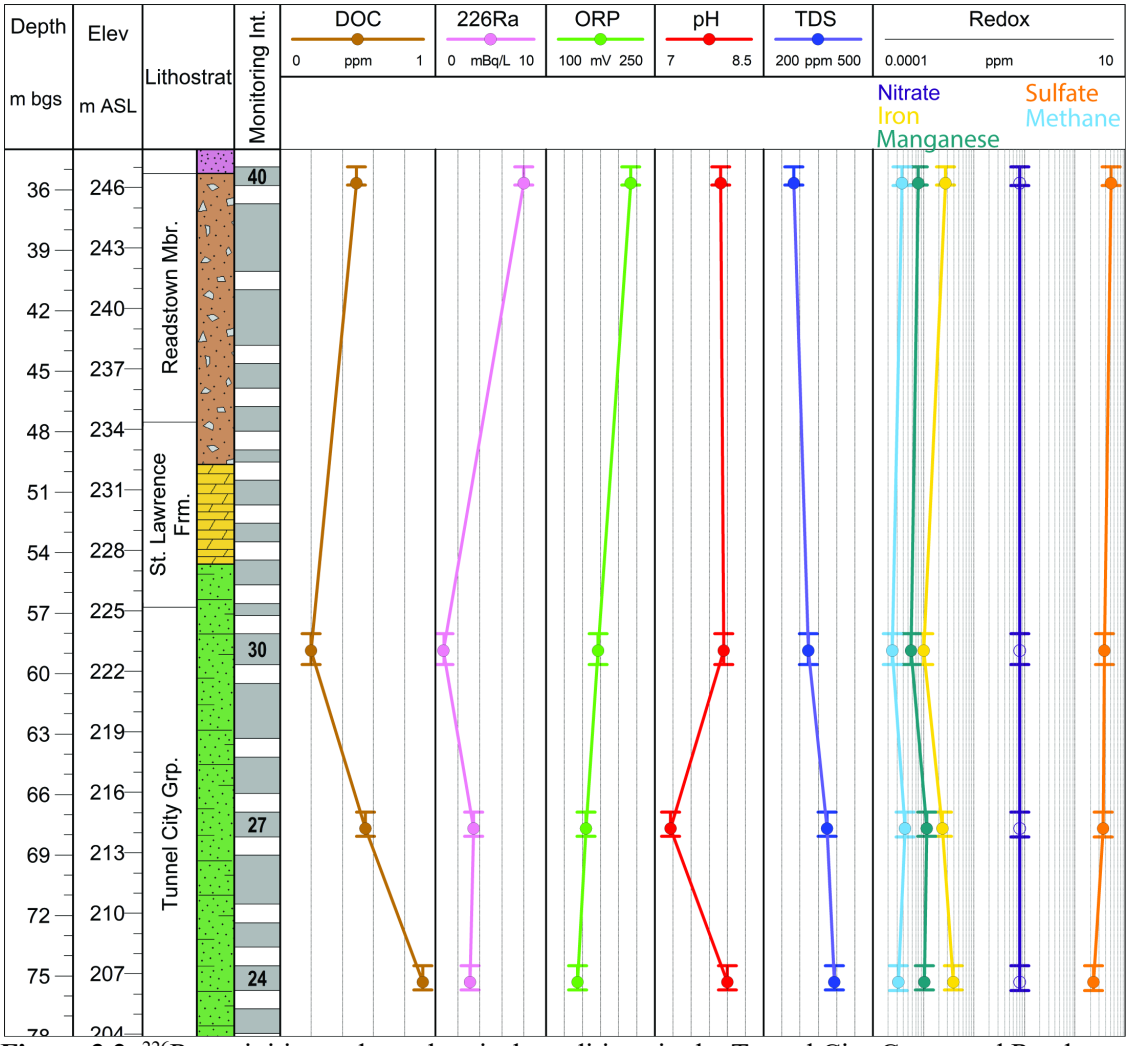

Figure 3.2 ^{226}Ra activities and geochemical conditions in the Tunnel City Group and Readstown Member at multi-level system (MLS) MP-16, located outside the influence of hydrocarbon contamination.[38] The bars above and below each data point indicate the length of each sampling interval. Open data points indicate the measurement is below the limit of detection (LOD) and is plotted as 0.5*LOD. Bgs = below ground surface, ALS = above sea level, DOC = dissolved organic carbon, ORP = oxidation-reduction potential, TDS = total dissolved solids. A complete stratigraphic column of the study site is shown in Figure B-1.

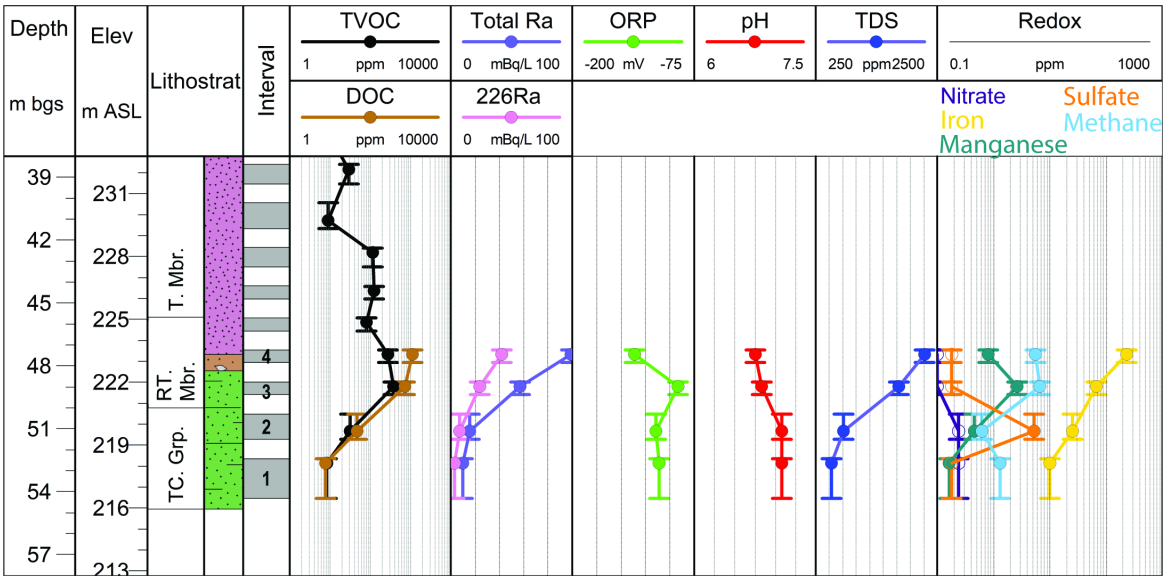

Figure 3.3 Ra activities and geochemical conditions within the Tunnel City Group and Readstown Member at multi-level system (MLS) MP-24S, located 60 m southeast of the DNAPL source zone and within the dissolved phase plume. The vertical distribution of the dissolved phase plume is denoted by total organic compound (TVOC) concentration. The bars above and below each data point indicate the length of each sampling interval. Open data points indicate the measurement is below the limit of detection (LOD) and is plotted as 0.5*LOD. Bgs = below ground surface, ALS = above sea level, TC = Tunnel City, RT = Readstown, T = Tonti, DOC = dissolved organic carbon, ORP = oxidation-reduction potential, TDS = total dissolved solids. A complete stratigraphic column of the study site is shown in Figure B-1.

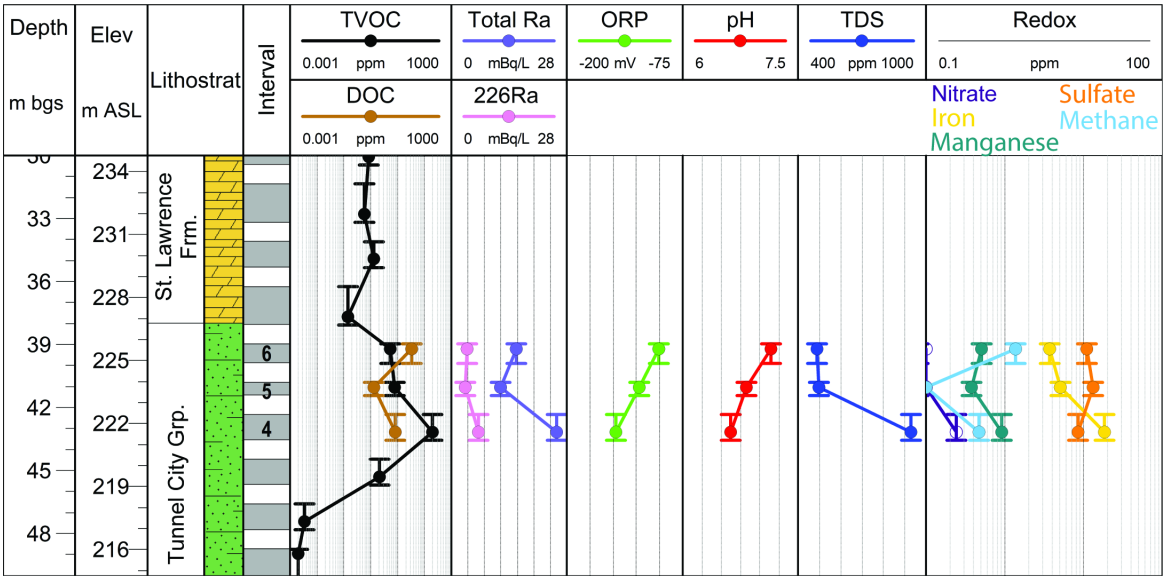

Figure 3.4 Ra activities and geochemical conditions within the Tunnel City Group at multi-level system (MLS) MP-19S, located 600 m downgradient of the DNAPL source zone and within the dissolved phase plume. The vertical distribution of the dissolved phase plume is denoted by total organic compound (TVOC) concentration. The bars above and below each data point indicate the length of each sampling interval. Open data points indicate the measurement is below the limit of detection (LOD) and is plotted as 0.5*LOD. Bgs = below ground surface, ALS = above sea level, DOC = dissolved organic carbon, ORP = oxidation-reduction potential, TDS = total dissolved solids. A complete stratigraphic column of the study site is shown in Figure B-1.

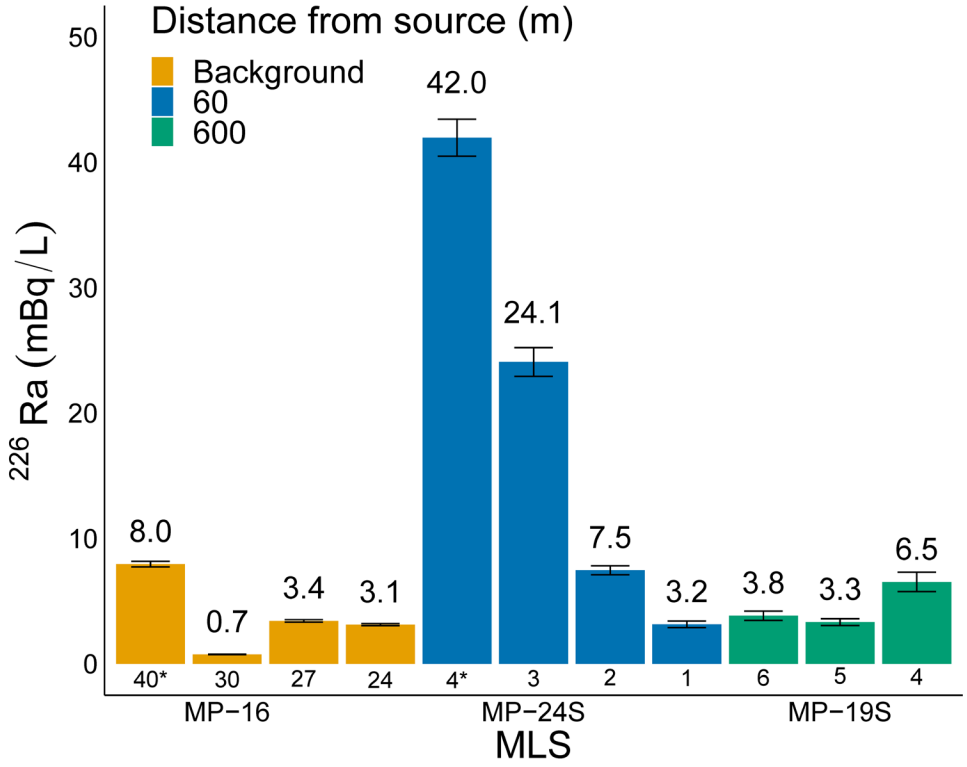

Figure 3.5 ^{226}Ra activities at sampled multi-level systems (MLS) relative to the distance downgradient from the DNAPL source zone. MLS MP-16 was sampled by Mathews, et al.[38] Numbers below the bars indicate the port intervals. *Port 4 at MP-24S and 40 at MP-16 are located in the Readstown Member, while all other samples are located in the Tunnel City Group.

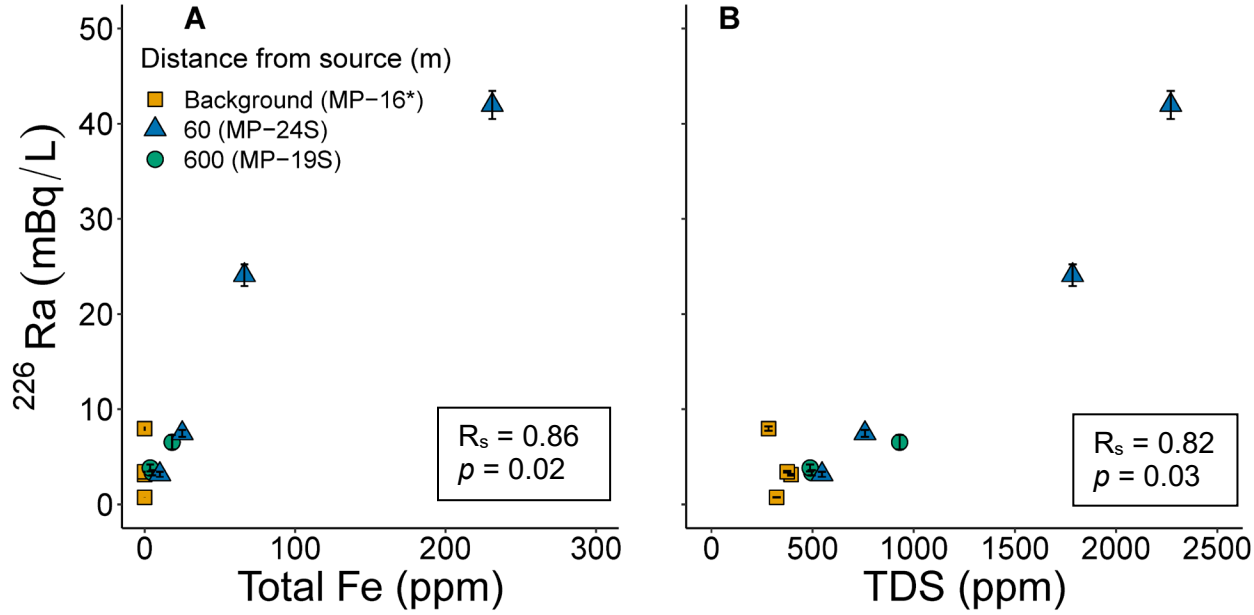

Figure 3.6 ^{226}Ra activity vs. A) total Fe concentration, and B) total dissolved solids (TDS) concentration. Data for MP-16 are plotted for comparison, but not included in the calculation of the correlation coefficient. R_s is the Spearman rank correlation coefficient, and p is the significance level.*Multi-level system MP-16 was sampled by Mathews, et al.[38]

3.4.2 Observed vs. maximum radium activities

Sequential extraction data quantifying the Ra activity associated with reducible phases (e.g., Fe and Mn (hydr)oxides) in Tunnel City Group core samples from eastern Wisconsin[45] were used to calculate the maximum aqueous ^{226}Ra or total Ra activity, Ra_{aq} in mBq/L aquifer, contributed from reducible phases in Equation 3.2:

$$Ra_{aq} = Ra_{ex} \times (1 - n) \times \rho \times \frac{1000\ cm^3}{L\ aquifer} \quad (3.2)$$

where Ra_{ex} is the exchangeable ^{226}Ra or total Ra activity in mBq/g associated with the reducible fraction, *n* is porosity, and ρ is dry bulk density in g/cm^3. Using *n* and ρ estimates of 0.17 and 2.2 g/cm^3 for the Tunnel City Group,[72] the corresponding $^{226}Ra_{aq}$ and total Ra_{aq} activities are 1100 1400 mBq/L, respectively. Mathews, et al.[38] measured the average total extractable ^{226}Ra activity in Tunnel City Group core from MP-16. Applying the ratio of the proportion of ^{226}Ra in the reducible fraction relative to the total exchangeable ^{226}Ra activity in the core from eastern Wisconsin (0.90) to the MP-16 data gives an average $^{226}Ra_{ex}$ corresponding to a maximum $^{226}Ra_{aq}$ activity of 5900 mBq/L, over 30 times above the Ra MCL of 185 mBq/L and well above the observed maximum activities of 42 mBq/L ^{226}Ra and 99 mBq/L total Ra within the plume. Potential explanations for the lower observed Ra activities include 1) only a fraction of the reducible phases is available for reduction in the aquifer, 2) a larger fraction of Ra is associated with non-redox sensitive phases (e.g., clays) at this location, 3) the sequential experiment fraction included more than reducible phases (leaching procedure is described in B-2), and 4) upon release from the reduction of Fe/Mn (hydr)oxides, a large fraction of associated Ra is re-sequestered back into aquifer solids. Nonetheless, these maximum estimates of naturally occurring Ra associated with the reducible fraction of the aquifer solids are enough to account for the elevated aqueous Ra activities within the dissolved phase plume.

3.4.3 Evaluation of Ra sinks

Important sinks for Ra in groundwater include mineral co-precipitation with sulfates and carbonates, and sorption to secondary phases such as Fe (hydr)oxides and clays. Geochemical modeling in PHREEQC indicates that Ra co-precipitation with barite (Ba, Ra)SO_4 and aragonite (Ca, Ra)CO_3 solid solutions are not important mechanisms for sequestering Ra within the plume. Saturation indices support undersaturation of (Ba, Ra)SO_4 and sulfate minerals (e.g., barite, celestine) at all ports. Similarly, (Ca, Ra)CO_3 is considered undersaturated for the majority of samples, except for MP-24S Port 4, which is at equilibrium. At equilibrium, results predict < 0.1% of Ra to be sequestered at this port by (Ca, Ra)CO_3 relative to the total activity in the initial solution (Table B-7). Therefore, sorption is predicted to be the dominant process controlling aqueous Ra activity at MP-24S and MP-19S. These results are in contrast to recent studies examining the release of wastewater from oil and gas production, which conclude that co-precipitation with sulfate/carbonate minerals is a dominant control on Ra accumulation in stream and floodplain sediments.[27, 73, 74]

Two sorption-only models were used to determine the potential importance of radium sinks: 1) sorption to HMO and HFO and 2) sorption to illite. Elemental analysis of MP-24S core samples by pXRF indicates median Fe and Mn concentrations of 2 and 0.004 wt %, respectively, in the upper Tunnel City Group, and 3 and 0.02 wt %, respectively, in the Readstown Member (Figure B-9); these concentrations were used for the mass of solid Fe(III) and Mn(III) in the model. Model results demonstrate that sorption to HFO and HMO accounts for 96-100% of the sorbed Ra relative to the total Ra activity in the initial solution, with the majority (≥ 85%) of Ra sorption occurring to HMO at the given geochemical conditions (e.g., pH, sorbent concentrations) (Table B-7). The pXRF results show a decrease of about half when comparing median solid Mn

concentrations at MP-24S to background at MP-16, and minimal change in median solid Fe concentrations (Figure B-9, B-10). Saturation indices indicate HMO undersaturation and HFO oversaturation at all ports, suggesting that Ra sorption to HFO, which are more abundant than HMO in this system, may be more important. However, the drop in pH of ~1 unit from background conditions (7.2-8.0) to within the plume (6.6-7.2), likely due to the presence of organic acids and acidity from methanogenesis,[75] may impact Ra sorption efficiency to HFO surfaces (Figures 3.2-3.4, Table B-1). The dominant surface charge of HFO will be positive below a pH of ~7.29,[54] resulting in decreased Ra sorption to HFO surfaces within the dissolved phase plume.

Elevated Al/K in the Tunnel City Group and Readstown Member indicates fine-grained sequences rich in K-feldspar and clays, compared to "cleaner" sandstones such as the Tonti Member (Figure B-9). The upper Tunnel City Group is rich in glauconite, an Fe- and K-rich phyllosilicate with a characteristic green color, low weathering resistance, and structure similar to illite.[76] Under oxic conditions, weathered glauconite may be coated with Fe (hydr)oxide.[77] Radium sorption to illite was considered and used as a proxy for glauconite and clay minerals in a separate model. Results indicate that Ra sorption to illite accounts for 83-98% of the Ra activity in the initial solution, with the fraction sorbed being lowest at MP-24S ports 3 and 4, likely because of elevated TDS and cation competition with divalent cations (e.g., Mg^{2+} and Ca^{2+}) in these samples (Table B-7). MP-24S Port 4 has the highest aqueous Ra activity and is located within the Readstown Member, which is more abundant in clay minerals with high cation exchange capacity compared to the Tunnel City Group (Figure B-9). Cation exchange occurring on planar surface sites accounts for all of the Ra sequestered by illite in the model, with no Ra sequestered by surface complexation on the weak site; this is expected for alkaline earth metals.[58] The low Na: (Ca + Mg) molar ratios (< 0.1) for groundwater samples are well below the values > 15 that are indicative of

cation exchange,[78] suggesting that cation exchange with Na^+ is not a dominant process at the site. Nonetheless, sorption to negatively-charged clay minerals such as illite, which are not redox-sensitive in contrast to Fe and Mn (hydr)oxides, likely plays an important role in sequestering Ra within the dissolved phase plume. Sorption to negatively-charged carbonate mineral surfaces (e.g., siderite, ankerite) was not considered, but is another potential Ra sink.[59] Saturation indices support siderite ($FeCO_3$) oversaturation in all samples from MP-24S and MP-19S, indicating siderite precipitation is favorable within the dissolved phase plume.

Similar to our results for Ra, Ba, and Sr, investigations at the Bemidji, Minnesota, oil spill site observe maximum concentrations of trace elements including As, Co, Ni, Ba, and Sr in the crude-oil source zone due to release from Fe (hydr)oxide reduction coupled to the oxidative degradation of dissolved hydrocarbons.[7, 79, 80] At the Bemidji site, concentrations of cations (Co, Ni, Ba, Sr) are attenuated further upgradient than As concentrations, and is attributed to different attenuation mechanisms. Cations are sequestered by sorption to negatively-charged mineral surfaces (e.g., siderite) in the Fe(III)-reducing zone, while As concentrations are controlled by sorption to positively-charged Fe (hydr)oxide surfaces at the leading edge of the plume due to As presence as various oxyanions in groundwater.[79, 80] The extent of the dissolved Ra plume at our site likely exists somewhere between MP-24S and MP-19S given that Ra activities return to near background levels at MP-19S. Elevated Ra activities do not extend as far downgradient as the elevated As concentrations at our site (Table B-3), suggesting that Ra attenuation may be more controlled by sorption to negatively-charged mineral surfaces (e.g., clays, siderite) than to positively-charged Fe (hydr)oxide surfaces within the dissolved phase plume. However, because the focus of this study was on Ra occurrence As concentrations were not analyzed at the background location, highlighting the need for follow-up studies investigating other trace elements

at the site. Sorption is difficult to predict given its dependence on mass, types, and heterogeneity of sorbents present, as well as the pH, ion concentrations, and redox state of the groundwater at a given location. Nonetheless, the geochemical models applied in this study demonstrate the importance of sorption processes for Ra sequestration in hydrocarbon-contaminated aquifers.

3.4.4 Implications

This study combines high-resolution multi-level system sampling and MC-ICPMS analysis of ultra-trace Ra activities to report the first investigation of Ra activities relative to biogeochemical zones in a hydrocarbon-contaminated aquifer. Our proposed conceptual model for Ra cycling at the site includes the enhanced release of Ra to groundwater 60 m downgradient of the source zone, likely due to geochemical conditions (e.g., methanogenic conditions, high TDS concentrations) resulting in the reductive dissolution of Fe and Mn (hydr)oxides and cation competition for sorption sites. 600 m downgradient of the source zone and near the middle of the dissolved phase plume, conditions are predominantly Fe(III)-reducing and Ra activity in groundwater is similar to background activities in the aquifer. Upon release near the source zone Ra resorbs downgradient where it is expected to encounter available sorption sites on negatively-charged secondary mineral phases (e.g., clays) within the dissolved phase plume, and Fe and Mn (hydr)oxides as geochemical conditions return to background further downgradient (e.g., higher pH, more oxic). The elevated Ra activities in groundwater near the DNAPL source zone demonstrate the potential secondary impacts of industrial waste released to the environment.

Further investigation is warranted in examining Ra activities in other hydrocarbon-contaminated aquifers. Other sites contaminated with complex organic mixtures, including wastewater and landfill leachate, also develop biogeochemical zones with the potential to impact the occurrence of geogenic contaminants including Ra.[2, 81-84] For example, disposal of treated

wastewater in Cape Cod, Massachusetts, features a series of biogeochemical zones in the subsurface, including an anoxic core with naturally occurring elements from sediment such as Fe, Mn, and As.[85, 86] Although total Ra activities at this site do not exceed the MCL and the pump-and-treat system prevents contaminants from migrating downgradient, Ra activities may exceed the MCL and migrate downgradient at other hydrocarbon-contaminated locations within the MCOAS, or in other aquifers with lower sorption capacities. Ra frequently exceeds the MCL under natural conditions in aquifers such as the MCOAS or North Atlantic Coastal Plain aquifer, but relatively little attention has been given to the impact of anthropogenic activities and evolving geochemical conditions on Ra occurrence in groundwater. The observation that Ra activities are elevated within the influence of hydrocarbon contamination suggests that Ra activities should be routinely analyzed alongside other trace elements when characterizing hydrocarbon-contaminated sites.

3.5 Acknowledgements

The authors thank Jessica Bulova and Olenka Forde of the Morwick G360 Groundwater Research Institute for assistance with field data collection. Rock samples in this study were collected and logged by Morwick G360 Institute students and staff, funded by NSERC Project Nos. IRCPJ 363783-06, 363783-11, and 363783-18 to B.L. Parker and curated at the Wisconsin Geological and Natural History Survey (WGNHS) core repository. We thank WGNHS for access to core 13001214 and 13006132, and lab facilities. Additional thanks to the Wisconsin State Laboratory of Hygiene Trace Metal Laboratory and James Lazarcik at the University of Wisconsin-Madison Core Facility for Advanced Water Analysis for laboratory analyses support, and to three anonymous reviewers that greatly improved the quality of this manuscript.

This study was funded by the Wisconsin Groundwater Research and Monitoring Program and the University of Wisconsin System. A.K. Wiersma is supported by the National Science Foundation Graduate Research Fellowship Program under Grant No. DGE-1747503. Any opinions, findings, and conclusions or recommendations expressed in this material are those of the authors and do not necessarily reflect the views of the National Science Foundation. Support was also provided by the Graduate School and the Office of the Vice Chancellor for Research and Graduate Education at the University of Wisconsin–Madison with funding from the Wisconsin Alumni Research Foundation.

3.6 References

1. U.S. Environmental Protection Agency. *Contaminated land*. 2021 [cited 2023; Available from: https://www.epa.gov/report-environment/contaminated-land].
2. Christensen, T.H., Kjeldsen, P., Bjerg, P.L., Jensen, D.L., Christensen, J.B., Baun, A., Albrechtsen, H.-J., and Heron, G., *Biogeochemistry of landfill leachate plumes.* Applied Geochemistry, **2001**. *16*: p. 659-718.
3. Christensen, T.H., Bjerg, P.L., Banwart, S.A., Jakobsen, R., Heron, G., and Albrechtsen, H.-J., *Characterization of redox conditions in groundwater contaminant plumes.* Journal of Contaminant Hydrology, **2000**. *45*: p. 165-241.
4. Borch, T., Kretzschmar, R., Kappler, A., Cappellen, P.V., Ginder-Vogel, M., Voegelin, A., and Campbell, K., *Biogeochemical redox processes and their impact on contaminant dynamics.* Environmental Science & Technology, **2010**. *44*(1): p. 15-23.
5. Lovley, D.R., Holmes, D.E., and Nevin, K.P., *Dissimilatory Fe(III) and Mn(IV) reduction.* Advances in Microbial Physiology, **2004**. *49*: p. 219-286.
6. Cozzarelli, I.M., Schreiber, M.E., Erickson, M.L., and Ziegler, B.A., *Arsenic cycling in hydrocarbon plumes: Secondary effects of natural attenuation.* Ground Water, **2016**. *54*(1): p. 35-45.
7. Ziegler, B.A., Schreiber, M.E., and Cozzarelli, I.M., *The role of alluvial aquifer sediments in attenuating a dissolved arsenic plume.* Journal of Contaminant Hydrology, **2017**. *204*: p. 90-101.
8. Ziegler, B.A., Ng, G.H.C., Cozzarelli, I.M., Dunshee, A.J., and Schreiber, M.E., *Arsenic in petroleum-contaminated groundwater near Bemidji, Minnesota Is predicted to persist for centuries.* Water, **2021**. *13*(11): p. 1485.
9. Ng, G.-H.C., Bekins, B.A., Cozzarelli, I.M., Baedecker, M.J., Bennett, P.C., Amos, R.T., and Herkelrath, W.N., *Reactive transport modeling of geochemical controls on secondary water quality impacts at a crude oil spill site near Bemidji, MN.* Water Resources Research, **2015**. *51*(6): p. 4156-4183.
10. Ziegler, B.A., McGuire, J.T., and Cozzarelli, I.M., *Rates of As and trace-element mobilization caused by Fe reduction in mixed BTEX–ethanol experimental plumes.* Environmental Science & Technology, **2015**. *49*(22): p. 13179-13189.
11. Güler, C., Kaplan, V., and Akbulut, C., *Spatial distribution patterns and temporal trends of heavy-metal concentrations in a petroleum hydrocarbon-contaminated site: Karaduvar coastal aquifer (Mersin, SE Turkey).* Environmental Earth Sciences, **2013**. *70*(2): p. 943-962.
12. Schreiber, M.E. and Cozzarelli, I.M., *Arsenic release to the environment from hydrocarbon production, storage, transportation, use and waste management*. Journal of Hazardous Materials, **2021**. *411*(5).
13. Wiedemeier, T.H., Swanson, M.A., Moutoux, D.E., Gordon, E.K., Wilson, J.T., Wilson, B.H., Kampbell, D.H., Haas, P.E., Miller, R.N., Hansen, J.E., and Chapelle, F.H. *Technical Protocol for evaluating natural attenuation of chlorinated solvents in groundwater*; U.S. Environmental Protection Agency: Washington, D.C., **1998**.
14. Smith, S., Dupont, R.R., and McLean, J.E., *Arsenic Release and Attenuation Processes in a Groundwater Aquifer During Anaerobic Remediation of TCE with Biostimulation*. Groundwater Monitoring & Remediation**, 2019**. *39*(3): p. 61-70.

15. Chen, M.A. and Kocar, B.D., *Radium sorption to iron (hydr)oxides, pyrite, and montmorillonite: implications for mobility.* Environmental Science & Technology, **2018**. *52*(7): p. 4023-4030.
16. Landa, E.R., Phillips, E.J.P., and Lovley, D.R., *Release of 226Ra from uranium mill tailings by microbial Fe(III) reduction.* Applied Geochemistry, **1991**. *6*(6): p. 647-652.
17. Cozzarelli, I.M., Baedecker, M.J., Mumford, A.C., Jaeschke, J.B., and Spencer, T.A., *Understanding the evolution of groundwater-contaminant plume chemistry emanating from legacy contaminant sources: An example from a long-term crude oil spill.* Ground Water Monitoring & Remediation, **2022**. *42*(4): p. 30-42.
18. Bekins, B.A., Cozzarelli, I.M., Erickson, M.L., Steenson, R.A., and Thorn, K.A., *Crude Oil Metabolites in Groundwater at Two Spill Sites.* Groundwater, **2016**. *54*(5): p. 681-691.
19. Podgorski, D.C., Zito, P., McGuire, J.T., Martinovic-Weigelt, D., Cozzarelli, I.M.; Bekins, B.A., and Spencer, R.G.M., *Examining Natural Attenuation and Acute Toxicity of Petroleum-Derived Dissolved Organic Matter with Optical Spectroscopy*. Environmental Science & Technology, **2018**. *52*(11): p. 6157-6166.
20. Bekins, B.A., Brennan, J.C., Tillitt, D.E., Cozzarelli, I.M., Illig, J.M., and Martinović-Weigelt, D., *Biological Effects of Hydrocarbon Degradation Intermediates: Is the Total Petroleum Hydrocarbon Analytical Method Adequate for Risk Assessment?* Environmental Science & Technology, **2020**. *54*(18): p. 11396-11404.
21. Sonne, A.T., Rasmussen, J.J., Höss, S., Traunspurger, W., Bjerg, P.L., and McKnight, U.S., *Linking ecological health to co-occurring organic and inorganic chemical stressors in a groundwater-fed stream system*. Sci. Total Environ., **2018**. *642*: p. 1153-1162.
22. Farag, A.M., Harper, D.D., Cozzarelli, I.M., Kent, D.B., Mumford, A.C., Akob, D.M., Schaeffer, T., and Iwanowicz, L.R., *Using Biological Responses to Monitor Freshwater Post-Spill Conditions over 3 years in Blacktail Creek, North Dakota, USA*. Archives of Environmental Contamination and Toxicology, **2022**. *83*: p. 253-271.
23. Finkelstein, M. and Kreiger, N., *Radium in drinking water and risk of bone cancer in Ontario youths: a second study and combined analysis.* Journal of Occupational and Environmental Medicine, **1996**. *53*: p. 305-311.
24. Canu, I.G., Laurent, O., Pires, N., Laurier, D., and Dublineau, I., *Health effects of naturally radioactive water ingestion: the need for enhanced studies.* Environmental health perspectives, **2011**. *119*(12): p. 1676-1680.
25. Langmuir, D. and Riese, A.C., *The thermodynamic properties of radium.* Geochimica et Cosmochimica Acta, **1985**. *49*: p. 1593-1601.
26. Sajih, M., Bryan, N.D., Livens, F.R., Vaughan, D.J., Descostes, M., Phrommavanh, V., Nos, J., and Morris, K., *Adsorption of radium and barium on goethite and ferrihydrite: A kinetic and surface complexation modelling study.* Geochimica et Cosmochimica Acta, **2014**. *146*: p. 150-163.
27. McDevitt, B., McLaughlin, M., Cravotta, C.A., Ajemigbitse, M.A., Van Sice, K.J., Blotevogel, J., Borch, T., and Warner, N.R., *Emerging investigator series: radium accumulation in carbonate river sediments at oil and gas produced water discharges: implications for beneficial use as disposal management.* Environmental Science: Processes & Impacts, **2019**. *21*(2): p. 324-338.
28. Ames, L.L., McGarrah, J.E., and Walker, B.A., *Sorption of trace constituents from aqueous solutions onto secondary minerals. II. Radium.* Clays & Clay Minerals, **1983**. *31*(5): p. 335-342.

29. Vinograd, V.L., Brandt, F., Rozov, K., Klinkenberg, M., Refson, K., Winkler, B., and Bosbach, D., *Solid–aqueous equilibrium in the BaSO4–RaSO4–H2O system: First-principles calculations and a thermodynamic assessment.* Geochimica et Cosmochimica Acta, **2013**. *122*: p. 398-417.
30. Szabo, Z., Fischer, J.M., and Hancock, T.C., *Principal aquifers can contribute radium to sources of drinking water under certain geochemical conditions*, in *Fact Sheet*. 2012: Reston, VA.
31. Lindsey, B.D., Cravotta, C.A., Szabo, Z., Belitz, K., and Stackelberg, P., *Relation between road-salt application and increasing radium concentrations in a low-pH aquifer, Southern New Jersey.* ACS ES&T Water, **2021**. *1*(12): p. 2541-2547.
32. McNaboe, L.A., Robbins, G.A., and Dietz, M.E., *Mobilization of radium and radon by deicing salt contamination of groundwater.* Water, Air, & Soil Pollution, **2017**. *228*(3).
33. Lazur, A., Vanderwerker, T., and Koepenick, K., *Review of implications of road salt use on groundwater quality—corrosivity and mobilization of heavy metals and radionuclides.* Water, Air, & Soil Pollution, **2020**. *231*(9).
34. Vinson, D.S., Tagma, T., Bouchaou, L., Dwyer, G.S., Warner, N.R., and Vengosh, A., *Occurrence and mobilization of radium in fresh to saline coastal groundwater inferred from geochemical and isotopic tracers (Sr, S, O, H, Ra, Rn).* Applied Geochemistry, **2013**. *38*: p. 161-175.
35. Gonneea, M.E., Morris, P.J., Dulaiova, H., and Charette, M.A., *New perspectives on radium behavior within a subterranean estuary.* Marine Chemistry, **2008**. *109*(3-4): p. 250-267.
36. McMahon, P.B., Vengosh, A., Davis, T.A., Landon, M.K., Tyne, R.L., Wright, M.T., Kulongoski, J.T., Hunt, A.G., Barry, P.H., Kondash, A.J., Wang, Z., and Ballentine, C.J., *Occurrence and sources of radium in groundwater associated with oil fields in the Southern San Joaquin Valley, California.* Environmental Science & Technology, **2019**. *53*(16): p. 9398-9406.
37. Tomita, J., Satake, H., Fukuyama, T., Sasaki, K., Sakaguchi, A., and Yamamoto, M., *Radium geochemistry in Na–Cl type groundwater in Niigata Prefecture, Japan.* Journal of Environmental Radioactivity, **2010**. *101*(3): p. 201-210.
38. Mathews, M., Scott, S.R., Gotkowitz, M.B., Hunt, R.J., and Ginder-Vogel, M., *Isotopic analysis of radium geochemistry at discrete intervals in the Midwestern Cambrian-Ordovician aquifer system.* Applied Geochemistry, **2022**. *142*.
39. Meyer, J.R., Parker, B.L., Arnaud, E., and Runkel, A.C., *Combining high resolution vertical gradients and sequence stratigraphy to delineate hydrogeologic units for a contaminated sedimentary rock aquifer system.* Journal of Hydrology, **2016**. *534*: p. 505-523.
40. Lima, G.D.P., Meyer, J.R., Khosla, K., Dunfield, K.E., and Parker, B.L., *Spatial variability of microbial communities in a fractured sedimentary rock matrix impacted by a mixed organics plume.* Journal of Contaminant Hydrology, **2018**. *218*: p. 110-119.
41. Lima, G., Parker, B., and Meyer, J., *Dechlorinating Microorganisms in a Sedimentary Rock Matrix Contaminated with a Mixture of VOCs.* Environmental Science & Technology, **2012**. *46*(11): p. 5756-5763.
42. GeoTrans Inc., *Second quarter 2003 progress report*, C.G. Hydrite Chemical Company, Wisconsin Facility. , Editor. 2003: 3005.002, Brookfield, Wisconsin.

43. HSI GeoTrans, *DNAPL Removal Report*. 1999: Hydrite Chemical Co., Cottage Grove, Wisconsin, Facility. p. 220.
44. McMahon, P.B. and Chapelle, F.H., *Redox Processes and Water Quality of Selected Principal Aquifer Systems*. Groundwater, **2008**. *46*(2): p. 259-271.
45. Mathews, M., Scott, S., Gotkowitz, M., and Ginder-Vogel, M., *Association of radionuclide isotopes with aquifer solids in the Midwestern Cambrian-Ordovician aquifer system* ACS Earth and Space Chemistry, **2021**. *5*(2): p. 268-278.
46. Morwick G360 Institute Database, **2020**.
47. Mai, H. and Dott, R.J., *A subsurface study of the St Peter sandstone in southern and eastern Wisconsin, WGNHS Information Circular Number 47.* 1985, Wisconsin Geological and Natural History Survey: Madison, Wisconsin.
48. Zambito, J.J.I., McLaughlin, P.I., Haas, L.D., Stewart, E.K., Bremmer, S.E., and Hurth, M.J., *Sampling methodologies and data analysis techniques for geologic materials using portable X-ray fluorescence (pXRF) elemental analysis*, in *Open-File Report 2016-02*. 2016, Wisconsin Geological and Natural History Survey. p. 12.
49. Helsel, D.R., Hirsch, R.M., Ryberg, K.R., Archfield, S.A., and Gilroy, E.J., *Statistical Methods in Water Resources*, in *U.S. Geological Survey Techniques and Methods, Book 4*. 2020, U.S. Geological Survey. p. 458.
50. R Core Team, *R: A language and environment for statistical computing.* 2020, R Foundation for Statistical Computing: Vienna, Austria.
51. Ball, J.W. and Nordstrom, D.K., *User's manual for WATEQ4F, with revised thermodynamic data base and text cases for calculating speciation of major, trace, and redox elements in natural waters*, in *Open-File Report 91-183*. 1991: U. S. Geological Survey. p. 193.
52. Giffaut, E., Grivé, M., Blanc, P., Vieillard, P., Colàs, E., Gailhanou, H., Gaboreau, S., Marty, N., Madé, B., and Duro, L., *Andra thermodynamic database for performance assessment: ThermoChimie.* Applied Geochemistry, **2014**. *49*: p. 225-236.
53. Glynn, P., *Solid-solution solubilities and thermodynamics: Sulfates, carbonates and halides.* Reviews in Mineralogy and Geochemistry, **2000**. *40*(1): p. 481-511.
54. Dzombak, D.A. and Morel, F.M.M., *Surface Complexation Modeling: Hydrous Ferric Oxide*. 1990: Wiley Interscience. 416.
55. Van Sice, K., Cravotta, C.A., McDevitt, B., Tasker, T.L., Landis, J.D., Puhr, J., and Warner, N.R., *Radium attenuation and mobilization in stream sediments following oil and gas wastewater disposal in western Pennsylvania.* Applied Geochemistry, **2018**. *98*: p. 393-403.
56. Pourret, O. and Davranche, M., *Rare earth element sorption onto hydrous manganese oxide: A modeling study.* Journal of Colloid and Interface Science, **2013**. *395*: p. 18-23.
57. Tonkin, J.W., Balistrieri, L.S., and Murray, J.W., *Modeling sorption of divalent metal cations on hydrous manganese oxide using the diffuse double layer model.* Applied Geochemistry, **2004**. *19*(1): p. 29-53.
58. Bradbury, M.H. and Baeyens, B., *Experimental and Modeling Investigations on Na-illite: Acid-Base Behaviour and the Sorption of Strontium, Nickel, Europium, and Uranyl*, in *Technical Report 04-02*. 2005, Paul Scherrer Institut, Villigen PSI: Nagra, Switzerland.
59. Jones, M.J., Butchins, L.J., Charnock, J.M., Pattrick, R.A.D., Small, J.S., Vaughan, D.J., Wincott, P.L., and Livens, F.R., *Reactions of radium and barium with the surfaces of carbonate minerals.* Applied Geochemistry, **2011**. *26*(7): p. 1231-1238.

60. Faure, G. and Mensing, T., *Isotopes: Principles and Applications*. 3rd ed. 2005, Hoboken, New Jersey: John Wiley & Sons, Inc. 897.
61. Bain, D.C. and Bacon, J.R., *Strontium isotopes as indicators of mineral weathering in catchments.* Catena, **1994**. *22*(3): p. 201-214.
62. Shand, P., Darbyshire, D.P.F., Love, A.J., and Edmunds, W.M., *Sr isotopes in natural waters: Applications to source characterisation and water–rock interaction in contrasting landscapes.* Applied Geochemistry, **2009**. *24*(4): p. 574-586.
63. Hunt, R.J., Bullen, T.D., Krabbenhoft, D.P., and Kendall, C., *Using stable isotopes of water and strontium to investigate the hydrology of a natural and a constructed wetland.* Groundwater, **1998**. *36*(3): p. 434-443.
64. Vinson, D.S., Lundy, J.R., Dwyer, G.S., and Vengosh, A., *Implications of carbonate-like geochemical signatures in a sandstone aquifer: Radium and strontium isotopes in the Cambrian Jordan aquifer (Minnesota, USA).* Chemical Geology, **2012**. *334*: p. 280-294.
65. Plechacek, A., Scott, S.R., Gotkowitz, M.B., and Ginder-Vogel, M., *Strontium and radium occurrence at the boundary of a confined aquifer system.* Applied Geochemistry, **2022**. *142*.
66. Banner, J.L., Musgrove, M., and Capo, R.C., *Tracing ground-water evolution in a limestone aquifer using Sr isotopes: Effects of multiple sources of dissolved ions and mineral-solution reactions.* Geology, **2004**. *22*(8): p. 687-690.
67. Szabo, Z., dePaul, V.T., Fischer, J.M., Kraemer, T.F., and Jacobsen, E., *Occurrence and geochemistry of radium in water from principal drinking-water aquifer systems of the United States.* Applied Geochemistry, **2012**. *27*(3): p. 729-752.
68. Markich, S.J., *Uranium speciation and bioavailability in aquatic systems: An overview.* The Scientific World Journal, **2002**. *2*: p. 756147.
69. Silva, R.J. and Nitsche, H., *Actinide Environmental Chemistry.* Radiochimca Acta, **1995**. *70-71*(Supplement): p. 377-396.
70. Porcelli, D., *Investigating groundwater processes using U- and Th-series nuclides*, in *Radioactivity in the Environment*, S. Krishnaswami and J.K. Cochran, Editors. 2008, Elsevier. p. 105-153.
71. Osmond, J.K., Cowart, J.B., and Ivanovich, M., *Uranium isotopic disequilibrium in ground water as an indicator of anomalies.* The International Journal of Applied Radiation and Isotopes, **1983**. *34*(1): p. 283-308.
72. Wisconsin Geological and Natural History Survey. *Porosity and density measurements*. **2023**. Available from: https://wgnhs.wisc.edu/maps-data/data/rock-properties/porosity-density-measurements-data/.
73. Lauer, N.E., Harkness, J.S., and Vengosh, A., *Brine Spills Associated with Unconventional Oil Development in North Dakota*. Environmental Science & Technology, **2016**. *50*(10): p. 5389-97.
74. Cozzarelli, I.M., Kent, D.B., Briggs, M., Engle, M.A., Benthem, A., Skalak, K.J., Mumford, A.C., Jaeschke, J., Farag, A., Lane, J.W. Jr., and Akob, D.M., *Geochemical and geophysical indicators of oil and gas wastewater can trace potential exposure pathways following releases to surface waters*. Sci. Total Environ., **2021**. *755*(Pt 1): p. 142909.
75. Bennett, P.C., Siegel, D.E., Baedecker, M.J., and Hult, M.F., *Crude oil in a shallow sand and gravel aquifer—I. Hydrogeology and inorganic geochemistry*. Applied Geochemistry, **1993**. *8*(6): p. 529-549.

76. Huggett, J.M., *Minerals: Glauconites and Green Clays.* Reference Module in Earth Systems and Environmental Sciences, **2013**.
77. Courbe, C., Velde, B., and Meunier, A., *Weathering of glauconites: reversal of the glauconitization process in a soil profile in Western France.* Clay Minerals, **1981**. *16*: p. 231-234.
78. Oden, J.H. and Szabo, Z., *Arsenic and radionuclide occurrence and relation to geochemistry in groundwater of the Gulf Coast Aquifer System in Houston, Texas, 2007–11*, in *Scientific Investigations Report 2015-5071*. 2015, U.S. Geological Survey: Reston, VA.
79. Jones, K.L., *Trace elements cycling in a crude oil-contaminated aquifer near Bemidji, Northern Minnesota*. Honors Thesis, Trinity University, **2020**.
80. Lacey, Z.M.A., *A modeling study of the mobilization and sequestration of trace metals in a crude-oil-contaminated aquifer*. Honors Thesis, Trinity University, **2021**.
81. Abrams, R.H., Loague, K., and Kent, D.B., *Development and testing of a compartmentalized reaction network model for redox zones in contaminated aquifers.* Water Resources Research, **1998**. *34*(6): p. 1531-1541.
82. Smith, R.L., Harvey, R.W., and LeBlanc, D.R., *Importance of closely spaced vertical sampling in delineating chemical and microbiological gradients in groundwater studies.* Journal of Contaminant Hydrology, **1991**. *7*: p. 285-300.
83. Bjerg, P.L., Tuxen, N., Reitzel, L.A., Albrechtsen, H.-J., and Kjeldsen, P., *Natural attenuation processes in landfill leachate plumes at three Danish sites.* Ground Water, **2011**. *49*(5): p. 688-705.
84. Delemos, J.L., Bostick, B.C., Renshaw, C.E., Stürup, S., and Feng, X., *Landfill-Stimulated Iron Reduction and Arsenic Release at the Coakley Superfund Site (NH)*. Environmental Science & Technology, **2006**. *40*(1): p. 67-73.
85. Kent, D.B., Davis, J.A., Anderson, L.C.D., Rea, B.A., and Waite, T.D., *Transport of chromium and selenium in the suboxic zone of a shallow aquifer: Influence of redox and adsorption reactions.* Water Resources Research, **1994**. *30*(4): p. 1099-1114.
86. Kent, D.B. and Fox, P.M., *The influence of groundwater chemistry on arsenic concentrations and speciation in a quartz sand and gravel aquifers.* Geochemical Transactions, **2004**. *5*(1): p. 1.

Chapter 4

Well construction and pumping impacts on the contribution of groundwater from stratigraphy with elevated radium activity

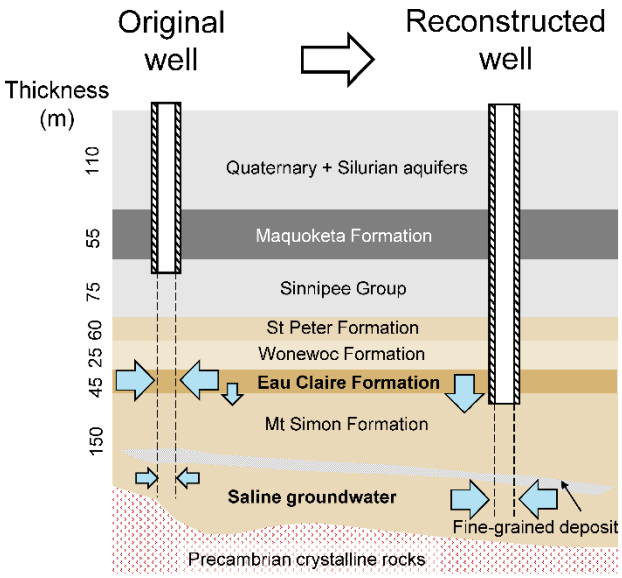

4.1 Abstract

The impact of well construction and pumping patterns on naturally occurring radium (Ra) activity observed at public supply wells completed in the Midwestern Cambrian-Ordovician aquifer system is not well understood. In this study, a steady-state MODFLOW groundwater flow model is developed for a portion of southeastern Wisconsin, USA, to evaluate the contribution of Ra-enriched groundwater from several units to public water supply wells with different well construction and pumping rates. Extending well casing just below the shale-rich Eau Claire Formation, an assumed Ra source, creates a strong vertical gradient that increases the flux from the Eau Claire Formation to the underlying Mt Simon Formation, a clean sandstone with limited

Amy K. Wiersma: Conceptualization, Methodology, Investigation, Formal Analysis, Writing – Original Draft and Review & Editing, Visualization. **Christopher Zahasky**: Methodology, Software, Investigation, Writing – Review & Editing. **Madeline B. Gotkowitz**: Conceptualization, Methodology, Formal Analysis, Writing – Review & Editing. **Matthew Ginder-Vogel**: Conceptualization, Writing – Review & Editing, Supervision.

sorption capacity; this flux increases with pumping rate. This well reconstruction strategy also doubles the contribution of groundwater from the base of the Mt Simon Formation, assumed to contain older, saline groundwater elevated in Ra activity. Reverse particle tracking confirms that hypothesized Ra sources can contribute to the well. Flow paths originate from the Eau Claire layer and the base of the Mt Simon, with travel times faster than the ^{226}Ra half-life that become faster with increasing pumping rate. These findings highlight how well field management can alter hydraulic gradients that enhance groundwater flow between units with different geochemistry and Ra activity, and suggest that well reconstruction to avoid Ra-rich stratigraphy may not be an effective long-term strategy for minimizing Ra activity in groundwater pumped from public supply wells.

4.2 Introduction

Naturally occurring groundwater contaminants have a larger effect on the quality of groundwater used for public supply than anthropogenic contaminants in U.S. principal aquifer systems, with elevated levels affecting water supplied to 31 million people.[1] Therefore, understanding the factors affecting geogenic contaminant occurrence and concentration in groundwater from public supply wells in various hydrogeologic settings is critical to groundwater management. Human activities that can impact the concentration of naturally occurring contaminants in groundwater include land use, well drilling and construction, and pumping rates and volumes that can cause subtle but substantial changes in geochemistry and associated trace element mobilization.[2] For example, public supply wells are often designed to maximize water yield, with open intervals connecting multiple aquifers with geochemically distinct water; this can result in chemical reactions which mobilize trace elements such as uranium, arsenic, and radium.[2] Pumping-induced changes to the hydraulic gradient can also impact concentrations of naturally-

occurring contaminants, such as the case in Modesto, California, where increases in summer pumping affect vertical hydraulic gradients and drive migration of shallow, uranium-enriched groundwater through the aquifer to supply wells.[3]

About 5 million people in the U.S. receive groundwater with elevated radium (Ra).[1] In 2000, the U.S. Environmental Protection Agency (EPA) set a Maximum Contaminant Level (MCL) for the total of ^{226}Ra and ^{228}Ra at 185 millibecquerels per liter (mBq/L), or 5 picocuries per liter (pCi/L),[4] to mitigate the increased risk of bone disease associated with long-term ingestion.[5, 6] A radioactive contaminant, Ra is produced via the decay of parent isotopes uranium (U) and thorium (Th) present in aquifer sediments, with ^{226}Ra ($t_{1/2}$ = 1600 yr) produced from the ^{238}U decay chain and ^{228}Ra ($t_{1/2}$ = 5.75 yr) produced from the ^{232}Th decay chain. Radium is mobilized from aquifer sediments to groundwater in geochemical conditions such as low dissolved oxygen and high total dissolved solids (TDS) concentration. Low dissolved oxygen can decrease the stability and limit the presence of iron and manganese (hydr)oxide minerals, important sorption surfaces for Ra.[7] High TDS can also result in elevated Ra in groundwater, as higher concentrations of other divalent cations such as calcium and magnesium outcompete Ra for sorption sites on aquifer solids.[8-10]

Radium activities above the U.S. Environmental Protection Agency (EPA) Maximum Contaminant Level (MCL) occur in about half of the principal U.S. aquifer systems; however, the Midwestern Cambrian-Ordovician aquifer system (MCOAS) has the greatest number of exceedances.[7] Nearly 70 percent of residents and 99 percent of communities in Wisconsin rely on groundwater for drinking water,[11] with the MCOAS being an important source throughout most of the state. In 2021, 17 Wisconsin public water systems violated the MCL for radium, uranium, or alpha particle emitters.[11] Water utilities with wells exceeding the MCL for Ra have adopted

several strategies for bringing systems into compliance, including well reconstruction or installation of expensive treatment systems. For example, some water utilities in southeastern Wisconsin have reconstructed wells to extend casing through shale-rich formations or abandoned the bottom of deeply drilled wells, with mixed results. The City of Fond du Lac, Wisconsin, installed a Ra treatment system for their well field at a cost of $32.1M.[12] Other water utilities choose to invest in an alternative water supply, such as the City of Waukesha, Wisconsin, which applied and received a variance from the Great Lakes Compact to use Lake Michigan water after struggling with groundwater depletion and elevated Ra activity, despite being outside the Great Lakes Basin.[13]

Radium activities have increased in the MCOAS in Wisconsin over nearly two decades,[14] suggesting that Ra compliance will continue to challenge water utilities. The reason for the increasing trend has not been identified. Potential human activities impacting Ra activities in public supply wells in eastern Wisconsin include 1) wells drilled to greater depths to avoid shallow groundwater contaminants (e.g., nitrate) access older groundwater elevated in Ra, and 2) alteration of hydraulic gradients due to groundwater pumping, with subsequent impacts on aquifer geochemistry and flow paths to wells. Public water supply wells in this region of the MCOAS are often cased over long intervals open to multiple units to maximize groundwater yield. While the units range in aqueous Ra activity, some will contribute a larger portion of groundwater to the well depending on factors such as unit thickness and hydraulic conductivity. Proposed geogenic sources of Ra in the MCOAS in eastern Wisconsin include shale-rich units,[15, 16] arkosic (> 25% feldspar) sandstones (^{228}Ra),[17] and Fe and Mn (hydr)oxide coatings on sandstone grains.[18] Shale-rich units such as the Maquoketa Formation and Eau Claire Formation have higher whole-rock and extractable Ra activity than sandstone or dolostone units in the MCOAS.[19, 20] Downward hydraulic

gradients may increase the recharge flux from these overlying shale-rich units with elevated solid-phase U, Th, and Ra content to the deep sandstone aquifer, which has relatively low sorption capacity.[19, 20] An additional Ra source in eastern Wisconsin is old, saline groundwater elevated in radioactivity that forms "lenses" of poor water quality at the base of the MCOAS (i.e., the base of the Mt Simon Formation).[16, 21-24]

While regional geochemical conditions impacting Ra activity are known, Ra activity is difficult to predict at the local scale due to spatial heterogeneity in mineralogy and geochemical conditions, as well as temporal variation in groundwater flow directions. Thus, a groundwater flow model developed for a specific region can be useful for understanding flow paths to wells and evaluating strategies for minimizing Ra activity in public supply wells. The purpose of this study is to evaluate the contribution of groundwater from Ra-enriched units in the MCOAS under different well construction and pumping scenarios. A steady-state groundwater flow model developed in MODFLOW is used to determine the contribution of groundwater from several Ra-rich units to wells in southeastern Wisconsin. Units assumed to have Ra-enriched groundwater include 1) the Eau Claire Formation, which includes Ra-rich shale facies, and 2) the base of the Mt Simon Formation, consisting of old, saline groundwater with elevated Ra activity. Reverse particle tracking is executed to determine flow paths and travel times to the well from modeled Ra-enriched layers. The model is also used to investigate potential causes of increasing radium activity at a public supply well in Brookfield, Wisconsin (Figure 4.1), following reconstruction to avoid Ra-rich shale facies in the Eau Claire Formation (described in Case Study background). Model results highlight how changes in well reconstruction and pumping can alter flow paths to the well, and help assess well reconstruction strategies for minimizing Ra activity in pumped groundwater.

4.2.1 Study site hydrogeology

In southeastern Wisconsin, the bedrock hydrostatigraphy consists of Paleozoic sedimentary units dipping gently to the east and south, and generally thickening to the east.[25] The MCOAS overlies Precambrian crystalline rock and is composed primarily of sandstone and dolostone units with interbedded siltstones and shales (Figure 4.2a). The major water-producing units in this deep system, in ascending order, are the sandstones of the Mt Simon, Wonewoc, and St. Peter Formations. The Eau Claire Formation is composed of shale and sandstone with a laterally extensive shale zone that forms an important aquitard over much of south-central Wisconsin.[25] In the study area of southeastern Wisconsin, shale within the Eau Claire Formation is limited in thickness and extent and is therefore not a regional-scale aquitard, but may be locally confining near the well of interest. The MCOAS in eastern Wisconsin is confined by the Maquoketa Formation, a shale with some dolomite that restricts vertical flow between the overlying Silurian dolostone aquifer and the underlying sandstone aquifer (Figure 4.1).[26] The Sinnipee Group dolostone, consisting of the Galena and Platteville Formations, is considered part of the Maquoketa confining unit where overlain by the Maquoketa shale, and therefore yields little water to wells in these areas.[27] The Maquoketa shale is overlain by the Silurian dolostone and Quaternary sand and gravel aquifers in eastern Wisconsin, both important shallow sources of public and domestic water supply in the region.

Groundwater provides the source of potable water to about 700,000 persons, or about 37 percent of the resident population of southeastern Wisconsin, and nearly 100 percent of the total supply in Waukesha County.[26] However, concentrated pumping from the deep aquifer in southeast Wisconsin and northern Illinois results in a large cone of depression that alters pre-development flow directions, diverting and capturing groundwater from great distances. Groundwater in the

MCOAS generally moves eastward from the regional potentiometric divide present in eastern Jefferson County. Vertical gradients were upward across the eastern portion of southeast Wisconsin prior to development. However, since the beginning of the 20th century, increasing groundwater pumping from deep, high-capacity wells has caused a decline in the potentiometric surface in the deep sandstone aquifers, reversing the vertical hydraulic gradient and inducing downward flow through the Maquoketa shale.[26] In the City of Brookfield, the location of the case study described below, hydraulic gradients were downward under pre-development conditions (Figure 4.1).

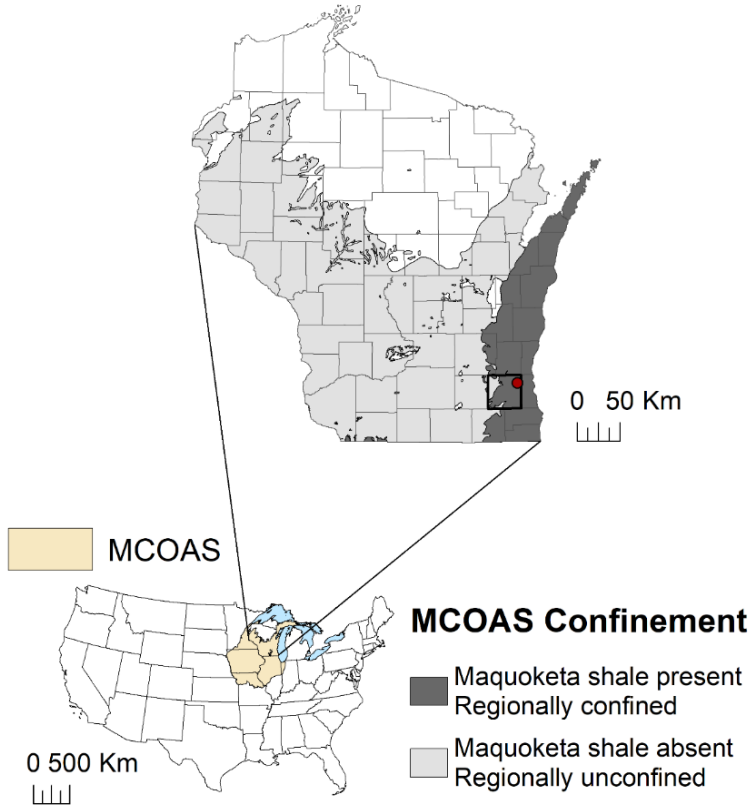

Figure 4.1 Study map showing the extent of the Midwestern Cambrian-Ordovician aquifer system (MCOAS), Waukesha County, and the city of Brookfield.

4.2.2 Case study background

In 1987, the city of Brookfield, Wisconsin, drilled Well 24 with an uncased interval open from the Sinnipee Group dolostone to the Mt Simon Formation sandstone (Figure 4.2a). Construction of wells with open intervals extending over several bedrock formations below the Maquoketa confining unit reduces the cost of casing while maximizing production, and is typical of high-capacity wells in southeastern Wisconsin.[26] Initial testing indicated elevated Ra activity above the Maximum Contaminant Level. Further testing identified specific intervals of green shale that were producing water with higher radium levels.[28] The well was reconstructed to seal off a "hot" zone from 300- and 330 m across the Eau Claire Formation at the bottom of the well casing (Figure 4.2a). The reconstruction was deemed a success, measuring an average Ra activity of 63 mBq/L (1.7 pCi/L) for eight samples collected within 24 hours after packer installation. However, data held by the Wisconsin Department of Natural Resources (2023)[29] demonstrate a steady increase in Ra activity at Well 24 over the past ~30 years. Ra activity was 189 mBq/L (5.1 pCi/L) in 2018 (Figure 4.2b). Radium activities in other wells operated by the City of Brookfield have also increased over the past two decades.[14] The reason for these increases in Ra activity is unknown.

4.3 Methods

4.3.1 Model design

The purpose of the model was to evaluate the contribution of several units with Ra-enriched groundwater to public supply wells in southeast Wisconsin, including: 1) shale facies in the Eau Claire Formation, and 2) the base of the Mt Simon Formation, where groundwater elevated in TDS and Ra is "trapped" by an overlying fine-grained deposit. The numerical model was designed to

be detailed enough to incorporate critical features (e.g., boundary conditions, unit thickness and hydraulic conductivity) influencing groundwater flow in the Brookfield area, but general enough to be representative of the aquifer system in southeast Wisconsin. The model was constructed using the finite-difference code MODFLOW-2005,[30, 31] and the pre- and post-processor Groundwater Vistas.[32] The regional stratigraphy for southeast Wisconsin defined by Feinstein et al. (2005)[25] was initially adopted and modified to provide greater resolution within the confined aquifer (i.e., units below the Maquoketa Shale) and simulate a fine-grained deposit near the base of the Mt Simon Formation.

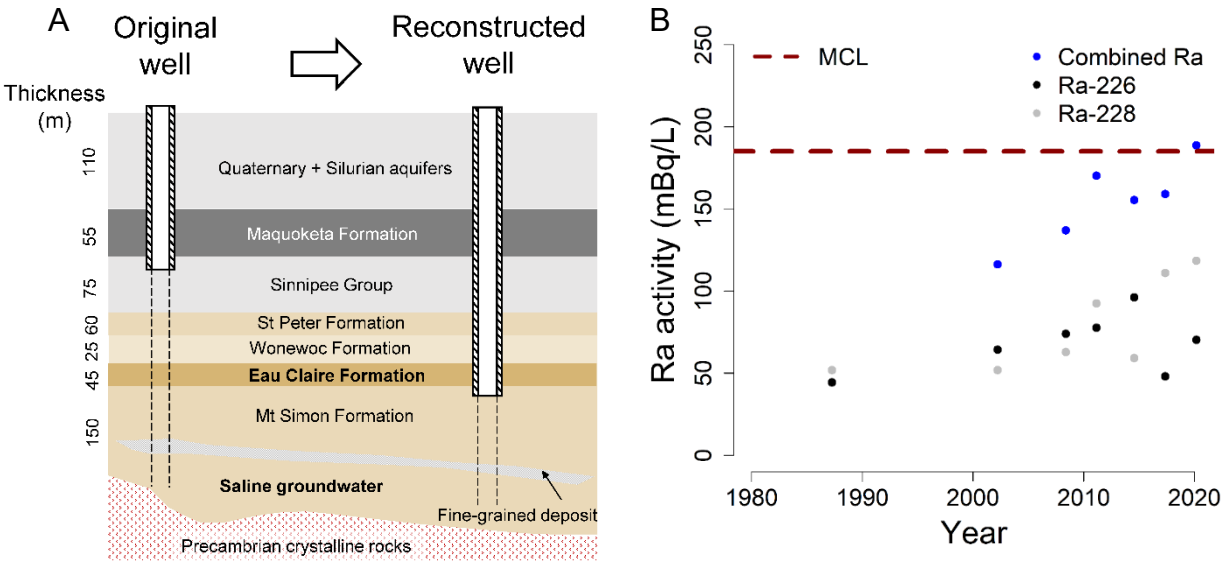

Figure 4.2 a) Conceptual model demonstrating original and reconstructed Brookfield Well 24. b) Radium (Ra) activity at Brookfield Well 24 following reconstruction in 1987 to seal off a shale facies within the Eau Claire Formation. MCL = maximum contaminant level.

The model grid includes 317 rows and 317 columns with uniform grid spacing of 30.54 m x 30.54 m. The model was designed to represent the area containing the city of Brookfield municipal wells, the 9.7 x 9.7 km (6 x 6 mi) Township of Brookfield. Recharge from precipitation to the shallow aquifer system was not simulated (Figure 4.3). This model focused on the deep flow system, where groundwater is recharged from constant head boundaries placed on the left and right sides of the model which simulate the regional west-to-east flow direction. Pre-development (pre-

1864) head values were used to simulate the effect of pumping on the flow field.[25] The bottom of the model is a no-flow boundary that represents the relatively impermeable, crystalline Precambrian basement. No-flow boundaries were also placed in the front and back of the model, approximately parallel to the regional groundwater flow direction.

The model consists of 13 layers of uniform thickness representing seven aquifers and two confining units (Figure 4.3) simulated with the Layer Property Flow package. The thicknesses of each layer were determined by averaging the thicknesses recorded in 17 geologic logs available from wells in the City of Brookfield. Hydraulic conductivities were estimated by averaging the calibrated minimum and maximum values reported in Feinstein et al. (2005);[25] Brookfield-specific values were used if available for a given layer (Table 4.1). The top elevation is defined as the land surface elevation. The uppermost layer is unconfined, and represents the unlithified glacial aquifer and the Silurian dolostone aquifer. The second layer represents the Maquoketa Formation. The third layer is the Sinnipee Group dolostone, which when present below the Maquoketa Formation, acts together with the Maquoketa Formation to confine the underlying aquifers.[25] Layers 4 and 5, respectively, represent the St Peter Formation sandstone and the Wonewoc Formation sandstone. Layer 6 represents the Eau Claire Formation, composed of sandstone and shale facies. Layers 7-11 and 13 represent the Mt Simon Formation sandstone. Layer 12 simulates a fine-grained deposit within the Mt Simon Formation reported as a 5 ft interval of red/green shale in 2 of the 4 geologic logs that include the Mt Simon Formation. This deposit is not continuous and mappable, but has been documented with a thickness of up to 15 ft in northern Illinois.[33]

Twenty-one wells were simulated with the Multi-Node Well 2 package.[34] These were distributed across the domain similar to the City of Brookfield well field. The primary well of interest is located in the center of the model domain to minimize any potential boundary effects on

model results. The initial heads were set equal to the top of layer one, and the model was run with the Preconditioned Conjugate-Gradient 2 solver.[35]

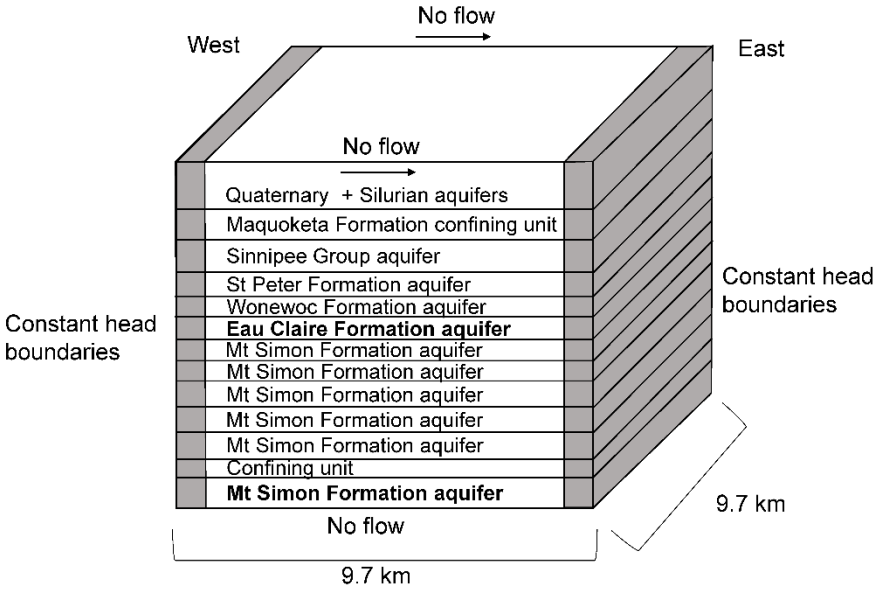

Figure 4.3 Model domain and boundary conditions. Layers in bold are radium-enriched stratigraphy. Model layer thicknesses are not to scale.

4.3.2 Particle tracking

Reverse particle tracking around the well of interest was executed using MODPATH version 7[36, 37] to determine if flow paths to the well originated from the modeled Ra-rich stratigraphy. Travel times from Ra-rich stratigraphy were also obtained and compared to the half-lives of ^{228}Ra and ^{226}Ra. The effective porosity for each layer was estimated using the maximum values reported in Feinstein et al. (2005)[25] (Table 4.2). Three circles of ten particles with three vertical release points were placed in each layer open to the well, as close as possible to the center of the model cell. The radius of the particle circle was based on the size of the cells and the principles of converging flow near a pumped well node.[38]

Table 4.1 Hydrostratigraphic sequence, model layering, thicknesses, and assigned horizontal and vertical hydraulic conductivities. The total thickness of layers 7-11 is 120 m.

Stratigraphic nomenclature		K_h (m/d)	K_v (m/d)	Thickness (m)	Model structure	Lithology
Group(s)	Formation					
Quaternary Silurian		0.53	0.012	110	Layer 1	Sand & gravel, glacial till; dolostone
	Maquoketa	0.046	0.000015	55	Layer 2	Shale
Sinnipee	Galena Platteville	0.012	0.00015	75	Layer 3	Dolostone
Ancell	St Peter	1.1	0.0061	60	Layer 4	Sandstone
	Wonewoc	2.6	0.012	25	Layer 5	Sandstone
	Eau Claire	0.73	0.0012	45	Layer 6	Sandstone and shale
Elk Mound	Mt Simon	1.1	0.0060	120	Layers 7-11	Sandstone
	Fine-grained deposit	0.046	0.000015	5	Layer 12	Shale
	Mt Simon	1.1	0.0060	25	Layer 13	Sandstone
Precambrian		Not simulated				Metamorphic, igneous

Table 4.2 Effective porosity values used for reverse particle tracking in MODPATH.

Model layer	Effective porosity
1, 4-11, 13	0.1
2, 3, 12	0.01

4.3.3 Vertical flux and the contribution of groundwater from stratigraphic units to the well

The flux across the shale-rich layer (e.g., Eau Claire Formation) to the underlying unit was obtained by plotting the mass balance by layer in the first layer of the underlying unit and using the "top inflow" estimate. The percent contribution of groundwater from each layer to the well was recorded in the .wel file. Hydrogeologic parameters such as hydraulic conductivity and layer thickness were manually adjusted to test the sensitivity of model results to the hydrogeologic parameters, and to ensure that results were not constrained by initial parameter estimates.

4.4 Results

4.4.1 Contribution of groundwater from radium-enriched layers to the well

Two versions of the model were used to evaluate the effects of well construction on results. One version simulated the original Brookfield Well 24 construction and one simulated the reconstructed Brookfield Well 24. When the well has original construction with an open interval from the Sinnipee Group to the Mt Simon Formation (layers 3-13), the Eau Claire (layer 6) contributes 10% of the groundwater pumped (Table 4.3). The simulation with the reconstructed well cased through the Eau Claire layer and open only to the Mt Simon (layers 7-13) results in no direct contribution from the Eau Claire layer. The contribution of groundwater from layer 13, below the fine-grained deposit, increases from 8.4% at the original well to 17% at the reconstructed well. The percent of well water contributed from other model layers under these two well construction scenarios is shown in Table C-1. The percent of water contributed from the base of the Mt Simon Formation (layer 13) to the well was evaluated with different well construction scenarios. The contribution from the base of the Mt Simon Formation decreases as the well casing is constructed shallower and the open interval is extended across more units (Table 4.4). Backfilling a well eliminates direct contribution from the base of the Mt Simon (layer 13) (Table 4.4).

Table 4.3 Percent of groundwater contributed from radium-enriched stratigraphy to original (open from Sinnipee Group to Mt Simon Formation, layers 3-13) and reconstructed Brookfield Well 24 (open to Mt Simon Formation, layers 7-13) with a steady-state pumping rate of 2,725 m^3/d.

Well 24 construction	Eau Claire layer contribution (%)	Bottom layer of Mt Simon contribution (%)
Original	10	8.4
Reconstructed	0	17

Table 4.4 Percent contribution from the base of the Mt Simon Formation to the well (layer 13), with different well open intervals. The last two rows indicate scenarios where wells originally open to the fine-grained deposit and bottom of the Mt Simon (layers 12-13) are backfilled.

Well open interval	Model layers	Contribution from the bottom layer of the Mt Simon (%)
Fine-grained deposit to bottom layer of Mt Simon	12-13	99
Mt Simon	11-13	50
Mt Simon	10-13	24
Mt Simon	9-13	20
Mt Simon	8-13	17
Mt Simon	7-13	17
Eau Claire to Mt Simon	6-13	14
Wonewoc to Mt Simon	5-13	10
St Peter to Mt Simon	4-13	8.4
Sinnipee to Mt Simon	3-13	8.4
Sinnipee to Mt Simon	3-11	0
Mt Simon	7-11	0

4.4.2 Vertical flux from the Eau Claire layer to the Mt Simon layer

The median flux from the Eau Claire (layer 6) to the underlying Mt Simon (layer 7) of 1500 ± 1202 m^3/d at the reconstructed well is higher (p = 0.07) compared to the median flux of 106 ± 6.8 m^3/d at the original well, and increases with the pumping rate at the reconstructed well (Figure 4.4). In contrast, the flux from the Maquoketa layer (layer 2) to the underlying Sinnipee layer (layer 3) is higher when the well has original construction with an interval open from the Sinnipee to the Mt Simon (layers 3-13), and increases with the pumping rate at the original well (Table C-2). Another model version was created to evaluate the effectiveness of distributing the pumping rate at the reconstructed well with two additional wells, to decrease the flux from the Eau Claire layer to the underlying Mt Simon layer. Two additional wells were placed 1000 m west and 1000 m east of the reconstructed well, and the total pumping rate originally applied at the reconstructed well was divided by three and assigned to all three wells. The additional wells were constructed similarly to the reconstructed well, with an interval open to the Mt Simon (layers 7-

13). The median flux from the Eau Claire layer to the underlying Mt Simon layer is not significantly less than the median flux associated with pumping at the reconstructed well only (p = 0.4) (Figure 4.5).

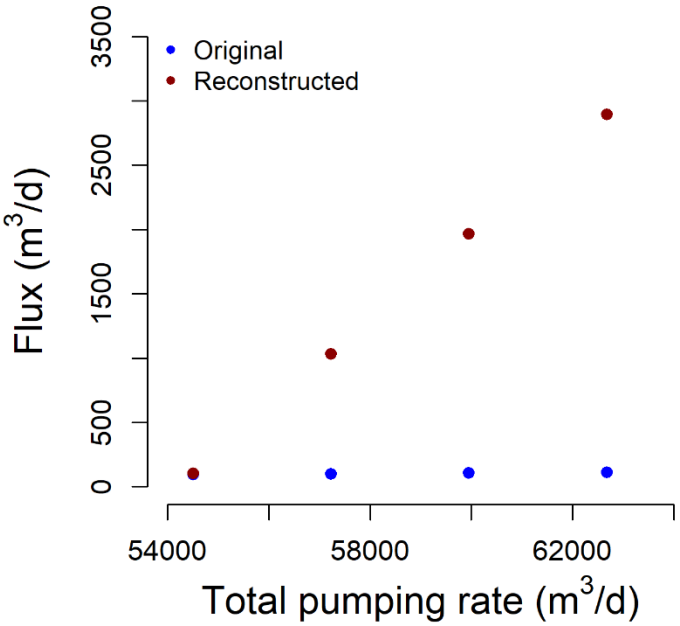

Figure 4.4 Flux from the Eau Claire (layer 6) to the underlying Mt Simon (layer 7) with increasing pumping rate at Well 24, under conditions of original and reconstructed casing depths. In the simulation, the additional 20 wells in the model are pumped at a rate of 2,725 m^3/d.

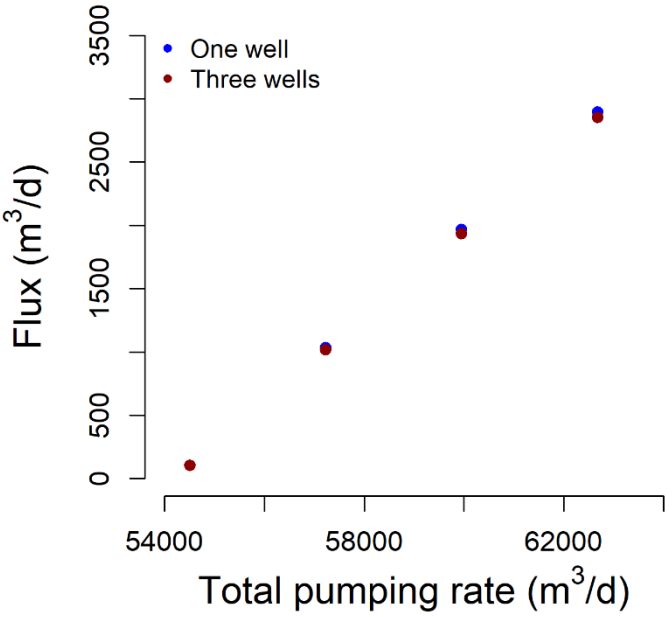

Figure 4.5 Flux from the Eau Claire (layer 6) to the underlying Mt Simon (layer 7) with pumping at the reconstructed well only ('one well'), and the pumping rate divided by three and assigned to the reconstructed well and two additional wells with the same construction (open interval from layers 7-13; 'three wells').

4.4.3 Travel times from radium-enriched stratigraphy to the well

The minimum, maximum, and average travel times from Ra-enriched stratigraphy to wells of various construction were obtained using reverse particle tracking around the wells. The travel times from the Eau Claire (layer 6) to the reconstructed well with an open interval to the Mt Simon (layers 7-13) and steady-state pumping rate of 2,725 m^3/d range from 0.69 days to 847 years with an average of 188 years (Table 4.5). The average travel time from the base of the Mt Simon Formation (layer 13) to a well with an interval open from the Sinnipee Group to the Mt Simon above the fine-grained deposit (layers 3-11) and steady-state pumping rate of 2,725 m^3/d is 293 years (Table 4.6). The average travel time from the base of the Mt Simon Formation decreases to 188 years when the casing is deepened and the well has an interval open only to the Mt Simon above the fine-grained deposit (layers 7-11) (Table 4.7). Travel times from the Maquoketa layer to a well with an open interval from the Sinnipee Group to the Mt Simon Formation (layers 3-13) were also obtained (Table C-3). In all cases, the travel times are faster when the pumping rate at the well is increased.

Table 4.5 Travel times from the Eau Claire (layer 6) to a well with an interval open to the Mt Simon (layers 7-13) for four simulations with increasing pumping at the well of interest. In all simulations, the additional 20 wells in the model have pumping rates of 2,725 m^3/d.

Total pumping rate (m^3/day)	Min travel time (days)	Max travel time (years)	Avg travel time (years)
54,501	177	831	408
57,225	0.69	847	188
59,950	0.34	558	136
62,675	0.23	405	112

Table 4.6 Travel times from the base of the Mt Simon (layer 13) to a well with an interval open from the Sinnipee to the Mt Simon located above the fine-grained deposit (layers 3-11) for four simulations with increasing pumping at the well of interest. In all simulations, the additional 20 wells in the model have pumping rates of 2,725 m^3/d.

Total pumping rate (m^3/day)	Min travel time (years)	Max travel time (years)	Avg travel time (years)
54,501	N/A	N/A	N/A
57,225	7.7	572	293
59,950	3.9	539	240
62,675	2.7	511	213

Table 4.7 Travel times from the base of the Mt Simon (layer 13) to a well with an interval open only to the Mt Simon located above the fine-grained deposit (layers 7-11) for four simulations with increasing pumping at the well of interest. In all simulations, the additional 20 wells in the model have pumping rates of 2,725 m^3/d.

Total pumping rate (m^3/day)	Min travel time (years)	Max travel time (years)	Avg travel time (years)
54,501	N/A	N/A	N/A
57,225	4.0	570	188
59,950	2.0	538	145
62,675	1.3	513	125

4.4.4 Sensitivity analysis

Hydrogeologic parameters including the horizontal and vertical conductivity of the Eau Claire, Mt Simon, and fine-grained deposit, as well as the thickness of the Eau Claire, fine-grained deposit, and base of the Mt Simon, were manually adjusted to test the sensitivity of model results to the respective hydrogeologic parameters. The sensitivity analysis was executed in both versions of the model version (original and reconstructed wells). All wells were simulated with a steady-state pumping rate of 2,725 m^3/d. Results are consistent over the range of values applied in the sensitivity analysis (Tables C-4 and C-5), indicating that model results are not sensitive to reasonable ranges in parameters (C-1).

4.5 Discussion

4.5.1 Flow paths and travel times support contribution from radium-enriched stratigraphy

Radium-enriched stratigraphic units in the MCOAS considered in this model include shale facies within the Eau Claire Formation and old, saline groundwater trapped near the base of the Mt Simon Formation. Reverse particle tracking delineates flow paths to the well, and confirms that groundwater pumped from the well can originate from the modeled Ra-enriched layers. Radium isotopes may undergo advective transport from these areas within the groundwater system to wells, depending on the isotope half-life, geochemical conditions, and fluxes. Radium-228 has a relatively short half-life of 5.75 years, and is therefore not likely to be transported far from its ^{232}Th parent nuclide before undergoing decay. This is supported by reverse particle tracking results, where the half-life of ^{228}Ra is much shorter than the average travel times for all simulations (Tables 4.5-4.7). However, the ^{228}Ra half-life is longer than the minimum travel times from the Eau Claire to the underlying Mt Simon layer, indicating potential ^{228}Ra transport to the well in this scenario (Table 4.5). In contrast, ^{226}Ra has a relatively long half-life of 1600 years, and is therefore more likely to be affected by geochemical conditions (e.g., low dissolved oxygen, high TDS) and be transported away from the site of ^{230}Th decay. Particle tracking results support this conclusion, where the ^{226}Ra half-life is longer than the minimum, maximum, and average travel times for all simulations.

4.5.2 Well reconstruction strategies to avoid Ra-enriched stratigraphy

When wells in Wisconsin exceed the Ra MCL, several well reconstruction strategies are often employed to reduce Ra activity before resorting to expensive Ra treatment systems. One of these strategies is reconstructing the well to extend well casing past shale-rich units with elevated solid

phase concentrations of Ra and parent isotopes U and Th. For example, the water utility in Cambria, Wisconsin, reduced Ra activity to acceptable levels by extending casing through fine-grained intervals of the Tunnel City Formation. The initial 10% flow contribution from the shale-rich Eau Claire layer to Well 24 simulated with original construction may explain the elevated Ra activity when the well was first drilled. While sealing off the Eau Claire Formation eliminates the direct contribution of groundwater from the shale facies to the well, changes in well construction influence other conditions in the groundwater system. For example, sealing off the Eau Claire Formation induces a strong vertical hydraulic gradient that becomes larger as pumping at the well is increased, increasing the flux from the Eau Claire layer to the underlying Mt Simon layer and resulting in faster travel times from the Eau Claire layer to the well. Distributing pumping at the reconstructed well with two additional wells does not reduce this flux, highlighting the importance of well construction. This increased flux has implications for Ra activities observed at public supply wells because compared to the Eau Claire Formation, the Mt Simon Formation is a relatively clean sandstone with a low Ra sorption capacity. However, this model does not consider the dilution of groundwater transported from the Eau Claire layer into the Mt Simon layer. The volume of water transported from the Eau Claire layer over a period of one year at the 2,897 m^3/d flux generated from a pumping rate of 8,175 m^3/d at the reconstructed well (Figure 4.4) would be only ~2.3% of the total volume of water in the underlying Mt Simon layer (4.7E+07 m^3). A transport model is needed to be able to simulate dilution and other processes and determine the increase in Ra activity in the underlying Mt Simon Formation with increased pumping over time. This well reconstruction strategy also approximately doubles the contribution of groundwater from the base of the Mt Simon Formation, which has elevated concentrations of Ra and TDS. Both of these factors are potential explanations for the increase in Ra activity at Well 24 over the 30 years

following well reconstruction to avoid the shale facies within the Eau Claire Formation, and suggest that extending casing past shale facies may not be an effective long-term strategy for reducing Ra activity at public supply wells.

Another strategy used to reduce Ra activity in public supply wells in southeast Wisconsin is backfilling the bottom of the well to reduce the contribution from the base of the aquifer system (Mt Simon), where saline, Ra-enriched groundwater may be present. While backfilling the well eliminates the direct contribution of groundwater from the base of the Mt Simon Formation (Table 4.4), model results indicate that increased pumping at wells with open intervals above the fine-grained deposit can yield faster travel times from the base of the Mt Simon Formation to the well (Table 4.6, Table 4.7). The travel times from the base of the Mt Simon Formation to these wells are also affected by the geology, with faster travel times as the fine-grained deposit is thinner and has higher hydraulic conductivity (transmissivity). An alternative strategy to avoid groundwater contribution from the base of the Mt Simon may be to initially construct wells with shallower casing depth (Table 4.4). However, this would likely result in groundwater contribution from the Ra-rich Eau Claire (layer 6). Overall, well reconstruction to avoid the base of the Mt Simon (e.g., backfilling) may not be an effective long-term strategy depending on the pumping rates and hydrogeologic properties of the fine-grained deposit, and may result in tradeoffs including decreased well yield.

4.5.3 Model limitations and future work

There are several assumptions and limitations associated with these simulations. The model only considers shale facies within the Eau Claire Formation and saline groundwater at the base of the Mt Simon Formation as sources of Ra-enriched groundwater, and does not consider Ra that may originate in dolostone or sandstone units (e.g., ^{228}Ra produced from ^{232}Th in arkosic

sandstone). It is also assumed that the Ra activity is homogeneous in the Ra-enriched stratigraphy, and has already been mobilized from solid phases to groundwater as a result of aquifer geochemical conditions such as low dissolved oxygen concentrations, high TDS, or low sorption capacity. Furthermore, the model only considers pure advection. In reality, Ra transport will be more controlled by molecular diffusion or advection, depending on several factors such as hydraulic conductivity of stratigraphic units and pumping rates at the well. It is anticipated that advection will be more important in the sandstone units with high hydraulic conductivity. Diffusion will be more important in shale units with low hydraulic conductivity, but advective transport from these units may become more important as pumping at the well increases (i.e., fluxes increase). Sorption is an important process dictating Ra transport, and retardation should therefore be incorporated for each model layer with geochemical conditions and sorption capacity in mind.

The next step in this work will be developing a transport model using USGS-MT3D[39, 40] to incorporate diffusion, dispersion, and retardation and simulate Ra activity at a well with similar well construction and pumping rates used in the groundwater flow model (Appendix C-2, Tables C-6 to C-10). Studies examining diffusion at the aquitard (shale)-aquifer interface highlight the need for high-resolution (i.e., cm-scale) models, which will increase the computing demands.[41, 42] High resolution is necessary in the z-direction to capture transport at the aquitard-aquifer interface due to the abrupt contrast in hydraulic conductivity, where transport in shale is dominated by diffusion and transport in sandstone is dominated by advection. Empirical data will be used to validate the model (e.g., temporal datasets of Ra activities and groundwater withdrawals associated with wells in Waukesha County). Nonetheless, results from this groundwater flow model help improve understanding of the contribution of groundwater from Ra-enriched stratigraphic units,

and evaluate factors affecting the success of well reconstruction strategies to reduce Ra activity. Complicating factors include multiple stratigraphic units with Ra-enriched groundwater within the MCOAS. Additionally, changes in well construction and pumping rates alter hydraulic gradients and the relative contribution from these units to pumped groundwater. Some changes in construction to improve groundwater quality and reduce Ra activity may result in decreased well yield, highlighting potential tradeoffs associated with well reconstruction strategies.

4.6 Conclusions

While the regional geochemical conditions associated with elevated Ra activities are well understood, less is known about how well construction and pumping rates may affect Ra activities observed at public supply wells. The developed groundwater flow model considers advective transport of groundwater from hypothesized sources of Ra within the MCOAS to public supply wells in southeastern Wisconsin, USA, including shale facies and saline groundwater at the base of the MCOAS. Changes in well construction and pumping patterns can alter hydraulic gradients, enhance groundwater exchange between units of different geochemistry, and change the relative contributions from Ra-enriched stratigraphy to public supply wells. Results suggest that well reconstruction to extend casing below shale facies may not be an effective long-term strategy for reducing Ra activity at public supply wells. Completing wells below shale facies in the Eau Claire Formation eliminates direct flow from the Eau Claire Formation to the well. However, this increases the flux of groundwater from the Eau Claire Formation to the underlying Mt Simon Formation, while also enhancing contribution from old, saline groundwater at the base of the Mt Simon Formation. While well reconstruction (e.g., backfilling the well) to avoid the base of the Mt Simon Formation eliminates direct contribution from old, saline groundwater at the base of the

aquifer, groundwater from this region of the aquifer may still be transported to the well depending on pumping rates and the hydrogeologic properties of the fine-grained deposit.

While these findings begin to evaluate the effectiveness of well reconstruction strategies to reduce Ra activity, they also highlight the need to simulate Ra activities in the aquifer with a transport model that can be used to further investigate transport from shale facies to underlying sandstones with low sorption capacity. These future modeling efforts should incorporate diffusion, dispersion, and retardation, and have high enough resolution to accurately capture Ra transport at the shale-aquifer interface and determine under what conditions transport will be dominated by diffusion or advection. These modeling efforts could then be extended to investigate the transport of other geogenic contaminants associated with shale mineralogy (e.g., uranium, arsenic). There are many considerations when reconstructing a well to reduce Ra activity, as it changes the source area of groundwater that flows to the well. Thus, reconstruction can lead to increased contribution of groundwater from other Ra-rich stratigraphy and may decrease well yield. Overall, treatment of groundwater elevated in Ra offers a low-risk, long-term solution compared to well reconstruction strategies designed to minimize Ra in pumped groundwater.

4.7 Acknowledgements

The authors thank Jim Rumbaugh for assistance with Groundwater Vistas. A.K.W. is supported by the National Science Foundation Graduate Research Fellowship Program under Grant No. DGE-1747503. Any opinions, findings, and conclusions or recommendations expressed in this material are those of the author(s) and do not necessarily reflect the views of the National Science Foundation. Support was also provided by the Graduate School and the Office of the Vice Chancellor for Research and Graduate Education at the University of Wisconsin–Madison with funding from the Wisconsin Alumni Research Foundation.

4.8 References

1. Belitz, K., Fram, M.S., Lindsey, B.D., Stackelberg, P.E., Bexfield, L.M., Johnson, T.D., Jurgens, B.C., Kingsbury, J.A., McMahon, P.B., and Dubrovsky, N.M., *Quality of groundwater used for public supply in the continental United States: A comprehensive assessment.* ACS ES&T Water, **2022**. *2*(12): p. 2645–2656.
2. Ayotte, J.D., Szabo, Z., Focazio, M.J., and Eberts, S.M., *Effects of human-induced alteration of groundwater flow on concentrations of naturally-occurring trace elements at water-supply wells.* Applied Geochemistry, **2011**. *26*(5): p. 747-762.
3. Bexfield, L.M. and Jurgens, B.C., *Effects of Seasonal Operation on the Quality of Water Produced by Public-Supply Wells.* **2014**. *52*(S1): p. 10-24.
4. U.S. Environmental Protection Agency, *National primary drinking water regulations*, in *Federal Register*. 2000.
5. Mays, C.W., Rowland, R.E., and Stehney, A.F., *Cancer risk from the lifetime intake of Ra and U isotopes.* Health Physics, **1985**. *48*(5): p. 635-47.
6. Finkelstein, M. and Kreiger, N., *Radium in drinking water and risk of bone cancer in Ontario youths: a second study and combined analysis.* Journal of Occupational and Environmental Medicine, **1996**. *53*: p. 305-311.
7. Szabo, Z., dePaul, V.T., Fischer, J.M., Kraemer, T.F., and Jacobsen, E., *Occurrence and geochemistry of radium in water from principal drinking-water aquifer systems of the United States.* Applied Geochemistry, **2012**. *27*(3): p. 729-752.
8. Tamamura, S., Takada, T., Tomita, J., Nagao, S., Fukushi, K., and Yamamoto, M., *Salinity dependence of 226Ra adsorption on montmorillonite and kaolinite.* Journal of Radioanalytical and Nuclear Chemistry, **2014**. *299*(1): p. 569-575.
9. Vinson, D.S., Tagma, T., Bouchaou, L., Dwyer, G.S., Warner, N.R., and Vengosh, A., *Occurrence and mobilization of radium in fresh to saline coastal groundwater inferred from geochemical and isotopic tracers (Sr, S, O, H, Ra, Rn).* Applied Geochemistry, **2013**. *38*: p. 161-175.
10. Nathwani, J.S. and Phillips, C.R., *Adsorption of 226Ra by soils in the presence of Ca2+ ions. Specific adsorption (II).* Chemosphere, **1979**. *8*(5): p. 293-299.
11. Wisconsin Department of Natural Resources, *Wisconsin Public Water Systems 2021 Annual Drinking Water Report*, **2022**.
12. Bergquist, L. *Fond du Lac to pay settlement over radium in drinking water.* Milwaukee Journal Sentinel, **2009**.
13. Luczaj, J. and Masarik, K., *Groundwater quantity and quality issues in a water-rich region: Examples from Wisconsin, USA.* Resources, **2015**. *4*(2): p. 323.
14. Dematatis, M., Plechacek, A., Mathews, M., Wright, D., Udenby, F., Gotkowitz, M., and Ginder-Vogel, M., *Spatial and temporal variability of radium in the Wisconsin Cambrian-Ordovician aquifer system* AWWA Water Science, **2020**.
15. Grundl, T., *Makoqueta shale as a radium source for the Cambro-Ordovician aquifer in Eastern Wisconsin*. 2000: Wisconsin Department of Natural Resources.
16. Weaver, T.R. and Bahr, J., *Geochemical evolution in the Cambrian-Ordovician sandstone aquifer, Eastern Wisconsin: 1. Major ion and radionuclide distribution.* Groundwater, **1991**. *29*(3): p. 350-356.

17. Stackelberg, P.E., Szabo, Z., and Jurgens, B.C., *Radium mobility and the age of groundwater in public-drinking-water supplies from the Cambrian-Ordovician aquifer system, north-central USA.* Applied Geochemistry, **2018**. *89*: p. 34-48.
18. Mathews, M., Gotkowitz, M., and Ginder-Vogel, M., *Effect of geochemical conditions on radium mobility in discrete intervals within the Midwestern Cambrian-Ordovician aquifer system.* Applied Geochemistry, **2018**. *97*: p. 238-246.
19. Mathews, M., Scott, S., Gotkowitz, M., and Ginder-Vogel, M., *Association of radionuclide isotopes with aquifer solids in the Midwestern Cambrian-Ordovician aquifer system* ACS Earth and Space Chemistry, **2021**. *5*(2): p. 268-278.
20. Mathews, M., Scott, S.R., Gotkowitz, M.B., Hunt, R.J., and Ginder-Vogel, M., *Isotopic analysis of radium geochemistry at discrete intervals in the Midwestern Cambrian-Ordovician aquifer system.* Applied Geochemistry, **2022**. *142*.
21. Siegel, D.I., *Sulfur isotope evidence for regional recharge of saline water during continental glaciation, North-Central United States.* Geology, **1990**. *18*: p. 1054-1056.
22. Grundl, T. and Cape, M., *Geochemical factors controlling radium activity in a sandstone aquifer.* Groundwater, **2006**. *44*(4): p. 518-527.
23. Franz, K.E., *Geochemistry of the sandstone and Silurian aquifers in eastern Wisconsin*. 1985, MS Thesis, Syracuse University. p. 103.
24. Weaver, T.R. and Bahr, J.M., *Geochemical evolution in the Cambrian-Ordovician sandstone aquifer, Eastern Wisconsin: 2. Correlation between flow paths and ground-water chemistry.* Groundwater, **1991**. *29*(4): p. 510-515.
25. Feinstein, D.T., Hart, D., Krohelski, J.T., Eaton, T.T., and Bradbury, K.R., *Simulation of regional groundwater flow in southeastern Wisconsin.* Southeastern Wisconsin Regional Planning Commission Technical Report, **2005**.
26. Southeastern Wisconsin Regional Planning Commission and Wisconsin Geological and Natural History Survey, *Groundwater Resources of Southeastern Wisconsin*. 2002. p. 203.
27. Young, H.L. and Siegel, D.I., *Summary of Ground-Water Hydrology of the Cambrian-Ordovician Aquifer System in the Northern Midwest, United States*, in *U.S. Geological Survey Professional Paper 1405-A*. 1992: Washington, D.C.
28. American Water Works Association, *News of the field - Radium reduction project successful.* American Water Works Association, **1987**. *79*(12).
29. Wisconsin Department of Natural Resources. *Public Drinking Water System Data*. 2023; Available from: https://dnr.wi.gov/dwsviewer.
30. Harbaugh, A.W., Langevin, C.D., Hughes, J.D., Niswonger, R.N., and Konikow, L.F., *MODFLOW-2005 version 1.12.00, the U.S. Geological Survey modular groundwater model: U.S. Geological Survey Software Release, 03 February 2017.* **2017**.
31. Harbaugh, A.W., *MODFLOW-2005: the U.S. Geological Survey modular ground-water model--the ground-water flow process*, in *Techniques and Methods*. 2005.
32. Rumbaugh, J.O. and Rumbaugh, D.B., *Guide to using Groundwater Vistas Version 7*. 2017.
33. Willman, H.B., Atherton, E., Buschbach, T.C., Collinson, C., Frye, J.C., Hopkins, M.E., Lineback, J.A., and Simon, J.A., *Handbook of Illinois stratigraphy: Illinois State Geological Survey Bulletin 95*, **1975**. 261 p.
34. Konikow, L.F., Hornberger, G.Z., Halford, K.J., and Hanson, R.T., *Revised multi-node well (MNW2) package for MODFLOW ground-water flow model.* U.S. Geological Survey Techniques and Methods, **2009**. *6*(A30): p. 67.

35. Hill, M.C., *Preconditioned conjugate-gradient 2 (PCG2), A computer program for solving ground-water flow equations*, in *U.S. Geological Survey Water-Resources Investigations Report 90-4048*. 1990: Denver, CO.
36. Pollock, D.W., *User guide for MODPATH Version 7—A particle-tracking model for MODFLOW*, in *Open-File Report*. 2016: Reston, VA. p. 41.
37. Pollock, D.W., *MODPATH v7.2.01: A particle-tracking model for MODFLOW: U.S. Geological Survey Software Release.* U.S. Geological Survey Software Release, **2017**.
38. Prickett, T.A. and Lonnquist, C.G., *Selected digital computer techniques for groundwater resource evaluation*, in *Illinois State Geological Survey Bulletin 55*. 1971, Illinois State Geological Survey: Urbana, IL.
39. Bedekar, V., Morway, E.D., Langevin, C.D., and Tonkin, M., *MT3D-USGS version 1.0.0: Groundwater Solute Transport Simulator for MODFLOW* U.S. Geological Survey Software Release, **2016**.
40. Bedekar, V., Morway, E.D., Langevin, C.D., and Tonkin, M., *MT3D-USGS version 1: A U.S. Geological Survey release of MT3DMS updated with new and expanded transport capabilities for use with MODFLOW6.* U.S. Geological Survey Techniques and Methods **2016**. *6*(A53): p. 69.
41. Falta, R.W. and Wang, W., *A semi-analytical method for simulating matrix diffusion in numerical transport models.* Journal of Contaminant Hydrology, **2017**. *197*: p. 39-49.
42. Chapman, S.W., Parker, B.L., Sale, T.C., and Doner, L.A., *Testing high resolution numerical models for analysis of contaminant storage and release from low permeability zones.* Journal of Contaminant Hydrology, **2012**. *136-137*: p. 106-16.

Chapter 5

Conclusions

5.1 Summary

In this dissertation, radium (Ra) activity in the Midwestern Cambrian-Ordovician aquifer system (MCOAS) is examined in relation to aquifer hydrogeochemical changes arising from natural and human-induced factors. A combination of field and modeling-based approaches are used to investigate Ra mobility when aquifer hydrogeochemical conditions evolve due to 1) the aquifer system transitioning from unconfined to confining conditions, 2) anthropogenic hydrocarbon spills to the subsurface, and 3) alteration of well construction and pumping rates. Collectively, this work identifies mobilization and sequestration mechanisms impacting Ra activity at local and regional aquifer scales.

In Chapter 2, groundwater samples are characterized along a regional flow path to identify geochemical factors responsible for elevated Ra activity at a complex hydrogeologic setting in east-central Wisconsin. Here, the MCOAS transitions from regionally unconfined to confined conditions and overlies crystalline Precambrian basement with erratic topography. Radium activities increase as the aquifer system becomes locally confined downgradient, and groundwater transitions from a younger, (Mg, Ca)-HCO_3-type to an older, Ca-(SO_4, Cl)-type. Multiple Ra mobilization mechanisms are identified, including the dissolution or absence of iron and manganese (hydr)oxide minerals and associated decrease in sorption capacity, and cation competition for sorption sites due to increasing TDS levels along the flow path. An interesting result of this study is that wells with long open boreholes and 'mixed' redox processes have the

highest Ra activity. These wells likely receive a larger portion of the old, anoxic water from transmissive Cambrian sandstones, emphasizing the influence of well construction on Ra activity.

In Chapter 3, the impact of shifting hydrogeochemical conditions resulting from a hydrocarbon spill on Ra activity is explored at a research site in south-central Wisconsin, where the MCOAS is regionally unconfined. Radium occurrence has not been studied in this setting, despite prior research demonstrating the mobilization of other geogenic contaminants in hydrocarbon-contaminated aquifers. The site is contaminated with a mixture of chlorinated solvents, ketones, and aromatics that have together migrated to the Tunnel City Group as a dense non-aqueous phase liquid (DNAPL). Multi-level systems are used to target groundwater sampling in the Tunnel City Group. Within the dissolved phase plume, an increase in TDS and decreases in oxidation-reduction potential and pH are observed in comparison to background conditions. ^{226}Ra activities are up to 10 times higher than background activity 60 m downgradient of the source zone. Correlations suggest that both the absence or dissolution of iron and manganese (hydr)oxides and cation competition for sorption sites contribute to the elevated Ra activities. 600 m downgradient and near the middle of the dissolved phase plume Ra activities return to near background. Modeling results demonstrate the importance of Ra re-sorption to available surface sites, including clays within the plume and Fe and Mn (hydr)oxides further downgradient. The elevated Ra activities within the plume suggest that Ra should be routinely evaluated alongside other geogenic contaminants at hydrocarbon-contaminated sites.

In Chapter 4, a steady-state groundwater flow model is developed to investigate how changes in well construction and pumping rates influence the contribution of groundwater from several hypothesized Ra sources to public supply wells drawing from the MCOAS in southeastern Wisconsin. Shales are enriched in Ra and parent isotopes U and Th; therefore, public water systems

in southeast Wisconsin are often advised to extend well casing past these facies (e.g., within the Eau Claire Formation) to reduce Ra activity in pumped groundwater. Results indicate the direct contribution from the Eau Claire layer is eliminated when the casing is extended; however, the change in well construction induces a strong downward hydraulic gradient that enhances flux from the Eau Claire to the underlying Mt Simon layer, a relatively clean sandstone with few sorption sites. Increased pumping at the reconstructed well enhances this flux, suggesting that increased groundwater use may lead to more contribution from Ra-enriched groundwater from the Eau Claire Formation. Additionally, the contribution of groundwater from the base of the Mt Simon Formation, elevated in TDS and radioactivity, approximately doubles with well reconstruction. These findings highlight how well field management can alter groundwater flow paths and enhance the exchange of groundwater between stratigraphic units with different geochemistry and Ra activity.

Together, these investigations demonstrate the impact hydrogeochemical conditions have on Ra mobility in groundwater, as well as how Ra mobility may change as hydrogeochemical conditions evolve as a result of both natural and human-induced processes. This research highlights the influence of multiple factors on aquifer hydrogeochemical conditions (e.g., redox, TDS, pH) and Ra activity in the MCOAS, including natural factors such as groundwater flow paths, confinement, and aquifer mineralogy, as well as anthropogenic factors such as the release of organic pollutants to the subsurface and well field management (e.g., construction, location). While these studies were conducted only in the MCOAS, the findings improve the fundamental understanding of Ra occurrence in subsurface systems and how environmental and human-controlled processes can influence Ra occurrence in groundwater.

5.2 Suggestions for future research

Several research questions remained unresolved in light of these findings. Further investigation is needed to determine potential reasons for increasing Ra activity in aquifer systems, such as the MCOAS in Wisconsin. A more detailed study examining well drilling trends (e.g., completion depth) and groundwater use in eastern Wisconsin over the past two decades would help determine if the construction of deeper wells or long-term water withdrawals are responsible for the recent increase in Ra activity. Additionally, the impact of other anthropogenic contaminants on Ra occurrence in the MCOAS is not well understood. For example, the Maquoketa shale is absent and the MCOAS is regionally unconfined in western Wisconsin; this increases the likelihood of migration of anthropogenic contaminants (e.g., nitrate, sodium chloride) to the deep aquifer system, and their potential interaction with Ra.

Furthermore, additional studies are needed to determine how other types of hydrocarbon-contaminated aquifers may affect Ra occurrence in groundwater. There are numerous sites across the U.S. contaminated with complex organic mixtures that differ from the composition examined in Chapter 3 of this dissertation, including sites contaminated by landfills and wastewater treatment plants. While Ra did not occur at levels above the Maximum Contaminant Level at the site examined here, it may be more extensively mobilized in other aquifers within the MCOAS or in other aquifer systems with a lower sorption capacity than the units examined in this work.

Lastly, the developed groundwater flow model in Chapter 4 should be used to create a smaller, high-resolution transport model that can be used to investigate Ra transport from Ra-rich shales to underlying sandstones under pumping conditions at a well cased through the shale. The model should incorporate additional processes including diffusion, dispersion, and retardation. Continuation of these modeling efforts could provide an estimate for changes in Ra activity in the

Mt Simon Formation due to Ra transport from an overlying shale facies over a relevant time scale (e.g., 30 years) and draw additional conclusions regarding the effectiveness of reconstructing wells past shale-rich formations to reduce Ra activities in public supply wells.

Appendix A

Supplementary Information for Chapter 2

Table A-1 Well-specific data, including well construction, water type, redox process, field parameters, isotopic measurements, and concentrations of cations and anions.

ID #	Date	Well depth (m)	Well type	Open borehole - Top	Open borehole - Bottom	Water type	Redox process	T (˚C)	pH	DO (mg/L)
Cluster 1										
1	8/19/2019	50	Household	Sinnipee Grp	Sinnipee Grp	Mg-HCO_3	Anoxic	15.8	7.6	0.2
2	8/12/2019	55	Household	Sinnipee Grp	Sinnipee Grp	Mg-HCO_3	Anoxic	12.0	7.6	0.2
3	7/15/2019	251	Public	Sinnipee Grp	Precambrian	Mg-HCO_3-SO_4	Oxic	11.6	7.4	2.7
4	7/15/2019	227	Public	Sinnipee Grp	Precambrian	Mg-Ca-HCO_3-SO_4	Oxic	12.7	7.4	5.2
5	8/12/2019	232	Public	Sinnipee Grp	Precambrian	Mg-Ca-Cl-HCO_3	Oxic	11.3	7.3	6.1
6	8/12/2019	86	Household	Sinnipee Grp	St Peter Fm	Mg-Ca-HCO_3	Suboxic	12.7	7.5	0.1
7	8/12/2019	69	Household	Sinnipee Grp	Sinnipee Grp	Mg-Ca-HCO_3	Suboxic	12.8	7.7	0.2
8	8/19/2019	32	Household	Sinnipee Grp	Sinnipee Grp	Mg-HCO_3	Suboxic	14.4	8.0	0.2
9	7/15/2019	251	Public	Sinnipee Grp	Cambrian	Mg-HCO_3	Oxic	11.6	7.8	6.1
10	7/15/2019	270	Public	Sinnipee Grp	Precambrian	Mg-Ca-HCO_3	Oxic	11.7	7.7	3.4
Cluster 2										
11	8/21/2019	54	Household	Sinnipee Grp	Prairie du Chien Grp	Ca-HCO_3	Anoxic	12.2	7.5	0.2
12	7/25/2019	98	Public	St Peter Fm	St Peter Fm	Ca-HCO_3	Oxic	10.7	7.4	2.5

[a]Sample not collected for analysis.
[b] Averaged data from Wisconsin DNR database. ± is calculated standard deviation.
ND = Non-detect, MDA = Minimum detectable activity.

ID #	Date	Well depth (m)	Well type	Open borehole - Top	Open borehole - Bottom	Water type	Redox process	T (˚C)	pH	DO (mg/L)
Cluster 2										
13	8/21/2019	31	Public	Sinnipee Grp	St Peter Fm	$Ca\text{-}HCO_3$	Oxic	16.4	7.3	2.1
14	7/25/2019	56	Public	St Peter Fm	St Peter Fm	$Ca\text{-}Mg\text{-}HCO_3$	Oxic	11.2	7.2	2.5
15	7/25/2019	149	Public	Jordan Fm	Elk Mound Grp	$Ca\text{-}HCO_3$	Anoxic	10.6	7.1	0.4
16	8/21/2019	46	Public	Sinnipee Grp	St Peter Fm	$Ca\text{-}HCO_3$	Anoxic	13.2	7.4	0.2
17	8/19/2019	62	Household	Sinnipee Grp	Sinnipee Grp	$Mg\text{-}HCO_3$	Suboxic	11.5	7.8	0.1
18	8/19/2019	62	Household	Sinnipee Grp	Sinnipee Grp	$Mg\text{-}HCO_3$	Anoxic	12.8	7.9	0.2
19	8/21/2019	47	Public	Sinnipee Grp	Sinnipee Grp	$Mg\text{-}HCO_3$	Suboxic	15.7	7.7	0.1
Cluster 3										
20	7/31/2019	322	Public	St Peter Fm	Precambrian	$Ca\text{-}HCO_3\text{-}Cl$	Mixed	13.0	7.6	0.5
21	7/17/2019	294	Public	Glenwood Fm	Precambrian	$Ca\text{-}Cl\text{-}HCO_3$	Anoxic	13.0	7.5	0.4
22	7/17/2019	346	Public	St Peter Fm	Precambrian	$Ca\text{-}HCO_3$	Oxic	12.5	7.6	0.8
23	7/17/2019	301	Public	St Peter Fm	Cambrian	$Ca\text{-}HCO_3$	Oxic	12.2	7.7	0.5
24	7/17/2019	278	Public	St Peter Fm	Elk Mound Grp	Ca-Cl	Mixed	12.8	7.5	0.6

ID #	Date	Well depth (m)	Well type	Open borehole - Top	Open borehole - Bottom	Water type	Redox process	T (°C)	pH	DO (mg/ L)
Cluster 3										
25	7/17/2019	265	Public	St Peter Fm	Precambrian	Ca-Cl	Mixed	12.0	7.4	0.8
26	7/17/2019	295	Public	St Peteer Fm	Precambrian	Ca-Cl	Mixed	12.5	7.2	0.8
27	7/15/2019	249	Public	Sinnipee Grp	Elk Mound Grp	Ca-SO_4-HCO_3	Oxic	11.6	7.1	5.0
28	715/2019	254	Public	Tunnel CityGrp	Precambrian	Ca-SO_4-Cl	Oxic	11.6	7.5	4.0
29	7/15/2019	241	Public	Sinnipee Grp	Wonewoc/Eau Claire Fms	Ca-SO_4-HCO_3	Mixed	12.2	7.5	3.8
30	7/17/2019	239	Public	St Peter Fm	Precambrian	Ca-Cl-HCO_3	Mixed	11.2	7.4	1.3
31	7/17/2019	312	Public	St Peter Fm	Precambrian	Ca-Cl-SO_4	Suboxic	12.4	7.4	0.4
32	8/12/2019	258	Irrigation	St Peter Fm	Mt Simon	Ca-HCO_3	Undetermined	13.0	7.7	[a]

ID #	Specific conductance (µS/cm)	Alkalinity (mg $CaCO_3$/L)	Na:Ca +Mg	Na: Cl	Ca (mg/ L)	Mg (mg/ L)	Na (mg/ L)	K (mg/ L)	Si (mg/ L)	Sr (mg/ L)	Ba (µg/ L)	Fe (µg/ L)	Mn (µg/ L)
Cluster 1													
1	759	310	0.06	0.2	82	74	6.5	3.3	22	3.2	100	1574	44
2	638	254	0.1	0.3	65	51	11	3.2	14	3.0	35	537	15
3	1080	254	0.1	0.2	85	61	14	4.1	12	7.3	44	28	17
4	1223	274	0.2	0.3	98	60	22	4.2	12	7.2	52	42	30
5	1344	294	0.2	0.2	116	78	23	4.9	9.7	9.6	51	30	29
6	699	194	0.2	0.7	47	32	14	2.2	12	1.6	27	12	7.6
7	671	178	0.3	0.9	46	29	16	2.4	11	1.6	23	19	36
8	450	214	0.2	1.5	39	34	12	1.9	12	1.3	23	< 6.4	20
9	692	230	0.2	0.4	54	41	11	3.1	16	3.1	63	< 6.4	6.8
10	617	189	0.2	0.7	38	29	12	2.6	13	3.4	44	23	5.1
Cluster 2													
11	575	307	0.02	0.1	97	49	1.6	1.9	6.0	0.07	27	< 6.4	89
12	675	306	0.04	0.2	80	43	3.6	1.5	7.4	0.24	23	< 6.4	< 3.4

ID #	Specific conductance (µS/cm)	Alkalinity (mg $CaCO_3$/L)	Na:Ca +Mg	Na: Cl	Ca (mg/ L)	Mg (mg/ L)	Na (mg/ L)	K (mg/ L)	Si (mg/ L)	Sr (mg/ L)	Ba (µg/ L)	Fe (µg/ L)	Mn (µg/ L)
Cluster 2													
13	785	309	0.07	0.2	85	45	6.2	2.5	7.1	0.12	47<	6.4	< 3.4
14	972	358	0.1	0.2	98	54	15	2.4	9.0	0.13	123	25	13
15	594	302	0.02	0.3	76	37	1.8	1.8	5.4	0.38	115	619	84
16	671	318	0.03	0.2	78	39	2.2	2.2	6.5	0.67	73	633.6	18
17	435	270	0.03	0.4	51	42	1.8	2.2	15.4	3.2	274	44	30
18	500	297	0.02	0.1	60	50	1.6	2.1	18	1.0	245	305	31
19	734	271	0.04	0.1	53	61	3.5	2.9	23	1.8	142	11	17
Cluster 3													
20	729	152	0.2	0.2	73	24	11	4.7	3.5	9.7	77	90	34
21	733	158	0.2	0.2	70	24	11	4.1	3.4	9.6	38	51	53
22	523	151	0.1	0.2	51	21	7.0	3.5	3.8	4.3	31	41	20
23	523	158	0.1	0.4	48	21	6.9	3.2	3.7	3.4	39	< 6.4	8.8
24	998	143	0.2	0.1	98	27	20	5.0	3.3	19	41	54	113

ID #	Specific conductance (µS/cm)	Alkalinity (mg $CaCO_3$/L)	Na:Ca +Mg	Na: Cl	Ca (mg/ L)	Mg (mg/ L)	Na (mg/ L)	K (mg/ L)	Si (mg/ L)	Sr (mg/ L)	Ba (µg/ L)	Fe (µg/ L)	Mn (µg/ L)
Cluster 3													
25	1172	144	0.2	0.1	115	30	23	5.7	3.3	34	33	66	132
26	965	154	0.3	0.2	98	24	20	5.6	3.5	9.1	39	85	87
27	944	187	0.1	0.2	110	40	13	5.3	6.2	12	30	9.0	25
28	1188	197	0.2	0.2	120	45	17	5.5	10	13	53	26	31
29	973	191	0.1	0.2	103	36	11	4.8	7.0	10	37	439	6.7
30	1138	222	0.1	0.1	124	36	15	4.3	3.5	13	49	281	66
31	1120	184	0.2	0.2	108	31	23	6.5	4.2	17	31	42	32
32	1001	206	0.1	0.2	75	29	11	4.2	3.5	10	50	31	31

ID #	HCO_3 (mg/L)	Cl (mg/L)	SO_4 (mg/L)	Br (mg/L)	^{226}Ra (mBq/L)	^{228}Ra (mBq/L)	$^{226}Ra/^{228}Ra$	Combined Ra (mBq/L)	^{226}Ra: Ba (x 10^{-8})	Sr: Ba	δ^2H (‰, VSMOW)	$\delta^{18}O$ (‰, VSMOW)
Cluster 1												
1	362	51	162	0.09	[a]	[a]	[a]	[a]	NA	51	-58	-8.5
2	299	56	123	0.09	[a]	[a]	[a]	[a]	NA	136	-67	-9.8
3	300	99	192	0.2	155 ± 37[b]	81 ± 30[b]	1.9	237 ± 67[b]	0.6	260	-69	-11
4	321	139	230	0.2	104 ± 41[b]	44 ± 22[b]	2.3	137 ± 56[b]	0.3	216	-70	-9.7
5	344	236	191	0.5	144 ± 13[b]	59 ± 30[b]	2.4	200 ± 41[b]	0.5	294	-73	-10
6	231	31	100	0.07	26 ± 20	44 ± 30	0.6	70 ± 36	0.2	93	-55	-8.1
7	212	26	119	0.08	19 ± 9.6	< MDA	[a]	< MDA	0.14	108	-57	-8.4
8	252	12	89	0.06	[a]	[a]	[a]	[a]	NA	87	-54	-8.1
9	271	42	97	0.1	74 ± 19	59 ± 19	1.3	133 ± 26	0.2	77	-68	-10
10	225	28	71	0.1	178 ± 19	137 ± 22	1.3	315 ± 30	0.7	120	-72	-10
Cluster 2												
11	360	21	95	< 0.05	59 ± 11	48 ± 19	1.2	107 ± 22	0.4	3.7	-66	-9.8
12	362	37	38	< 0.04	30[b]	48[b]	0.6	78[b]	0.2	17	-66	-9.6

ID #	HCO_3 (mg/L)	Cl (mg/L)	SO_4 (mg/L)	Br (mg/L)	^{226}Ra (mBq/L)	^{228}Ra (mBq/L)	$^{226}Ra/^{228}Ra$	Combined Ra (mBq/L)	^{226}Ra: Ba (x 10^{-8})	Sr: Ba	δ^2H (‰, VSMOW)	δ^{18} (‰, VSMOW)
Cluster 2												
13	364	51	39	< 0.05	19 ± 8.5	37 ± 20	0.5	55.5 ± 22.2	0.06	3.8	-61	-9.2
14	423	127	55	< 0.04	[a]	ND[b]	[a]	48.1 ± 11.1[b]	NA	1.7	-64	-9.3
15	359	8.4	34	< 0.04	33 ± 17	7.4 ± 17	5.9	40.7 ± 23.7	0.05	5.2	-66	-9.5
16	376	16	27	< 0.05	85 ± 15	44 ± 19	1.9	130 ± 22.2	0.2	14	-62	-9.4
17	317	6.9	29	0.04	33 ± 18	19 ± 23	2.0	51.8 ± 28.9	0.02	18	-62	-9.3
18	347	17	42	0.05	[a]	[a]	[a]	[a]	NA	6.5	-65	-9.4
19	318	38	84	0.06	19 ± 8.1	7.4 ± 19	2.1	26.6 ± 20.4	0.02	19	-63	-9.3
Cluster 3												
20	181	103	64	1.2	104 ± 19	107 ± 22	1.0	211 ± 29.6	0.2	197	-118	-17
21	188	111.4	64	1.1	141 ± 19	59.2 ± 29.6	2.4	200 ± 33.3	0.6	400	-116	-16
22	180	48	50	0.5	126 ± 30	1.5 ± 22	85	126 ± 36.6	0.7	217	-120	-17
23	188	26	65	0.2	167 ± 44	41 ± 22	4.1	207 ± 48.1	0.7	137	-111	-16
24	169	240	84	2.3	200 ± 26[b]	96 ± 22[b]	2.1	296 ± 33.3[b]	0.8	731	-119	-17

ID #	HCO_3 (mg/L)	Cl (mg/L)	SO_4 (mg/L)	Br (mg/L)	^{226}Ra (mBq/L)	^{228}Ra (mBq/L)	$^{226}Ra/^{228}Ra$	Combined Ra (mBq/L)	^{226}Ra: Ba (x 10^{-8})	Sr: Ba	δ^2H (‰, VSMOW)	$\delta^{18}O$ (‰, VSMOW)
Cluster 3												
25	170	272	151	2.6	148 ± 22	133 ± 22	1.1	281 ± 30	0.7	1618	-118	-17
26	183	204	97	1.7	104 ± 26	126 ± 26	0.8	229 ± 37	0.4	361	-116	-16
27	222	89	268	0.6	181 ± 37[b]	185 ± 19[b]	1.0	366 ± 44[b]	1.0	604	-95	-14
28	232	148	272	1.0	85.1 ± 22	81.4 ± 22	1.0	167 ± 30	0.3	395	-93	-13
29	225	74	232	0.5	222 ± 30	155 ± 22	1.4	377 ± 37	1.0	443	-98	-14
30	261	177	156	1.6	152 ± 15	141 ± 22	1.1	292 ± 30	0.5	421	-82	-12
31	210	209	177	2.0	118 ± 30	15 ± 22	7.8	133 ± 37	0.6	876	-102	-15
32	243	68	97	0.7	126 ± 26	37 ± 22	3.4	163 ± 37	0.4	313	-84	-12

ID #	$\delta^{34}S_{SO4}$ (‰, VCDT)	$^{87}Sr/^{86}Sr$	$^{234}U/^{238}U$
Cluster 2			
13	1.3 ± 0.3	0.709266 ± 0.000008	1.9 ± 0.002
14	0.97 ± 0.1	0.710278 ± 0.000009	2.8 ± 0.002
15	-0.62 ± 0.1	0.710139 ± 0.000007	6.7 ± 0.005
16	-1.5 ± 0.4	0.710201 ± 0.000009	9.3 ± 0.007
17	10 ± 0.3	0.710392 ± 0.000006	2.3 ± 0.051
18	9.0 ± 0.5	0.710880 ± 0.000010	3.3 ± 0.05
19	12 ± 0.2	0.710653 ± 0.000009	3.9 ± 0.028
Cluster 3			
20	17 ± 0.4	0.711100 ± 0.000007	16.3 ± 0.005
21	16 ± 0.3	0.710925 ± 0.000007	10.8 ± 0.006
22	15 ± 0.3	0.710950 ± 0.000009	16.9 ± 0.009
23	14 ± 0.3	0.710699 ± 0.000007	16.0 ± 0.010
24	17 ± 0.4	0.710922 ± 0.000007	9.2 ± 0.004

ID #	$\delta^{34}S_{SO4}$ (‰, VCDT)	$^{87}Sr/^{86}Sr$	$^{234}U/^{238}U$
Cluster 1			
1	10 ± 0.1	0.710497 ± 0.000008	6.3 ± 0.015
2	3.3 ± 0.4	0.710528 ± 0.000005	5.8 ± 0.015
3	1.5 ± 0.2	0.710485 ± 0.000009	5.1 ± 0.005
4	-2.1 ± 0.2	0.710453 ± 0.000008	3.1 ± 0.003
5	0.25 ± 0.3	0.710733 ± 0.000007	5.6 ± 0.087
6	0.34 ± 0.2	0.710800 ± 0.000007	3.9 ± 0.011
7	3.6 ± 0.1	0.710681 ± 0.000009	3.4 ± 0.012
8	1.8 ± 0.2	0.710952 ± 0.000007	2.3 ± 0.004
9	14 ± 0.3	0.710429 ± 0.000009	7.1 ± 0.013
10	19 ± 0.4	0.710430 ± 0.000010	7.1 ± 0.014
Cluster 2			
11	4.1 ± 0.2	0.709248 ± 0.000009	1.9 ± 0.001
12	3.2 ± 0.2	0.710491 ± 0.000008	5.5 ± 0.002

ID #	$\delta^{34}S_{SO4}$ (‰, VCDT)	$^{87}Sr/^{86}Sr$	$^{234}U/^{238}U$
Cluster 3			
25	19 ± 0.2	0.710759 ± 0.000006	10.1 ± 0.003
26	20 ± 0.3	0.711155 ± 0.000008	11.0 ± 0.003
27	21 ± 0.4	0.710470 ± 0.000008	17.2 ± 0.006
28	20 ± 0.1	0.710459 ± 0.000007	18.0 ± 0.010
29	19 ± 0.2	0.710500 ± 0.000006	12.6 ± 0.004
30	16 ± 0.3	0.710769 ± 0.000007	11.3 ± 0.005
31	19 ± 0.1	0.710990 ± 0.000008	17.4 ± 0.004
32	8.0 ± 0.5	0.710756 ± 0.000008	8.9 ± 0.005

Table A-2 Summary of standards used for $^{87}Sr/^{86}Sr$, $[^{234}U/^{238}U]$, and $\delta^{34}S_{SO4}$ analyses with MC-ICPMS.

Analysis	Primary Standard	Secondary Standard	Additional standards
$[^{234}U/^{238}U]$	NIST Natural Uranium	High Purity Standards Uranium	CASS-6 Seawater
$^{87}Sr/^{86}Sr$	NIST SRM 987	High Purity Standards Strontium	CASS-6 Seawater
$\delta^{34}S_{SO4}$	High Purity Standards Sulfur	Optima Sulfuric Acid	CASS-6 Seawater IAEA-S-1

Table A-3 MC-ICPMS measurements of the CASS-6 seawater standard compared to reported literature values.

Analysis	Measured CASS-6 value (this study)	Literature value	Reference
$[^{234}U/^{238}U]$	1.145 ± 0.027	1.145	Henderson (2002)[1]
$^{87}Sr/^{86}Sr$	0.709165 ± 0.000016	0.709167 ± 0.000009	Zaky et al. (2019)[2]
$\delta^{34}S_{SO4}$	+21.03 ± 0.34	+21 ± 0.13	Böttcher et al. (2007)[3]

A-1 Supporting methods for HCA analysis

Measurements below the limit of detection were replaced by the detection limit.[4] Parameters were analyzed for frequency distribution, and parameters demonstrating a non-normal distribution were log-transformed. All data was centered by subtracting the mean and standardized by dividing by the standard deviation of the respective parameter using the scale() function in R.[5, 6] The HCA analysis using Euclidian distance and Ward's Link cluster method was performed in R using the agnes() function in the 'cluster' package.[7] The results were visualized as a dendrogram using the fviz_dend() function in the 'factoextra' package (Figure A-1).[8] The phenon line, the line at which the number of clusters is defined, was selected at a height at which the dendrogram was divided into the minimum amount of groups that explain the majority of variation in hydrogeochemical properties associated with samples.[9]

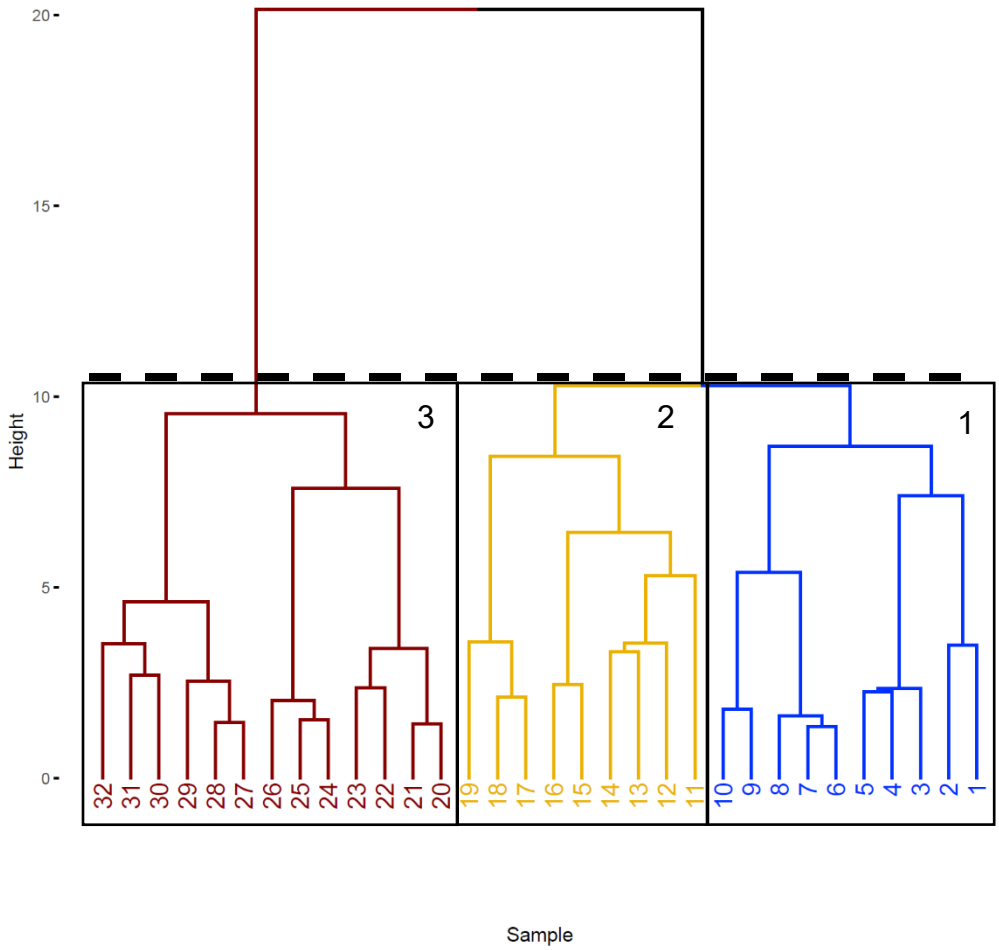

Figure A-1 Dendrogram showing the results of the hierarchical cluster analysis. Cluster 1 (blue) is comprised of 10 samples, Cluster 2 (yellow) is comprised of 9 samples, and Cluster 3 (red) is comprised of 13 samples. The dashed line is the phenon line.

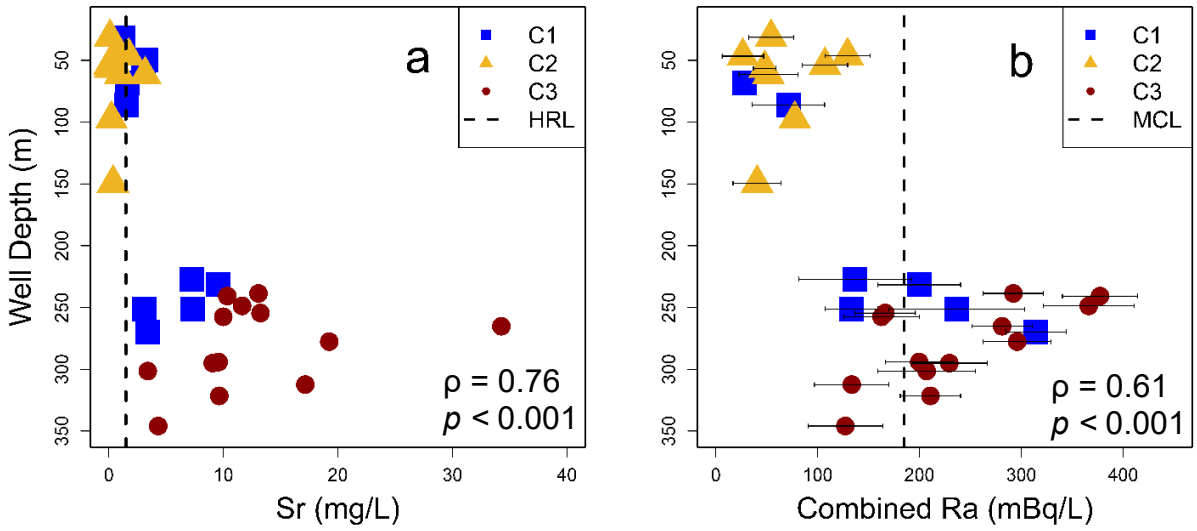

Figure A-2 Well depth vs. a) strontium (Sr) concentration, and b) combined Ra ($^{226}Ra + ^{228}Ra$) activity, for groundwater sample clusters. The dashed line in (a) indicates the U.S. EPA Health Reference Level of 1.5 mg/L for Sr, while the dashed line in (b) indicates the U.S. EPA Maximum Contaminant Level of 185 mBq/L for combined Ra. ρ = Spearman rank correlation coefficient, *p* = significance level.

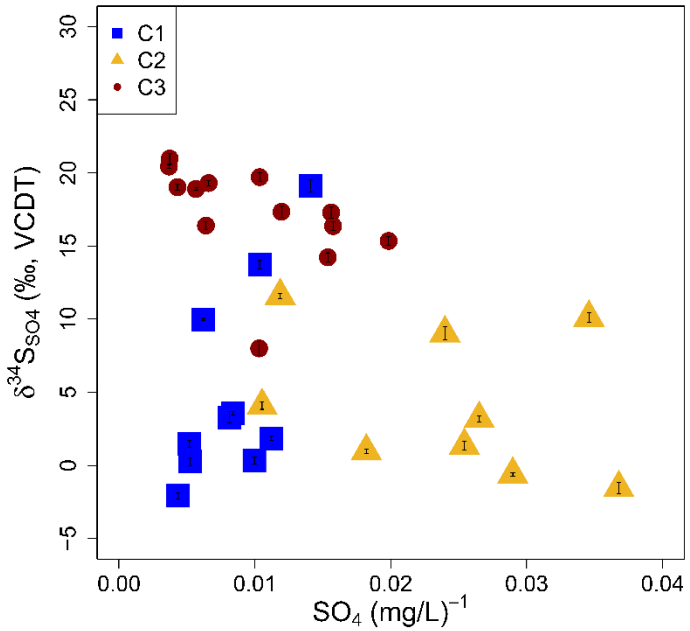

Figure A-3 Sulfate (SO_4) concentration vs. $\delta^{34}S_{SO4}$ value for groundwater sample clusters. Samples with $\delta^{34}S_{SO4}$ values ~0‰ indicate sulfide oxidation as the source of sulfate, while samples with $\delta^{34}S_{SO4}$ values ~20‰ indicate Silurian gypsum as the source of sulfate.

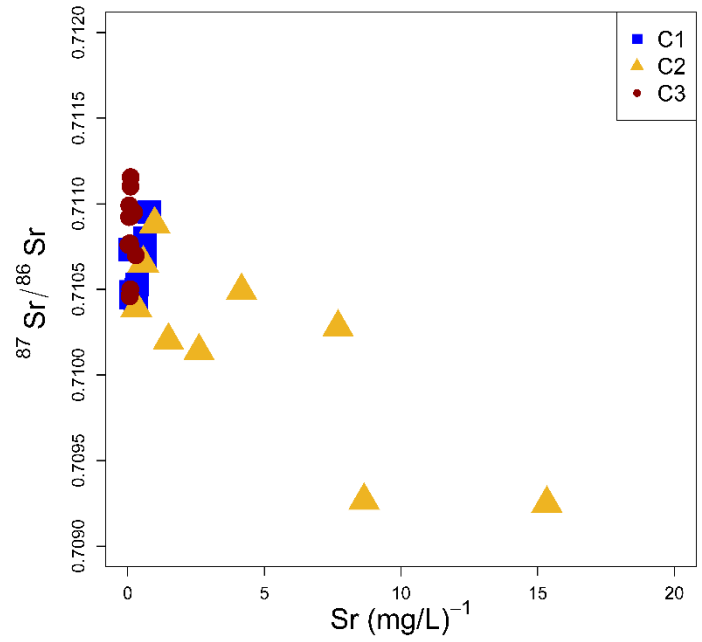

Figure A-4 1/Sr concentration vs. $^{87}Sr/^{86}Sr$ value for groundwater sample clusters. The linear trend indicates two-component mixing, with the first component demonstrating high Sr concentrations and high $^{87}Sr/^{86}Sr$ ratios and the second component demonstrating low Sr concentrations and low $^{87}Sr/^{86}Sr$ ratios.

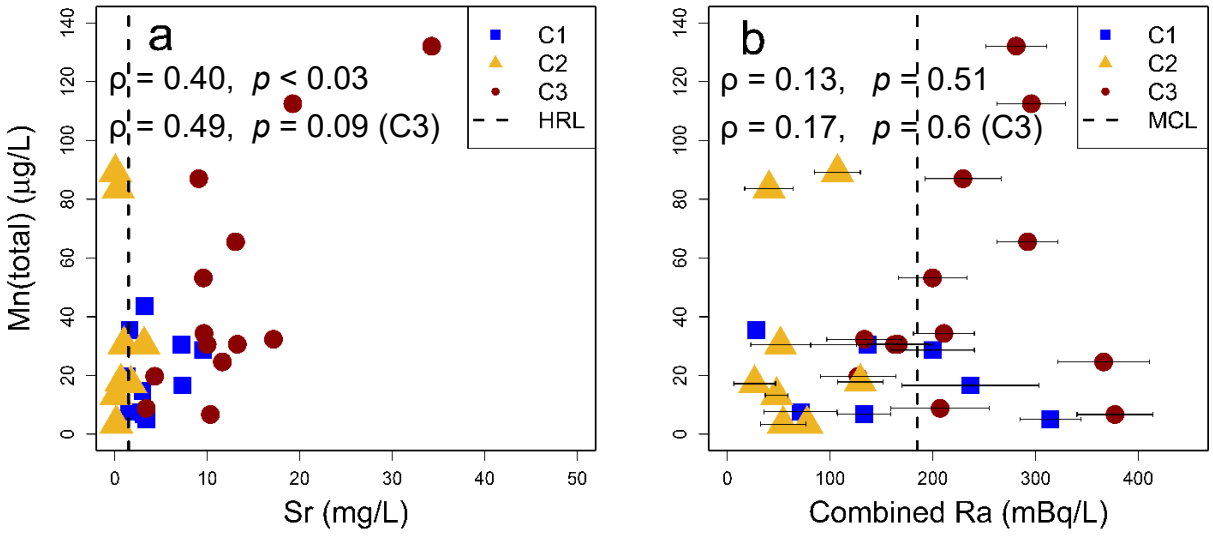

Figure A-5 Mn concentration vs. a) strontium (Sr) concentration and b) combined Ra (^{226}Ra + ^{228}Ra) activity, for groundwater sample clusters. The dashed line in (a) indicates the U.S. EPA Health Reference Level of 1.5 mg/L for Sr, while the dashed line in (b) indicates the U.S. EPA Maximum Contaminant Level of 185 mBq/L for combined Ra. ρ = Spearman rank correlation coefficient, *p* = significance level. The moderate correlations between Mn and Sr suggest that the absence or dissolution of Mn (hydr)oxides is an important Sr mobilization mechanism at the study site.

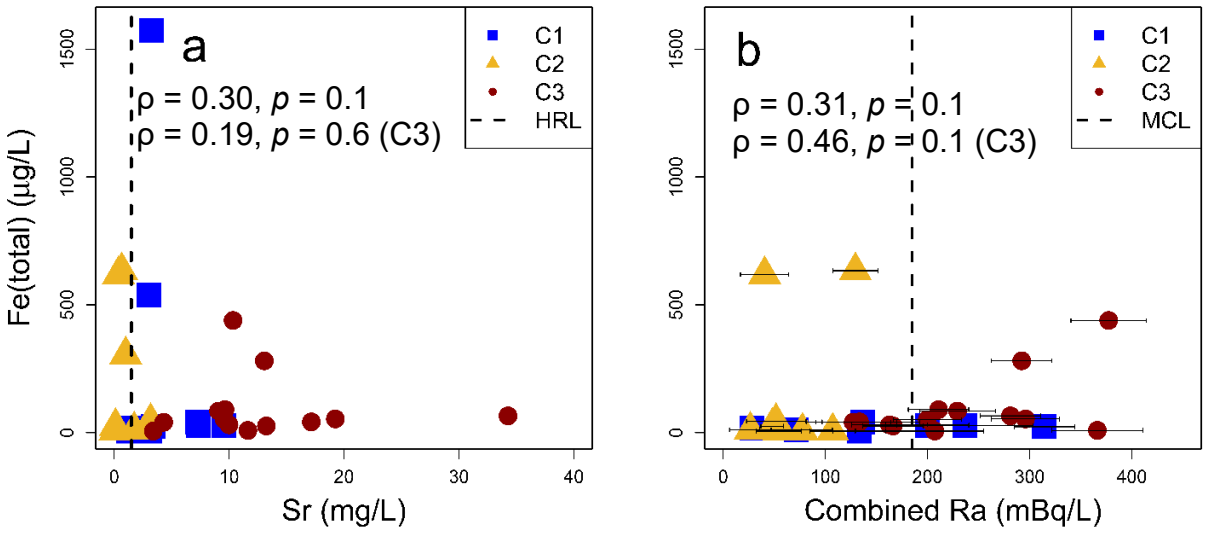

Figure A-6 Fe concentration vs. a) strontium (Sr) concentration and b) combined Ra (^{226}Ra + ^{228}Ra) activity, for groundwater sample clusters. The dashed line in (a) indicates the U.S. EPA Health Reference Level of 1.5 mg/L for Sr, while the dashed line in (b) indicates the U.S. EPA Maximum Contaminant Level of 185 mBq/L for combined Ra. ρ = Spearman rank correlation coefficient, *p* = significance level. The moderate correlation between Fe and Ra in Cluster 3 samples suggests that the absence or dissolution of Fe (hydr)oxides is an important Ra mobilization mechanism in these samples.

Table A-4 Mineral saturation indices calculated in PHREEQC.

	Mineral						
ID#	Dolomite	Calcite	Aragonite	Gypsum	Barite	Celestine	Strontianite
Cluster 1							
1	0.89	0.36	0.21	-1.5	0.38	-1.2	-0.55
2	0.37	0.16	0.01	-1.6	-0.08	-1.3	-0.65
3	0.18	0.08	-0.07	-1.4	0.15	-0.75	-0.45
4	0.27	0.15	0.00	-1.2	0.25	-0.71	-0.46
5	0.23	0.13	-0.02	-1.3	0.16	-0.70	-0.42
6	-0.20	-0.10	-0.26	-1.8	-0.21	-1.6	-1.1
7	-0.08	-0.02	-0.18	-1.7	-0.21	-1.5	-0.95
8	0.78	0.32	0.17	-1.9	-0.34	-1.7	-0.65
9	0.50	0.24	0.08	-1.8	0.08	-1.4	-0.48
10	0.05	0.01	-0.14	-2.0	-0.09	-1.4	-0.51
Cluster 2							
11	0.47	0.31	0.15	-1.6	-0.30	-3.1	-2.3
12	0.13	0.14	-0.02	-2.0	-0.69	-2.9	-1.9
13	0.18	0.12	-0.03	-2.0	-0.45	-3.1	-2.2
14	-0.04	0.04	-0.12	-1.8	0.13	-3.0	-2.3
15	-0.51	-0.16	-0.31	-2.0	-0.01	-2.7	-1.9
16	0.38	0.25	0.10	-2.1	-0.35	-2.5	-1.3
17	0.79	0.37	0.21	-2.3	0.31	-1.8	-0.31
18	1.1	0.50	0.34	-2.1	0.36	-2.2	-0.75
19	0.82	0.27	0.12	-1.9	0.35	-1.7	-0.71
Cluster 3							
20	-0.28	0.01	-0.14	-1.8	0.05	-0.99	-0.35
21	-0.36	-0.04	-0.19	-1.8	-0.24	-0.98	-0.38
22	-0.36	-0.07	-0.22	-2.0	-0.38	-1.4	-0.61
23	-0.24	-0.02	-0.17	-1.9	-0.17	-1.4	-0.64
24	-0.30	0.04	-0.11	-1.5	-0.13	-0.59	-0.14
25	-0.46	-0.02	-0.17	-1.3	-0.07	-0.18	-0.02
26	-0.96	-0.25	-0.40	-1.4	-0.01	-0.77	-0.77
27	-0.76	-0.23	-0.39	-1.1	0.09	-0.42	-0.68
28	0.15	0.21	0.06	-1.1	0.32	-0.38	-0.22
29	-0.06	0.12	-0.04	-1.2	0.14	-0.50	-0.36
30	-0.02	0.19	0.04	-1.3	0.12	-0.59	-0.25
31	-0.25	0.06	-0.09	-1.3	-0.04	-0.40	-0.21
32	0.35	0.30	0.15	-1.6	-0.02	-0.85	-0.06

A-2 Discussion of SO_4^{2-} and Cl^- sources

Mechanisms that may be responsible for the increase in sulfate (SO_4^{2-}) and chloride (Cl^-) concentrations include 1) dissolution of evaporites such as gypsum ($CaSO_4$),[10-12] 2) oxidation of sulfides,[11] 3) stagnation zones at the base of the aquifer,[13, 14] or 4) SO_4^{2-}-rich brines transported from the Michigan Basin during a Pleistocene flow reversal.[10, 15] In this study, dissolution of gypsum contributing to SO_4^{2-} concentrations is supported by undersaturation with respect to gypsum for all samples, with a median SI of -1.7 ± 0.33 (Table A-4), and a moderate correlation between Ca^{2+} and SO_4^{2-} ($\rho = 0.50$, $p < 0.005$). Additionally, multiple samples from each of the three sample clusters have $\delta^{34}S_{SO4}$ values near + 20‰, within the range reported for Silurian gypsum (Figure A-3).[16] Silurian evaporites do not occur locally within the MCOAS of eastern Wisconsin, but are present in the nearby Michigan Basin.[11, 15, 16] Therefore, this $\delta^{34}S_{SO4}$ signature reflects the recharge of saline, SO_4^{2-}-rich water to eastern Wisconsin from the Michigan Basin during a Pleistocene glaciation flow-reversal event.[15] This event is further supported by the moderate negative correlation ($\rho = -0.69$, $p < 0.001$) between $\delta^{34}S_{SO4}$ values and $\delta^{18}O$ values. However, due to the lack of vertically discrete data, it is unclear if concentrated brine remnants are present at the base of the aquifer at the study site. Oxidation of sulfides as a source of SO_4^{2-} is indicated by low $\delta^{34}S_{SO4}$ values (~0 ‰),[11, 15, 17] resulting in SO_4^{2-} concentrations as high as 230 mg/L. Sulfide minerals such as pyrite have been documented within Cambrian-Ordovician bedrock of eastern Wisconsin, including a Sulfide Cement Horizon at the top of the St. Peter sandstone.[18-20] Additionally, the presence of a groundwater stagnation zone at the base of the aquifer cannot be ruled out in the study area. Similar to the Brownsville well in Weaver and Bahr (1991),[12] the wells in the city of Fond du Lac are located on the flank of a substantial low in Precambrian basement,[21, 22] with restricted recharge and an increased groundwater residence time that has permitted increased dissolution of Cl^--bearing minerals. These results suggest that

enhanced mineral dissolution due to local confinement and a groundwater stagnation zone is likely the dominant control on the composition shift. However, unconfined conditions also result in sulfide oxidation that generates an additional source of SO_4^{2-}.

A-3 Discussion of [$^{234}U/^{238}U$] disequilibrium

The extreme disequilibrium of [$^{234}U/^{238}U$] is well-documented in the MCOAS, and is attributed to it being a very deep and old hydrologic system, where the U roll front system is slow and stable and U is dispersed over a large area by precipitation on quartz grains.[23] If this is the case, the redox boundary would not be substantially advancing downgradient. Alternatively, the extreme disequilibrium could be due to increased mobility of ^{234}U, resulting from a diffuse redox boundary where there is considerable transport of ^{234}U before reprecipitation.[23] It is possible that variations in flow and geochemistry from the Pleistocene glaciation could have had an influence on the [$^{234}U/^{238}U$] ratio.[17, 24] In this scenario, the episodic glacial recharge of oxic water could have dissolved U-bearing minerals within the aquifer rocks, or in eroded and crushed shales or igneous and metamorphic rocks transported by glaciers.[24, 25] This would result in preferential leaching of ^{234}U due to α-recoil effects, until reducing aquifer conditions were encountered or re-established and U precipitated out of solution. If it is assumed that reducing conditions were resumed in the aquifer after the glaciation, the subsequent [$^{234}U/^{238}U$] ratio would remain until a different recharge event brings in a new supply of oxic water.[26]

A-4 References

1. Henderson, G.M., *Seawater (234U/238U) during the last 800 thousand years.* Earth and Planetary Science Letters, **2002**. *199*: p. 97-110.
2. Zaky, A.H., Brand, U., Buhl, D., Blamey, N., Bitner, M.A., Logan, A., Gaspard, D., and Popov, A., *Strontium isotope geochemistry of modern and ancient archives: tracer of secular change in ocean chemistry.* Canadian Journal of Earth Sciences, **2019**. *56*(3): p. 245-264.
3. Böttcher, M.E., Brumsack, H.J., and Dürselen, C.D., *The isotopic composition of modern seawater sulfate: I. Coastal waters with special regard to the North Sea.* Journal of Marine Systems, **2007**. *67*(1-2): p. 73-82.
4. Cloutier, V., Lefebvre, R., Therrien, R., and Savard, M.M., *Multivariate statistical analysis of geochemical data as indicative of the hydrogeochemical evolution of groundwater in a sedimentary rock aquifer system.* Journal of Hydrology, **2008**. *353*(3): p. 294-313.
5. Becker, R.A., Chambers, J. M. and Wilks, A. R, *The New S Language*. 1st ed. 1988, New York: Wadsworth & Brooks/Cole.
6. R Core Team, *R: A language and environment for statistical computing.* 2020, R Foundation for Statistical Computing: Vienna, Austria.
7. Maechler, M., Rousseeuw, P., Struyf, A., Hubert, M., Hornik, K., *cluster: Cluster Analysis Basics and Extensions. R package version 2.1.0*. 2019.
8. Kassambara, A. and Mundt, F., *factoextra: Extract and Visualize the Results of Multivariate Data Analyses. R package version 1.0.7*. 2020.
9. Monjerezi, M., Vogt, R.D., Aagaard, P., Gebru, A.G., and Saka, J.D.K., *Using 87Sr/86Sr, δ18O and δ2H isotopes along with major chemical composition to assess groundwater salinization in lower Shire valley, Malawi.* Applied Geochemistry, **2011**. *26*(12): p. 2201-2214.
10. Franz, K.E., *Geochemistry of the sandstone and Silurian aquifers in eastern Wisconsin*. 1985, MS Thesis, Syracuse University. p. 103.
11. Perry, E.C., Grundl, T., and Gilkeson, R.H., *H, O, and S isotopic study of the groundwater in the Cambrian-Ordovician aquifer system of northern Illinois*, in *Isotope Studies of Hydrologic Processes*. 1982, NIU Press. p. 35-43.
12. Weaver, T.R. and Bahr, J., *Geochemical evolution in the Cambrian-Ordovician sandstone aquifer, Eastern Wisconsin: 1. Major ion and radionuclide distribution.* Groundwater, **1991**. *29*(3): p. 350-356.
13. Ryling, R.W., *A preliminary study of the distribution of saline water in the bedrock aquifers of Eastern Wisconsin*, in *U.S. Geological Survey Information Circular Number 5*. 1961.
14. Weaver, T.R. and Bahr, J.M., *Geochemical evolution in the Cambrian-Ordovician sandstone aquifer, Eastern Wisconsin: 2. Correlation between flow paths and ground-water chemistry.* Groundwater, **1991**. *29*(4): p. 510-515.
15. Siegel, D.I., *Sulfur isotope evidence for regional recharge of saline water during continental glaciation, North-Central United States.* Geology, **1990**. *18*: p. 1054-1056.
16. Claypool, G.E., Holser, W.T., Kaplan, I.R., Sakai, H., and Zak, I., *The age curves of sulfur and oxygen isotopes in marine sulfate and their mutual interpretation.* Chemical Geology, **1980**. *28*: p. 199-260.

17. Gilkeson, R.H., Perry, E.C., Cowart, J.B., and Holtzman, R.B., *Isotopic studies of the natural sources of radium in groundwater in Illinois*, in *Research Report 187*. 1984, Final Report submitted to the Bureau of Reclaimation, U.S. Department of the Interior.
18. Luczaj, J.A., McIntire, M.J., and Olson Hunt, M.J., *Geochemical characterization of trace MVT mineralization in Paleozoic sedimentary rocks of Northeastern, Wisconsin, USA.* Geosciences, **2016**. *6*(29).
19. Schreiber, M.E., Simo, J.A., and Freiberg, P.G., *Stratigraphic and geochemical controls on naturally occurring arsenic in groundwater, eastern Wisconsin, USA.* Hydrogeology Journal, **2000**. *8*(2): p. 161-176.
20. Thornburg, K. and Sahai, N., *Arsenic occurrence, mobility, and retardation in sandstone and dolomite formations of the Fox River Valley, Eastern Wisconsin.* Environmental Science & Technology, **2004**. *38*(19): p. 5087-5094.
21. Newport, T.G., *Geology and ground-water resources of Fond Du Lac County, Wisconsin*, in *Water Supply Paper 1604*. 1962, U.S. Geological Survey: Washington, D.C. p. 197.
22. Skalbeck, J.D., Koski, A.J., and Peterson, M.T., *Estimation of Precambrian basement topography in Central and Southeastern Wisconsin from 3D modeling of gravity and aeromagnetic data.* Journal of Applied Geophysics, **2014**. *106*: p. 187-195.
23. Osmond, J.K., Cowart, J.B., and Ivanovich, M., *Uranium isotopic disequilibrium in ground water as an indicator of anomalies.* The International Journal of Applied Radiation and Isotopes, **1983**. *34*(1): p. 283-308.
24. Young, H.L. and Siegel, D.I., *Summary of Ground-Water Hydrology of the Cambrian-Ordovician Aquifer System in the Northern Midwest, United States*, in *U.S. Geological Survey Professional Paper 1405-A*. 1992: Washington, D.C.
25. Gilkeson, R.H. and Cowart, J.B., *Radium, radon and uranium isotopes in groundwater from Cambrian-Ordovician sandstone aquifers in Illinois*. 1987, Chelsea, MI Lewis Publishers.
26. Kelly, W.R., Panno, S.V., Hackley, K.C., Hadley, D.R., and Mannix, D.H., *Hydrogeological and Geochemical Controls on Radium and Uranium in the St. Peter Sandstone Aquifer in the Middle Illinois Water Supply Planning Region*, in *Report of Investigation 125* 2021, Illinois State Water Survey.

Appendix B

Supplementary information for Chapter 3

B-1 Details of analytical methods

B-1.1 Groundwater sample collection and preservation

Groundwater samples were collected from Westbay® MLS (https://www.westbay.com) using a MOSDAX sample probe with an onboard pressure transducer. The Westbay MLSs sampled for this study each include between 1.2 and 1.9 m depth-discrete monitoring intervals isolated by packers. Nine of the eleven monitoring intervals selected for sampling were less than 1.2 m in length and the other two were between 1.5 and 1.9 m in length. In preparation for sampling, four 250-mL stainless steel sample containers were connected to the MOSDAX sample probe and evacuated using a peristaltic pump. Once the containers were evacuated to a pressure < 2-3 psi the valve between the probe and the containers is shut using a MAGI I control module. The probe and connected containers are then lowered down the Westbay multilevel system casing on a wireline using a hand winch until they are about 1 m below the port providing access to the monitoring interval of interest. At that point, an arm on the probe is extended using the control module. The probe and connected containers are then lifted to a position about 0.3 m above the port and then lowered back down until the arm engages with a grove in the casing that lands the probe in the port. The MAGI control module is then used to extend a shoe that pushes the sample probe against the port creating a hydraulic connection between the probe and the groundwater outside the MLS casing in the monitoring interval. The ambient formation fluid pressure is measured and then sample collection is initiated by opening the valve between the evacuated containers and the probe. The valve is closed once the pressure in the system has equilibrated back

to the original formation fluid pressure. The probe is disconnected from the port using the control module and then the probe and sample containers are then lifted back to the surface using the winch. Once at the surface the sample containers were opened and the groundwater was decanted into laboratory containers. Field parameters including pH, ORP, TDS, and temperature were measured with a Myron L Company Ultrameter II. Samples for metal and isotopic analysis were filtered (0.45 μm) and preserved at pH < 2 with Optima grade hydrochloric acid (HCl), while samples for other general chemical analyses were only filtered. All groundwater samples were kept on ice in the field and stored at 4˚C until analysis.

B-1.2 General chemical analyses

Groundwater samples were analyzed for alkalinity, metals, and anions at the University of Wisconsin-Madison Core Facility for Advanced Water Analysis. A Mettler Toledo G-20 compact titrator was used to measure total alkalinity within 24 hours of sample collection. Samples were analyzed for metals with an Agilent 5110 inductively-coupled plasma optical emission spectrometer. Concentrations of thorium (^{232}Th) and uranium (^{238}U) were measured with an Agilent 8900 inductively-coupled plasma mass spectrometer. Anion (e.g., sulfate, chloride, nitrate) concentrations were determined using a Thermo Scientific Dionex ICS-2100 ion chromatography system with a Dionex IonPac AS-11 separation column and an IonPac AG-11 guard column.

B-1.3 Isotopic analyses

Analyses of radium (^{228}Ra/^{226}Ra), uranium ([^{234}U/^{238}U]), and strontium (^{87}Sr/^{86}Sr) isotopes in groundwater samples were performed with a multi-collector inductively-coupled plasma mass spectrometer (MC-ICPMS) at the Wisconsin State Laboratory of Hygiene Trace Elements Laboratory. Samples were purified by ion exchange chromatography prior to analyses following methods described in Mathews, et al. (2021, 2022).[1, 2] Data for duplicate measurements are

presented in Table B-4, and standards used for [$^{234}U/^{238}U$] and $^{87}Sr/^{86}Sr$ measurements are summarized in Table B-5. Prior to purification by ion exchange chromatography, samples for ^{226}Ra and ^{228}Ra analysis were spiked with 100 µL of a ^{228}Ra solution purified from a Th solution (initial $^{226}Ra/^{228}Ra$: 0.8197). The ^{228}Ra spike was calibrated to the average literature values for rock standards AGV-2, BCR-2, and TML.[1] The validity of calibration was then checked against additional aliquots of AGV-2, BCR-2, TML, and SBC-1. The measured $^{226}Ra/^{228}Ra$ ratio was used to calculate the amount of ^{226}Ra for each sample, converted from fg/g solution Ra activity to mBq/L water. Further information about the spike calibration can be found in Mathews, et al. (2021).[1] Prior to each $^{226}Ra/^{228}Ra$ analysis, the MC-ICPMS ion counter detector was calibrated with a dilute ^{238}U tuning solution. Mass bias in the $^{226}Ra/^{228}Ra$ analysis was corrected by analyzing a natural uranium solution for $^{238}U/^{235}U$. City of Madison Well 19 water (MWU 19) and Pheasant Branch spring water were used as internal standards for ^{226}Ra and ^{228}Ra analyses. The MWU 19 sample gave $^{226}Ra = 1.62 \pm 0.05$ and $^{228}Ra = 2.06 \pm 0.07$, in good agreement with the long-term average of 1.60 ± 0.06 and 2.03 ± 0.13 (n = 11). The Pheasant Branch sample gave $^{226}Ra = 0.20 \pm 0.01$ and $^{228}Ra = 0.70 \pm 0.04$, in good agreement with the long-term average of 0.574 ± 0.315 (n = 8). The Pheasant Branch sample was also measured for $^{87}Sr/^{86}Sr$, giving 0.709272 ± 0.000007, consistent with values measured for this spring in Hunt and Steuer (2000)[3] (listed as Frederick Spring 1). Strontium and uranium isotope data for standards listed in Table B-5 are listed in Table B-6.

Table B-1 Measured field and redox parameters. MLS = multi-level system, DBS = depth below surface, TDS = total dissolved solids, and ORP = oxidation-reduction potential. MLS MP-16 was sampled by Mathews et al.[1]

MLS	Strat Unit	Port	Sampling Date	DBS (m)	pH	TDS (ppm)	ORP (mV)	Total Fe (ppm)	Total Mn (ppb)	Sulfate (ppm)	Nitrate (ppm)	Methane (ppb)
MP-16	Readstown	40	11/16/19	35 – 36	7.91	283	217	0.0027	0.79	5.21	< LOD	0.38
MP-16	Tunnel city	30	11/16/19	58 – 60	7.95	322	172	0.0010	0.56	3.81	< LOD	0.24
MP-16	Tunnel City	27	11/16/19	67 – 68	7.22	375	155	0.0024	1.17	3.65	< LOD	0.43
MP-16	Tunnel City	24	11/15/19	74 – 76	8.00	394	143	0.0039	1.04	2.31	< LOD	0.32
MP-19S	Tunnel City	6	09/15/21	39-40	7.15	488	-101	3.70	506	11.0	< 0.08	1366
MP-19S	Tunnel City	5	09/15/21	41-42	6.83	496	-122	5.08	374	13.2	< 0.08	68.1
MP-19S	Tunnel City	4	09/15/21	42-44	6.62	930	-147	18.3	913	8.4	< 0.24	466
MP-24S	Readstown	4	09/15/21	48-49	6.75	2270	-136	231	809	< 0.18	< 0.08	5508
MP-24S	Tunnel City	3	09/15/21	49-50	6.83	1785	-92	66.3	2616	< 0.18	< 0.08	6693
MP-24S	Tunnel City	2	09/15/21	51-52	7.08	759	-114	25.0	451	5.2	< 0.24	616
MP-24S	Tunnel City	1	09/15/21	53-55	7.08	547	-111	10.1	161	< 0.18	< 0.24	1297

Table B-2 Additional measured parameters and major ions. MLS = multi-level system, DBS = depth below surface. Units are in ppm unless otherwise specified. MLS MP-16 was sampled by Mathews et al.[1]

MLS	Strat Unit	Port	Sampling Date	Open interval (DBS, m)	DOC	Alkalinity (mg $CaCO_3$/L)	T (˚C)	Cl	Ca	Mg	K	Na	Si
MP-16	Readstown	40	11/16/19	35 – 36	0.49	226	10.0	4.1	55	26	2.6	0.64	6.1
MP-16	Tunnel city	30	11/16/19	58 – 60	0.20	260	10.0	7.4	63	31	1.9	0.56	6.2
MP-16	Tunnel City	27	11/16/19	67 – 68	0.55	328	10.2	< LOD	75	38	1.9	0.85	6.2
MP-16	Tunnel City	24	11/15/19	74 – 76	0.92	348	10.8	0.73	75	41	1.5	1.0	6.2
MP-19S	Tunnel City	6	09/15/21	39-40	34	307	11.0	38	70	42	< 1.0	2.3	7.4
MP-19S	Tunnel City	5	09/15/21	41-42	1.3	289	12.0	45	69	43	< 0.35	2.6	6.6
MP-19S	Tunnel City	4	09/15/21	42-44	8.1	334	11.5	240	126	63	< 1.1	8.9	11
MP-24S	Readstown	4	09/15/21	48-49	1130	665	11.6	510	299	140	2.0	16	11
MP-24S	Tunnel City	3	09/15/21	49-50	717	430	12.5	471	247	128	< 0.35	12	7.1
MP-24S	Tunnel City	2	09/15/21	51-52	47	248	13.8	174	100	53	< 0.35	5.3	9.9
MP-24S	Tunnel City	1	09/15/21	53-55	7.8	219	13.2	119	68	45	< 0.35	2.2	7.2

Table B-3 ^{238}U, ^{232}Th, Ba, Sr, and As concentrations, Ra activities, and additional isotopic measurements. Uncertainty represents instrumental error, calculated as the absolute value of 2σ, unless otherwise indicated. MLS = multi-level system, DBS = depth below surface. MLS MP-16 was sampled by Mathews et al.[1]

MLS	Strat Unit	Port	Sampling Date	DBS (m)	^{238}U (ppt)[a]	[^{234}U/ ^{238}U]	^{232}Th (ppt)[a]	Total Ra (mBq/ L)	^{226}Ra (mBq/ L)	^{228}Ra (mBq/ L)	$^{87}Sr/^{86}Sr$	Sr (ppb)	Ba (ppb)	As (ppb)
MP-16	Readst -own	40	11/16/19	35 – 36	254 ± 2	11.1 ± 0.006	0.09 ± 0.02	NA	8.0 ± 0.23	NA	0.709653 ± 0.000008	45.9	27.7	NA
MP-16	Tunnel City	30	11/16/19	58 – 60	563 ± 2	6.5 ± 0.002	0.07 ± 0.01	NA	0.74 ± 0.02	NA	0.710077 ± 0.000007	53.9	8.82	NA
MP-16	Tunnel City	27	11/16/19	67 – 68	763 ± 2	5.0 ± 0.002	0.05 ± 0.01	NA	3.4 ± 0.10	NA	0.710596 ± 0.000007	60.4	22.3	NA
MP-16	Tunnel City	24	11/15/19	74 – 76	607 ± 4	6.9 ± 0.002	0.08 ± 0.02	NA	3.1 ± 0.09	NA	0.710892 ± 0.000008	57.7	17.9	NA
MP-19S	Tunnel City	6	09/15/21	39-40	< 370	3.5 ± 0.003	< 124	15.8 ± 1.5	3.8 ± 0.37	12.0 ± 1.2	0.710487 ± 0.000005	62.5	13.9	27.9
MP-19S	Tunnel City	5	09/15/21	41-42	< 122	3.9 ± 0.004	< 124	11.9 ± 1.0	3.3 ± 0.27	8.5 ± 0.69	0.710955 ± 0.000008	59.5	15.4	24.4
MP-19S	Tunnel City	4	09/15/21	42-44	< 122	3.4 ± 0.004	< 124	25.6 ± 3.0	6.5 ± 0.77	19.0 ± 2.3	0.709909 ± 0.000008	106	104	47.8
MP-24S	Readst -own	4	09/15/21	48-49	< 122	2.3 ± 0.02	< 124	99.1 ± 3.6	42.0 ± 1.5	57.2 ± 2.0	0.709382 ± 0.000007	236	309	81.4
MP-24S	Tunnel City	3	09/15/21	49-50	< 122	1.9 ± 0.02	< 124	56.8 ± 2.7	24.1 ± 1.2	32.7 ± 1.6	0.710813 ± 0.000007	237	1052	72.4
MP-24S	Tunnel City	2	09/15/21	51-52	< 122	1.7 ± 0.01	< 124	15.6 ± 0.75	7.5 ± 0.36	8.1 ± 0.39	0.710537 ± 0.000007	91.0	43.2	18.2
MP-24S	Tunnel City	1	09/15/21	53-55	< 122	3.6 ± 0.01	< 124	9.9 ± 0.83	3.2 ± 0.26	6.7 ± 0.56	0.712565 ± 0.000008	65.7	19.3	26.6

[a]Uncertainty represents standard deviation of triplicate measurements

Table B-4 Duplicate measurements for [$^{234}U/^{238}U$], $^{87}Sr/^{86}Sr$, and $^{226}Ra/^{228}Ra$ analyses with MC-ICPMS. MLS = multi-level system, SD = standard deviation.

MLS	Port	[$^{234}U/^{238}U$]	[$^{234}U/^{238}U$] SD	Total Ra (mBq/L)	Total Ra SD (mBq/L)	^{226}Ra (mBq/L)	^{226}Ra SD (mBq/L)	^{228}Ra (mBq/L)	^{228}Ra SD (mBq/L)	$^{87}Sr/^{86}Sr$	$^{87}Sr/^{86}Sr$ SD
MP-19S	6	3.465 3.328	0.0964	15.8 5.75	7.11	3.83 2.77	0.746	12.0 2.98	6.36	0.710487 0.710491	0.000003
MP-19S	5	3.850 3.571	0.197	11.9 11.1	0.560	3.33 3.97	0.453	8.53 7.11	1.01	0.710955 0.710955	0.00000001
MP-19S	4	3.391 3.119	0.192	25.6 15.1	7.38	6.53 7.53	0.710	19.0 7.59	8.09	0.709909 0.709923	0.00001
MP-24S	4	2.277 1.361	0.648	99.1 101	1.33	42.0 40.8	0.833	57.2 60.2	2.17	0.709382 0.709377	0.000004
MP-24S	3	1.862 1.034	0.395	56.8 48.5	5.87	24.1 23.1	0.699	32.7 25.4	5.17	0.710813 0.710774	0.00003
MP-24S	2	1.715 1.749	0.0238	15.6 18.1	1.79	7.46 9.94	1.75	8.12 8.18	0.0384	0.710537 0.710529	0.000006
MP-24S	1	3.562 2.148	1.00	9.87 20.9	7.79	3.16 9.28	4.33	6.72 11.6	3.46	0.712565 0.712615	0.00004

Table B-5 Standards used for [$^{234}U/^{238}U$] and $^{87}Sr/^{86}Sr$ analyses with MC-ICPMS.

Analysis	Primary Standard	Secondary Standard	Additional standards
[$^{234}U/^{238}U$]	NIST Natural Uranium	High Purity Standards Uranium	AGV-2, BCR-2, TML, SBC-1
$^{87}Sr/^{86}Sr$	NIST SRM 987	High Purity Standards Strontium	AGV-2, BCR-2, TML, SBC-1

Table B-6 Analytical data for standards used for [$^{234}U/^{238}U$] and $^{87}Sr/^{86}Sr$ analyses with MC-ICPMS.

Standard	$^{87}Sr/^{86}Sr$[a]	2σ Abs.	$(^{234}U)/(^{238}U)$[b]	2σ Abs.
AGV-2 (1)	0.703958	0.000007	1.002	0.001
AGV-2 (2)	0.703968	0.000008	1.004	0.001
AGV-2 (3)	0.703967	0.000006		
BCR-2 (1)	0.704999	0.000010	1.012	0.001
BCR-2 (2)	0.704996	0.000011	1.011	0.001
BCR-2 (3)	0.705007	0.000008		
SBC-1 (1)	0.724108	0.000008	1.010	0.002
SBC-1 (2)	0.724118	0.000006	1.008	0.001
SBC-1 (2)	0.724105	0.000008		
TML (1)	0.705577	0.000007	1.009	0.001
TML (2)	0.705577	0.000008	1.008	0.001
TML (3)	0.705585	0.000008		

[a]Strontium isotope ratios are reported relative to NBS987 $^{87}Sr/^{86}Sr = 0.71024$.
[b]Uranium activity ratios relative to the $^{234}U/^{238}U$ equilibrium value of Cheng et al. (2013).[4]

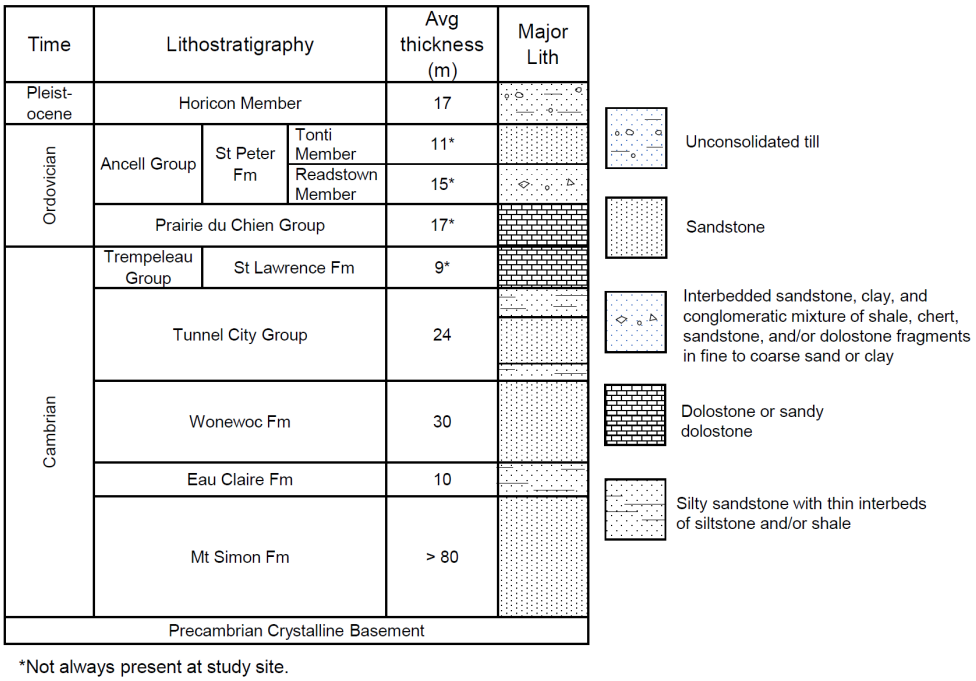

Figure B-1 Generalized study site stratigraphy. Modified from Meyer et al. (2016).[5]

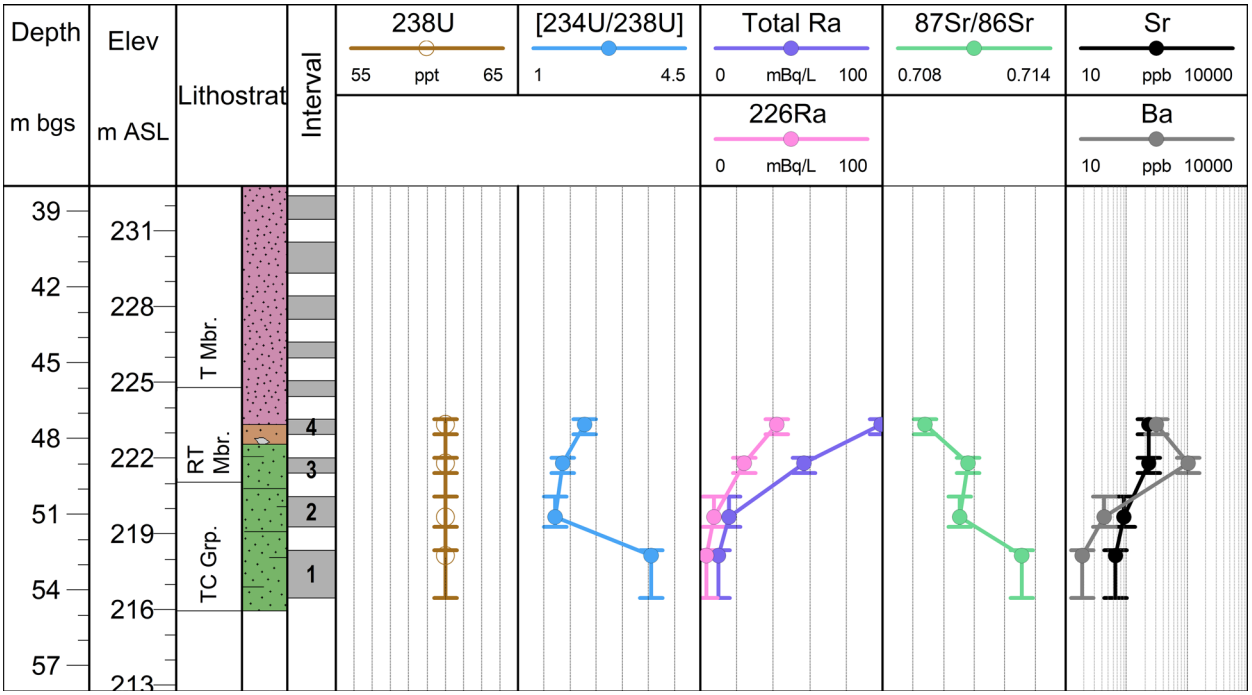

Figure B-2 Depth profile of ^{238}U, Sr, and Ba concentrations, [$^{234}U/^{238}U$], $^{87}Sr/^{86}Sr$, and Ra activities at multi-level system (MLS) MP-24S. The bars above and below each data point indicate the length of each sampling interval. Open data points indicate the measurement is below the limit of detection (LOD) and is plotted as 0.5*LOD. Bgs = below ground surface, ASL = above sea level, TC = Tunnel City, RT = Readstown, T = Tonti.

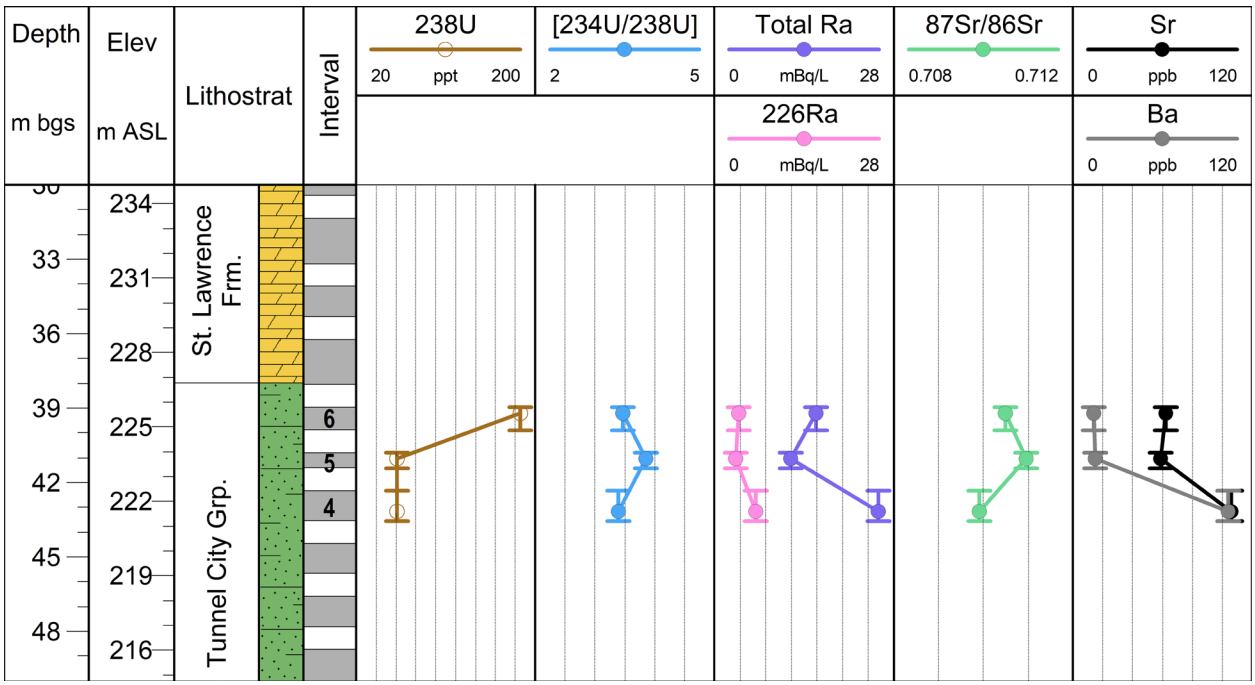

Figure B-3 Depth profile of ^{238}U, Sr, and Ba concentrations, [$^{234}U/^{238}U$], $^{87}Sr/^{86}Sr$, and Ra activities at multi-level system (MLS) MP-19S. The bars above and below each data point indicate the length of each sampling interval. Open data points indicate the measurement is below the limit of detection (LOD) and is plotted as 0.5*LOD. Bgs = below ground surface, ASL = above sea level.

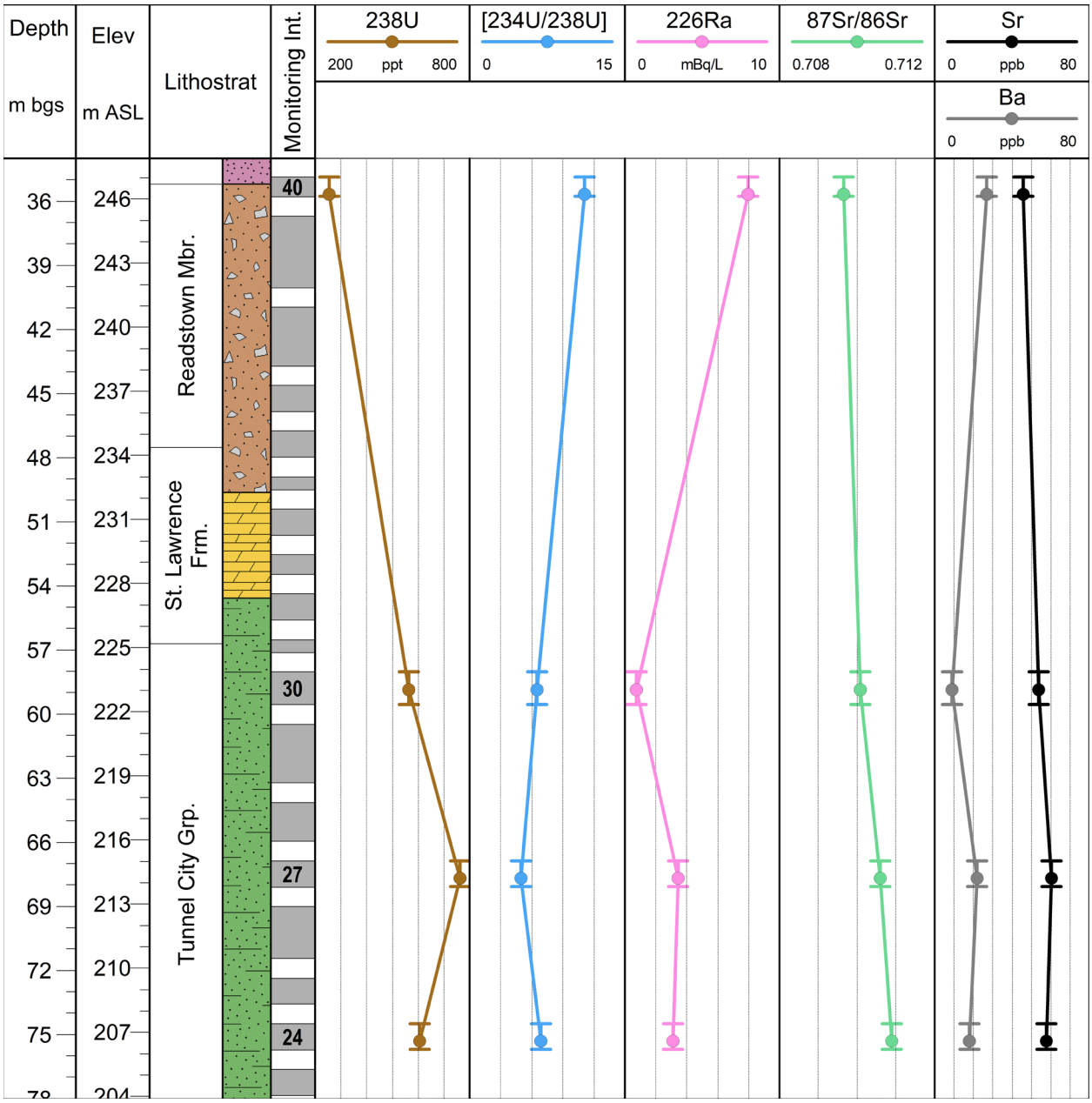

Figure B-4 Depth profile of ^{238}U, Sr, and Ba concentrations, [$^{234}U/^{238}U$], $^{87}Sr/^{86}Sr$, and ^{226}Ra activities at multi-level system (MLS) MP-16.[1] The bars above and below each data point indicate the length of each sampling interval. Bgs = below ground surface, ASL = above sea level.

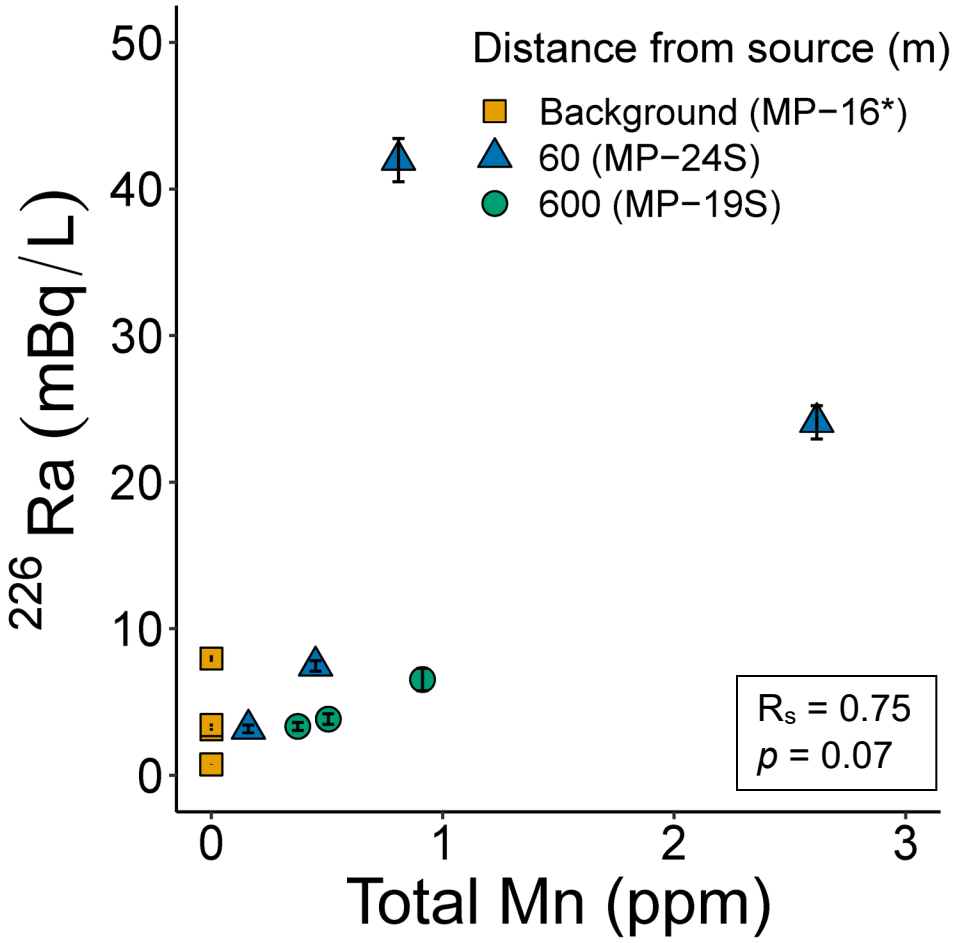

Figure B-5 ^{226}Ra activity vs. total dissolved Mn concentration. Data from the background multi-level system (MP-16) analyzed in Mathews, et al.[1] is plotted for comparison, but not included in the calculation of correlation coefficients. R_s = Spearman rank correlation coefficient. *p* = significance level. *Multi-level system MP-16 was sampled by Mathews, et al.[1]

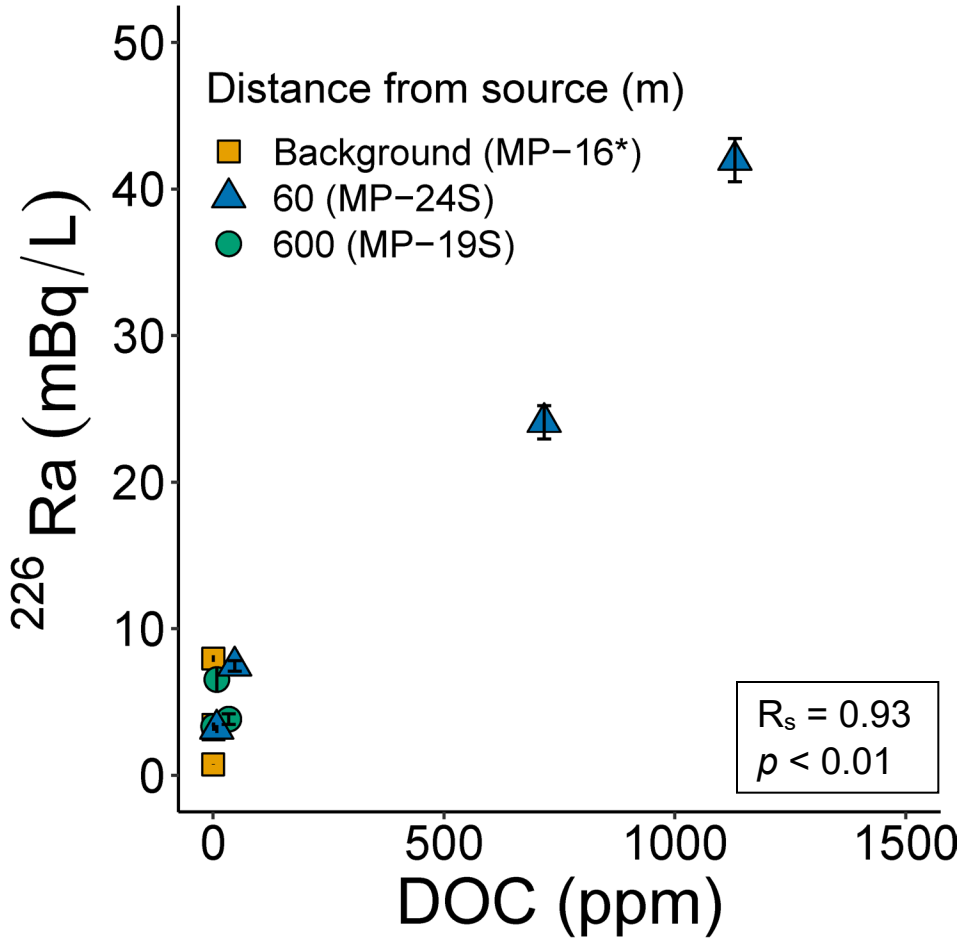

Figure B-6 ^{226}Ra activity vs. dissolved organic carbon (DOC) concentration. Data from the background multi-level system (MP-16) analyzed in Mathews, et al.[1] is plotted for comparison, but not included in the calculation of correlation coefficients. R_s = Spearman rank correlation coefficient. p = significance level. *Multi-level system MP-16 was sampled by Mathews, et al.[1]

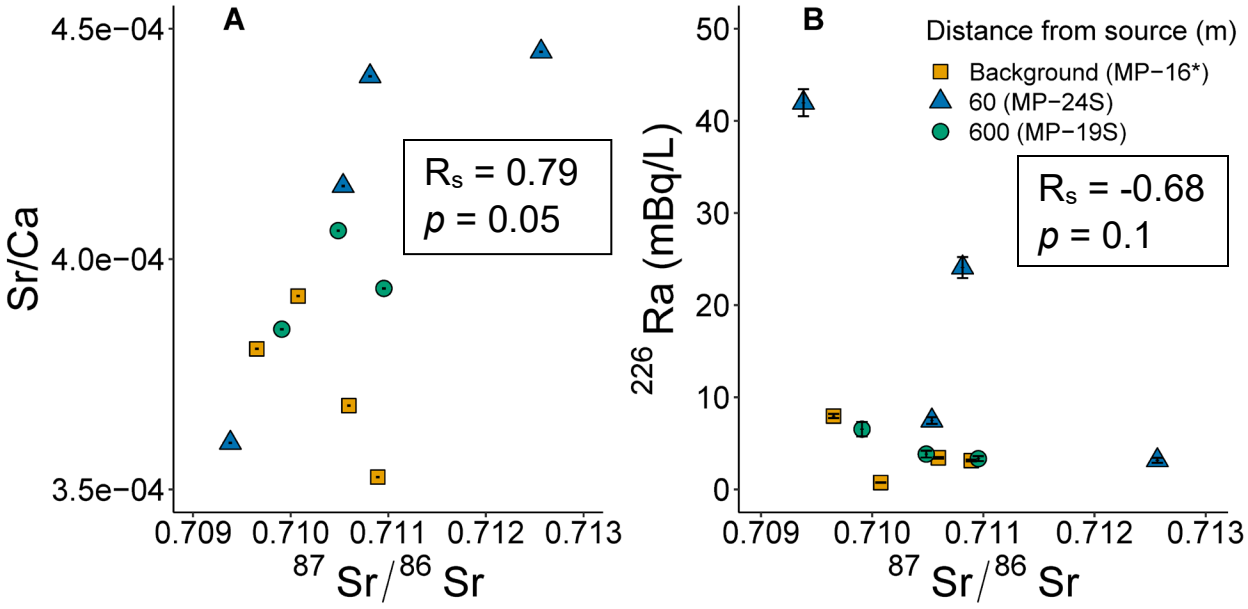

Figure B-7 Aqueous $^{87}Sr/^{86}Sr$ vs. A) Sr/Ca and B) ^{226}Ra activity. Data from the background multi-level system (MP-16) analyzed in Mathews, et al.[1] is plotted for comparison, but not included in the calculation of correlation coefficients. R_s = Spearman rank correlation coefficient. *p* = significance level. *Multi-level system MP-16 was sampled by Mathews, et al.[1]

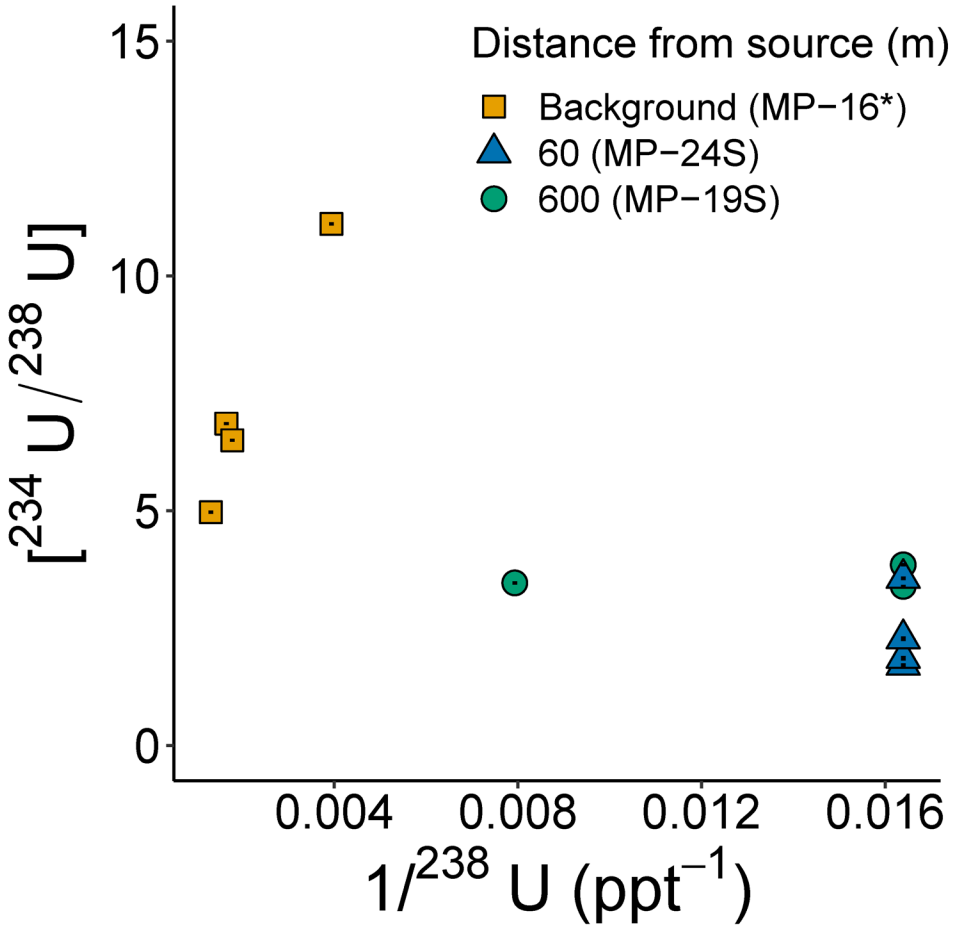

Figure B-8 Inverse ^{238}U concentration vs. [$^{234}U/^{238}U$]. ^{238}U measurements less than the limit of detection (LOD) are plotted as 0.5*LOD. *Multi-level system MP-16 was sampled by Mathews, et al.[1]

B-2 Description of sequential extraction procedure from Mathews et al.[2]

Sequential extractions were performed on pulverized Tunnel City Group core from Sheboygan County, Wisconsin, using a rock-to-extractant ratio of 1:10. The first fraction targeted water-soluble ions using an anoxic, synthetic groundwater consisting of a saturated solution of trace-metal-grade calcium carbonate in ultrapure water and an adjusted initial pH of 8. The second fraction used 1 M trace-metal-grade acetic acid added to the solid from the previous step, and targeted carbonate minerals and sorbed metals (acido-soluble fraction). The last fraction targeted reducible phases (e.g., Fe and Mn (hydr)oxides) using 0.04 M hydroxylamine hydrochloride in

25% v/v acetic acid as the reducing agent. Additional details regarding the sequential extraction procedure and whole-rock digestion are described in Mathews et al.[2]

Table B-7 Summary of results from three PHREEQC models evaluating Ra sequestration. Units are in moles unless specified otherwise. SS = solid solution, HFO = hydrous iron oxides, HMO = hydrous

		Co-precipitation		HFO + HMO sorption				Illite sorption	
Sample	Initial aq. Ra ($\times 10^{-16}$)	$RaCO_3$ SS ($\times 10^{-18}$)	% precip. in $(Ca,Ra)CO_3$	Ra, HFO ($\times 10^{-18}$)	% sorbed to HFO	Ra, HMO ($\times 10^{-18}$)	% sorbed to HMO	Ra, illite ($\times 10^{-18}$)	% sorbed to illite
MP-19S Port 4	8.0	0	0	11	1.4	780	98	760	95
MP-19S Port 5	4.1	0	0	3.0	0.74	400	99	400	98
MP-19S Port 6	4.7	0	0	2.0	0.44	470	100	460	97
MP-24S Port 1	3.9	0	0	2.0	0.52	383	99.4	370	97
MP-24S Port 2	9.1	0	0	5.8	0.64	900	99	870	95
MP-24S Port 3	29	0	0	46	1.6	2900	98	2400	83
MP-24S Port 4	51	2.75	0.054	550	11	4300	85	4400	86

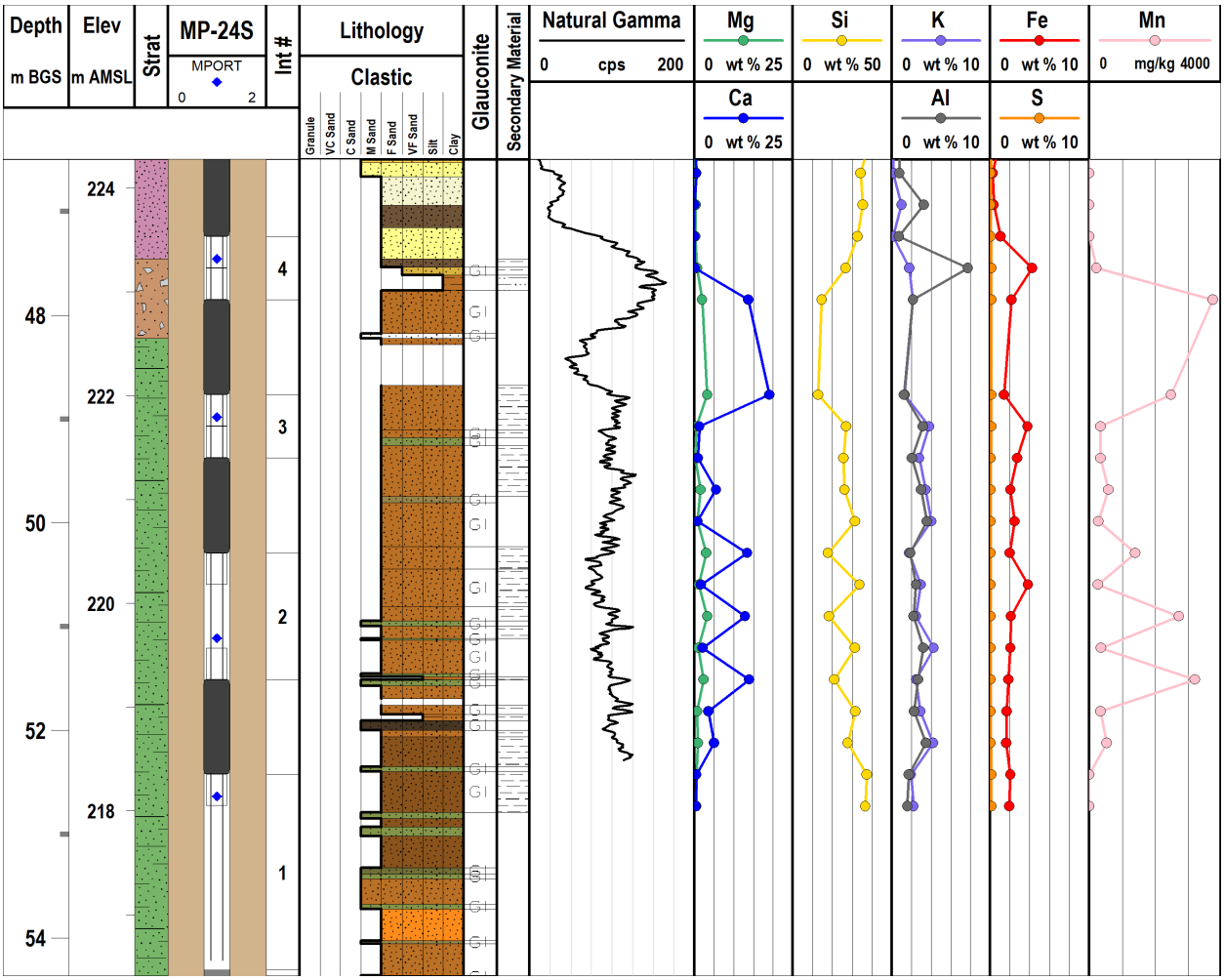

Figure B-9 Solid phase elemental composition of MP-24S core as measured by portable X-ray fluorescence. Elemental weight abundance is presented as either parts per million (mg/kg) or weight percent (%), with 1% = 10,000 mg/kg. Measurements less than the limit of detection are plotted as zero. BGS = below ground surface, AMSL = above mean sea level, cps = counts per second.

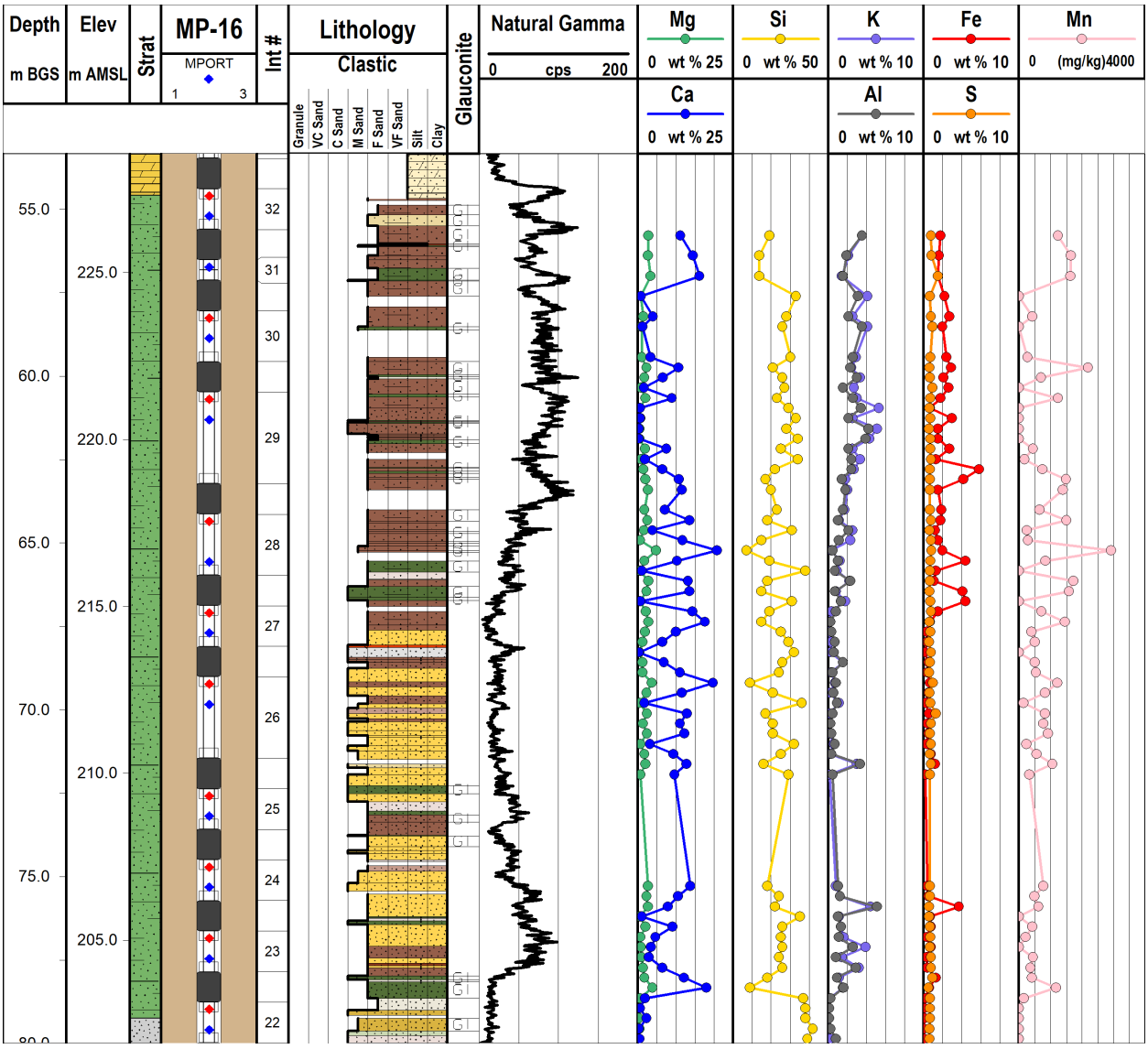

Figure B-10 Solid phase elemental composition of MP-16 core as measured by portable X-ray fluorescence. Elemental weight abundance is presented as either parts per million (mg/kg) or weight percent (%), with 1% = 10,000 mg/kg. Measurements less than the limit of detection are plotted as zero. BGS = below ground surface, AMSL = above mean sea level, cps = counts per second.

B-3 Additional details of geochemical modeling and example PHREEQC codes for Ra co-precipitation and sorption

Concerns with model accuracy and error due to the low initial Ra concentrations used in PHREEQC were evaluated by increasing initial Ra concentrations by three orders of magnitude in each of the models, and comparing results to output from the original models. Results were the same for PHREEQC models evaluating Ra co-precipitation and sorption to illite. Model results evaluating Ra sorption to hydrous iron oxides (HFO) and hydrous manganese oxides (HMO) were different for the sample with the lowest initial Ra concentration (MP-24S Port 1 with initial Ra concentration of 3.9×10^{-16} M), indicating the model censored initial concentrations starting somewhere between 3.9×10^{-16} to 4.1×10^{-16} M Ra. The results for this sample were corrected in post-processing by multiplying the true initial Ra concentration by the fraction sorbed to HFO and the fraction sorbed to HMO, as obtained by the model run with initial concentrations three orders of magnitude higher.

B-3.1 Example PHREEQC model for Ra co-precipitation

```
TITLE Radium cycling in a hydrocarbon plume , MP-19S Port 4
# DATABASE C:\Program Files (x86)\USGS\Phreeqc Interactive 3.4.0-12927\database\phreeqc.dat
# Program to evaluate radium co-precipitation with barite (BaSO4) and aragonite (CaCO3) solid solutions
# Ra species and phases from thermodynamic database of Giffaut et al. (2014) Andra thermodynamic database for performance assessment: ThermoChimie. Applied Geochemistry, 49: 225-236.
# Thermochimie SIT.DAT database for PHREEQC accessed at https://www.thermochimie-tdb.com/pages/publi.php
# Thermodynamic data for Ra(SO4)(s) and Ra(CO3)(s) from Langmuir, Donald, and Riese, A.C. (1985) The thermodynamic properties of radium: Geochimica et Cosmochimica Acta (49)1593-1601.

SOLUTION_MASTER_SPECIES
#element        species alk      gfw_formula   element_gfw
   Ra           Ra+2           0    Ra            226.02

SOLUTION_SPECIES
#radium aqueous species
```

```
#Ra+2
Ra+2 = Ra+2
   log_k     0
#RaOH+
-1.000H+ + 1.000Ra+2 + 1.00H2O = RaOH+
   log_k     -13.49
   delta_h   60.417 kJ/mol    #85LAN/RIE
#Ra(OH)2
-2.00H+ + 1.000Ra+2 + 2.000H2O = Ra(OH)2
   log_k     -28.07
   delta_h   112.197 kJ/mol
#RaCl+
+1.000Ra+2 + 1.000Cl- = RaCl+
   log_k     -0.1    #85LAN/RIE
   delta_h   2.479 kJ/mol
#RaCl2
+1.000Ra+2 + 2.00Cl- = RaCl2
   log_k     -0.1
   delta_h   0.495 kJ/mol
#RaHCO3+
+1.000H+ + 1.000Ra+2 + 1.000CO3-2 = RaHCO3+
   log_k     10.92   #01ILE/TWE
#RaCO3
+1.000Ra+2 + 1.000CO3-2 = RaCO3
   log_k     2.5   #99SCH
   delta_h   4.496 kJ/mol
#RaSO4
+1.000Ra+2 + 1.000SO4-2 = RaSO4
   log_k     2.76
   delta_h   5.472 kJ/mol
#RaF+
+1.000Ra+2 + 1.000F- = RaF+
   log_k     0.48   #87BRO/WAN

#Starting solution composition: groundwater sample collected at MP-19S Port 4
SOLUTION 1 MP-19S Port 4
   temp      11.48
   pH        6.62
   pe        0.92
   redox     pe
   units     mg/l
   density   1
   Al        0.1  #guesstimate
   Alkalinity 334 as Ca0.5(CO3)0.5
   Ba        104 ug/l
   Br        0.002
```

```
   Ca       126
   Cl       240
   F       0.14
   Fe       18.3
   K       0.84
   Mg       62.7
   Mn       913 ug/l
   N(5)     0.12
   Na       8.9
   Ra       7.99e-16 Mol/l
   S(6)     8.4
   Si       11.1 as Si
   Sr       106 ug/l
   -water    1 # kg

PHASES
#Radium solid phases from sit.dat and Langmuir and Riese, included in sit.dat
Ra(cr)
   Ra = Ra+2 + 2e-
   log_k     98.44
   delta_h   -528.025 kJ
   -analytical_expression -0.0881751 0 42193.6 0 0 0
Ra(NO3)2(s)
   Ra(NO3)2 = 2NO3- + Ra+2
   log_k     -2.21
   delta_h   49.981 kJ
Ra(SO4)(s)
   Ra(SO4) = Ra+2 + SO4-2
   log_k     -10.26     #Langmuir and Riese (1985) GCA(49)1593-1601
   delta_h   -9.4 kcal    #Langmuir and Riese (1985) GCA(49)1593-1601
   -analytical_expression -3.44327 0 -2032.41 0 0 0
RaCl2:2H2O(s)
   RaCl2:2H2O = 2Cl- + 2H2O + Ra+2
   log_k     -0.73
   delta_h   32.221 kJ
   -analytical_expression 4.91469 0 -1682.97 0 0 0
Ra(OH)2(s)
   Ra(OH)2 + 2H+ = 2H2O + Ra+2
   log_k     30.99
   delta_h   -149.762 kJ
   -analytical_expression 4.75269 0 7822.65 0 0 0
Ra(CO3)(s)
   Ra(CO3) = CO3-2 + Ra+2
   log_k     -8.3    #Langmuir and Riese (1985) GCA(49)1593-1601
   delta_h   -2.8 kcal    #Langmuir and Riese (1985) GCA(49)1593-1601
   -analytical_expression -5.95418 0 -699.407 0 0 0
```

```
#Mineral phases from wateq4f.dat not included in phreeqc.dat
Magnesite
   MgCO3 = CO3-2 + Mg+2
   log_k     -8.029
   delta_h   -6.169 kcal
Dolomite
   CaMg(CO3)2 = 2CO3-2 + Ca+2 + Mg+2
   log_k     -17.09
   delta_h   -9.436 kcal
   -Vm       64.5 cm3/mol
Dolomite(d)
   CaMg(CO3)2 = 2CO3-2 + Ca+2 + Mg+2
   log_k     -16.54
   delta_h   -11.09 kcal
Dolomite2
   Ca0.5Mg0.5CO3 = CO3-2 + 0.5Ca+2 + 0.5Mg+2
   log_k     -8.5045     #-17.09/2
   delta_h   -4.718 kcal   # -9.436/2
Chlorite
   Mg5Al2Si3O10(OH)8 + 16H+ = 2Al+3 + 6H2O + 3H4SiO4 + 5Mg+2
   log_k     68.38
   delta_h   -151.494 kcal
Kmica
   KAl3Si3O10(OH)2 + 10H+ = 3Al+3 + 3H4SiO4 + K+
   log_k     12.703
   delta_h   -59.376 kcal
Mirabilite
   Na2SO4:10H2O = 10H2O + 2Na+ + SO4-2
   log_k     -1.114
   delta_h   18.987 kcal
Birnessite
   MnO2 + 4H+ + 2e- = 2H2O + Mn+2
   log_k     43.601

#Iron, manganese, and sulfate minerals from various sources
Schwert(1.75)
   Fe8O8(OH)4.5(SO4)1.75 + 20.5H+ = 8Fe+3 + 12.5H2O + 1.75SO4-2
   log_k     18    #Bigham and others (1996, GCA 60:2111-2121)
Schwert(1.00)
   Fe8O8(OH)6.0(SO4)1.00 + 22H+ = 8Fe+3 + 14H2O + SO4-2
   log_k     9.6    #Majzlan and others (2004, GCA 68:1049-1059)
Fe(OH)2_(a)
   Fe(OH)2 + 2H+ = Fe+2 + 2H2O
   log_k     12.76    #sit.dat
   delta_h   -99.096 kJ    #sit.dat
```

```
Mn-siderite
   Fe0.95Mn0.05CO3 = CO3-2 + 0.95Fe+2 + 0.05Mn+2
   log_k     -10.89
   delta_h   -2.48 kcal
   -Vm       29.2 cm3/mol
Rhodochrosite
   MnCO3 = CO3-2 + Mn+2
   log_k     -11.13
   delta_h   -1.43 kcal
   -Vm       31.1 cm3/mol
Manganite
   MnOOH + 3H+ + e- = 2H2O + Mn+2
   log_k     25.34
#  Mn+2 = Mn+3 + e-
#  log_k          -25.51
#  MnOOH + 3 H+ = Mn+3 + 2 H2O # combined above reactions from wateq4f.dat
#   log_k -0.17
Pyrochroite
   Mn(OH)2 + 2H+ = 2H2O + Mn+2
   log_k     15.2
Basaluminite
   Al4(OH)10SO4 + 10H+ = 4Al+3 + 10H2O + SO4-2
   log_k     22.7  #Wateq
Gypsum
   CaSO4:2H2O = Ca+2 + 2H2O + SO4-2
   log_k     -4.58
   delta_h   -0.109 kcal
   -analytical_expression 68.2401 0 -3221.51 -25.0627 0 0
   -Vm       73.9 cm3/mol   #172.18/2.33 (Vm H2O = 13.9 cm3/mol)
Ettringite
   Ca6Al2.02(SO4)2.79(OH)12.48:26H2O + 12.48H+ = 2.02Al+3 + 6Ca+2 + 38.48H2O +
2.79SO4-2
   log_k     61.82
# Myneni and others (1998, Chemical Geology, 148:1-19) log_k     -112.9 (+ 12.48*14)
Epsomite
   MgSO4:7H2O = 7H2O + Mg+2 + SO4-2
   log_k     -2.14
   delta_h   2.82 kcal
Todorokite
   Mn7O12:3H2O + 24H+ + 10e- = 15H2O + 7Mn+2
   log_k     225.6759   #expressed as Mn+2, llnl.dat
Sylvite
   KCl = Cl- + K+
   log_k     0.9121
   delta_h   17.221 kJ   #Robie, Hemingway, and Fisher (1978, USGS Bull 1452)
Celestine
```

```
   SrSO4 = SO4-2 + Sr+2
   log_k     -6.63
   delta_h   -1.037 kcal
   -analytical_expression -14805.9622 -2.4660924 756968.533 5436.3588 -40553604 0
SrSiO3
   SrSiO3 + H2O = H2SiO4-2 + Sr+2
   log_k     -8.1162    # 14.8438 - 22.96, llnl.dat
Barite
   BaSO4 = Ba+2 + SO4-2
   log_k     -9.97
   delta_h   6.35 kcal
   -analytical_expression 136.035 0 -7680.41 -48.595 0 0

SOLID_SOLUTIONS 1
   (BaRa)SO4_ss
      -comp1 Barite 0
      -comp2 Ra(SO4)(s) 0
      -tempk 298.15
      -Gugg_nondim 2.34 0    #Guess, Glynn (2000), Table 1c (BaSr)SO4
   (CaRa)CO3_ss
      -comp1 Aragonite 0
      -comp2 Ra(CO3)(s) 0
      -tempk 298.15
      -Gugg_nondim 2.66 -1.16    #Guess, Glynn (2000), Table 2 (CaSr)CO3

USE solution 1
USE solid_solutions 1

TITLE MP-19S Port 4 Co-precipitation

SELECTED_OUTPUT 1
   -file              MP-19S_Port4_co-precip_only.sel
   -simulation        false
   -distance          false
   -time              false
   -molalities        Ra+2  RaCl+  RaCl2  RaCO3
                      RaF+  RaHCO3+  RaOH+  RaSO4
                      Ra(OH)2
   -saturation_indices  Anhydrite  Aragonite  Barite  Birnessite
                      Calcite  Celestine  Dolomite(d)  Dolomite2
                      Epsomite  Fe(OH)3(a)  Al(OH)3(a)  Gypsum
                      Halite  Manganite  Rhodochrosite  Schwert(1.75)
                      Siderite  Strontianite  Sylvite  Witherite
                      Ra(SO4)(s)  Ra(CO3)(s)  Mirabilite  Kaolinite
                      Illite
   -solid_solutions     (BaRa)SO4_ss  (CaRa)CO3_ss
```

```
#User punch statements allow display of computed parameters in selected output
USER_PUNCH 1
   -headings pH Al.ug Mn.ug Sr.ug Ba.ug Ra.pg Ca.mg Mg.mg Fe.mg Na.mg K.mg SO4.mg
Alk.mg Cl.mg Br.mg NO3.mg F.mg Si.mg TDS.mg SC.uS IonStr.mol SR_BaRa_SO4ss
SI_BaRa_SO4ss SR_ccCaRa_CO3ss SI_ccCaRa_CO3ss SR_CaRa_CO3ss SI_CaRa_CO3ss
MOLES_BaRaSO4_ss MOLES_BaSO4_ss MOLES_RaSO4_ss xBaSO4 xRaSO4 kBaSO4
kRaSO4 kssSO4 SRssSO4 SIssSO4 MOLES_CaRaCO3_ss MOLES_CaCO3_ss
MOLES_RaCO3_ss xCaCO3 xRaCO3 kCaCO3 kRaCO3 KssCO3 SRssCO3 SIssCO3
   -start
 10 PUNCH -LA("H+")
 20 PUNCH TOT("Al")*GFW("Al")*1e6
 30 PUNCH TOT("Mn")*GFW("Mn")*1e6
 40 PUNCH TOT("Sr")*GFW("Sr")*1e6
 50 PUNCH TOT("Ba")*GFW("Ba")*1e6
 60 PUNCH TOT("Ra")*GFW("Ra")*1e12
 70 PUNCH TOT("Ca")*GFW("Ca")*1e3
 80 PUNCH TOT("Mg")*GFW("Mg")*1e3
 90 PUNCH TOT("Fe")*GFW("Fe")*1e3
100 PUNCH TOT("Na")*GFW("Na")*1e3
110 PUNCH TOT("K")*GFW("K")*1e3
120 PUNCH TOT("S(6)")*(GFW("S")+4*GFW("O"))*1e3
130 PUNCH ALK*GFW("Alkalinity")*1e3
140 PUNCH TOT("Cl")*GFW("Cl")*1e3
150 PUNCH TOT("Br")*GFW("Br")*1e3
160 PUNCH TOT("N(5)")*(GFW("N")*3*GFW("O"))*1e3
170 PUNCH TOT("F")*GFW("F")*1e3
180 PUNCH TOT("Si")*GFW("Si")*1e3
190 TDS = 1e3*(TOT("Ca")*GFW("Ca") + TOT("Mg")*GFW("Mg") +
TOT("Na")*GFW("Na") + TOT("K")*GFW("K") + TOT("S(6)")*(GFW("S")+4*GFW("O")) +
TOT("Cl")*GFW("Cl") + TOT("Br")*GFW("Br") + TOT("F")*GFW("F") +
ALK*GFW("Alkalinity")+ TOT("N(5)")*(GFW("N")+3*GFW("O")) +
TOT("Si")*(GFW("Si")+2*GFW("O")) + TOT("Fe")*GFW("Fe") + TOT("Al")*GFW("Al") +
TOT("Mn")*GFW("Mn"))
200 PUNCH TDS
210 PUNCH SC
220 PUNCH MU
230 SR_BaRa_SO4ss = SR("Barite")+ SR("Ra(SO4)(s)")
240 SI_BaRa_SO4ss = LOG10(SR_BaRa_SO4ss)
250 PUNCH SR_BaRa_SO4ss
260 PUNCH SI_BaRa_SO4ss
270 SR_ccCaRa_CO3ss = SR("Calcite") + SR("Ra(CO3)(s)")
280 SI_ccCaRa_CO3ss = LOG10(SR_ccCaRa_CO3ss)
290 PUNCH SR_ccCaRa_CO3ss
300 PUNCH SI_ccCaRa_CO3ss
310 SR_CaRa_CO3ss = SR("Aragonite") + SR("Ra(CO3)(s)")
```

```
320 SI_CaRa_CO3ss = LOG10(SR_CaRa_CO3ss)
330 PUNCH SR_CaRa_CO3ss
340 PUNCH SI_CaRa_CO3ss
350 MOLES_BaRaSO4_ss = LIST_S_S("(BaRa)SO4_ss", count, comp$, moles)
360 IF MOLES_BaRaSO4_ss = 0 THEN GOTO 470
370 MOLES_BaSO4_ss = SUM_S_S("(BaRa)SO4_ss", "Ba")
380 MOLES_RaSO4_ss = SUM_S_S("(BaRa)SO4_ss", "Ra")
390 xBaSO4 = MOLES_BaSO4_ss / MOLES_BaRaSO4_ss
400 xRaSO4 = MOLES_RaSO4_ss / MOLES_BaRaSO4_ss
410 kBaSO4 = 10^(LK_PHASE("Barite"))
420 kRaSO4 = 10^(LK_PHASE("Ra(SO4)(s)"))
430 KssSO4 = 10^(xBaSO4*log10(kBaSO4) + xRaSO4*log10(kRaSO4))
440 REM SRssSO4 is sum of saturation ratios (IAP/K) of pure phases. SRssSO4 >1.0 indicates
solid solution should form. SRssSO4 = 1.0 indicates equilibrium with solid solution
450 SRssSO4 = SR("Barite") + SR("Ra(SO4)(s)")
460 SIssSO4 = LOG10(SRssSO4)
470 PUNCH MOLES_BaRaSO4_ss
480 PUNCH MOLES_BaSO4_ss
490 PUNCH MOLES_RaSO4_ss
500 PUNCH xBaSO4
510 PUNCH xRaSO4
520 PUNCH kBaSO4
530 PUNCH kRaSO4
540 PUNCH KssSO4
550 PUNCH SRssSO4
560 PUNCH SIssSO4
570 MOLES_CaRaCO3_ss = LIST_S_S("(CaRa)CO3_ss", count, comp$, moles)
580 IF MOLES_CaRaCO3_ss = 0 THEN GOTO 690
590 MOLES_CaCO3_ss = SUM_S_S("(CaRa)CO3_ss", "Ca")
600 MOLES_RaCO3_ss = SUM_S_S("(CaRa)CO3_ss", "Ra")
610 xCaCO3 = MOLES_CaCO3_ss / MOLES_CaRaCO3_ss
620 xRaCO3 = MOLES_RaCO3_ss / MOLES_CaRaCO3_ss
630 kCaCO3 = 10^(LK_PHASE("Calcite"))
640 kRaCO3 = 10^(LK_PHASE("Ra(CO3)(s)"))
650 KssCO3 = 10^(xCaCO3*log10(kCaCO3) + xRaCO3*log10(kRaCO3))
660 REM SRssCO3 is sum of saturation ratios (IAP/K) of pure phases. SRssCO3 >1.0 indicates
solid solution should form. SRssCO3 = 1.0 indicates equilibrium with solid solution.
670 SRssCO3 = SR("Aragonite") + SR("Ra(CO3)(s)")
680 SIssCO3 = LOG10(SRssCO3)
690 PUNCH MOLES_CaRaCO3_ss
700 PUNCH MOLES_CaCO3_ss
710 PUNCH MOLES_RaCO3_ss
720 PUNCH xCaCO3
730 PUNCH xRaCO3
740 PUNCH kCaCO3
750 PUNCH kRaCO3
```

```
760 PUNCH KssCO3
770 PUNCH SRssCO3
780 PUNCH SIssCO3
   -end

END
```

B-3.2 Example PHREEQC model for Ra sorption to hydrous iron oxides (HFO) and hydrous manganese oxides (HFO)

```
TITLE Radium cycling in a hydrocarbon plume, MP-19S Port 4

# DATABASE C:\Program Files (x86)\USGS\Phreeqc Interactive 3.4.0-
12927\database\phreeqc.dat
# Program to assess potential for radium sorption to hydrous Fe oxides (HFO) and hydrous
manganese oxides (HMO)
# Ra species and phases from thermodynamic database of Giffaut et al. (2014) Andra
thermodynamic database for performance assessment: ThermoChimie. Applied Geochemistry,
49: 225-236.
# Thermochimie SIT.DAT database for PHREEQC accessed at https://www.thermochimie-
tdb.com/pages/publi.php
# Thermodynamic data for Ra(SO4)(s) and Ra(CO3)(s) from Langmuir, Donald, and Riese, A.C.
(1985) The thermodynamic properties of radium: Geochimica et Cosmochimica Acta (49)1593-
1601.

SOLUTION_MASTER_SPECIES
#element        #species alk    #gfw_formula #element_gfw
   Ra           Ra+2           0    Ra             226.02

SOLUTION_SPECIES
#Radium aqueous species
#Ra+2
Ra+2 = Ra+2
   log_k     0
#RaOH+
-1.000H+ + 1.000Ra+2 + 1.00H2O = RaOH+
   log_k     -13.49
   delta_h   60.417 kJ/mol    #85LAN/RIE
#Ra(OH)2
-2.00H+ + 1.000Ra+2 + 2.000H2O = Ra(OH)2
   log_k     -28.07
   delta_h   112.197 kJ/mol
#RaCl+
+1.000Ra+2 + 1.000Cl- = RaCl+
   log_k     -0.1    #85LAN/RIE
   delta_h   2.479 kJ/mol
```

```
#RaCl2
+1.000Ra+2 + 2.00Cl- = RaCl2
   log_k     -0.1
   delta_h   0.495 kJ/mol
#RaHCO3+
+1.000H+ + 1.000Ra+2 + 1.000CO3-2 = RaHCO3+
   log_k     10.92   #01ILE/TWE
#RaCO3
+1.000Ra+2 + 1.000CO3-2 = RaCO3
   log_k     2.5    #99SCH
   delta_h   4.496 kJ/mol
#RaSO4
+1.000Ra+2 + 1.000SO4-2 = RaSO4
   log_k     2.76
   delta_h   5.472 kJ/mol
#RaF+
+1.000Ra+2 + 1.000F- = RaF+
   log_k     0.48    #87BRO/WAN

#Starting solution composition: groundwater sample collected at MP-19S Port 4
SOLUTION 1 MP-19S Port 4
   temp      11.48
   pH        6.62
   pe        0.92
   redox     pe
   units     mg/l
   density   1
   Al        0.1 #guesstimate
   Alkalinity 334 as Ca0.5(CO3)0.5
   Ba        104 ug/l
   Br        0.002
   Ca        126
   Cl        240
   F         0.14
   Fe        18.3
   K         0.84
   Mg        62.7
   Mn        913 ug/l
   N(5)      0.12
   Na        8.9
   Ra        7.99e-016 Mol/l
   S(6)      8.4
   Si        11.1 as Si
   Sr        106 ug/l
   -water    1 # kg
```

```
PHASES
#Radium solid phases from sit.dat and Langmuir and Riese, included in sit.dat
Ra(cr)
   Ra = Ra+2 + 2e-
   log_k     98.44
   delta_h   -528.025 kJ
   -analytical_expression -0.0881751 0 42193.6 0 0 0
Ra(NO3)2(s)
   Ra(NO3)2 = 2NO3- + Ra+2
   log_k     -2.21
   delta_h   49.981 kJ
Ra(SO4)(s)
   Ra(SO4) = Ra+2 + SO4-2
   log_k     -10.26    #99SCH, 85LAN/RIE
   delta_h   -9.4 kcal
   -analytical_expression -3.44327 0 -2032.41 0 0 0
RaCl2:2H2O(s)
   RaCl2:2H2O = 2Cl- + 2H2O + Ra+2
   log_k     -0.73
   delta_h   32.221 kJ
   -analytical_expression 4.91469 0 -1682.97 0 0 0
Ra(OH)2(s)
   Ra(OH)2 + 2H+ = 2H2O + Ra+2
   log_k     30.99
   delta_h   -149.762 kJ
   -analytical_expression 4.75269 0 7822.65 0 0 0
Ra(CO3)(s)
   Ra(CO3) = CO3-2 + Ra+2
   log_k     -8.3   #85LAN/RIE
   delta_h   -2.8 kcal
   -analytical_expression -5.95418 0 -699.407 0 0 0

#Mineral phases from wateq4f.dat not included in phreeqc.dat
Magnesite
   MgCO3 = CO3-2 + Mg+2
   log_k     -8.029
   delta_h   -6.169 kcal
Dolomite
   CaMg(CO3)2 = 2CO3-2 + Ca+2 + Mg+2
   log_k     -17.09
   delta_h   -9.436 kcal
   -Vm       64.5 cm3/mol
Dolomite(d)
   CaMg(CO3)2 = 2CO3-2 + Ca+2 + Mg+2
   log_k     -16.54
   delta_h   -11.09 kcal
```

```
Dolomite2
   Ca0.5Mg0.5CO3 = CO3-2 + 0.5Ca+2 + 0.5Mg+2
   log_k     -8.5045  #17.09/2
   delta_h   -4.718 kcal   #9.436/2
Chlorite
   Mg5Al2Si3O10(OH)8 + 16H+ = 2Al+3 + 6H2O + 3H4SiO4 + 5Mg+2
   log_k     68.38
   delta_h   -151.494 kcal
Kmica
   KAl3Si3O10(OH)2 + 10H+ = 3Al+3 + 3H4SiO4 + K+
   log_k     12.703
   delta_h   -59.376 kcal
Mirabilite
   Na2SO4:10H2O = 10H2O + 2Na+ + SO4-2
   log_k     -1.114
   delta_h   18.987 kcal
Birnessite
   MnO2 + 4H+ + 2e- = 2H2O + Mn+2
   log_k     43.601

#Iron, manganese, and sulfate minerals from various sources
Schwert(1.75)
   Fe8O8(OH)4.5(SO4)1.75 + 20.5H+ = 8Fe+3 + 12.5H2O + 1.75SO4-2
   log_k     18   #Bigham and others (1996, GCA 60:2111-2121)
Schwert(1.00)
   Fe8O8(OH)6.0(SO4)1.00 + 22H+ = 8Fe+3 + 14H2O + SO4-2
   log_k     9.6   #Majzlan and others (2004, GCA 68:1049-1059)
Fe(OH)2_(a)
   Fe(OH)2 + 2H+ = Fe+2 + 2H2O
   log_k     12.76   #sit.dat
   delta_h   -99.096 kJ   #sit.dat
Mn-siderite
   Fe0.95Mn0.05CO3 = CO3-2 + 0.95Fe+2 + 0.05Mn+2
   log_k     -10.89
   delta_h   -2.48 kcal
   -Vm       29.2 cm3/mol
Rhodochrosite
   MnCO3 = CO3-2 + Mn+2
   log_k     -11.13
   delta_h   -1.43 kcal
   -Vm       31.1 cm3/mol
Manganite
   MnOOH + 3H+ + e- = 2H2O + Mn+2
   log_k     25.34
#   Mn+2 = Mn+3 + e-
#   log_k          -25.51
```

```
#   MnOOH + 3 H+ = Mn+3 + 2 H2O # combined above reactions from wateq4f.dat
#   log_k -0.17
Pyrochroite
   Mn(OH)2 + 2H+ = 2H2O + Mn+2
   log_k     15.2
Basaluminite
   Al4(OH)10SO4 + 10H+ = 4Al+3 + 10H2O + SO4-2
   log_k     22.7   #Wateq
Gypsum
   CaSO4:2H2O = Ca+2 + 2H2O + SO4-2
   log_k     -4.58
   delta_h   -0.109 kcal
   -analytical_expression 68.2401 0 -3221.51 -25.0627 0 0
   -Vm       73.9 cm3/mol
Ettringite
   Ca6Al2.02(SO4)2.79(OH)12.48:26H2O + 12.48H+ = 2.02Al+3 + 6Ca+2 + 38.48H2O +
2.79SO4-2
   log_k     61.82
#Myneni and others (1998, Chemical Geology, 148:1-19) log_k     -112.9 (+ 12.48*14)
Epsomite
   MgSO4:7H2O = 7H2O + Mg+2 + SO4-2
   log_k     -2.14
   delta_h   2.82 kcal
Todorokite
   Mn7O12:3H2O + 24H+ + 10e- = 15H2O + 7Mn+2
   log_k     225.6759   #expressed as Mn+2, llnl.dat
Sylvite
   KCl = Cl- + K+
   log_k     0.9121
   delta_h   17.221 kJ   #Robie, Hemingway, and Fisher (1978, USGS Bull 1452)
Celestine
   SrSO4 = SO4-2 + Sr+2
   log_k     -6.63
   delta_h   -1.037 kcal
   -analytical_expression -14805.9622 -2.4660924 756968.533 5436.3588 -40553604 0
SrSiO3
   SrSiO3 + H2O = H2SiO4-2 + Sr+2
   log_k     -8.1162   #14.8438 - 22.96, llnl.dat
Barite
   BaSO4 = Ba+2 + SO4-2
   log_k     -9.97
   delta_h   6.35 kcal
   -analytical_expression 136.035 0 -7680.41 -48.595 0 0

#Phase added for adsorption modeling
Fix_H+
```

```
   H+ = H+
   log_k     0

#Minerals are allowed to precipitate, but not dissolve
EQUILIBRIUM_PHASES 1
   Fe(OH)3(a) 0 0
   Manganite 0 0

SURFACE_MASTER_SPECIES
# Hydrous Ferric Oxide, Goethite or Fe(OH)3(a), monoprotic, diffuse double layer model of
Dzombak and Morel (1990)
   Hfo_s        Hfo_sOH       #HFO, strong sites, equilibrium
   Hfo_w        Hfo_wOH     #HFO, weak sites, equilibrium
   Hfop_s       Hfop_sOH     #HFO, strong sites, specified
   Hfop_w       Hfop_wOH  #HFO, weak sites, specified

# Hydrous Manganese Oxide, Birnessite or manganite, monoprotic, diffuse double layer model
of Tonkin et al. (2004)
   Hmo_x        Hmo_xOH      #HMO, strong sites, equilibrium
   Hmo_y        Hmo_yOH      #HMO, weak sites, equilibrium
   Hmop_x       Hmop_xOH   #HMO, strong sites, specified
   Hmop_y       Hmop_yOH   #HMO, weak sites, specified
SURFACE_SPECIES
#Hydrous Ferric Oxide, Hfo, surfaces from Dzombak and Morel (1990, Surface Complexation
Modeling, Hydrous Ferric Oxide: New York, John Wiley & Sons, 393 p.)

#strong binding site—Hfo_s
Hfo_sOH = Hfo_sOH
   log_k     0
H+ + Hfo_sOH = Hfo_sOH2+
   log_k     7.29    #Dzombak and Morel, 1990 -logKa1,int Table 5.7(pKa range 7.15 to 7.43)
Hfo_sOH = Hfo_sO- + H+
   log_k     -8.93   #Dzombak and Morel, 1990 -logKa1,int Table 5.7(pKa range 7.15 to 7.43)
#weak binding site—Hfo_w
Hfo_wOH = Hfo_wOH
   log_k     0
H+ + Hfo_wOH = Hfo_wOH2+
   log_k     7.29    #Dzombak and Morel, 1990 -logKa1,int Table 5.7(pKa range 7.15 to 7.43)
Hfo_wOH = Hfo_wO- + H+
   log_k     -8.93   #Dzombak and Morel, 1990 -logKa1,int Table 5.7(pKa range 7.15 to 7.43)

#Ra sorption by HFO equilibrium expressions by Sajih et al. 2014, GCA.146.150–163
(supplementary S3-S4)
Hfo_sOH + Ra+2 = Hfo_sOHRa+2
   log_k     6.66
Hfo_wOH + Ra+2 = Hfo_wORa+ + H+
```

```
   log_k     -5.67

#Hydrous Manganese Oxide, Hmo, surfaces from Tonkin et al. (2004, Applied Geochemistry 19,
29-53, Table 4)
Hmo_xOH = Hmo_xOH    #a = 0.64,  fraction of total sites as XOH
   log_k     0
H+ + Hmo_xOH = Hmo_xOH2+
   log_k     2.35    #logKa2(XOH) (pKa range 2.269 to 2.422 at 95% CI; protons on right)
Hmo_xOH = Hmo_xO- + H+
   log_k     -6.06   #logKa2(XOH) (pKa range 6.017 to 6.096 at 95% CI; protons on right)
Hmo_yOH = Hmo_yOH   #1-a = 0.36,  fraction of total sites as YOH
   log_k     0
H+ + Hmo_yOH = Hmo_yOH2+
   log_k     2.35   #logKa2(YOH) (pKa range 2.269 to 2.422 at 95% CI; protons on right)
Hmo_yOH = Hmo_yO- + H+
   log_k     -6.06   #logKa2(YOH) (pKa range 6.017 to 6.096 at 95% CI; protons on right)

#Ra surface species estimated using LFER and LOG_Kmoh after Tonkin et al. (2004, table5 &
fig. 15) and Porret-Davranche (2013, tables 2 and 3)
#LFER: log_KXOMe+  =  -1.372 + logKMOH * 0.273
#LFER: log_KXOMeOH =  -8.422 + logKMOH * 0.916
#LFER: log_KYOMe+  = -11.987 + logKMOH * 2.198
#LFER: log_KYOMeOH = -16.557 + logKMOH * 1.969
#Radium, log_Kmoh = 0.51
Hmo_xOH + Ra+2 = Hmo_xORa+ + H+    #KXOMe+
   log_k     -1.2
H2O + Hmo_xOH + Ra+2 = Hmo_xORaOH + 2H+    #KXOMeOH
   log_k     -8
Hmo_yOH + Ra+2 = Hmo_yORa+ + H+    #KYOMe+
   log_k     -10.9
H2O + Hmo_yOH + Ra+2 = Hmo_yORaOH + 2H+    #KYOMeOH
   log_k     -15.6

#For specified fixed amount of surfaces, notation Hfop_ and Hmop_ is used
#Surface and speciation constants are repeated using above notation
#Hydrous Ferric Oxide (HFO) specified amount as FeIII solid
#strong binding site—Hfop_s
Hfop_sOH = Hfop_sOH
   log_k     0
H+ + Hfop_sOH = Hfop_sOH2+
   log_k     7.29   #Dzombak and Morel, 1990 -logKa1,int Table 5.7(pKa range 7.15 to 7.43)
Hfop_sOH = Hfop_sO- + H+
   log_k     -8.93   #Dzombak and Morel, 1990 -logKa1,int Table 5.7(pKa range 7.15 to 7.43)
#weak binding site—Hfop_w
Hfop_wOH = Hfop_wOH
   log_k     0
```

```
H+ + Hfop_wOH = Hfop_wOH2+
   log_k     7.29   #Dzombak and Morel, 1990 -logKa1,int Table 5.7(pKa range 7.15 to 7.43)
Hfop_wOH = Hfop_wO- + H+
   log_k     -8.93   #Dzombak and Morel, 1990 -logKa1,int Table 5.7(pKa range 7.15 to 7.43)
#Ra sorption by HFO equilibrium expressions by Sajih et al. 2014, GCA.146.150–163
(supplementary S3-S4)
Hfop_sOH + Ra+2 = Hfop_sOHRa+2
   log_k     6.66
Hfop_wOH + Ra+2 = Hfop_wORa+ + H+
   log_k     -5.67

# Hydrous Manganese Oxide, Hmo, specified amount as MnIII solid
Hmop_xOH = Hmop_xOH   #a = 0.64,  fraction of total sites as XOH
   log_k     0
Hmop_xOH  + H+ = Hmop_xOH2+
   log_k     2.35   #logKa2(XOH) (pKa range 2.269 to 2.422 at 95% CI; protons on right)
Hmop_xOH = Hmop_xO- + H+
   log_k     -6.06   #logKa2(XOH) (pKa range 6.017 to 6.096 at 95% CI; protons on right)
Hmop_yOH = Hmop_yOH   #1-a = 0.36,  fraction of total sites as YOH
   log_k     0
Hmop_yOH  + H+ = Hmop_yOH2+
   log_k     2.35   #logKa2(YOH) (pKa range 2.269 to 2.422 at 95% CI; protons on right)
Hmop_yOH = Hmop_yO- + H+
   log_k     -6.06   #logKa2(YOH) (pKa range 6.017 to 6.096 at 95% CI; protons on right)

# Surface complexation constants for specified HMO surface
#Ra surface species estimated using LFER and LOG_Kmoh after Tonkin et al. (2004, table5 &
fig. 15) and Porret-Davranche (2013, tables 2 and 3)
#LFER: log_KXOMe+  =  -1.372 + logKMOH * 0.273
#LFER: log_KXOMeOH =  -8.422 + logKMOH * 0.916
#LFER: log_KYOMe+  = -11.987 + logKMOH * 2.198
#LFER: log_KYOMeOH = -16.557 + logKMOH * 1.969
#Radium, LOG_Kmoh = 0.51
Hmop_xOH + Ra+2 = Hmop_xORa+ + H+
   log_k     -1.2
Hmop_xOH + Ra+2 + H2O = Hmop_xORaOH + 2H+
   log_k     -8
Hmop_yOH + Ra+2 = Hmop_yORa+ + H+
   log_k     -10.9
Hmop_yOH + Ra+2 + H2O = Hmop_yORaOH + 2H+
   log_k     -15.6

SURFACE 1
#Hydrous Ferric Oxide, Hfo, surfaces from Dzombak and Morel (1990, Surface Complexation
Modeling: New York, John Wiley and Sons, 393 p.)
#Autocatalytic surface produced by kinetic oxidation OF FeII and precipitation of Fe(OH)3(a)
```

```
#HFO surface area 5.34E+4 m2/mol (=600 m2/g as FeOOH * 89 g/mol) with 0.005 mol strong sites, 0.2 mol weak sites (Dzombak and Morel, 1990, p. 92-94)
   Hfo_sOH Fe(OH)3(a)      equilibrium_phase 0.005  53400
   Hfo_wOH Fe(OH)3(a)      equilibrium_phase 0.2
#Specify HFO surface available in addition to autocatalytic
#Divide HFO conc. g/kg by 89 and then multiply strong sites by 0.005 and weak sites by 0.2
#HFO 20 g/kg is 20,000 mg/L as FeIII, 5.62e-5 mol strong sites/mol HFO = 0.005 mol sites x 1 g / 89 g/mol, 2.25e-3 mol weak sites/mol HFO = 0.2 mol sites x 1 g / 89 g/mol
   Hfop_sOH    5.62e-006    600       20
   Hfop_wOH    0.000225

#Hydrous Manganese Oxide, Hmo, surfaces from Tonkin et al. (2004, Applied Geochemistry 19, 29-53, Table 4)
#Autocatalytic surface produced by kinetic oxidation of MnII and precipitation of MnOOH
# HMO surface area 7.833E+4 m2/mol (= 746 m2/g * 105 g/mol);
#Xsites 0.141 mol/mol = 0.64*105 g/mol*2.1e-3 mol sites/g and Ysites 0.079 mol/mol = 0.36*105 g/mol*2.1e-3 mol sites/g
   Hmo_xOH Manganite       equilibrium_phase 0.141  78330
   Hmo_yOH Manganite       equilibrium_phase 0.079
#Specify HMO surface available in addition to autocatalyic
#HMO conc 0.35 g/kg (350 mg HMO/L); Asp 746 m2/g; 2.1x10-3 mol total sites/g; MnO2:H2O = 105 g/mol
##  Xsites 1.34e-3 mol = 0.64 * 2.1e-3 mol sites/g * 1 g; Ysites 0.76e-3 mol/g = 0.36 * 2.1e-3 mol sites/g * 1 g
   Hmop_xOH    0.000134    746       0.35
   Hmop_yOH    7.56e-005
   -donnan 1e-010

USE equilibrium_phases 1
USE solution 1
USE surface 1

TITLE MP-19S Port 4 Sorption to HFO and HMO

SELECTED_OUTPUT 1
   -file              MP-24S_Port4_sorption_Only_HFO_HMO.sel
   -simulation          false
   -distance           false
   -time               false
   -molalities          Ra+2  RaCl+  RaCl2  RaCO3
                      RaF+  RaHCO3+  RaOH+  RaSO4
                      Ra(OH)2  Hfo_wORa+  Hfo_sOHRa+2  Hfop_wORa+
                      Hfop_sOHRa+2  Hmo_xORa+  Hmo_xORaOH  Hmo_yORa+
                      Hmo_yORaOH  Hmop_xORa+  Hmop_xORaOH  Hmop_yORa+
                      Hmop_yORaOH
   -saturation_indices  Anhydrite  Aragonite  Barite  Birnessite
```

```
                Calcite Celestine Dolomite(d) Dolomite2
                Epsomite Fe(OH)3(a) Al(OH)3(a) Gypsum
                Halite Manganite Rhodochrosite Schwert(1.75)
                Siderite Strontianite Sylvite Witherite
                Ra(SO4)(s) Ra(CO3)(s) Mirabilite Kaolinite
                Illite

#User punch statements allow display of computed parameters in selected output
USER_PUNCH 1
   -headings pH Al.ug Mn.ug Sr.ug Ba.ug Ra.pg Ca.mg Mg.mg Fe.mg Na.mg K.mg SO4.mg
Alk.mg Cl.mg Br.mg NO3.mg F.mg Si.mg TDS.mg SC.uS IonStr.mol Ra_Hfo Ra_Hmo Ra_sor
   -start
 10 PUNCH -LA("H+")
 20 PUNCH TOT("Al")*GFW("Al")*1e6
 30 PUNCH TOT("Mn")*GFW("Mn")*1e6
 40 PUNCH TOT("Sr")*GFW("Sr")*1e6
 50 PUNCH TOT("Ba")*GFW("Ba")*1e6
 60 PUNCH TOT("Ra")*GFW("Ra")*1e12
 70 PUNCH TOT("Ca")*GFW("Ca")*1e3
 80 PUNCH TOT("Mg")*GFW("Mg")*1e3
 90 PUNCH TOT("Fe")*GFW("Fe")*1e3
100 PUNCH TOT("Na")*GFW("Na")*1e3
110 PUNCH TOT("K")*GFW("K")*1e3
120 PUNCH TOT("S(6)")*(GFW("S")+4*GFW("O"))*1e3
130 PUNCH ALK*GFW("Alkalinity")*1e3
140 PUNCH TOT("Cl")*GFW("Cl")*1e3
150 PUNCH TOT("Br")*GFW("Br")*1e3
160 PUNCH TOT("N(5)")*(GFW("N")*3*GFW("O"))*1e3
170 PUNCH TOT("F")*GFW("F")*1e3
180 PUNCH TOT("Si")*GFW("Si")*1e3
190 TDS = 1e3*(TOT("Ca")*GFW("Ca") + TOT("Mg")*GFW("Mg") +
TOT("Na")*GFW("Na") + TOT("K")*GFW("K") + TOT("S(6)")*(GFW("S")+4*GFW("O")) +
TOT("Cl")*GFW("Cl") + TOT("Br")*GFW("Br") + TOT("F")*GFW("F") +
ALK*GFW("Alkalinity")+ TOT("N(5)")*(GFW("N")+3*GFW("O")) +
TOT("Si")*(GFW("Si")+2*GFW("O")) + TOT("Fe")*GFW("Fe") + TOT("Al")*GFW("Al") +
TOT("Mn")*GFW("Mn"))
200 PUNCH TDS
210 PUNCH SC
220 PUNCH MU
230 Ra_Hfo = MOL("Hfo_sOHRa+2")+MOL("Hfo_wORa+")+ MOL("Hfop_sOHRa+2")+
MOL("Hfop_wORa+")
240 Ra_Hmo =
MOL("Hmo_xORa+")+MOL("Hmo_xORaOH")+MOL("Hmo_yORa+")+MOL("Hmo_yORaO
H")  +
MOL("Hmop_xORa+")+MOL("Hmop_xORaOH")+MOL("Hmop_yORa+")+MOL("Hmop_yO
RaOH")
```

```
250 Ra_sor = Ra_Hfo + Ra_Hmo
260 PUNCH Ra_Hfo
270 PUNCH Ra_Hmo
280 PUNCH Ra_sor
   -end

END
```

B-3.3 Example PHREEQC model for Ra sorption to illite

```
TITLE Radium cycling in a hydrocarbon plume, MP-19S Port 4

#DATABASE C:\Program Files (x86)\USGS\Phreeqc Interactive 3.4.0-
12927\database\phreeqc.dat
#Program to assess potential for Ra sorption to illite
#Ra species and phases from thermodynamic database of Giffaut et al. (2014) Andra
thermodynamic database for performance assessment: ThermoChimie. Applied Geochemistry,
49: 225-236.
#Thermochimie SIT.DAT database for PHREEQC accessed at https://www.thermochimie-
tdb.com/pages/publi.php
# Thermodynamic data for Ra(SO4)(s) and Ra(CO3)(s) from Langmuir, Donald, and Riese, A.C.
(1985) The thermodynamic properties of radium: Geochimica et Cosmochimica Acta (49)1593-
1601.

SOLUTION_MASTER_SPECIES
#element        #species alk    #gfw_formula #element_gfw
   Ra           Ra+2           0    Ra             226.02

SOLUTION_SPECIES
#Radium aqueous species
#Ra+2
Ra+2 = Ra+2
   log_k    0
#RaOH+
-1.000H+ + 1.000Ra+2 + 1.00H2O = RaOH+
   log_k    -13.49
   delta_h   60.417 kJ/mol   #85LAN/RIE
#Ra(OH)2
-2.00H+ + 1.000Ra+2 + 2.000H2O = Ra(OH)2
   log_k    -28.07
   delta_h   112.197 kJ/mol
#RaCl+
+1.000Ra+2 + 1.000Cl- = RaCl+
   log_k    -0.1   #85LAN/RIE
   delta_h   2.479 kJ/mol
#RaCl2
```

```
+1.000Ra+2 + 2.00Cl- = RaCl2
   log_k     -0.1
   delta_h   0.495 kJ/mol
#RaHCO3+
+1.000H+ + 1.000Ra+2 + 1.000CO3-2 = RaHCO3+
   log_k     10.92  #01ILE/TWE
#RaCO3
+1.000Ra+2 + 1.000CO3-2 = RaCO3
   log_k     2.5   #99SCH
   delta_h   4.496 kJ/mol
#RaSO4
+1.000Ra+2 + 1.000SO4-2 = RaSO4
   log_k     2.76
   delta_h   5.472 kJ/mol
#RaF+
+1.000Ra+2 + 1.000F- = RaF+
   log_k     0.48   #87BRO/WAN

#Starting solution composition: groundwater sample collected at MP-19S Port 4
SOLUTION 1 MP-19S Port 4
   temp      11.48
   pH        6.62
   pe        0.92
   redox     pe
   units     mg/l
   density   1
   Al        0.1 #guesstimate
   Alkalinity 334 as Ca0.5(CO3)0.5
   Ba        104 ug/l
   Br        0.002
   Ca        126
   Cl        240
   F         0.14
   Fe        18.3
   K         0.84
   Mg        62.7
   Mn        913 ug/l
   N(5)      0.12
   Na        8.9
   Ra        7.99e-16 Mol/l
   S(6)      8.4
   Si        11.1 as Si
   Sr        106 ug/l
   -water    1 # kg

PHASES
```

```
#Radium solid phases from sit.dat and Langmuir and Riese, included in sit.dat
Ra(cr)
   Ra = Ra+2 + 2e-
   log_k     98.44
   delta_h   -528.025 kJ
   -analytical_expression -0.0881751 0 42193.6 0 0 0
Ra(NO3)2(s)
   Ra(NO3)2 = 2NO3- + Ra+2
   log_k     -2.21
   delta_h   49.981 kJ
Ra(SO4)(s)
   Ra(SO4) = Ra+2 + SO4-2
   log_k     -10.26   #99SCH, 85LAN/RIE
   delta_h   -9.4 kcal  #Langmuir and Riese (1985) GCA(49)1593-1601
   -analytical_expression -3.44327 0 -2032.41 0 0 0
RaCl2:2H2O(s)
   RaCl2:2H2O = 2Cl- + 2H2O + Ra+2
   log_k     -0.73
   delta_h   32.221 kJ
   -analytical_expression 4.91469 0 -1682.97 0 0 0
Ra(OH)2(s)
   Ra(OH)2 + 2H+ = 2H2O + Ra+2
   log_k     30.99
   delta_h   -149.762 kJ
   -analytical_expression 4.75269 0 7822.65 0 0 0
Ra(CO3)(s)
   Ra(CO3) = CO3-2 + Ra+2
   log_k     -8.3  #Langmuir and Riese (1985) GCA(49)1593-1601
   delta_h   -2.8 kcal  #Langmuir and Riese (1985) GCA(49)1593-1601
   -analytical_expression -5.95418 0 -699.407 0 0 0

#Mineral phases from wateq4f.dat not included in phreeqc.dat
Magnesite
   MgCO3 = CO3-2 + Mg+2
   log_k     -8.029
   delta_h   -6.169 kcal
Dolomite
   CaMg(CO3)2 = 2CO3-2 + Ca+2 + Mg+2
   log_k     -17.09
   delta_h   -9.436 kcal
   -Vm       64.5 cm3/mol
Dolomite(d)
   CaMg(CO3)2 = 2CO3-2 + Ca+2 + Mg+2
   log_k     -16.54
   delta_h   -11.09 kcal
Dolomite2
```

```
   Ca0.5Mg0.5CO3 = CO3-2 + 0.5Ca+2 + 0.5Mg+2
   log_k     -8.5045 #17.09/2
   delta_h   -4.718 kcal  #9.436/2
Chlorite
   Mg5Al2Si3O10(OH)8 + 16H+ = 2Al+3 + 6H2O + 3H4SiO4 + 5Mg+2
   log_k     68.38
   delta_h   -151.494 kcal
Kmica
   KAl3Si3O10(OH)2 + 10H+ = 3Al+3 + 3H4SiO4 + K+
   log_k     12.703
   delta_h   -59.376 kcal
Mirabilite
   Na2SO4:10H2O = 10H2O + 2Na+ + SO4-2
   log_k     -1.114
   delta_h   18.987 kcal
Birnessite
   MnO2 + 4H+ + 2e- = 2H2O + Mn+2
   log_k     43.601

#Iron, manganese, and sulfate minerals from various sources
Schwert(1.75)
   Fe8O8(OH)4.5(SO4)1.75 + 20.5H+ = 8Fe+3 + 12.5H2O + 1.75SO4-2
   log_k     18   #Bigham and others (1996, GCA 60:2111-2121)
Schwert(1.00)
   Fe8O8(OH)6.0(SO4)1.00 + 22H+ = 8Fe+3 + 14H2O + SO4-2
   log_k     9.6   #Majzlan and others (2004, GCA 68:1049-1059)
Fe(OH)2_(a)
   Fe(OH)2 + 2H+ = Fe+2 + 2H2O
   log_k     12.76  #sit.dat
   delta_h   -99.096 kJ   #sit.dat
Mn-siderite
   Fe0.95Mn0.05CO3 = CO3-2 + 0.95Fe+2 + 0.05Mn+2
   log_k     -10.89
   delta_h   -2.48 kcal
   -Vm       29.2 cm3/mol
Rhodochrosite
   MnCO3 = CO3-2 + Mn+2
   log_k     -11.13
   delta_h   -1.43 kcal
   -Vm       31.1 cm3/mol
Manganite
   MnOOH + 3H+ + e- = 2H2O + Mn+2
   log_k     25.34
#  Mn+2 = Mn+3 + e-
#  log_k          -25.51
#  MnOOH + 3 H+ = Mn+3 + 2 H2O # combined above reactions from wateq4f.dat
```

```
#  log_k -0.17
Pyrochroite
   Mn(OH)2 + 2H+ = 2H2O + Mn+2
   log_k     15.2
Basaluminite
   Al4(OH)10SO4 + 10H+ = 4Al+3 + 10H2O + SO4-2
   log_k     22.7  #Wateq
Gypsum
   CaSO4:2H2O = Ca+2 + 2H2O + SO4-2
   log_k     -4.58
   delta_h   -0.109 kcal
   -analytical_expression 68.2401 0 -3221.51 -25.0627 0 0
   -Vm       73.9 cm3/mol  #172.18 / 2.33  (Vm H2O = 13.9 cm3/mol)
Ettringite
   Ca6Al2.02(SO4)2.79(OH)12.48:26H2O + 12.48H+ = 2.02Al+3 + 6Ca+2 + 38.48H2O +
2.79SO4-2
   log_k     61.82
#Myneni and others (1998, Chemical Geology, 148:1-19) log_k     -112.9 (+ 12.48*14)
Epsomite
   MgSO4:7H2O = 7H2O + Mg+2 + SO4-2
   log_k     -2.14
   delta_h   2.82 kcal
Todorokite
   Mn7O12:3H2O + 24H+ + 10e- = 15H2O + 7Mn+2
   log_k     225.6759  #expressed as Mn+2, llnl.dat
Sylvite
   KCl = Cl- + K+
   log_k     0.9121
   delta_h   17.221 kJ  #Robie, Hemingway, and Fisher (1978, USGS Bull 1452)
Celestine
   SrSO4 = SO4-2 + Sr+2
   log_k     -6.63
   delta_h   -1.037 kcal
   -analytical_expression -14805.9622 -2.4660924 756968.533 5436.3588 -40553604 0
SrSiO3
   SrSiO3 + H2O = H2SiO4-2 + Sr+2
   log_k     -8.1162   #14.8438 - 22.96, llnl.dat
Barite
   BaSO4 = Ba+2 + SO4-2
   log_k     -9.97
   delta_h   6.35 kcal
   -analytical_expression 136.035 0 -7680.41 -48.595 0 0

#Phase added for adsorption modeling
Fix_H+
   H+ = H+
```

```
   log_k     0

SURFACE_MASTER_SPECIES
#Two site protolysis non electrostatic surface complexation and cation exchange model of
Bradbury and Baeyens (2005)
   Illiteb_w     Illiteb_wOH   #weak site b

SURFACE_SPECIES
Illiteb_wOH = Illiteb_wOH
   log_k     0
#protolysis reactions
H+ + Illiteb_wOH = Illiteb_wOH2+
   log_k     8.5 #Bradbury and Baeyens (2009), Table 9
Illiteb_wOH = Illiteb_wO- + H+
   log_k     -10.5  #Bradbury and Baeyens (2009), Table 9
#Surface complexation reaction
Illiteb_wOH + Ra+2 = Illiteb_wORa+ + H+
   log_k     -5  #Bradbury and Baeyens (2005), Table 9.5

SURFACE 1
   Illiteb_wOH    0.04 #Bradbury and Baeyens (2009), Table 9, site capacity in mol/kg
   -no_edl

EXCHANGE_MASTER_SPECIES
   Illite_ex     Illite_ex-

EXCHANGE_SPECIES
#exchange on planar sites
Illite_ex- = Illite_ex-
   log_k     0
Illite_ex- + Na+ = NaIllite_ex
   log_k     0
2NaIllite_ex + Ra+2 = Ra(Illite_ex)2 + 2Na+
   log_k     1.04  #Bradbury and Baeyens (2009), Table 5
H+ + NaIllite_ex = HIllite_ex + Na+
   log_k     0    #Bradbury and Baeyens (2009), Table 5
NaIllite_ex + K+ = KIllite_ex + Na+
   log_k     1.1 #Bradbury and Baeyens (2009), Table 5
2NaIllite_ex + Mg+2 = Mg(Illite_ex)2 + 2Na+
   log_k     1.04   #Bradbury and Baeyens (2009), Table 5
2NaIllite_ex + Ca+2 = Ca(Illite_ex)2 + 2Na+
   log_k     1.04   #Bradbury and Baeyens (2009), Table 5
3NaIllite_ex + Al+3 = Al(Illite_ex)3 + 3Na+
   log_k     1   #Bradbury and Baeyens (2009), Table 5

EXCHANGE 1
```

```
   NaIllite_ex 0.225
#Bradbury and Baeyens (2004), cation exchange capacity for Na-illite is 225 meq/kg
   -pitzer_exchange_gammas true

USE exchange 1
USE solution 1
USE surface 1

TITLE MP-19S Port 4 Sorption to Illite

SELECTED_OUTPUT 1
   -file              MP-19S_Port4_sorption_Only_Illite_no_equil.sel
   -simulation        false
   -distance          false
   -time              false
   -molalities        Ra+2  RaCl+  RaCl2  RaCO3
                      RaF+  RaHCO3+  RaOH+  RaSO4
                      Ra(OH)2  IlliteORa+  Ra(Illite_ex)2
   -saturation_indices  Anhydrite  Aragonite  Barite  Birnessite
                      Calcite  Celestine  Dolomite(d)  Dolomite2
                      Epsomite  Fe(OH)3(a)  Al(OH)3(a)  Gypsum
                      Halite  Manganite  Rhodochrosite  Schwert(1.75)
                      Siderite  Strontianite  Sylvite  Witherite
                      Ra(SO4)(s)  Ra(CO3)(s)  Mirabilite  Kaolinite
                      Illite

USER_PUNCH 1
   -headings pH Al.ug Mn.ug Sr.ug Ba.ug Ra.pg Ca.mg Mg.mg Fe.mg Na.mg K.mg SO4.mg
Alk.mg Cl.mg Br.mg NO3.mg F.mg Si.mg TDS.mg SC.uS IonStr.mol Ra_Illite.mol Ra_ex.mol
Ra_SC.mol
   -start
 10 PUNCH -LA("H+")
 20 PUNCH TOT("Al")*GFW("Al")*1e6
 30 PUNCH TOT("Mn")*GFW("Mn")*1e6
 40 PUNCH TOT("Sr")*GFW("Sr")*1e6
 50 PUNCH TOT("Ba")*GFW("Ba")*1e6
 60 PUNCH TOT("Ra")*GFW("Ra")*1e12
 70 PUNCH TOT("Ca")*GFW("Ca")*1e3
 80 PUNCH TOT("Mg")*GFW("Mg")*1e3
 90 PUNCH TOT("Fe")*GFW("Fe")*1e3
100 PUNCH TOT("Na")*GFW("Na")*1e3
110 PUNCH TOT("K")*GFW("K")*1e3
120 PUNCH TOT("S(6)")*(GFW("S")+4*GFW("O"))*1e3
130 PUNCH ALK*GFW("Alkalinity")*1e3
140 PUNCH TOT("Cl")*GFW("Cl")*1e3
150 PUNCH TOT("Br")*GFW("Br")*1e3
```

```
160 PUNCH TOT("N(5)")*(GFW("N")*3*GFW("O"))*1e3
170 PUNCH TOT("F")*GFW("F")*1e3
180 PUNCH TOT("Si")*GFW("Si")*1e3
190 TDS = 1e3*(TOT("Ca")*GFW("Ca") + TOT("Mg")*GFW("Mg") +
TOT("Na")*GFW("Na") + TOT("K")*GFW("K") + TOT("S(6)")*(GFW("S")+4*GFW("O")) +
TOT("Cl")*GFW("Cl") + TOT("Br")*GFW("Br") + TOT("F")*GFW("F") +
ALK*GFW("Alkalinity")+ TOT("N(5)")*(GFW("N")+3*GFW("O")) +
TOT("Si")*(GFW("Si")+2*GFW("O")) + TOT("Fe")*GFW("Fe") + TOT("Al")*GFW("Al") +
TOT("Mn")*GFW("Mn"))
200 PUNCH TDS
210 PUNCH SC
220 PUNCH MU
230 Ra_Illite = MOL("Ra(Illite_ex)2")+MOL("IlliteORa+")
240 PUNCH Ra_Illite
250 Ra_ex = MOL("Ra(Illite_ex)2")
260 PUNCH Ra_ex
270 Ra_SC = MOL("IlliteORa+")
280 PUNCH Ra_SC
   -end

END
```

B-4 References

1. Mathews, M., Scott, S., Gotkowitz, M., and Ginder-Vogel, M., *Association of radionuclide isotopes with aquifer solids in the Midwestern Cambrian-Ordovician aquifer system* ACS Earth and Space Chemistry, **2021**. *5*(2): p. 268-278.
2. Mathews, M., Scott, S.R., Gotkowitz, M.B., Hunt, R.J., and Ginder-Vogel, M., *Isotopic analysis of radium geochemistry at discrete intervals in the Midwestern Cambrian-Ordovician aquifer system.* Applied Geochemistry, **2022**. *142*.
3. Hunt, R.J. and Steuer, J.J., *Simulation of the Recharge Area for Frederick Springs, Dane County, Wisconsin*. 2000, U.S. Geological Survey. p. 33.
4. Cheng, H., Lawrence Edwards, R., Shen, C.-C., Polyak, V.J., Asmerom, Y., Woodhead, J., Hellstrom, J., Wang, Y., Kong, X., Spötl, C., Wang, X., and Calvin Alexander, E., *Improvements in 230Th dating, 230Th and 234U half-life values, and U–Th isotopic measurements by multi-collector inductively coupled plasma mass spectrometry.* Earth and Planetary Science Letters, **2013**. *371-372*: p. 82-91.
5. Meyer, J.R., Parker, B.L., Arnaud, E., and Runkel, A.C., *Combining high resolution vertical gradients and sequence stratigraphy to delineate hydrogeologic units for a contaminated sedimentary rock aquifer system.* Journal of Hydrology, **2016**. *534*: p. 505-523.

Appendix C

Supplementary information for Chapter 4

Table C-1 Percent contribution of groundwater from each stratigraphic unit to Brookfield Well 24 Original, with an open interval from the Sinnipee Group to the Mt Simon Formation (layers 3-13), and to Brookfield Well 24 Reconstructed, with an open interval to the Mt Simon Formation (layers 7-13), at a pumping rate of 2,725 m^3/d.

Well 24 Construction	Sinnipee (layer 3)	St Peter (layer 4)	Wonewoc (layer 5)	Eau Claire (layer 6)	Mt Simon (layers 7-11)	Fine-grained deposit (layer 12)	Base of Mt Simon (layer 13)
Original	0.34	20	20	10	41	0.07	8.4
Reconstructed	0	0	0	0	83	0.14	17

Table C-2 Flux from Layer 2 (the Maquoketa Formation) to Layer 3 (the Sinnipee Group) when the well of interest is constructed with an open interval from the Sinnipee Group to the Mt Simon Formation (layers 3-13, 'original'), and an open interval to the Mt Simon Formation (layers 7-13, 'reconstructed') for four simulations with increased pumping at the well of interest. In all simulations, the 20 background wells have pumping rates of 2,725 m^3/d.

Total pumping rate (m^3/day)	Flux, original (m^3/d)	Flux, reconstructed (m^3/d)
54,501	599	599
57,225	626	619
59,950	652	639
62,675	679	660

Table C-3 Travel times from the Maquoketa Formation (layer 2) to a well open from the Sinnipee Group to the Mt Simon Formation (layers 3-13) obtained by reverse particle tracking around the well, for four simulations with increased pumping at the well of interest. In all simulations, the 20 background wells have pumping rates of 2,725 m^3/d.

Total pumping rate (m^3/day)	Min travel time (days)	Max travel time (years)	Avg travel time (years)
54,501	98.5	575	445
57,225	64	507	300
59,950	48	455	242
62,675	38	433	212

Table C-4 Results from the sensitivity analysis for the model with the originally constructed well. Only those simulations with changes from base runs to the Eau Claire layer contribution, fine-grained deposit contribution, bottom layer Mt Simon contribution, and flux from the Eau Claire layer to the underlying Mt Simon layer are included.

Model with original well					
Hydrostratigraphic unit and Hydrologic Characteristic Varied	Hydrologic Value Simulated	Eau Claire Layer Contribution (%) Base run: 10%	Fine-grained Deposit Contribution (%) Base run: 0.07%	Bottom layer Mt Simon Contribution (%) Base run: 8.4%	Flux from Eau Claire to Mt Simon (m^3/d) Base run: 103 m^3/d
Eau Claire Layer					
K_h (m/d)	0.18	2.7	0.076	9.1	17
	1.1	15	0.067	8.0	17
K_v (m/d)	0.000012	10	0.070	8.4	0.32
	0.0014	10	0.071	8.4	111
Thickness (m)	30	7.0	0.073	8.7	133
	80	17	0.065	7.8	60
Fine-grained Deposit					
K_h (m/d)	0.000091	10	0.00014	8.4	104
	0.091	10	0.14	8.4	103
Thickness (m)	1	10	0.014	8.4	105
	10	10	0.14	8.4	103
Mt Simon Layer					
K_h (m/d)	0.37	15	0.10	4.2	91
	1.8	7.7	0.054	11	97
K_v (m/d)	0.000037	10	0.070	8.4	22
	0.012	10	0.071	8.4	108

Table C-5 Results from the sensitivity analysis for the model with the reconstructed well. Only those simulations with changes from base runs to the Eau Claire layer contribution, fine-grained deposit contribution, bottom layer Mt Simon contribution, and flux from the Eau Claire layer to the underlying Mt Simon layer are included.

Model with reconstructed well					
Hydrostratigraphic unit and Hydrologic Characteristic Varied	Hydrologic Value Simulated	Eau Claire Layer Contribution (%) Base run: 0%	Fine-grained Deposit Contribution (%) Base run: 0.14%	Bottom Layer Mt Simon Contribution (%) Base run: 17%	Flux from Eau Claire to Mt Simon (m^3/d) Base run: 1034 m^3/d
Eau Claire Layer					
K_h (m/d)	0.18	0	0.14	17	971
	1.1	0	0.14	17	1072
K_v (m/d)	0.000012	0	0.14	17	44
	0.0014	0	0.14	17	1081
Thickness (m)	30	0	0.14	17	1122
	80	0	0.14	17	894
Fine-grained Deposit					
K_h (m/d)	0.000091	0	0.00028	17	1035
	0.091	0	0.28	17	1033
Thickness (m)	1	0	0.028	17	1052
	10	0	0.28	17	1027
Mt Simon Layer					
K_h (m/d)	0.37	0	0.41	16	1771
	1.8	0	0.086	17	752
K_v (m/d)	0.000037	0	0.14	17	239
	0.012	0	0.14	17	1071

C-1 Sensitivity analysis results

The results of the sensitivity analysis show that the contribution of groundwater from the Eau Claire (layer 6) to the originally constructed well is sensitive to the K_h and thickness of the Eau Claire layer and the K_h of the Mt Simon layers. The contribution of groundwater from the fine-grained deposit to the original and reconstructed wells is sensitive to the K_h and thickness of the fine-grained deposit, and the K_h of the Mt Simon layers. The K_h of the Mt Simon layers influences the contribution of groundwater from the bottom layer of the Mt Simon to the original

well, but does not have a significant effect on the contribution of groundwater from the bottom layer of the Mt Simon to the reconstructed well. Lastly, the flux from the Eau Claire layer to the underlying Mt Simon layer in the model with the originally constructed well is sensitive to the K_h, K_v, and thickness of the Eau Claire layer, and K_v of the Mt Simon layers. In the model with the reconstructed well, the flux from the Eau Claire layer to the underlying Mt Simon layer is sensitive to the K_v of the Eau Claire layer, as well as the K_h and K_v of the Mt Simon layers.

C-2 Solute transport modeling using MT3D-USGS

C-2.1 MT3D inputs

Dispersion, diffusion, and retardation were simulated using MT3D-USGS in steady-state mode with the groundwater flow model discussed in Chapter 4.[1, 2] Initial Ra concentrations were set to 925 mBq/L (25 pCi/L) in layers considered Ra "sources." These layers include the Maquoketa Formation shale (layer 2), Eau Claire Formation sandstone (layer 6), the fine-grained deposit within the Mt Simon Formation sandstone (layer 12), and the bottom layer of the Mt Simon (layer 13). Specified constant concentration boundaries were used on the left and right sides of the model, set as 925 mBq/L (25 pCi/L) in layers considered Ra sources and 0 mBq/L in all other layers. Radium sources were simulated across the entirety of the respective shale layer, as whole-rock Ra analysis of triplicate shale samples, including the Maquoketa Formation and Eau Claire Formation, demonstrate small variability.[3, 4] Longitudinal dispersivity of 1 m was estimated from the data of Gelhar et al. (1992)[5], with horizontal transverse dispersivity assigned as one order of magnitude lower than longitudinal dispersivity, and vertical transverse dispersivity assigned as two orders of magnitude lower than longitudinal dispersivity.[6] The effective molecular diffusion coefficient was estimated by correcting the molecular diffusion coefficient in open water by a tortuosity factor.[6] A value of 8.85×10^{-10} m^2/s was used for the Ra molecular diffusion coefficient

in open water.[7] Tortuosity factors of 0.1 for clay and 0.7 for sand were obtained from de Marsily (1986);[8] the tortuosity factor of 0.1 used for dolostone was scaled based on permeability relative to clay and sand.

Chemical reaction data for calculation of the retardation factor (R_f) includes effective porosity (Table 4.2), bulk density, and distribution coefficients (K_d). Bulk densities of modeled units were estimated using data from the Wisconsin Geology and Natural History Survey.[9] Radium sorption was simulated with a linear isotherm in MT3D. Retardation factors for Ra reported in the literature were converted to K_d values entered in MT3D using estimated porosities and bulk densities. A Ra R_f value of 10^4 was used for the oxic upper aquifer (layer 1), within the range reported for oxygenated, neutral pH groundwater.[10-12] The Maquoketa Shale and lower aquifer units (layers 2-13) were assumed anoxic due to confinement, and were therefore assigned a lower Ra R_f value of 10^3, consistent with reported values for anoxic groundwater.[10] First-order decay of ^{226}Ra and ^{228}Ra was also simulated by including half-lives of 1,600 and 5.75 years, respectively.

C-2.2 Preliminary MT3D results

C-2.2.1 ^{228}Ra

Simulations described for the MODFLOW flow model were also executed with MT3D-USGS using the fully-implicit finite-difference solver to obtain average ^{226}Ra and ^{228}Ra activities at the well in the center of the model under various well construction and pumping rates. The steady-state weighted average ^{228}Ra activity at the well was negligible (10^{-4}-10^{-5} pCi/L, or 10^{-3}-10^{-4} mBq/L) for all scenarios, as the majority of ^{228}Ra decays over the simulation due to its short half-life (5.75 years). This result provides support that ^{228}Ra is sourced from local ^{232}Th, and thus is not

transported far in the aquifer system. Therefore, the model results discussed below are only reported for ^{226}Ra.

C-2.2.2 Original vs. reconstructed well

When all Ra sources are simulated at a steady-state pumping rate of 2,725 m^3/d, the steady-state weighted average ^{226}Ra activity is 148 mBq/L (4.0 pCi/L) at the well with original construction (open from Sinnipee Group to Mt Simon Formation, layers 3-13), and increases to 237 mBq/L (6.4 pCi/L) when the well is reconstructed to extend past the Eau Claire layer (open to Mt Simon only, layers 7-11).

C-2.2.3 Radium source contributions

Radium sources were also simulated one at a time to evaluate their contribution to the original and reconstructed well. The Eau Claire layer and the bottom layer of the Mt Simon are the top contributors of Ra activity at both the original and reconstructed well, and the Ra activity contributed from the bottom layer of the Mt Simon approximately doubles when the well is reconstructed (Table C-6).

Table C-6 Average ^{226}Ra activity observed at the original and reconstructed wells when ^{226}Ra sources are simulated one at a time, at a steady-state pumping rate of 2,725 m^3/d.

Simulated source	^{226}Ra – original (mBq/L)	^{226}Ra – reconstructed (mBq/L)
Maquoketa Formation	4.4	0.36
Eau Claire Formation	74	81
Fine-grained deposit	0.52	1.4
Bottom of Mt Simon Formation	67	137

C-2.2.4 Increased pumping rate at the reconstructed well

Radium activities were evaluated with increasing pumping rates at the reconstructed well. When all sources are considered, ^{226}Ra activities at the reconstructed well do not exhibit a trend as the pumping rate at the reconstructed well is doubled and tripled (Table C-7). When Ra sources are evaluated one at a time and pumping is increased at the reconstructed well, trends in ^{226}Ra activity observed at the well vary by source (Table C-8).

Table C-7 Average ^{226}Ra activity observed at the reconstructed well when all ^{226}Ra sources are simulated and the pumping rate at the well is increased.

Pumping rate at reconstructed well (m^3/d)	^{226}Ra (mBq/L)
2,725	237
5,450	192
8,175	229

Table C-8 Average ^{226}Ra activity observed at the reconstructed well when ^{226}Ra sources are simulated one at a time and the pumping rate at the well is increased.

	Pumping rate at reconstructed well (m^3/d)		
Simulated source	2,725	5,450	8,175
	^{226}Ra (mBq/L)		
Maquoketa layer	0.36	0.78	1.0
Eau Claire layer	81	81	93
Fine-grained deposit	1.4	0.52	19
Bottom layer of Mt Simon	137	137	137

C-2.2.5 Distribution of pumping with additional wells

Total pumping was distributed across the reconstructed well and two additional wells with either original or reconstructed well construction. The Ra activity at the reconstructed well rises with the pumping rate for both scenarios (Table C-9).

Table C-9 Average ^{226}Ra activity observed at the reconstructed well when all ^{226}Ra sources are simulated and the pumping rate at the reconstructed well is distributed with two additional wells of either original or reconstructed well construction.

Total pumping rate across three wells (m^3/d)	Construction of additional wells	
	Original	Reconstructed
	^{226}Ra (mBq/L)	
2,725	192	192
5,450	192	204
8,175	237	237

C-2.2.6 Backfilling wells to reduce radium activity

Well construction was varied to evaluate the effectiveness of constructing wells shallower to reduce Ra activity at the well. The ^{226}Ra activity decreases when both the original and reconstructed well are backfilled to avoid contribution from the fine-grained deposit and the bottom of the Mt Simon Formation (Table C-10).

Table C-10 Average ^{226}Ra activity observed at the well when all ^{226}Ra sources are simulated and well construction is changed to avoid the fine-grained deposit (layer 12) and bottom layer of the Mt Simon (layer 13).

Well open interval	Model layers	^{226}Ra (mBq/L)
Sinnipee to Mt Simon (Original)	3-13	148
Sinnipee to top of fine-grained deposit	3-11	96
Entire Mt Simon (Reconstructed)	7-13	237
Mt Simon above fine-grained deposit	7-11	115

C-3 Numerical dispersion and the grid Peclet number

Oscillations in Ra activities are observed at the reconstructed well when pumping is increased (e.g., Tables C-7, C-8) and may be an artifact of numerical dispersion often encountered in numerical transport models.[13] The grid Peclet number, P_e, can be calculated using Equation C-1[6] and used to determine the criteria required to reduce numerical dispersion:

$$P_e = \frac{v\Delta x}{D} = \frac{\Delta x}{\alpha_L} \qquad \text{(C-1)}$$

where v is the advective velocity, Δx is the model grid spacing, D is the molecular diffusion coefficient, and α_L is the longitudinal dispersivity. When $P_e \leq 2$, physical dispersion dominates over numerical dispersion.[6] Using a grid spacing of 30.54 m and a molecular diffusion coefficient of 5.4E-05 m^2/d, P_e can be calculated for the model with the original well and the model with the reconstructed well. A steady-state pumping rate of 2,725 m^3/d is applied at all 21 model wells to yield a flux from the Eau Claire layer to the underlying Mt Simon layer in m^3/d. This flux can be converted to v by dividing by the model area in m^2. This yields a P_e of 0.6 for the model with the original well and 6 for the model with the reconstructed well.

The maximum v and corresponding maximum flux from the Eau Claire layer to the underlying Mt Simon layer required to keep $P_e \leq 2$ at the current model grid spacing can be calculated by setting the $P_e = 2$ and rearranging Equation C-1 to solve for v. Multiplying v by the model area yields a maximum flux of 330 m^3/d, where transport is dispersion (mechanical dispersion + diffusion)-dominant at a flux < 330 m^3/d, and advection-dominant at a flux > 330 m^3/d. Similarly, the maximum grid spacing required to keep $P_e \leq 2$ in the model with the reconstructed well can be calculated by rearranging Equation C-1 to solve for Δx, which yields a maximum grid spacing of 10 m; however, grid spacing will need to be smaller if pumping rate is increased at the well (i.e., v increases). Therefore, a finer resolution model with grid spacing ≤ 10 m could be implemented in future efforts.

C-4 Effect of hydraulic conductivity on advective flux from shale to the aquifer

The pumping rate at the reconstructed well is one important factor dictating the flux from the shale-rich Eau Claire layer to the underlying Mt Simon sandstone layer. However, the

hydraulic properties of the shale-rich unit, or the ratio of the hydraulic conductivity of the shale-rich unit to the hydraulic conductivity of the underlying sandstone, is also likely important in determining whether the flow regime from the shale-rich layer to the sandstone layer will be dominated by advection or diffusion. In this study, the K_v of the Eau Claire Formation was modeled as 0.0012 m/d, an estimate for southeastern Wisconsin. In other regions of southern Wisconsin (e.g., Dane County) the Eau Claire Formation has a more laterally extensive shale facies and thus has a lower K_v. Therefore, additional model runs were executed to decrease the vertical hydraulic conductivity of the Eau Claire layer by two orders of magnitude (i.e., K_v = 0.00012 and 0.000012 m/d), to demonstrate corresponding changes in the flux from the Eau Claire layer to the underlying Mt Simon layer (Figure C-1). The steady-state pumping rate at the well was held constant at 2,725 m^3/d. For reference, a K_v of 0.000012 m/d is on the same order of magnitude as the Maquoketa confining unit. These results demonstrate that the K_v of the Eau Claire layer or other shale-rich units will be an important factor in determining whether transport from the shale-rich units to the underlying aquifer will be advection or dispersion-dominant.

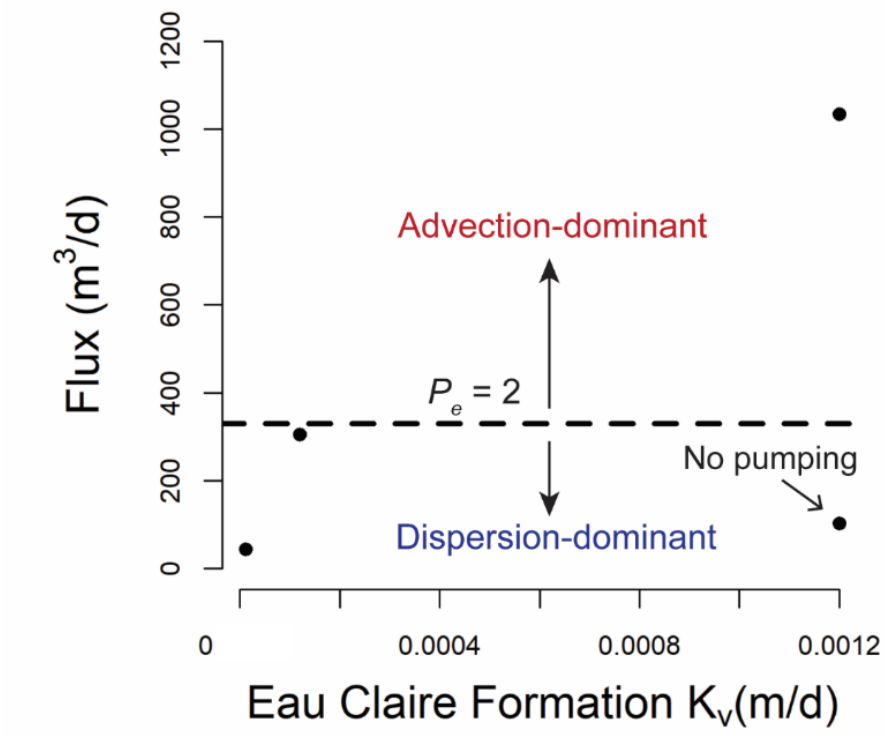

Figure C-1 Flux from the Eau Claire (layer 6) to the Mt Simon (layer 7) as a function of the Eau Claire vertical hydraulic conductivity (K_v). A constant steady-state pumping rate of 2,725 m^3/d is applied at each well in the model; flux without pumping at the reconstructed well as well as the minimum flux of 330 m^3/d required to keep the grid Peclet number (P_e) ≤ 2 at current model conditions are shown for reference.

C-5 Conclusions and future work

While these modeling efforts begin to incorporate diffusion, dispersion, and retardation, future efforts must address the observed oscillatory behavior (e.g., Tables C-7, C-8) and high mass balance concentration errors associated with model results. In some situations, the model results with simulated decay of ^{226}Ra are higher than results without simulated decay. These issues may be a consequence of numerical dispersion often encountered with transport modeling.[13] In some cases, numerical dispersion may be limited by using a different solver package; however, the steady-state approach used here can only be executed using the fully-implicit finite difference solver in Groundwater Vistas. In particular, transport at the aquifer-aquitard interface examined in

this work is complex. A smaller model with a simpler layer structure and fine resolution, especially in the z-direction, is required to minimize numerical dispersion and capture Ra transport from shale-rich layers to underlying aquifers. A cm-scale model may be required, as demonstrated by another study in which MT3D was unable to simulate solute transport at an aquifer-aquitard interface with 0.2 m grid spacing.[14] An analytical solution could be used to assess the validity of the results from the refined numerical model. While an analytical solution does not currently exist for the specific initial and boundary conditions used in this current model, the model boundary conditions could be revised such that the well of interest serves as a boundary condition, and an 2-D analytical solution for radial flow in a confined aquifer with an extraction well can be applied.[15]

C-6 References

1. Bedekar, V., Morway, E.D., Langevin, C.D., and Tonkin, M., *MT3D-USGS version 1.0.0: Groundwater Solute Transport Simulator for MODFLOW* U.S. Geological Survey Software Release, **2016**.
2. Bedekar, V., Morway, E.D., Langevin, C.D., and Tonkin, M., *MT3D-USGS version 1: A U.S. Geological Survey release of MT3DMS updated with new and expanded transport capabilities for use with MODFLOW6.* U.S. Geological Survey Techniques and Methods **2016**. *6*(A53): p. 69.
3. Mathews, M., Scott, S., Gotkowitz, M., and Ginder-Vogel, M., *Association of radionuclide isotopes with aquifer solids in the Midwestern Cambrian-Ordovician aquifer system* ACS Earth and Space Chemistry, **2021**. *5*(2): p. 268-278.
4. Mathews, M., Scott, S.R., Gotkowitz, M.B., Hunt, R.J., and Ginder-Vogel, M., *Isotopic analysis of radium geochemistry at discrete intervals in the Midwestern Cambrian-Ordovician aquifer system.* Applied Geochemistry, **2022**. *142*.
5. Gelhar, L.W., Welty, C., and Rehfeldt, K.R., *A critical review of data on field-scale dispersion in aquifers.* Water Resources Research, **1992**. *28*(7): p. 1955-1974.
6. Zheng, C. and Bennett, G.D., *Applied Contaminant Transport Modeling*. 2nd ed. 2002, New York: John Wiley and Sons, Inc.
7. Rumble, J.R.J., Bruno, T.J., and Doa, M.J.E., *CRC Handbook of Chemistry and Physics: A Ready-Reference Book of Chemical and Physical Data*. 101st ed. 2020, Boca Raton, FL: CRC Press, Taylor & Francis Group.
8. de Marsily, G., *Quantitative Hydrogeology: Groundwater Hydrology for Engineers*. 1986, San Diego: Academic Press. 440.
9. Wisconsin Geological and Natural History Survey. *Porosity and density measurements*. 2023; Available from: https://wgnhs.wisc.edu/maps-data/data/rock-properties/porosity-density-measurements-data/.
10. Copenhaver, S.A., Krishnaswami, S., Turekian, K.K., Epler, N., and Cochran, J.K., *Retardation of 238U and 232Th decay chain radionuclides in Long Island and Connecticut aquifers.* Geochimica et Cosmochimica Acta, **1993**. *57*(3): p. 597-603.
11. Krishnaswami, S., Graystein, W.C., and Turekian, K.K., *Radium, thorium and radioactive lead isotopes in groundwaters: Application to the in situ determination of adsorption-desorption rate constants and retardation factors.* Water Resources Research, **1982**. *18*(6): p. 1633-1675.
12. Luo, S., Ku, T.-L., Roback, R., Murrell, M., and McLing, T.L., *In-situ radionuclide transport and preferential groundwater flows at INEEL (Idaho): decay-series disequilibrium studies.* Geochimica et Cosmochimica Acta, **2000**. *64*(5): p. 867-881.
13. Zheng, C. and Wang, P., *MT3DMS : a modular three-dimensional multispecies transport model for simulation of advection, dispersion, and chemical reactions of contaminants in groundwater systems; documentation and user's guide*. 1999, Environmental Laboratory Engineer Research and Development Center.
14. Rezaei, A., Zhan, H., and Zare, M., *Impact of thin aquitards on two-dimensional solute transport in an aquifer.* Journal of Contaminant Hydrology, **2013**. *152*: p. 117-36.

15. Wallis, I., Prommer, H., Post, V., Vandenbohede, A., and Simmons, C.T., *Simulating MODFLOW-based reactive transport under radially symmetric flow conditions.* Groundwater, **2013**. *51*(3): p. 398-413.